



# Atomic scale insight into platinum based catalysts supported on chlorinated gamma-alumina

Ana Teresa Fialho Batista

## ► To cite this version:

Ana Teresa Fialho Batista. Atomic scale insight into platinum based catalysts supported on chlorinated gamma-alumina. Catalysis. Université de Lyon, 2019. English. NNT : 2019LYSEN062 . tel-03510238

**HAL Id: tel-03510238**

**<https://theses.hal.science/tel-03510238>**

Submitted on 4 Jan 2022

**HAL** is a multi-disciplinary open access archive for the deposit and dissemination of scientific research documents, whether they are published or not. The documents may come from teaching and research institutions in France or abroad, or from public or private research centers.

L'archive ouverte pluridisciplinaire **HAL**, est destinée au dépôt et à la diffusion de documents scientifiques de niveau recherche, publiés ou non, émanant des établissements d'enseignement et de recherche français ou étrangers, des laboratoires publics ou privés.



Numéro National de Thèse : 2019LYSEN062

## **THESE de DOCTORAT DE L'UNIVERSITE DE LYON**

opérée par  
**l'Ecole Normale Supérieure de Lyon**

**Ecole Doctorale N°206**  
**Ecole Doctorale de Chimie (Chimie, Procédés, Environnement)**

**Discipline : Chimie**

Soutenue publiquement le 15/11/2019, par :  
**Ana Teresa FIALHO BATISTA**

---

# **Atomic scale insight into platinum based catalysts supported on chlorinated gamma-alumina**

Exploration à l'échelle atomique de catalyseurs constitués de platine supporté sur alumine gamma chlorée

---

Devant le jury composé de :

VAN BOKHOVEN, Jeroen	Professeur ETH Zürich	Rapporteur
GIORGIO, Suzanne	Professeure des Universités CiNaM Marseille	Rapporteuse
LOFFREDA, David	Directeur de Recherche ENS de Lyon	Examineur
LE PELTIER, Fabienne	Ingénieure expert Axens	Examinatrice
GAY, Anne-Sophie	Ingénieure de recherche IFP Energies nouvelles	Examinatrice
RAYBAUD, Pascal	Ingénieur de recherche (H.D.R.) IFP Energies nouvelles	Directeur de thèse



# Acknowledgements

I would like to thank IFP Energies Nouvelles for the opportunity and funding to develop this work, which was conducted at the *Catalyse par les métaux et les solides acido-basiques* Department of the *Catalyse, biocatalyse et separation* Direction.

I would like to thank the jury members, David Loffreda and Fabienne Le Peltier, and the examiners, Jeroen van Bokhoven and Suzanne Giorgio, for having kindly accepted to read and judge this work.

I am grateful to my super team of supervisors: Pascal Raybaud, Fabrice Diehl, Céline Chizallet and Anne-Sophie Gay. They always worked with me and with each other in a constructive way. Their guidance, teachings and always pertinent discussions and corrections have allowed me to grow as a researcher.

I am thankful to all the colleagues who have welcomed me in the department and guided me throughout this work. Tivadar Cseri, former head of the department, for the interest shown in my work and motivating words. Reforming engineers Cécile Thomazeau, Thibaud Nardin and Jacques Lavy for their interest in my work and interesting discussions, and the reforming team Carine Guegan, Clara Voisin, Pascal Galguen and Cedrik Popelin for training me and guiding me in the laboratory.

I would like to acknowledge all the colleagues of the *Physique et analyse* Direction who have contributed immensely to this work. Anne-Lise Taleb, the master of the electron microscope, who trained me in STEM with kind and motivating words, who took an interest in my work from the start, who is always ready to help, to give counsel and to try something new, and with whom I shared great moments of conversation and laughter. Christèle Legens, for guiding me into the world of synchrotrons and XAS and keeping the good spirits and motivation while on the night shift. Laurent Lemaitre also keeps his smile on at 4 a.m. in a beamline and graciously participated in our synchrotron runs. Mickael Rivallan for accompanying and guiding me through NMR experiments and managing the cooperation with the CRMN as well as planning and interpretation of the IR experiments. Leonor Catita for participation on the last NMR experiments and associated data treatment as well as



useful discussions and counsel. Nicolas Girod for his participation in a synchrotron run and Isabelle Clemençon for the IR experiments.

The immensely valuable contribution of the IPCMS colleagues, in particular from Ovidiu Ersen, Walid Baaziz and Georgian Melinte, is here acknowledged as well as the lovely welcome offered by the whole IPCMS team. Thank you for sharing your expertise with me, in the form of advice, discussion, corrections and all the data you have produced, and for making me feel at home in your laboratory.

Likewise I would like to thank the CRMN team for their kind welcome and Anne Lesage and David Gajan for a fruitful and dynamic collaboration. In particular Dorothea Wisser who performed all the experiments and guided me in to the practicalities of solid state NMR while being kind, optimistic and resilient in the face of the Linux interface and of CP conditions that refuse to be found.

I would like to thank the ESRF FAME beamline staff for ensuring the success of our synchrotron runs. Jean-Louis Hazemann and Olivier Proux for their valuable advice for the data treatment. Antonio Aguilar-Tapia for being available to share “his” reactor and expertise, for pleasant discussions each time we met and for being a great session chair at CICAT XXVI. I would also like to thank Yves Joly from Institut Néel for having taken the time to introduce me to the FDMNES code and for performing useful calculations.

I would like to thank all the friends I have made during this work. My office mates for my first two years, Ester and Sophie for the (sometimes scientific) discussions and laughs. My office mates for my last year, Paul and Charlie. Colleagues on the path of the PhD who became friends, Damien, Larissa, Angelique, Elsy, Adrien, Olivier, Charlotte, Venkat. Fellow chemical engineers Angel, Kirill, Pierre-Yves.

I would like to thank my parents and my brother for their understanding and resilience in their unconditional and lasting support. I would like to thank Diogo for taking on this adventure by my side.

“You know,  
our hands reach out by themselves for the things we like.  
There’s no way to stop them.”  
– Natsume Soseki in *Sanshiro: a Novel*



# Abstract

Bifunctional heterogeneous catalysts consisting of metallic sites and acidic sites are used in various processes and the impact of active site proximity in catalytic efficiency can be expressed as an “intimacy criterion” according to the literature. Platinum supported on chlorinated  $\gamma$ - $\text{Al}_2\text{O}_3$  is the traditional catalyst for catalytic naphtha reforming and is at the core of the present work. Herein, a multi-technique approach, including HR-HAADF-STEM, electron tomography, high field MAS NMR, HERFD-XANES, EXAFS, and DFT calculations, was applied to determine the location of the metallic and acidic sites on the  $\text{Al}_2\text{O}_3$  support crystallites for Pt/ $\gamma$ - $\text{Al}_2\text{O}_3$ -Cl catalysts and to estimate the distance between such sites. The samples, representative of the industrial catalysts, were synthesized so as to vary the distance between the two types of sites as a function of three key parameters: %Pt, %Cl and  $\text{Al}_2\text{O}_3$  crystallite size and shape.

By building the first DFT model of crystallite edge between the (110) and (100) surfaces, an improved  $^1\text{H}$  NMR peak assignment was proposed and it was found that  $\mu_1\text{-OH}$  on the edge are preferably exchanged with Cl. STEM analysis showed that reduced Pt nanoparticles are of 0.9 nm and that around 20% of Pt is in the form of single atoms, which are stabilized by Cl. By electron tomography it was revealed that Pt nanoparticles are mostly located on the edges of alumina crystallites and that the quantified inter-Pt particles distance is directly tuned through %Pt. A first geometrical model of the location of Pt and Cl on the catalyst is proposed. The improved understanding of the location of active sites and their proximity in catalytic reforming catalysts gained through this work paves the way to catalyst improvement based on tuning of active site location.

**Key-words:** platinum, alumina, chlorine, STEM, DFT, NMR, XANES, EXAFS, tomography, nanoparticle, edge, reforming

# Résumé

Plusieurs procédés industriels utilisent des catalyseurs hétérogènes bifonctionnels avec des sites actifs métalliques et acides. L'influence de la distance entre les deux types de site actif sur l'activité et la sélectivité du catalyseur a souvent été décrite par un « critère d'intimité » dans la littérature. Les travaux reportés dans la présente thèse revisitent ce critère en étudiant des catalyseurs constitués de nanoparticules de platine supportées sur alumine gamma chlorée, utilisés en reformage catalytique des coupes pétrolières de type naphtas. Plusieurs techniques, dont la microscopie HR-HAADF-STEM, la tomographie électronique, les spectroscopies RMN MAS à hauts champs, HERFD-XANES, EXAFS et la simulation quantique (DFT), ont été utilisées pour déterminer la localisation des sites métalliques et acides sur les cristallites du support de façon à estimer la distance inter-sites. Les échantillons ont été préparés en faisant varier trois paramètres : teneur en Pt, teneur en Cl et taille et forme des cristallites.

Grâce au premier modèle DFT d'arête entre les surfaces (110) et (100) de l'alumine, une attribution plus détaillée des signaux  $^1\text{H}$  NMR a été proposée montrant que les hydroxyles  $\mu_1\text{-OH}$  des arêtes sont plus favorablement échangés avec le Cl. L'étude STEM a révélé des nanoparticules de Pt de 0.9 nm et des atomes isolés qui représentent environ 20% du Pt et qui sont stabilisés par le Cl. Par tomographie électronique, il a été montré que les nanoparticules de Pt sont localisées sur les arêtes des cristallites et que la distance entre elles varie en fonction du %Pt. Enfin, un modèle géométrique du système catalytique Pt/ $\gamma\text{-Al}_2\text{O}_3\text{-Cl}$  est proposé. Grâce à cette compréhension avancée de la localisation des sites actifs, ce travail ouvre la voie à des améliorations futures des performances de cette famille de catalyseurs grâce au contrôle à l'échelle atomique de l'emplacement des sites actifs.

**Mots clés :** platine, alumine, chlore, STEM, DFT, RMN, XANES, EXAFS, tomographie, nanoparticule, arête, reformage

# Résumé étendu

De nombreux procédés catalytiques industriels mettent en œuvre un catalyseur bifonctionnel constitué de nanoparticules de platine supportées sur alumine- $\gamma$  chlorée. Parmi ceux-ci, le reformage catalytique des coupes pétrolières de type naphthas permet la production d'essence à haut indice d'octane. La proximité entre les deux types de site actif (métallique et acide de Brønsted dopé par le chlore) et leur position relative peuvent avoir un impact sur les performances du catalyseur. Dans les travaux reportés dans la présente thèse, ces catalyseurs ont été étudiés à l'échelle atomique de façon à déterminer la localisation précise du platine et du chlore sur le support et quantifier la distance inter-sites.

Deux séries de catalyseurs avec différentes teneurs en Pt et en Cl ont été préparées sur deux supports d'alumine gamma préparés à partir de boehmites commerciales produites par Sasol® (PuralSB3 et TH100) présentant des cristallites de différentes tailles et morphologies. En faisant varier simultanément les teneurs en Pt et Cl, autour des niveaux utilisés dans l'industrie, il est attendu que la distance entre les sites actifs varie aussi et qu'un éventuel effet du Cl sur la phase métallique ou sur le support soit mis en évidence. Des échantillons d'alumine chlorée ont également été préparés pour étudier la chloration du support indépendamment de la présence de Pt.

Quatre techniques avancées ont été utilisées pour permettre cette étude à l'échelle atomique : la microscopie HR-HAADF-STEM (High Resolution High Annular Angle Dark Field Detector Scanning Transmission Electron Microscopy), la tomographie électronique, les spectroscopies HERFD-XANES et EXAFS (High Energy Resolved Fluorescence Detection X-ray Absorption Near Edge Structure et Extended X-ray Absorption Fine Structure), la RMN MAS (Magic Angle Spinning) à hauts champs et la simulation quantique (DFT, Density Functional Theory). Cette approche multi-technique a permis une caractérisation très avancée des catalyseurs.

En premier lieu, l'étude des deux support d'alumine gamma montre que les cristallites de TH100 sont larges et ont une forme parallélépipédique alors que celles de PuralSB3 sont plus petites et arrondies. Ainsi, les cristallites de PuralSB3 ont un rapport arête/surface supérieur à celui des cristallites de TH100.

Pour ces deux supports, le spectre de RMN du proton présente les caractéristiques attendues pour l'alumine gamma. Cependant, les différences constatées entre les spectres des deux alumines ne peuvent pas s'expliquer au moyen de l'attribution empirique classique. Grâce à la simulation quantique du déplacement chimique du proton des groupes OH, nous montrons que les spectres RMN de l'alumine ne peuvent pas être complètement décrits par la seule prise en compte des surfaces de l'alumine gamma. Une attribution correcte plus fine des signaux RMN a pu être proposée grâce à la construction du premier modèle quantique d'arêtes de l'alumine localisées à l'intersection des surfaces (110) et (100) où les groupes  $\mu_1$ -OH sont plus stables et correspondent au signal RMN à 0 ppm. La région du spectre entre 1 et 3 ppm est attribué non seulement à des  $\mu_2$ -OH mais aussi à d'autres  $\mu_1$ -OH présents sur les arêtes et sur les surfaces, et accepteurs de l'hydrogène. Les hydroxyles qui sont donneurs dans la liaison d'hydrogène génèrent les signaux larges à haut déplacement chimique. Il a été aussi démontré que le chlore est préférentiellement échangé avec les  $\mu_1$ -OH des arêtes. Le chlore est localisé sur les arêtes jusqu'à 1.4%Cl pour PuralSB3 et seulement jusqu'à 0.5%Cl pour TH100, dans ce cas, pour les teneurs supérieures, le chlore excédentaire est échangé avec des OH de surface. De ce fait, on peut s'attendre à ce que ces sites d'arête jouent un rôle important pour la catalyse. Le suivi par RMN de la chloration des alumines pourrait être une méthode pour déterminer le ratio arête/surface d'une alumine donnée.

Ensuite, la phase métallique de platine supporté sur l'alumine chlorée a été étudiée par microscopie STEM et par spectroscopie XAS pour les catalyseurs avec les deux teneurs en Pt et Cl les plus extrêmes de 0.3 et 1%Pt et 0.1 et 1.4%Cl. Dans l'état oxyde le platine se présente sous la forme de complexes oxychlorures monoatomiques  $\text{PtCl}_x\text{O}_y$  dont le rapport  $x/y$  varie avec la teneur en Cl. Après réduction, les nanoparticules de platine sont formées avec une taille de 0.9 nm, qui est indépendante de la teneur en Pt ou en Cl, et avec une morphologie bi-planaire aplatie. Des atomes isolés (stabilisés par ajout de chlore) sont aussi identifiés et ils correspondent à environ 20% des atomes de platine supporté. L'analyse STEM d'un catalyseur après test a révélé la stabilité des atomes isolés et des nanoparticules, ce qui confirme la pertinence de l'étude sur catalyseur frais.

L'étude par tomographie électronique a montré que près de 80% des nanoparticules de Pt sont localisées sur les arêtes des cristallites ou sur des défauts (de type marches). Cette

localisation est en compétition thermodynamique avec celle sur les surfaces, d'après les premiers calculs quantiques de nano-agrégats de type  $Pt_{13}$  sur les arêtes  $\gamma-Al_2O_3-Cl$ . Il est possible que certains effets cinétiques ou géométriques favorisent la position sur les arêtes pendant la réduction. La distance entre les nanoparticules de Pt quantifiée par une analyse mathématique des volumes segmentés, démontre une distribution statistique des particules sur le support, ce qui suggère que les sites d'ancrage du platine sont abondants. Cette distance entre nanoparticules de Pt est directement contrôlée par la teneur en Pt.

Enfin, un modèle géométrique des catalyseurs du type  $Pt/\gamma-Al_2O_3-Cl$  a été proposé, prenant en compte de façon explicite la morphologie (rapport arête/surface) des cristallites d'alumine ainsi que leur taille. Le modèle prédit correctement la teneur en Cl pour laquelle les sites d'arête sont saturés. La distance entre les deux types de sites actifs, ici défini comme étant la distance entre les nanoparticules de Pt et le Cl, a été estimée pour certains scénarii. Elle varie, en moyenne, de 1.1 nm pour la PuralSB3 (1%Cl) à 2.4 nm pour la TH100 (0.4%Cl). L'existence d'une liaison directe Pt-Cl ne peut pas être écartée, en tenant compte de certains modèles quantiques de nano-agrégats  $Pt_{13}$  sur une arête chlorée. Cette distance dépend de trois paramètres : la localisation des nanoparticules de Pt, le type de support et la teneur en Cl.

Une compréhension avancée de la nature et de l'emplacement des sites actifs et de leur proximité dans les catalyseurs de reformage catalytique a donc été acquise grâce à ces travaux. Nous espérons que cela permettra dans le futur d'ouvrir de nouvelles voies rationnelles d'amélioration des performances de cette famille de catalyseurs grâce à un meilleur contrôle à l'échelle atomique des sites actifs.





<b>Acknowledgements .....</b>	<b>i</b>
<b>Abstract.....</b>	<b>v</b>
<b>Résumé .....</b>	<b>vi</b>
<b>Résumé étendu.....</b>	<b>vii</b>
<b>Introduction .....</b>	<b>1</b>
<b>1 State of the Art.....</b>	<b>5</b>
1.1 Catalytic Reforming: objectives, main reactions and processes .....	7
1.1.1 Main reactions.....	8
1.1.2 Industrial catalytic reforming processes.....	9
1.2 Industrially used catalysts.....	13
1.2.1 Bifunctionality in catalytic reforming catalysts .....	13
1.2.2 Catalyst types .....	15
1.2.3 Catalyst preparation.....	16
1.2.4 Catalyst poisoning, deactivation and regeneration .....	18
1.2.5 Conclusion .....	20
1.3 $\gamma$ -alumina .....	20
1.3.1 Crystal Structure .....	21
1.3.2 Morphology of alumina crystallites and exposed surfaces .....	23
1.3.3 Surface hydroxyl groups .....	24
1.3.4 Conclusion .....	35
1.4 Chlorine doping of $\gamma$ -alumina.....	36
1.4.1 Chlorination mechanism.....	36
1.4.2 Acidity of chlorinated alumina .....	38
1.4.3 Conclusion .....	40
1.5 Supported Platinum.....	40
1.5.1 Supported Pt in oxide state .....	41
1.5.2 Supported Pt in reduced state .....	44
1.5.3 Conclusion .....	54
1.6 Conclusion and strategy.....	56
<b>2 Methodology and Standard characterization of materials .....</b>	<b>59</b>
2.1 Catalyst preparation methods .....	61
2.1.1 Strategy for catalyst formulations.....	61
2.1.2 Alumina support preparation .....	63
2.1.3 Catalyst preparation.....	64

2.2	Characterization techniques and modelling methods.....	68
2.2.1	Standard techniques.....	68
2.2.2	Advanced techniques.....	74
2.2.3	DFT molecular modelling.....	102
2.3	Standard characterization of prepared materials.....	107
2.3.1	Alumina supports and acidified aluminas .....	107
2.3.2	Pt/alumina-Cl catalysts .....	108
<b>3</b>	<b>Location and environment of <math>\gamma</math>-alumina hydroxyl groups and chlorine .....</b>	<b>119</b>
Beyond $\gamma$ -Al <sub>2</sub> O <sub>3</sub> Crystallite Surfaces: the Hidden Features of Edges Revealed by Solid-State <sup>1</sup> H NMR and DFT		
	Calculations .....	121
	Abstract .....	121
	1. Introduction .....	122
	2. Materials and methods.....	123
	3. Results and Discussion .....	124
	4. Conclusion.....	130
	References .....	131
	Supporting Information.....	134
<b>4</b>	<b>Platinum supported on <math>\gamma</math>-Al<sub>2</sub>O<sub>3</sub>-Cl .....</b>	<b>159</b>
4.1	Samples with 0.1%Cl loading .....	161
4.1.1	Oxide catalysts .....	161
4.1.2	Reduced catalysts.....	170
4.2	Samples with 1.4%Cl loading .....	187
4.2.1	Oxide catalysts .....	187
4.2.2	Detailed microscopic study of TH100-1.4%Cl catalysts by advanced HAADF-STEM techniques ..	196
4.2.3	Reduced catalysts.....	218
4.3	Conclusion.....	230
<b>5</b>	<b>Site proximity assessment .....</b>	<b>233</b>
5.1	Location of metallic and acidic sites in Pt/ $\gamma$ -Al <sub>2</sub> O <sub>3</sub> -Cl catalysts .....	235
5.1.1	Location of acidic sites (summary) .....	235
5.1.2	Location of metallic sites (summary).....	236
5.1.3	<sup>1</sup> H NMR study of Pt/ $\gamma$ -Al <sub>2</sub> O <sub>3</sub> -Cl catalysts.....	236
5.2	Geometric models to evaluate site proximity in Pt/ $\gamma$ -Al <sub>2</sub> O <sub>3</sub> -Cl catalysts .....	242
5.2.1	First simple 2D geometric model.....	242
5.2.2	Morphology dependent geometrical model accounting for the location of Cl and Pt .....	247
5.3	Conclusion.....	256

<b>Conclusion .....</b>	<b>257</b>
<b>Perspectives .....</b>	<b>261</b>
<b>References.....</b>	<b>263</b>
<b>Appendixes.....</b>	<b>277</b>
A.    XANES spectra and EXAFS fitting of reference compounds.....	279
B.    XRD diffractograms of PuralSB3 and TH100 $\gamma$ -aluminas.....	282
C.    Consumed H <sub>2</sub> volume and temperature of maximum H <sub>2</sub> consumption issued from TPR analysis of PuralSB3 impregnated+calcined materials and oxide catalysts .....	283
D.    E <sub>0</sub> edge energy value found for each sample analysed by XAS.....	284
E.    XANES spectra of reduced 0.3%Pt/TH100-0.1%Cl .....	286
F.    EXAFS Pt-Pt path amplitude at high wavenumber.....	287
G.    EXAFS fitting of reduced catalysts with both Pt-O <sub>long</sub> and Pt-Al paths.....	288
H.    Supporting Information for publication draft of section 4.2.2 .....	290
I.    Catalytic test protocol.....	298
J.    IR analysis .....	299



# Introduction

Highly dispersed platinum supported on oxide materials is generally used as a catalyst for several applications, such as petroleum refining, petrochemicals, exhaust gas treatment from combustion engines and even treatment of volatile organic compounds (VOC) in streams. In the case of catalytic naphtha reforming, the oxide support used industrially is  $\gamma$ -alumina doped with chlorine to enhance its Brønsted acidity, resulting in a bifunctional catalyst combining hydro/dehydrogenation function and isomerization function.

This process is one of the key units in a refinery since the 1950's, allowing for low-octane heavy naphtha to be transformed into high-octane compounds for the production of good quality gasoline and the production of hydrogen. It is an essential piece of the puzzle for the refiner, as the unit's operation may be adapted to maximize the production of reformate with a fixed octane number, of aromatics (BTX) for petrochemicals or to maximize hydrogen production [1].

Catalytic naphtha reforming relies on isomerization, dehydrogenation and (dehydro)cyclization reactions to transform linear alkanes into aromatics and iso-alkanes. These reactions occur through bifunctional mechanisms that include diffusion of intermediates from the metallic site to the acid site. For bifunctional catalysis an "intimacy criterion" was defined by Weisz [2] that defines the maximum distance that can be allowed between the two different types of sites so that diffusion between them is not a limiting step. Even if this criterion is respected, the relative location of the two types of sites can deviate the mechanism towards undesired reactions of hydrogenolysis, (hydro)cracking or coke formation., negatively impacting desired product selectivity.

For other industrial bifunctional catalysts, such as zeolite based hydrocracking catalysts, it has been possible to explore the dynamics of inter-site distance and location with relative ease, as in zeolites the acid sites have defined positions and the metal phase location can be changed between a binder (such as alumina) and the zeolite [3]. That is not the case for catalytic reforming catalysts, as Pt is directly supported on the chlorinated alumina and the precise location of both the acid sites and of the supported metal on the alumina support remain unknown as well as the inter-site distance.

The challenging objective of this work is thus to find the location of the metallic phase and of the acid active sites (enhanced by Cl) on the surface of the  $\gamma$ -alumina support for the Pt/ $\gamma$ -Al<sub>2</sub>O<sub>3</sub>-Cl catalyst and to estimate the distance between the two types of active sites. There is also a particular interest on the chlorination of the support and on the possible impact of chlorine on the metallic phase.

The strategy employed is to study at an atomic scale a set of catalysts prepared so as to attempt to tune the distance between the two types of active sites by varying three parameters: platinum loading (from 0.3 to 1%<sub>w/w</sub>), chlorine loading (from 0.1 to 1.4%<sub>w/w</sub>) and alumina crystallite size and shape (choice of two different  $\gamma$ -alumina supports). Throughout the work it is considered that acid sites are in the proximity of Cl atoms, whose location is thus studied as proxy for acid site location. The materials will be prepared so as to be representative of industrial catalysts. To reach this goal, four main advanced characterization and modeling techniques will be employed:

The use of current aberration corrected microscopes allows for atomic resolution, thus High Annular Angle Dark Field Detector Scanning Transmission Electron Microscopy (HAADF-STEM) will be the method of choice for characterization of Pt nanoparticle size, shape and dispersion on the support. In addition, advanced in situ STEM and electron tomography techniques will also be employed to follow the reduction steps of the platinum particles and obtain a 3D representation of the catalyst, respectively.

High Energy Resolved Fluorescence Detection X-ray Absorption Near Edge Structure and Extended X-ray Absorption Fine Structure (HERFD-XANES and EXAFS) are local and element specific X-ray absorption techniques that will provide information on Pt electronic structure and neighbouring environment. A dedicated operando reactor will be to perform in situ re-reduction of the catalysts prior to acquisition in fluorescence mode with a crystal analyser, which provides high resolution in the XANES portion of the spectra.

High field solid state MAS <sup>1</sup>H NMR will be used to study surface hydroxyl groups (potential Brønsted acid sites) and the chlorination of the support. As the thermal treatment of the samples results in relatively low proton signals, a high field 800 MHz spectrometer was used for optimal sensitivity and resolution.

Density Functional Theory calculations undertaken on the large structural *library* of bare, hydrated and chlorinated alumina surfaces and supported Pt nanoparticle models developed in previous works are used to rationalize experimental results. In particular, the simulation of proton chemical shifts by DFT will be crucial for NMR spectra interpretation. In addition, new models for alumina edges will be proposed.

This multi technique approach will allow for a detailed investigation of the catalysts of interest at the atomic scale.

An overview of the relevant literature is laid out in Chapter 1, highlighting how the actual state of the art does not answer these challenging questions of Pt nanoparticle and acid site/Cl location on  $\gamma$ -Al<sub>2</sub>O<sub>3</sub>.

In Chapter 2, the materials prepared according to the defined strategy are listed and their preparation method is described. The different characterization techniques, associated protocols and calculation methods used are presented, with particular attention to the advanced techniques that are at the core of this work. Preliminary characterization by classic techniques of the prepared samples is also included in this chapter.

In Chapter 3, the study of the two chosen alumina supports' surface hydroxyl groups by <sup>1</sup>H NMR is presented in the form of the recently published work "*Beyond  $\gamma$ -Al<sub>2</sub>O<sub>3</sub> crystallite surfaces: the hidden features of edges revealed by Solid-State <sup>1</sup>H NMR and DFT calculations*" [4]. The two alumina supports are studied in terms of their crystallite morphology, surface hydroxyl groups and impact suffered by Cl doping in order to determine its location. Improved <sup>1</sup>H NMR peak assignment will be proposed based on DFT calculations of proton chemical shifts and considering the first  $\gamma$ -alumina edge DFT model.

Chapter 4 is dedicated to the characterization of catalysts in reduced and oxide state, in particular the supported platinum phase and is focused on samples with extreme Pt and Cl loadings. Thus STEM and XAS characterizations are employed to search for an impact of support type, platinum loading and chlorine loading on the metallic phase and to find the location of Pt nanoparticles on the support. DFT simulations also evaluate the relative stability of Pt nanoparticles in various possible locations. A part of the chapter is constituted by a to be submitted publication on the detailed study of two catalysts by advanced electron



microscopy methods whose purpose is to identify a preferential location of Pt nanoparticles on  $\gamma$ -alumina and to quantify of average inter-Pt nanoparticle distances.

In Chapter 5, a geometric model of the Pt/ $\gamma$ -Al<sub>2</sub>O<sub>3</sub>-Cl catalyst system is proposed to estimate the distance between Pt nanoparticles and Cl atoms (as acid sites are in their vicinity). Additional 2D <sup>1</sup>H-<sup>1</sup>H NMR results are presented aimed at investigating an impact of platinum on the dipolar coupling between surface hydroxyls. The construction of the catalyst geometric model is then described which allows quantification of inter-site distance and to identify the major parameters that influence it.

Finally, the main conclusions and challenging perspectives to the present work will be provided.

This work was developed at IFP Energies Nouvelles, in close cooperation with the Institut de Physique et Chimie des Matériaux de Strasbourg (Strasbourg) for the STEM experiments, with the Centre de RMN à Très Hauts Champs (Villeurbanne) for the NMR experiments and with the ESRF for the XAS experiments.

# **Chapter 1**

## **State of the art**



## ***1.1 Catalytic Reforming: objectives, main reactions and processes***

The objective of the catalytic reforming process is to produce high octane reformat for the gasoline pool from low octane streams. This allows for the valorisation of those streams, that otherwise could not be added to the gasoline blending stock, which needs to have at least 95 RON (research octane number).

The feedstock for catalytic reforming consists of heavy naphtha, which is a mixture of C<sub>6</sub>-C<sub>12</sub> hydrocarbons, mostly n-paraffins (linear alkanes), naphtenes (cycloalkanes) and aromatics, the proportion depending on crude oil origin, for straight run (SR) naphtha, or process of origin, for synthetic naphtha [1]. It is important to note that SR naphtha has only traces of olefins (alkenes), which is not true for naphtha from Fluid Catalytic Cracking (FCC) or visbreaker units [1]. Olefins do not exist in crude oil and are formed in refining processes by thermal degradation, namely in the vacuum distillation columns, whose distillates feed FCC and thermal cracking units like the visbreaker.

Figure 1-1 shows that n-paraffins with increasingly longer chains have lower RON. Without change in carbon number, RON can be increased by transforming n-paraffins into iso-paraffins (branched) or aromatics and by transforming naphtenes to aromatics, which is the role of reforming units.

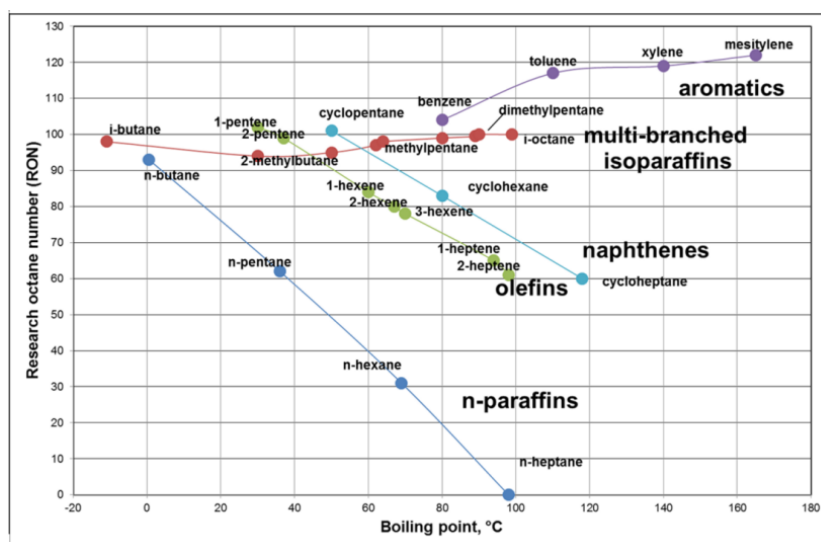
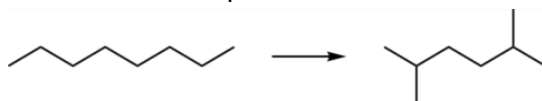


Figure 1-1 - Research octane numbers of different hydrocarbons in function of their boiling point [5].

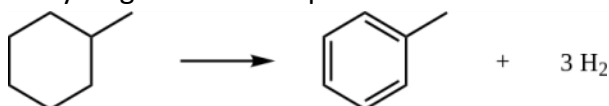
### 1.1.1 Main reactions

The following reactions allow the desired transformations:

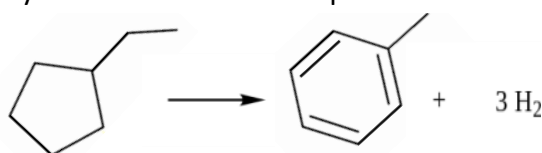
a) Isomerization of paraffins



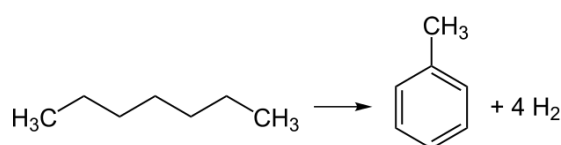
b) Dehydrogenation of naphthenes



c) Dehydroisomerization of naphthenes



d) Dehydrocyclization of paraffins



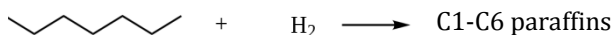
The first observations are:

- the highest octane number gain results from reactions d) (from RON 0 to 120 in the example [6]) and c) (from RON 91 to 120, in the example [6,7])
- all reactions except a) produce hydrogen, thus causing an increase in the number of molecules and being favoured by low pressure (in particular low  $P(H_2)$ ).

These units produce hydrogen as a valuable side-product and operate under  $H_2$  pressure.

Other undesired reactions will take place under the used conditions, which cause a loss in gasoline yield (molecules containing at least 5 carbon atoms,  $C_5^+$ ):

e) Hydrogenolysis and hydrocracking



f) Coking

Hydrogenolysis consists of breaking of terminal C-C bonds, forming  $C_1$ - $C_2$ , and hydrocracking occurs mostly on the middle of the molecule and is favoured for longer chains [7]. Both these reactions consume hydrogen and are thus favoured by higher pressures. Coking is the process of formation and condensation of high molecular weight polyaromatics, producing  $H_2$ , resulting in catalyst deactivation.

The challenge is to balance this complex set of reactions to achieve maximum gasoline yield. As mentioned, lower  $H_2$  pressure will favour dehydrocyclization but also coking, whereas increased  $H_2$  pressure, to control coking, favours hydrogenolysis and hydrocracking. The same dilemma is present for the choice of temperature, as reactions b), c) and d) are endothermic, favoured by increase in temperature, which also favours cracking due to its highest energy of activation [7]. Typical operating temperatures are around  $500^\circ\text{C}$  [6]. A bi-functional (metal-acid) catalyst is used to promote these reactions.

### 1.1.2 Industrial catalytic reforming processes

An industrial reforming unit consists of three main zones:

1) Pre-treatment of feedstock [1,8]:

to remove catalyst poisons such as arsenic, lead and copper (permanent poisoning) and sulphur, oxygen and nitrogen compounds (reversible poisoning). The nature and content of these impurities in the feedstock will depend on its origin. For example, visbreaker naphtha carries organometallic compounds, unlike SR naphtha which has virtually none. Pre-treatment is performed in hydrotreatment units working under hydrogen pressure where  $\text{CoMoS}/\text{Al}_2\text{O}_3$  type catalysts are employed. After this reactor, the produced  $\text{H}_2\text{S}$ ,  $\text{NH}_3$  and water are stripped from the treated stream.

2) Reaction section that differs depending on the type of process [8]:

- Semi-regenerative (SR)

The semi-regenerative process works in continuous operation over long periods of time (up to 1 year) and is then shut down for in situ catalyst regeneration. During operation the catalyst activity will decrease, mainly due to coke deposition, which is made up for with increasing process temperature. With catalyst deactivation being a major operation factor, these units work at high pressure, 14-17 bar, to prevent coke formation as much as possible. This is the older process used in catalytic reforming hydrocarbons, very few new units are built nowadays.

The unit consists of three or four fixed bed radial down flow adiabatic reactors in series, packed with catalyst in extruded pellet form, with intermediary furnaces between them. The first reactor is smaller than the second, and so on. A scheme is presented in Figure 1-2.

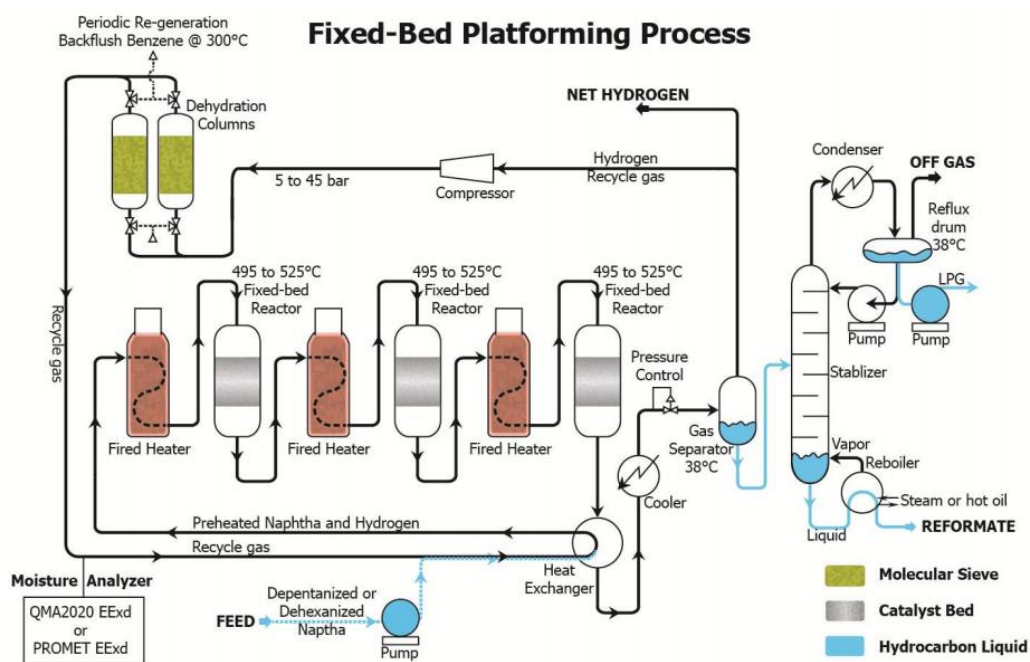


Figure 1-2 - Scheme of a semi-regenerative reforming process [9].

- Cyclic

This process avoids shut downs for catalyst regeneration thanks to a fifth reactor, called swing reactor, which can be used in place of any of the other reactors while its catalyst bed is being regenerated. Here all the reactors have the same size.

This greater regeneration flexibility allows for lower operation pressures, even if it means the catalyst in each reactor may be exhausted in less than one month. Lower pressure means higher  $C_5^+$  and  $H_2$  yields and higher reformate RON.

One disadvantage is that each reactor will alternate from reducing to oxidizing atmosphere more often, which is demanding on construction materials and involves additional safety procedures.

- Continuous Catalyst Regenerative (CCR)

As the name indicates, these units have a continuously moving bed of catalyst beads that goes through the reactors and is then fed to a regeneration unit, before returning to the first reactor where fresh catalyst make-up may be added to maintain its quantity. This is currently the most popular process, as it makes up the vast majority of new catalytic reforming units.

The continuous regeneration of the catalyst allows for even lower operation pressures, inferior to 10 bar, and a steady production of high purity hydrogen and high RON reformate.

There are two main commercial processes of this type, shown in Figure 1-3. Process a) was developed by UOP and it has the four reactors stacked on top of each other while b) was historically developed by IFPEN and consists of four individual reactors where catalyst moves from the bottom of one to the top of the following.



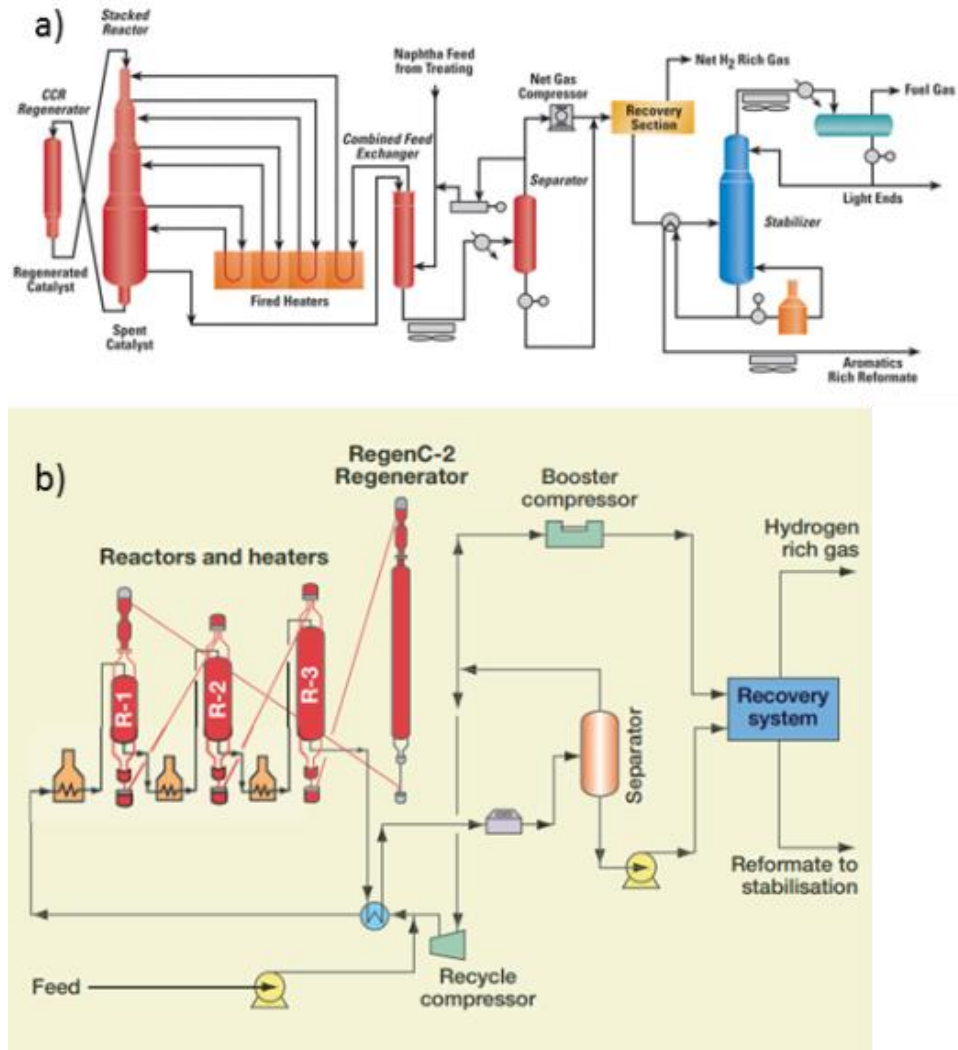


Figure 1-3 - Schemes of the two main types of regenerative process, a) UOP's Platforming Process [10] and b) Axen's Octanizing Process [11].

### 3) Product separation:

After the reaction section, the product stream is separated into a gaseous ( $C_1$ - $C_4$  and  $H_2$ ) and a liquid stream (reformate,  $C_5^+$ ) in a flash. Part of the hydrogen is compressed and recycled to the reactor feed. The reformate is fed to a stabilization column to eliminate light compounds still present.

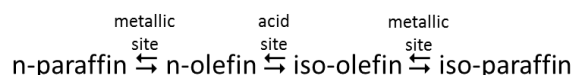
Catalyst design depends strongly on the type of unit employed and all stages of operation must be considered.

## 1.2 Industrially used catalysts

### 1.2.1 Bifunctionality in catalytic reforming catalysts

Catalytic reforming employs bifunctional metal-acid catalysts. The metallic active sites are located on ultra-dispersed platinum nanoparticles (NPs) or clusters, which activate dehydrogenation in reforming conditions, and undesired hydrogenolysis (needs several adjacent metallic active sites [12] and is more relevant for large Pt particles [13]) [14]. Brønsted acid sites are located on the alumina support (which acidity is enhanced by doping) [15], catalysing isomerization, cyclization and also the undesired cracking steps. Note that cyclization is also believed to occur on metallic sites [14].

The presence of the two types of sites in one catalyst gives rise to bifunctional reaction mechanisms, distinct from the two corresponding monofunctional ones. The bifunctional mechanism passes by an olefinic intermediate [16] created by dehydrogenation in the metal sites that suffers isomerization/cyclization in the acid sites by forming a carbocation. This implies diffusion of these intermediates from one type of site to the other. This is illustrated by the reaction of paraffin isomerization:



For paraffin isomerization a significant increase in n-hexane conversion to iso-hexanes was found by Weisz [2] when using a mixture of *Pt-only* and *acid-only* materials compared to their isolated performances. Due to this, Weisz also defined an *intimacy criterion* between the two sites, the condition for which there is no diffusional limitation of intermediates, that depends on gas-phase diffusivity of the intermediates and the distance between the two types of active sites. His work showed, as a demonstration of the requirement for hexane isomerization, that as the materials particle size is decreased the obtained iso-hexane conversion approaches that of an impregnated catalyst (both sites in same material).

This criterion is still object of study [3,17,18] for zeolite based bifunctional catalysts in which the acid sites occur on structurally defined positions in the zeolite. In those cases the distance between sites can be adjusted while using model catalysts comparable to the commercial ones by depositing the metallic phase on the binder used for catalyst shaping, for

example [3]. Since the location of the active sites is not defined for catalytic reforming catalysts, the study of the intimacy criterion for these catalysts is currently limited to the use of two distinct monofunctional materials, as did Weisz [2].

Another example of a bifunctional mechanism, characteristic of catalytic reforming, is that of dehydrocyclization of n-paraffins to form aromatics. A possible mechanism for n-heptane dehydrocyclization is illustrated in Figure 1-4.

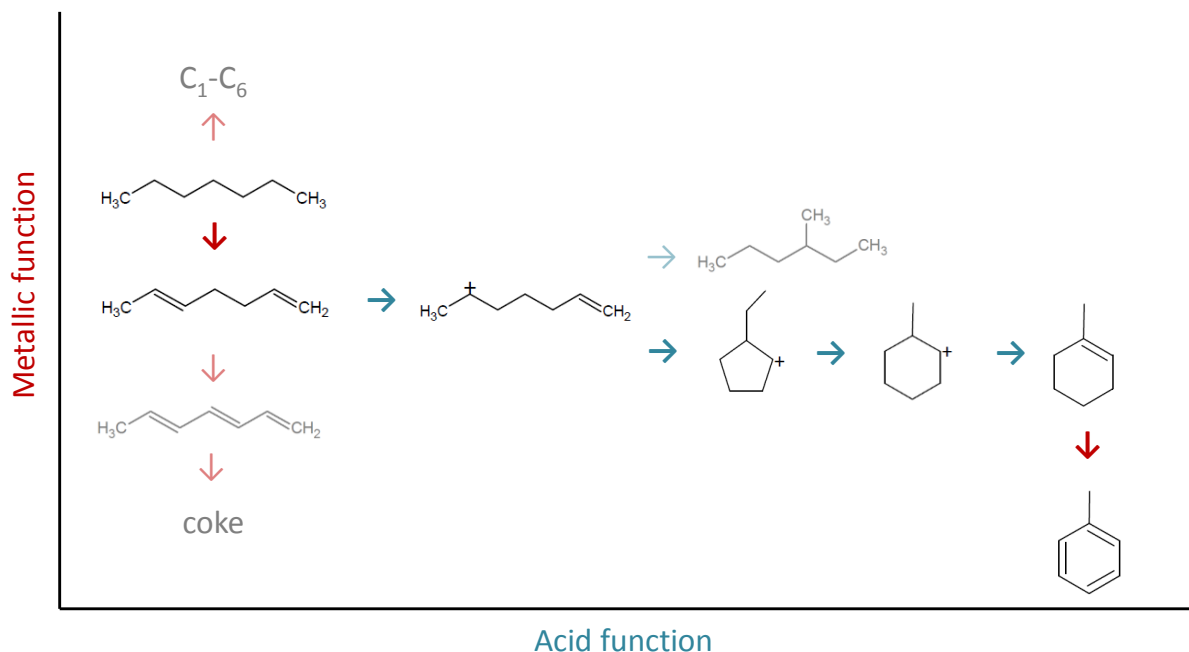


Figure 1-4 – Diagram of a possible mechanism for n-heptane dehydrocyclization, with potential undesirable reactions also shown in lighter colours, adapted from [7,13,19].

Although the dehydrocyclization bifunctional mechanism is still debated [19], it is believed hydrogenation and dehydrogenation steps occur in metallic sites while isomerization, cyclisation and cycle enlargement steps take place through the acid sites. Davis [13] showed that even though dehydrocyclization can occur both on *Pt/acidic-support* and *Pt/non-acidic-support* catalysts, the bifunctional catalyst (and thus the bifunctional reaction mechanism) is faster and more selective compared to the metal-only material.

Even if the intimacy criterion for mass transport is respected and there is adequate conversion it does not guarantee selectivity. In the case of n-heptane dehydrocyclization the desired product is toluene, leading to a large gain in octane number. Intermediates can be intercepted and suffer the undesired reactions shown in lighter colours in Figure 1-4 to form light hydrocarbons, coke and iso-heptanes for example.

The acid and metallic functions of commercial catalysts are balanced to tune their selectivity to a certain degree (not too much acidity to prevent cracking, small metal particles to prevent hydrogenolysis) [7]. What is not currently known and therefore cannot be tuned is the relative position of the active sites and distance between them which can dictate to which degree intermediates are intercepted.

### 1.2.2 Catalyst types

Industrially, catalytic reforming processes employ three main types of bifunctional catalysts:

- a) Monometallic platinum supported on chlorine doped  $\gamma$ -alumina ( $\text{Pt}/\gamma\text{-Al}_2\text{O}_3\text{-Cl}$ ) with 0.2-0.6%<sub>w/w</sub>Pt (most frequent 0.3%) and 1.0-1.1%<sub>w/w</sub>Cl; used in semi-regenerative units in the form of extrudates
- b) Bimetallic platinum-rhenium supported on chlorine doped  $\gamma$ -alumina ( $\text{Pt-Re}/\gamma\text{-Al}_2\text{O}_3\text{-Cl}$ ) with 0.2-0.6%<sub>w/w</sub>Pt; 0.25-0.45%<sub>w/w</sub>Re (balanced or skewed respectively) and 1.0-1.1%<sub>w/w</sub>Cl; used in semi-regenerative and cyclic units in the form of extrudates
- c) Bimetallic platinum-tin supported on chlorine doped  $\gamma$ -alumina ( $\text{Pt-Sn}/\gamma\text{-Al}_2\text{O}_3\text{-Cl}$ ) with 0.2-0.6%<sub>w/w</sub>Pt; 0.2-0.5%<sub>w/w</sub>Sn (most frequent 0.3% of each) and 1.0-1.1%<sub>w/w</sub>Cl; used in continuous regenerative units in the form of beads

Monometallic catalyst a) was the first used in semi-regenerative processes but it has been replaced by the Pt-Re catalyst b). The presence of Re allows for a more stable catalyst with a longer life time, as the second metal stabilizes the metallic phase and is resistant to coke deposition. The incorporation of Re is believed to promote the hydrogenation of adsorbed hydrocarbons, minimizing coking [20]. The development of the Pt-Re catalyst allowed for lower hydrogen pressures in semi-regenerative units. However, rhenium is very active for hydrogenolysis making it necessary to perform a sulphurization passivation step before using the catalyst. [7,8] The skewed catalyst (unbalanced metal composition, higher Re content) is more suited for the treatment of heavier naphtha cuts  $\text{C}_9\text{-C}_{10}$  and is more resistant to coke. [21].

Continuous regenerative units use the Pt-Sn catalyst c). The addition of tin increases selectivity and prevents metal particle sintering during the coke combustion step of catalyst regeneration [8]. One of the factors that bring forth a better selectivity (than monometallic catalysts) is that tin inhibits strong acid sites of the alumina support, responsible for

hydrocracking, but does not impact acid sites of intermediate strength that are needed for dehydrocyclization and isomerization [22]. Another one is that tin also has an impact on the metallic Pt phase by 1) a geometric effect defined by the dilution of Pt atoms by Sn atoms in a nanoparticle [23], which reduces the occurrence of hydrogenolysis or/and 2) an electronic effect of tin on Pt atoms [24], influencing the adsorption and desorption of hydrocarbons. . Recent DFT studies proposed that the dual effect of dilution and ductility of the PtSn cluster also impacts hydrogen adsorption [25]. The nature of the supported Sn species present depends on the preparation method and is still a topic of discussion. The work of Jahel [26] characterizing of Pt-Sn (Cl) catalysts using Mössbauer spectroscopy prepared by sol-gel technique and by successive impregnation of the metals showed that: 1) the Sn species present on the reduced sol-gel prepared catalyst are SnO<sub>2</sub>, Sn(II), Sn(0) and Sn(IV); 2) the Sn species present on the reduced successive impregnation catalyst are Sn(II), Pt<sub>x</sub>Sn (alloy) and SnO<sub>2</sub> [27].

The study of trimetallic (or even multimetallic) catalysts (using In or Ce, for example) has increased in the later years in order to clarify the metals' interaction [28] and the effects on activity and selectivity, since various patents [29] indicate the use of more than two metals in industrial catalysts.

### **1.2.3 Catalyst preparation**

The preparation method has an impact on the nature of the metallic phase and acid sites of catalytic reforming catalysts. The catalysts must have a support with adequate mechanical properties and porosity, the correct acidity to have a bifunctional mechanism but not too much cracking, and platinum nanoparticles with uniform distribution through the support and high dispersion (accessible atoms vs total).

#### **1.2.3.1 Monometallic Pt/Al<sub>2</sub>O<sub>3</sub>-Cl catalysts**

The classic reforming catalyst is prepared by diffusional impregnation of the  $\gamma$ -alumina support with a solution of platinum precursor, such as hexachloroplatinic acid H<sub>2</sub>PtCl<sub>6</sub>. The support is saturated with water and then put into contact with the H<sub>2</sub>PtCl<sub>6</sub> solution, meaning the precursor must diffuse from the external solution to the centre of the extrudates or beads in the aqueous phase.

Oxide support impregnation is a complex operation involving various phenomena of surface charging, electrostatic and pH effects, the possibility of dissolution of the support, etc. For the specific case of impregnation of alumina with hexachloroplatinic acid, despite different adsorption models having been proposed, three main points should be taken in consideration [7]:

- Alumina's surface OH groups grant it a point of zero charge (PZC) between 8 and 9, and there is a pH buffering effect at the surface that influences bulk solution pH.
- The nature of the platinum species in the impregnation solution depends on its pH, which can be influenced both at surface and bulk by contact with alumina. Below pH 4 the main species in solution are considered to be  $\text{PtCl}_6^{2-}$  and  $\text{PtCl}_5(\text{H}_2\text{O})^-$  [30].
- The platinum species effectively adsorbed on the surface were found to lose chlorine coordination, possibly by exchanging Cl with  $-\text{OH}_2^+$  groups at the surface [30].

To insure the uniform distribution of Pt through the support pellet, hydrochloric acid is added to the impregnation solution [6]. If only  $\text{H}_2\text{PtCl}_6$  is used, an egg-shell distribution of the active species is obtained due to the strong irreversible interactions of the species with the support and the fact that the quantity of precursor employed is below the surface saturation level [31]. One of the first ideas was that  $\text{Cl}^-$  would act as a competitor ion for  $\text{PtCl}_6^{2-}$ , forcing it to diffuse to the interior of the pores to adsorb [32]. Instead of a physical competition for adsorption sites, other work [33] suggests that there is little to no Cl adsorption during co-impregnation with Pt and that it is the increased ionic strength of the solution that delays Pt adsorption by reducing its adsorption equilibrium constant.

After impregnation, the catalyst is dried to remove the remaining solution in the pores. For this type of impregnation and in presence of HCl, it may be considered that the platinum precursor is mostly anchored at the surface [30] and its distribution will not change during drying. Drying is followed by calcination under dry air between 500 and 600°C, which transforms the adsorbed Pt species into a  $\text{Pt}^{\text{IV}}$ -oxygen-chlorine complex. Calcination will also reduce the chlorine content, especially if the air contains traces of water. The catalyst is finally activated by reduction with hydrogen between 500 and 550°C, forming dispersed  $\text{Pt}^0$  clusters [7].

### 1.2.3.2 Bimetallic Pt-Re/Al<sub>2</sub>O<sub>3</sub>-Cl catalysts

These catalysts are also prepared by diffusional impregnation with the same platinum precursor, H<sub>2</sub>PtCl<sub>6</sub>, and a rhenium precursor, often NH<sub>4</sub>ReO<sub>4</sub>. Successive or co-impregnations of the two precursors can be performed and HCl is also added to the impregnation solution [7].

### 1.2.3.3 Bimetallic Pt-Sn/Al<sub>2</sub>O<sub>3</sub>-Cl catalysts

Again, these catalysts can be prepared by successive or co-impregnations of hexachloroplatinic acid and tin precursors, usually SnCl<sub>2</sub> or SnCl<sub>4</sub>. Introduction of tin in the alumina sol-gel and then platinum impregnation is also a common preparation method for Pt-Sn catalysts [7].

During co-impregnation, the Pt and Sn salts in solution form bimetallic chlorinated complexes [34] such as PtCl<sub>3</sub>(SnCl<sub>3</sub>)<sup>2-</sup>. It is important to impregnate a pre-chlorinated alumina to avoid platinum precipitation due to the adsorption of chlorine onto the support, destroying the bimetallic complex [8]. This method results in a strong Pt-Sn interaction [35].

When successive impregnations are performed, it is preferable to impregnate the tin salts on a calcined (or oxidized) Pt/Al<sub>2</sub>O<sub>3</sub> intermediate since part of the platinum oxide complex reacts with the tin salt to form again a bimetallic complex [36]. This leads to a higher metal interaction than when the impregnation order is the inverse (tin then platinum) [37].

The same tin salt can be added to the alumina precursor suspension during support preparation. After the final alumina calcination, tin is in an oxide state uniformly distributed through the support [38]. The support with the tin oxide is then impregnated with the platinum precursor. During co-impregnation, due to the different behaviour of the Pt and Sn salts, obtaining a uniform distribution of both metals through the support is not straight forward. Tin oxide is in strong interaction with the alumina support and will not suffer redistribution during further thermal treatments, so this method assures a good distribution of both metallic species on the support [38].

### 1.2.4 Catalyst poisoning, deactivation and regeneration

Sulphur compounds in the feed are converted to H<sub>2</sub>S over the catalytic reforming catalyst, in reactor conditions, which will be strongly bonded to the metal phase, remaining as a stable

adsorbed species over a wide range of operation conditions [8]. Sulphur will not only block the metallic sites but also change its electronic properties. There is also the concept of irreversibly adsorbed sulphur (interacting with metal only and leading potentially to platinum sulphide phase) and reversibly adsorbed sulphur that can be desorbed. Smaller highly dispersed metal clusters, which have a strong interaction with the support, are less sensitive to sulphur poisoning. This poisoning ultimately inhibits dehydrogenation and reduces its activity.

Nitrogen compounds decompose to ammonia and neutralize the acid function of the catalyst as well. Ammonia absorption is reversible and catalytic activity can be recovered after eliminating nitrogen compounds from the feed during the naphtha hydrotreating step [8].

Another threat to catalyst acidity is chlorine elution in the presence of water. Decreased chlorine loading causes not only a loss in acidity that perturbs the bifunctional balance of the catalysts but also leads to increased sintering of the metallic phase [7].

The catalyst is still subjected to metal poisoning by iron from pipe corrosion and if conversion naphtha is used in the feedstock. The metals can form a combination with platinum that is not catalytically active [8].

During operation, various side reactions cause the deposit of carbonaceous material on the catalyst, which is called coking. Along a fixed bed reactor there will be a coke profile with a maximum towards the bottom of the reactor. At first feed contact, coke deposits mainly on metallic sites before moving to the acid sites [39]. Again, highly dispersed platinum nanoparticles are more resistant to coke deposition since coke precursors' adsorption is less favourable than on big particles [40]. Increased support acidity tends to increase coke formation by polymerization mechanisms. Deactivation by coking is mostly reversible by burning the carbonaceous material under controlled conditions [7].

Catalyst regeneration consists of the following main steps [7]:

- Purge with nitrogen to remove hydrocarbons and hydrogen for safety
- Combustion of coke under controlled conditions. Air is used as oxygen source and the temperature should be at a minimum of 400°C. Temperature must be closely controlled to avoid runaway or hotspots causing loss of support surface area and/or



alumina phase transition. This operation causes metal oxidation and sintering motivated by water formation, which also induces leaching of chlorine.

- Oxychlorination of the catalyst for metal re-dispersion and chlorine loading control. A chlorine precursor (generally a short length chloroalkane) and sometimes controlled amounts of water are introduced with air at 500°C. Chlorine allows the formation of a mobile  $\text{Pt}^{(\text{IV})}\text{O}_x\text{Cl}_y$  film that turns into dispersed nanoparticles upon reduction [41] and Cl is adsorbed onto the support to enhance its acidity. As excessive acidity favours undesired cracking, the Cl loading it is controlled by the water vapour.
- Nitrogen purge to eliminate oxygen and to dry the remaining water.
- Metal reduction with a hydrogen stream of the highest purity possible (an economical compromise for the refiner). After this step a sulphurization may be conducted, for Pt-Re catalysts for example.

### 1.2.5 Conclusion

Catalytic reforming units employ bifunctional catalysts consisting of a metallic phase (mono or bimetallic using Pt and Sn or Re) supported on chlorine doped alumina for enhanced acidity. These two types of active sites allow for more selective reaction mechanisms than their monofunctional counterparts. Their synthesis involves impregnation with metal precursor salts and hydrochloric acid. Chlorine has a strong influence on the species deposited on the support and their evolution during the consequent thermal treatments. During operation in an industrial unit, poisons, such as sulphur and ammonia, and coke deposition on the active sites will reduce catalyst activity/selectivity. Regeneration is then necessary to eliminate as much of those components as possible and bring the catalyst back to optimal performance.

A more detailed description of the main constituent parts of the  $\text{Pt}/\text{Al}_2\text{O}_3\text{-Cl}$  catalyst is presented in the following sections.

## 1.3 $\gamma$ -alumina

Aluminium oxide or alumina  $\text{Al}_2\text{O}_3$  exists in different crystallographic forms or polymorphs, which upon sufficient heating will all transform into the stable  $\alpha\text{-Al}_2\text{O}_3$  or corundum (oxide ions in an hexagonal close packing array and all Al cations octahedrally coordinated). Figure

1-5 presents a scheme of the transformation of alumina polymorphs, starting with the alumina precursor boehmite.

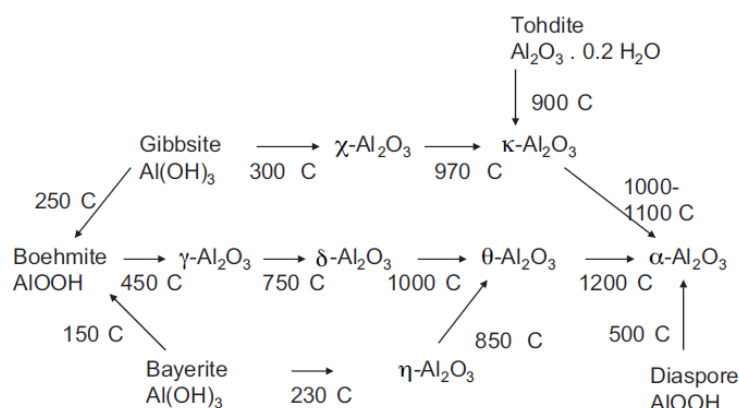


Figure 1-5 - Scheme of the solid transformations of alumina [42].

### 1.3.1 Crystal Structure

The  $\gamma$ - $\text{Al}_2\text{O}_3$  polymorph is widely used in the catalysis industry as a support for metal or sulphide active phases. This alumina is preferred as a support due to its thermal stability below  $600^\circ\text{C}$ , its acid-basic characteristics and high surface area ( $200\text{--}300\text{ m}^2/\text{g}$ ) [43]. Numerous studies of this and other alumina polymorphs' crystallographic and surface properties are fuelled by the economic interest in this product, with the high purity alumina market being evaluated at 980 million\$ in 2017 [44]. Despite that, there is still discussion among authors regarding their crystallographic structure and nature of surface sites.

As can be seen in Figure 1-5,  $\gamma$ - $\text{Al}_2\text{O}_3$  is obtained from the topotactic decomposition of the oxy-hydroxide (boehmite) by loss of water and structure collapse. Classically,  $\gamma$ - $\text{Al}_2\text{O}_3$  is considered to be a defective spinel ( $\text{AB}_2\text{X}_4$ ) by assuming it is a stoichiometric form of aluminium oxide that has a different arrangement from corundum ( $\alpha$ - $\text{Al}_2\text{O}_3$ ) [45]. For proper stoichiometry, since only one cation type exists in alumina, some of the cationic sites must be considered vacant, leading to the  $\square_{2(2/3)}\text{Al}_{21(1/3)}\text{O}_{32}$  formula when  $\gamma$ -alumina is considered similar in structure to the Mg-spinel  $\text{MgAl}_2\text{O}_4$  based on the spinel cubic unit cell [46]. The existence of vacancies raises the question of how these vacancies are distributed between the two types of cationic sites, tetrahedral and octahedral. Theoretically, considering the defective spinel lattice, the percentage of tetrahedral Al cations is restricted to the range

25% - 37.5%, with the remaining cations occupying octahedral positions, but a consensus was never reached on the empirical percentage despite numerous studies [46].

The existence of bulk pentacoordinated Al cations was reported in NMR studies [47], suggesting that the spinel type structure may not be the most adequate to describe this alumina.

On the basis of quantum simulation, Krokidis et al. [48] proposed a non-spinel structure for which no structural vacancies are invoked, oxygen atoms are in a fcc (or ccp) sublattice and 25% of Al cations are in tetrahedral positions (Figure 1-6). By density functional theory (DFT) calculations, they found this  $\gamma$ - $\text{Al}_2\text{O}_3$  structure obtained from the dehydration of boehmite as being more stable (lower free energy) than many others proposed in the literature (spinel like, hydrogen sponge [49]...). This process was considered to occur in two stages, first water elimination with the collapse of boehmite structure and second the migration of aluminium cations. The percentage of aluminium cations on tetrahedral positions agrees with previous reports from NMR and simulated XRD patterns are considered in good agreement with experimental ones. This alumina model was used by Digne et al. [50,51] to study the alumina surfaces, building the bulk alumina representation of Figure 1-6. The computational work of Paglia et al. [52] is in agreement that non-spinel structures are more stable and in better agreement with experimental XRD data.

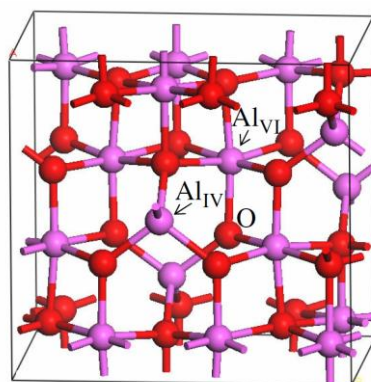


Figure 1-6 - Non-spinel alumina bulk model [51], red balls - oxygen atoms and purple balls - aluminum atoms.

Besides, a structure of alumina containing bulk hydrogen, remaining from the dehydration of boehmite and occupying cationic and interstitial sites, was proposed by Sohlberg *et al.* [46]. These authors considered  $\gamma$ - $\text{Al}_2\text{O}_3$  to be a sequence of compounds with varying H content following the formula  $\text{H}_{3m}\text{Al}_{2-m}\text{O}_3$ . This proposal has since been disregarded [42,49,53,54].

### 1.3.2 Morphology of alumina crystallites and exposed surfaces

As  $\gamma\text{-Al}_2\text{O}_3$  is obtained by the topotatic decomposition of boehmite, the morphology of the alumina crystallites is inherited from its precursor [55]. Depending on the synthesis method used to prepare the boehmite (from aluminium alkoxides or from aluminium salts) and the conditions used (such as pH or ionic force of solution), different sizes and shapes of boehmite crystallites can be obtained. There is also a correspondence between the exposed surfaces of boehmite and the ones of the formed alumina [51].

As Figure 1-7 illustrates, various crystallite shape models have been proposed, with the rhombic geometry (a and f) being the most commonly accepted [51,56].

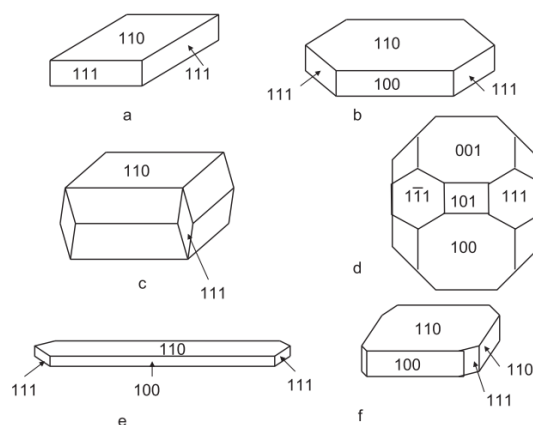


*Figure 1-7 - Alumina crystallite shape models ; a) rhombic, b) lamellar, c) bulky, d) cuboctahedral, e) fibrous, f) rhombic [42].*

Different authors found that the most exposed surface terminations of  $\gamma\text{-Al}_2\text{O}_3$  are the (110) surface, contributing to around 70% of exposed area, and the (100) and (111) that together make up the remaining 30% [51,55,57].

An HR-TEM study [56] of a platelet-like  $\gamma$ -alumina ( $S_{\text{BET}}=70\text{m}^2/\text{g}$ ) with rhombus facets (thickness 10-20 nm, short diagonal 50-70 nm) found (110) and (111) type surfaces. The (110) surface exhibited steps and ledges of (111) type in the  $[\bar{1}10]$  direction, effect that is supported by another DFT study [58]. The crystallite's internal porosity/voids was found to be composed of (100) and (111) planes. A degree of surface amorphization was found to occur upon aqueous active phase impregnation.

The acidity of  $\gamma$ -alumina is usually attributed to both Lewis and Brønsted acid sites [59]. The Lewis sites are coordinatively unsaturated (CUS)  $\text{Al}^{3+}$  atoms. The coordination of these sites

is still debated. Some works suggest CUS  $Al_V$  are the Lewis sites [60], while IR studies using pyridine and CO suggest that there should be Lewis sites of differing coordination [61]. The surface hydroxyl groups (but not necessarily all of them) are considered to be Brønsted acid sites [15]. Works referring to the protonation of some bases [15] and to the isomerization activity of  $\gamma$ -alumina attest to its Brønsted acidity [62].

### 1.3.3 Surface hydroxyl groups

The nature of the surface of alumina has been studied by infrared spectroscopy (IR) and nuclear magnetic resonance spectroscopy (NMR), among other techniques, showing the existence of surface hydroxyl groups even after high temperature treatments. Over time, a number of surface models were presented in order to identify different types of OH groups and attribute them to the components consistently found in the IR spectrum of  $\gamma$ - $Al_2O_3$  (Figure 1-8).

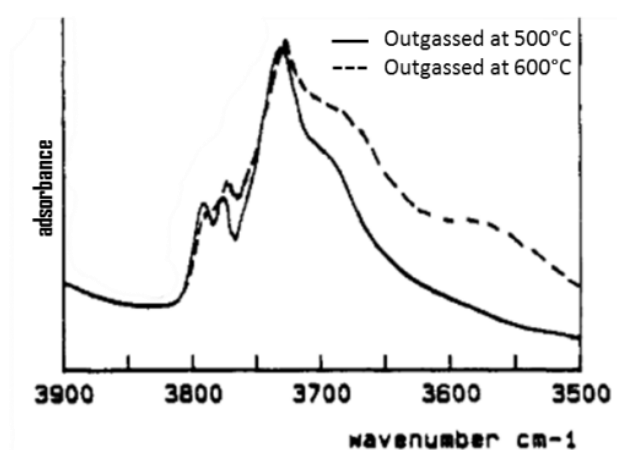


Figure 1-8 - IR spectra of  $\gamma$ -alumina outgassed at 500°C and 600°C [63].

Initially authors focused on the five main OH bands: 3800-3785; 3780-3760; 3745; 3735-3730; 3710  $cm^{-1}$ , while more recently two minor bands at 3690 and 3590  $cm^{-1}$  have been also taken into consideration. Some of the proposed assignments of these bands to surface OH groups are described in the next section, followed by some NMR studies of alumina's surface hydroxyls.

### 1.3.3.1 IR spectra attribution

#### 1.3.3.1.1 Peri's model

In a first attempt to explain alumina's IR spectrum [64], Peri [65] developed a model of the (100) surface based on a defective spinel bulk structure, which the author took as predominant, with a top layer of oxide ions only. He concluded five types of *free* (not H-bonded) hydroxyl ions exist after considering that the dehydration of the surface occurs by condensation of OH pairs creating defects (coordinatively unsaturated sites, anions or cations) and that differ on the number of  $O^{2-}$  neighbours. These five types of free OH, depicted in Figure 1-9, where attributed to the IR bands considering that the vibration frequency of an OH group is determined by the local charge density, and so the number of oxide ion neighbours. Broader and lower frequency bands were assigned to H-bonded groups.

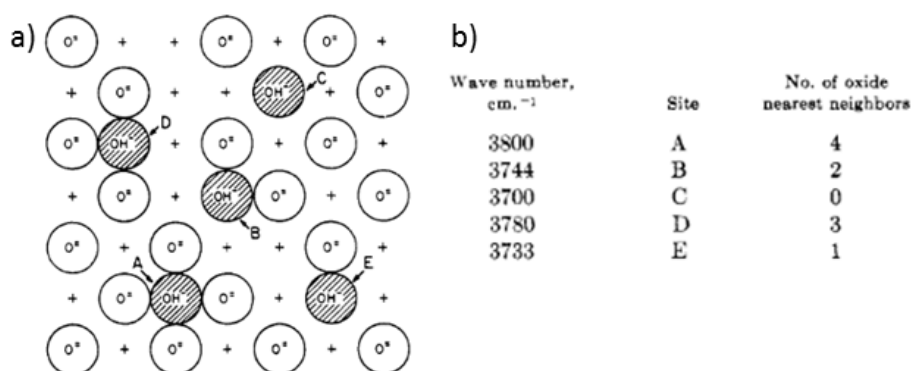


Figure 1-9 – Illustration of Peri's model with a) type of isolated hydroxyls on (100) surface, + denotes Al in lower layer, white circles are oxide ions; and b) IR band attribution [65].

#### 1.3.3.1.2 Tsyganenko and Filimonov's model

Seven years after Peri, Tsyganenko and Filimonov [66] published their study of the IR spectra in the OH range of various metal oxides, including  $\gamma-Al_2O_3$ , considered spinel-like, for which a model of (100) and (111) plane surfaces was presented. The authors suggested that the existence of different IR features is due to the oxygen atom of the hydroxyl group being bounded to one, two or three metal atoms, with all O-Metal bonds being equivalent. Since higher oxygen coordination reduces stretching vibration frequency, the three types of OH I, II and III, as illustrated in Figure 1-10, are attributed to the IR bands in order of frequency diminution and other lower frequency bands are again assigned to H-bonding groups. The

remaining two main bands are explained by differences in the coordination of the metal atoms bonded to each type of OH group, as both tetrahedrally and octahedrally coordinated Al can be found on the surface of  $\gamma\text{-Al}_2\text{O}_3$ . These three types of OH are referred to in more recent works as  $\mu_1\text{-OH}$  (type I),  $\mu_2\text{-OH}$  (type II) and  $\mu_3\text{-OH}$  (type III).

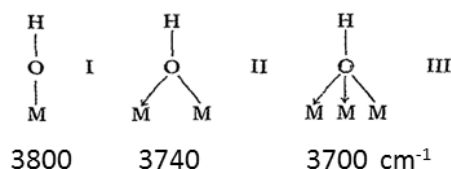


Figure 1-10 - Depiction of the three types of hydroxyls suggested by Tsyganenko and corresponding IR band [66].

### 1.3.3.1.3 Knözinger and Ratnasamy's model

In 1978, Knözinger and Ratnasamy [67] established one of the most complete models of alumina surfaces and OH band attribution [64]. These authors considered the (110), (100) and (111) ideal surface planes based on the defective spinel structure, without reconstruction, to be as follows:

- a) (111) plane: A layer – one third of cations in octahedral interstices and the remaining in tetrahedral interstices ; B layer – all cations in octahedral interstices
- b) (110) plane: C layer –half of cations in octahedral interstices, other half in tetrahedral ones, between rows of oxygen atoms; D layer – all cations in octahedral interstices
- c) (100) plane - all cations in octahedral interstices

These surface layers are covered by hydroxyl groups that can occur in five types, shown in Figure 1-11. Knözinger and Ratnasamy concluded that the vibrational frequency of free hydroxyl groups depends on their net charge, the most negative charge corresponding to the highest frequency.

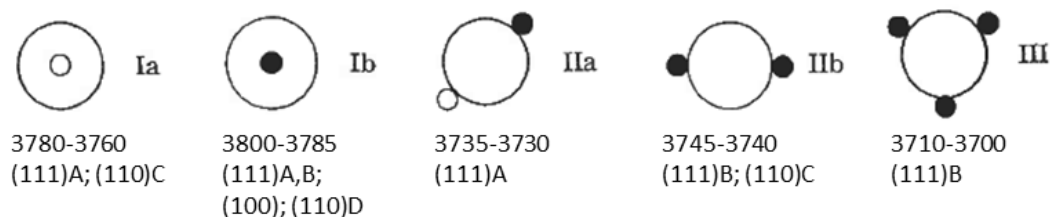


Figure 1-11 - Five types of hydroxyls proposed by Knözinger and Tatnasamy, the corresponding IR band in  $\text{cm}^{-1}$  and type of surface in which they are present; large circles-OH, small filled circle- $\text{Al}_{\text{VI}}$ , small circle- $\text{Al}_{\text{IV}}$  [67].

This model is in agreement with Tsyganenko's attribution and considers the coordination of the adjacent Al atoms in a more detailed way. It should also be noted that surface reconstruction can greatly influence which sites are available, as Sohlberg [46] showed by proposing that in the relaxed (110)C surface tetrahedral Al cations drop into vacant interstices in the next layer and so are no longer accessible on the surface.

#### 1.3.3.1.4 Busca's model

By comparing the IR spectra of various normal, inverted and defective spinels, Busca et al. [63,68] proposed an assignment (Figure 1-12) taking into account the existence of cation vacancies in defective spinels and attributing a more important role to the coordination of adjacent Al atoms than Knözinger and Ratnasamy did. In recent reviews [42,59] the same author outlined the possible importance of the edges and corners formed between the surfaces (, as they can be expected to exhibit Al sites with low coordination (presumably  $\text{Al}_{\text{IV}}$  type) and thus with specific OH groups and/or stronger Lewis acidity if dehydrated.

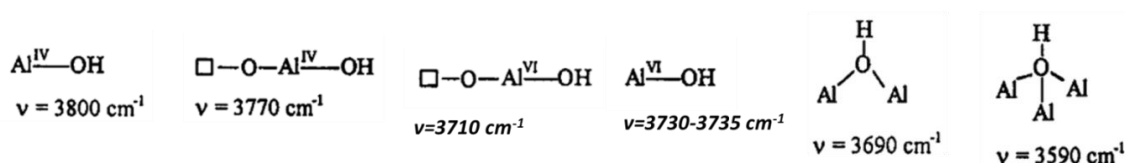


Figure 1-12 - Scheme of hydroxyls attributed by Busca to six IR OH bands [63,64].



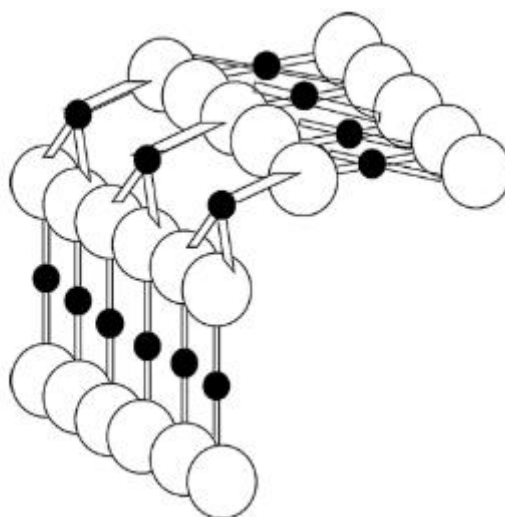


Figure 1-13 – Empirical model of (110)-(100) edge proposed by Busca [42].

#### 1.3.3.1.5 Digne's model

Based on the alumina bulk model of Krokidis [48], Digne et al. [50,51] studied by DFT the dehydrated surfaces resulting from slicing the bulk perpendicularly to the (110), (100) and (111) directions, simulated their hydration, and thus interaction with water molecules, and finally simulated the stretching frequencies of the resulting OH groups providing an assignment of the experimental bands.

The dehydrated (100) surface presents aluminium atoms with coordination five ( $Al_V$ ) and threefold coordinated oxygen atoms. The dehydrated (110) surface exhibits  $Al_{IV}$  from octahedral bulk positions,  $Al_{III}$  from tetrahedral bulk interstices and twofold and threefold coordinated oxygen atoms. In this case, surface relaxation has a strong impact, with  $Al_{IV}$  atoms dropping inward and all surface oxygen atoms relaxing upward. This is in contrast with Sohlberg's proposal that relaxation of (110C) surface is done by  $Al_{III}$  atoms dropping into vacant interstices in the next layer [46]. The (111) surface cannot be stabilized without a minimum level of hydroxylation. Illustrations of the three surface models resulting from Digne's model are represented in Figure 1-14.

With the dehydrated (110) and (100) surfaces as starting point, the interaction of water with these surfaces was simulated to find which hydroxyls are formed during hydration. In the case of the (111) surface, the authors started with the fully hydrated surface and studied its dehydration.

Water adsorption energies obtained, the thermal stability of the surfaces was studied and the optimal conditions of OH concentration and temperature which minimize surface energy were found. The authors found that the (100) is totally dehydrated above 600K, the (111) surface is fully hydrated up to 800K and the (110) surface has an intermediate behaviour. These results were validated by comparing the calculated surface energy (1400 mJ/m<sup>2</sup>) with empirical values from calorimetry measurements at 979K (1340 mJ/m<sup>2</sup>), and more recently by thermogravimetric quantification of the number of OH groups as a function of the temperature and the water partial pressure [69].

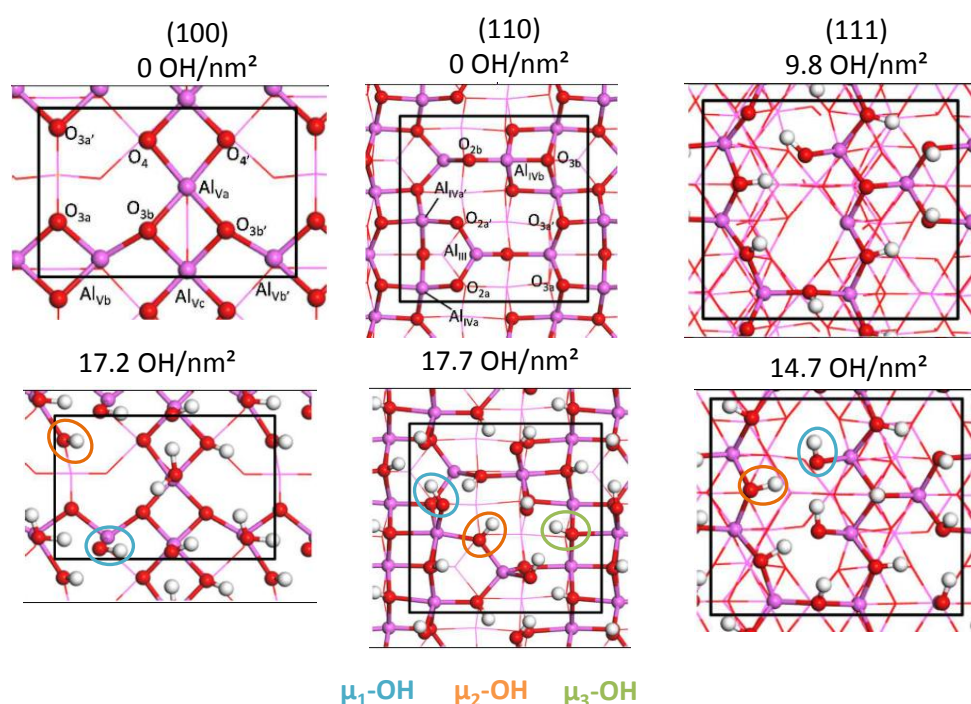


*Figure 1-14 – Top view of dehydrated and hydrated alumina surfaces issued from Digne's model, adapted from [69], some hydroxyl groups are highlighted according to their type.*

Finally, a vibrational analysis of the OH groups found in the hydration study was conducted. The authors' model predicts that (110) surface accounts for 74% of the total area, the (100) surface for 16% and the (111) surface for 10% and this was taken into account for the contribution of each surface's OH groups to the spectra. In general, it was found that:

- OH groups engaged in H-bonds are responsible for the broad experimental feature at 3000-3500 cm<sup>-1</sup>
- The higher frequencies (3800-3760 cm<sup>-1</sup>) correspond to terminal  $\mu_1$ -OH

- Two and threefold coordinated hydroxyls,  $\mu_2$ -OH and  $\mu_3$ -OH, have lower frequencies (3710-3590  $\text{cm}^{-1}$ )

Table 1-1 summarizes Digne's attribution.

*Table 1-1 - Digne's attribution of specific hydroxyls to experimental IR bands by the calculated vibration frequency [51].*

$\nu_{\text{range}}$ ( $\text{cm}^{-1}$ )	$\nu_{\text{calc}}$ ( $\text{cm}^{-1}$ )	Site	Surface
3800-3785	3842	HO- $\mu_1$ -Al <sub>IV</sub>	(110)
3780-3760	3777	HO- $\mu_1$ -Al <sub>VI</sub>	(100)
3745	3752	HO- $\mu_3$ -Al <sub>VI</sub>	(111)
3735-3730	3736	HO- $\mu_1$ -Al <sub>V</sub>	(110)
	3732	HO- $\mu_2$ -Al <sub>V</sub>	(111)
3710-3690	3707	HO- $\mu_2$ -Al <sub>VI</sub>	(110)
	3690	HO- $\mu_2$ -Al <sub>VI</sub>	(111)
3590	3589	HO- $\mu_3$ -Al <sub>VI</sub>	(100)

#### **1.3.3.1.6 Koerin's model**

In his PhD work, Koerin [70] proposed a OH band attribution based primarily on empirical correlations. Koerin studied the IR spectra of a series of alumina samples with crystallites that varied in size and morphology, and thus with different proportions of exposed surface planes and of edges and corners. The attribution described in Table 1-2 was accomplished by searching correlations between the proportion of each band of the spectrum with the proportion of each plane and edges/corners of the different samples. This proportion of exposed planes and edges was obtained by fitting the three peaks of the X-ray diffractograms of the corresponding boehmites with the Scherrer formula [71], thus determining three dimensions of the boehmite crystallite. These were transposed to the  $\gamma$ -alumina crystallite considering the topotactic transformation. The advantage of this approach is that it does not rest on an initial choice of bulk  $\gamma$ -Al<sub>2</sub>O<sub>3</sub> model, as is the case of the previous studies.

*Table 1-2 - Koerin's attribution of specific hydroxyl groups to experimental IR bands [70]*

$\nu$ (cm <sup>-1</sup> )	Site	Surface
3790	HO- $\mu_1$ -Al <sub>IV</sub>	(110)/(100) edge/corner
3772	-	(111)
3754	HO- $\mu_1$ -Al <sub>VI</sub>	(100)
3727	HO- $\mu_1$ -Al <sub>V</sub>	(110)
3704	HO- $\mu_2$ -Al <sub>VI</sub>	all
3684	HO- $\mu_2$ -(Al <sub>IV</sub> , Al <sub>VI</sub> )	all
3667	HO- $\mu_2$ -Al <sub>VI</sub>	(111)

### **1.3.3.1.7 Conclusion**

Despite continuous studies in the past decades resulting in the evolution of alumina surface models, the attribution of the IR OH bands of  $\gamma$ -Al<sub>2</sub>O<sub>3</sub> is still under discussion.

At the head of the efforts is Peri's work, which was limited in using only a model of the spinel (100) surface. Tsyganenko's model introduced the important idea that the number of metal atoms the hydroxyl is attached to is determining of its vibration frequency. The much accredited study of Knözinger and Ratnasamy presents a model of all possible termination surfaces of  $\gamma$ -Al<sub>2</sub>O<sub>3</sub> and OH groups that can be formed in each surface, but does not consider surface reconstruction. Busca built on Knözinger's work by adding into consideration the influence of cation vacancies. Digne presented a novel approach based on a non-spinel bulk model and DFT study of the hydration of alumina surfaces that considers surface relaxation but lacks a model description of edges and corners. In a purely empirical approach, Koerin defies the mostly theoretical models presented so far by not having his attribution biased by an initial choice of bulk model. At last the influence of edges/corners is proposed by Busca and Koerin, however this concept would be more convincing if supported by a theoretical model of those edge/corner structures or an experimental characterization at the atomic scale.

For comparison, Table 1-3 summarizes the attributions made in the six models described.

Table 1-3 - Comparison of the IR OH band attribution by the six works considered in this section.

$\nu_{\text{range}}$ (cm <sup>-1</sup> )	Peri [65]	Tsyganenko [66]	Knözinger [67]		Busca [63]	Digne [51]		Koerin [70]	
3800-3785	A	I	Ib (Al <sub>VI</sub> )	(111)A,B / (100) (110)D	HO-Al <sub>IV</sub>	HO-μ <sub>1</sub> -Al <sub>IV</sub>	(110)	HO-μ <sub>1</sub> -Al <sub>IV</sub>	(110)/(100) edge/corner
3780-3760	D	-	Ia (Al <sub>IV</sub> )	(111)A / (110)C	HO-Al <sub>IV</sub> -O-□	HO-μ <sub>1</sub> -Al <sub>VI</sub>	(100)	-	(111)
3745	B	II	IIb (Al <sub>VI</sub> , Al <sub>IV</sub> )	(111)B / (110)C		HO-μ <sub>3</sub> -Al <sub>VI</sub>	(111)	HO-μ <sub>1</sub> -Al <sub>VI</sub>	(100)
3735-3730	E	-	IIa (Al <sub>VI</sub> , Al <sub>IV</sub> )	(111)A	HO-Al <sub>VI</sub>	HO-μ <sub>1</sub> -Al <sub>IV</sub>	(110)	HO-μ <sub>1</sub> -Al <sub>V</sub>	(110)
						HO-μ <sub>2</sub> -Al <sub>V</sub>	(111)		
3710-3690	C	III	III (Al <sub>VI</sub> )	(111)B	HO-Al <sub>VI</sub> -O-□	HO-μ <sub>2</sub> -Al <sub>VI</sub>	(110)	HO-μ <sub>2</sub> -Al <sub>VI</sub>	all
					HO-(Al, Al)	HO-μ <sub>2</sub> -Al <sub>VI</sub>	(111)	HO-μ <sub>2</sub> -(Al <sub>IV</sub> , Al <sub>VI</sub> )	all
3667	-	-	-	-	-	-	-	HO-μ <sub>2</sub> -Al <sub>VI</sub>	(111)
3590	-	H-bonding	-	-	HO-(Al, Al, Al)	HO-μ <sub>3</sub> -Al <sub>VI</sub>	(100)	-	-

### 1.3.3.2 NMR studies

The surface hydroxyls of  $\gamma$ - $\text{Al}_2\text{O}_3$  have been also studied by solid state (SS)  $^1\text{H}$  magic angle spinning (MAS) NMR and recently higher field spectrometers and refined pulse sequences have allowed for better resolution and new approaches.

DeCanio *et al* [72] obtained the  $^1\text{H}$  MAS NMR spectrum of  $\gamma$ - $\text{Al}_2\text{O}_3$  calcined at  $400^\circ\text{C}$ , which presented two main peaks at -0.4 and 2.2 ppm that were assigned to basic and acidic OH groups respectively. Deuteration of the sample resulted in the detection of more peaks, including a very broad contribution near 7 ppm that was attributed to adsorbed water by comparison with silica-alumina. Hietala *et al* [73] found the same two peaks at 0 and 2.5 ppm on alumina calcined at  $607^\circ\text{C}$ , also relating lower chemical shift ( $\delta$ ) with lower acidity. The spectra obtained are shown in Figure 1-15.

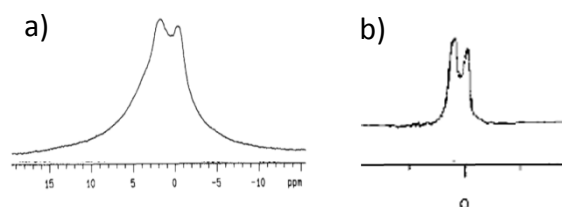


Figure 1-15 -  $^1\text{H}$  NMR of  $\gamma$ - $\text{Al}_2\text{O}_3$  calcined at a)  $400^\circ\text{C}$  [72] and at b)  $607^\circ\text{C}$  [73].

More recently, Delgado *et al.* [74] also obtained the same spectrum for alumina dehydrated at  $500^\circ\text{C}$ . In agreement with previous work, it was considered that the peaks at  $\approx 2\text{ppm}$  and above correspond to  $\text{HO-}\mu_3$  /  $\text{HO-}\mu_2$  and the peak at  $\approx 0$  ppm corresponds to  $\text{HO-}\mu_1$ . To assign the peaks in more detail, DFT calculations of chemical shifts were performed on a model (110) surface model with two degrees of hydration ( $3 \text{ H}_2\text{O}/\text{unit cell}$  and  $2 \text{ H}_2\text{O}/\text{unit cell}$ ). The calculated chemical shifts and corresponding OH groups of interest are presented in Table 1-4. It is worth to note that the chemical shift of H-bonded hydroxyls is higher than the chemical shift of the corresponding free OH.

Table 1-4 – Free surface hydroxyls and corresponding calculated chemical shifts issued from Delgado's work [74].

Site (110)	Calculated $\delta_{\text{OH}}$ (ppm)
$\text{HO-}\mu_1\text{-Al}_{\text{IV}}$	0.3
$\text{HO-}\mu_2\text{-Al}_{\text{V}}$	1.6-2.2
$\text{HO-}\mu_2\text{-(Al}_{\text{IV}}, \text{Al}_{\text{V}})$	2.5-2.9
$\text{HO-}\mu_3\text{-(Al}_{\text{IV}}, \text{Al}_{\text{VI}}, \text{Al}_{\text{VI}})$	4.5

The very complete study of Taoufik et al. [75] employed a high field spectrometer and combined  $^1\text{H}$  MAS NMR,  $^1\text{H}$ - $^{27}\text{Al}$  D-HMQC MAS NMR and  $^1\text{H}$ - $^1\text{H}$  DQ MAS NMR to assign the peaks and propose a topology for the surface sites. Their  $^1\text{H}$  spectrum of alumina calcined and dehydrated at  $500^\circ\text{C}$  presents a) a sharp peak at  $-0.2$  ppm; b) two overlapping peaks at  $1.5$  and  $2$  ppm; c) a shoulder at  $2.5$  ppm; d) a broad peak centred at  $3$  ppm. The classical assignment of  $\text{HO}-\mu_1$  to the  $\approx 0$  ppm signal and of  $\text{HO}-\mu_2$  to  $\approx 2$  ppm peaks was experimentally confirmed by comparing the experimental and calculated  $^1\text{H}$ - $^{27}\text{Al}$  RESPDOR fraction.

The assignment of the five peaks described above to specific hydroxyls was done on the basis of the  $^1\text{H}$ - $^{27}\text{Al}$  D-HMQC spectrum, shown in Figure 1-16. The through-space correlations allow each  $^1\text{H}$  signal from an OH to be associated with the type of  $\text{Al}_x$  that are in the proximity to that hydroxyl. To confirm the assignment, the coupling constant ( $C_Q$ ) calculated by DFT on several cluster models of alumina was compared to the experimental value. The peak assignment thus obtained is summarized in Table 1-5 and relevant spectra are presented in Figure 1-16.

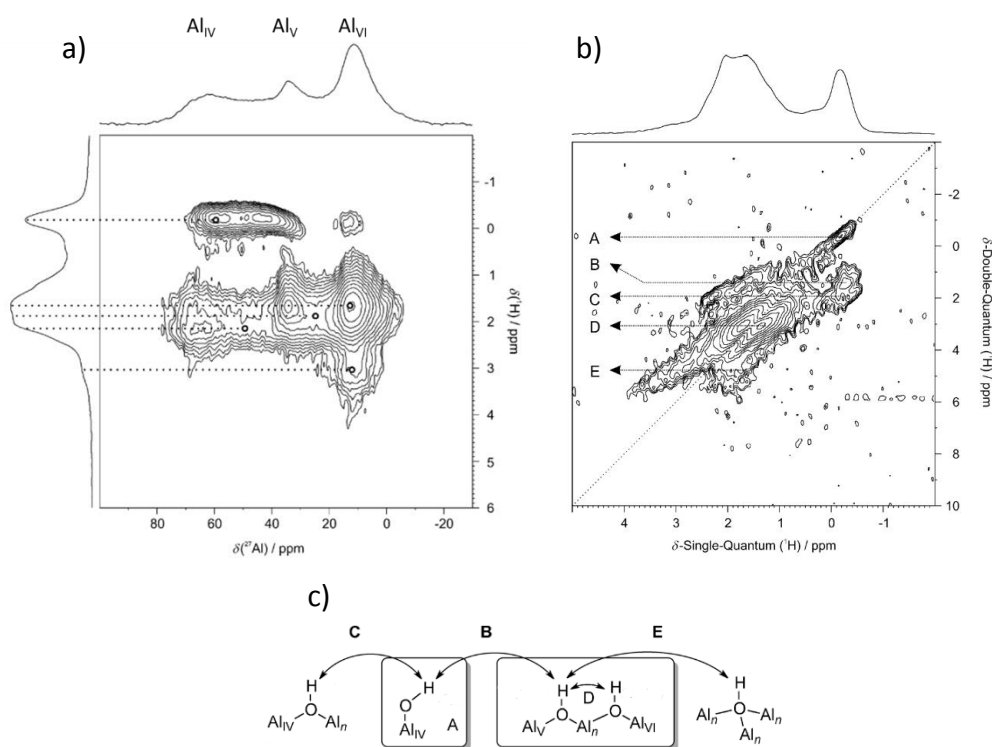


Figure 1-16 -  $\gamma\text{-Al}_2\text{O}_3$  calcined at  $500^\circ\text{C}$  [75]: a)  $^1\text{H}$ ,  $^1\text{H}$ - $^{27}\text{Al}$  D-HMQC MAS NMR spectra and Al projection; b)  $^1\text{H}$ - $^1\text{H}$  DQ MAS NMR spectrum; c) topology suggestion for hydroxyls at surface.

Table 1-5 –  $^1\text{H}$  NMR peak assignment by Taoufik *et al.* [75].

Al-OH type	$^1\text{H}$ (ppm)	$^{27}\text{Al}$ (ppm)
HO- $\mu_1$ -Al <sub>IV</sub>	-0.2	70
HO- $\mu_2$ -(Al <sub>VI</sub> , Al <sub>n</sub> )	2.3-0.8	16
HO- $\mu_2$ -(Al <sub>V</sub> , Al <sub>n</sub> )	2.2-1.5	39
HO- $\mu_2$ -(Al <sub>IV</sub> , Al <sub>n</sub> )	2.5-1.9	76
HO- $\mu_3$ -(Al <sub>n</sub> )	4.0-2.5	n.d.

The double quantum  $^1\text{H}$ - $^1\text{H}$  DQ MAS correlations are indicative of the proximity between the OH groups, leading to a proposed surface site topology. Unfortunately, without an atomistic model of alumina surface, this proximity based topology analysis is difficult to achieve and the interpretation of these experimental results is lacking a more precise location proposal for each type of OH group.

Another interesting study to be mentioned is that of Wischert *et al* [76]. These authors showed that  $^{27}\text{Al}$  NMR is mostly sensitive to the more hydrated fractions of an alumina sample, meaning low hydration areas are not seen in experimental results, by comparing the  $C_Q$  and  $\delta$  calculated for all alumina surfaces issued from Krokidis' [48] bulk model in specific degrees of hydration with the  $C_Q$  and  $\delta$  obtained experimentally by  $\{^1\text{H}\}$   $^{27}\text{Al}$  CP NMR.

In a recent study, Perras *et al* [77] were able to observe Brønsted acid sites (OH groups) of different materials (silica and silica-alumina) and measure the O-H bond length with sub-picometer precision using  $^{17}\text{O}$  NMR, further showing the efficiency of modern NMR techniques to probe the nature of surface hydroxyls.

### 1.3.4 Conclusion

$\gamma\text{-Al}_2\text{O}_3$  is an aluminium oxide polymorph obtained from the topotactic decomposition of the aluminium oxy-hydroxide boehmite. Its crystal structure was for long considered to be that of a defective spinel,  $\square_{2(2/3)}\text{Al}_{21(1/3)}\text{O}_{32}$ , but more recent works have suggested non-spinel structures. The most exposed surface is considered to be the (110), followed by (100) and (111).

IR studies of alumina's surface hydroxyl groups show five main bands. Various attribution attempts have been made over the years, but overall bands at higher wavenumber are associated with the most basic hydroxyls ( $\mu_1$ ) and bands at lower wavenumber are



associated with more acidic hydroxyls ( $\mu_2$  and  $\mu_3$ ). In  $^1\text{H}$  MAS NMR, the most basic OH groups are believed to have the lowest chemical shift, around 0 ppm.

## 1.4 Chlorine doping of $\gamma$ -alumina

Catalytic naphtha reforming catalysts employ alumina doped with around 1%<sub>w/w</sub> chlorine to have the right acidity needed for the isomerization function without too much undesired cracking. Another process that employs chlorine doped alumina, but at higher loadings up to 8%<sub>w/w</sub>, is the isomerization of light naphtha, a unit also dedicated to the production of high octane compounds [19].

### 1.4.1 Chlorination mechanism

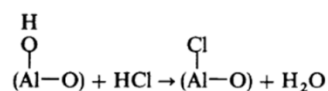
The chlorination of alumina has been the subject of various works [70,78–83]. Although there are key common points between those studies, the results also depend on the method and conditions of chlorination.

The chemisorption of gaseous HCl on dry  $\gamma$ -alumina was studied using IR spectroscopy by Peri [78], Tanaka and Ogasawara [79] and Kytöki and Lindblad [81] who also used  $^1\text{H}$  MAS NMR. Although the alumina pre-treatment and HCl contact conditions, notably temperature, vary among these studies, it was commonly found that:

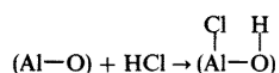
- The intensity of IR bands of isolated hydroxyls diminishes, mainly 3790 and 3775  $\text{cm}^{-1}$
- An intense and broad new band appears at 3500  $\text{cm}^{-1}$

Thus, two main reactions can be considered [81]:

- the exchange reaction of HCl with surface hydroxyls with the formation of water:



- the dissociation of HCl on (Al-O) surface sites resulting in an Al-Cl group and a new hydroxyl:



The first explains the reduction in intensity of the free hydroxyl bands with both IR and NMR results (also by Hietala *et al* [73]) showing that the most basic OH (higher wavenumber in IR [84]) are the first to be exchanged. It is possible that some more acidic groups are also

exchanged as an impact on the  $3730\text{ cm}^{-1}$  band (see Table 1-3 for attribution) is also observed [81]. The broad band appearing at  $3500\text{ cm}^{-1}$  is explained by the creation of new OH groups by the dissociation of HCl [81], which can in turn be involved in H bonding [79]. The possibility of this band being absorbed water molecules formed in the exchange reaction was proved wrong by Tanaka and Osagawara [79]. The increased acidity of the newly formed OH groups has been explained by the electron withdrawing effect of the Cl atom on the adjacent hydroxyl [79].

Marczewski et al. [80] studied the reaction of gaseous  $\text{Cl}_2$  on dry  $\gamma$ -alumina calcined at  $550^\circ\text{C}$ . They found that  $\text{Cl}_2$  reacts with surface hydroxyls and surface oxygen anions to form Al-Cl or Al-OCl groups and new Lewis acid sites by the electron withdrawing effect of Cl on an adjacent CUS  $\text{Al}^{3+}$  (and Brønsted sites at lower temperatures)[83].

Koerin [70] performed the chlorination of alumina with HCl in aqueous media and studied the resulting surface OH groups after thermal treatment at  $450^\circ\text{C}$  under vacuum by IR spectroscopy (Figure 1-17) and MAS NMR. His results agree with the ones mentioned above: the  $3790$  and  $3772\text{ cm}^{-1}$  bands disappear with increasing Cl content as do, to a lesser extent, the bands at  $3754$  and  $3727\text{ cm}^{-1}$  and a broad band at  $3600\text{ cm}^{-1}$  appears. The  $3667\text{ cm}^{-1}$  band also increases in intensity except for the highest Cl content. NMR spectra show again that the most basic hydroxyls are exchanged by the disappearance of the  $^1\text{H}$  peak at  $\delta=0\text{ppm}$ . A chlorination mechanism was thus proposed (according to the author's band attribution):

- Up to  $0.6\text{ Cl/nm}^2$  the most basic  $\mu_1\text{-OH}$  on the (110) surface and (110)/(100) edge are exchanged by Cl. Exchange with  $\mu_1\text{-OH}$  on the (100) surface can also occur.
- Between  $0.6$  and  $0.9\text{ Cl/nm}^2$  new hydroxyls are created
- Above  $0.9\text{ Cl/nm}^2$  more acidic hydroxyls,  $\mu_2\text{-OH}$  on (111) surface, are also exchanged

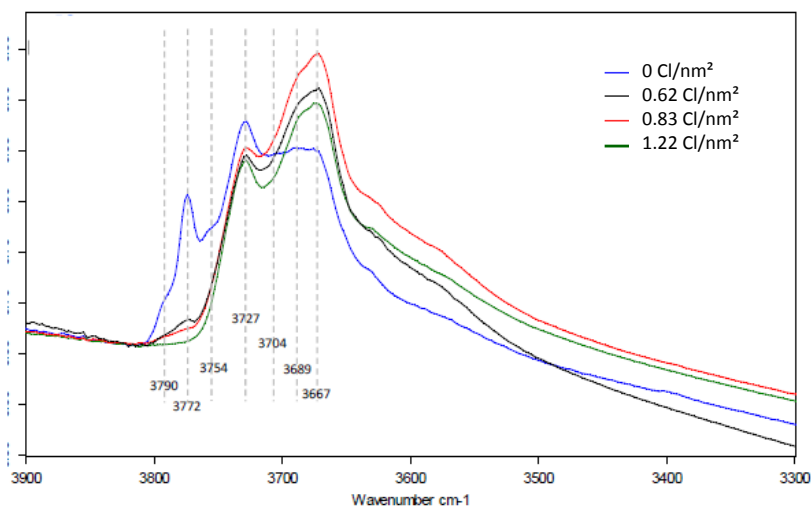


Figure 1-17 – IR spectra of  $\gamma$ -alumina with increasing Cl loadings [70].

The chlorinated surfaces of  $\gamma$ -alumina were studied by Digne et al. [82] using DFT calculations. The substitution of various hydroxyls by chloride ions was investigated having as starting point the hydrated surface models developed in previous works [50,51] with given hydroxyl coverages. The theoretical results were validated by IR measurements. The total OH and Cl surface coverage was assumed to remain constant for (low) Cl contents typical of catalytic naphtha reforming. It was found that  $\mu_1$ -OH on the (110) and (100) surfaces are preferably exchanged forming  $\mu_1$ -Cl, as these hydroxyls are isolated and the one single Al-Cl bond distance is easily optimized. On the other hand, the exchange of  $\mu_2$  and  $\mu_3$ -OH is less favourable energetically (at the low chlorine coverage considered here,  $< 1\%$  Cl corresponding to reforming catalysts) since the relaxation of two or three Al-Cl distances would lead to strong local deformations. Hydroxyls involved in H bonding, as the ones on the (111) surface that exhibits a strong H bond network, are also less likely to be exchanged as having a  $\text{OH}\cdots\text{Cl}$  hydrogen bond instead would make them less stable. The experimental broadening of bands assigned to  $\mu_2$  and  $\mu_3$ -OH ( $3670\text{ cm}^{-1}$ ) is explained by an increase in stretching frequency of some hydroxyls due to the weakening of H bonds by the presence of Cl.

### 1.4.2 Acidity of chlorinated alumina

The increase of the acidity of doped alumina can be investigated using basic probe molecules or model test reactions, as done in various studies [15,79,83,85–87].

A popular method, already mentioned above, is following the desorption of pyridine by Fourier transform IR spectroscopy. Some works describe the absorption band of pyridinium ion at  $1540\text{ cm}^{-1}$  for chlorinated aluminas [79], whereas it is not formed on pure alumina. A DFT study [82] of pyridine adsorption on the (100) surface explained the experimental result by the weakening of the hydrogen bond network upon chlorination that causes the H bond donor hydroxyls to be more labile. For higher chlorine loadings, up to 8%, the surface is destabilized with increasing Cl coverage due to the lateral repulsion between Cl anions.

Other studies do not find the characteristic band of pyridinium ion and are thus unable to identify a change of the Brønsted acidity using pyridine [15,85,87]. In such a case, this molecule is thus more useful to study Lewis acid sites (CUS  $\text{Al}^{3+}$ ), allowing to distinguish qualitatively their acidity between strong (tetrahedral Al), moderate (tetrahedral and octahedral Al) and weak Lewis acid sites. It is observed that the amount of medium and (mainly) strong Lewis sites augments with increasing chlorination (1% and 1,4%<sub>w/w</sub> Cl) [85,87].

Other bases stronger than pyridine, such as piperidine, have been found to protonate on alumina [15]. 2,6-dimethylpyridine adsorption can be used to selectively probe the strongest Lewis acid sites [88]. CO adsorption at low temperatures (<100 K) can be used to study both Lewis and Brønsted sites [61,64], as CO also interacts with the hydroxyl groups.

The desorption of probe basic molecules can also be followed by NMR, as described by Guillaume et al. [86] who studied the desorption of trimethylphosphine (TMP) by  $^{31}\text{P}$  SS MAS NMR (Figure 1-18). The spectra of adsorbed TMP on alumina presents two mains peaks, one due to Brønsted sites (with proton transfer) and the other due to Lewis sites. The intensity of these peaks remaining after desorption at a given temperature is indicative of the acid strength of the sites. In agreement with the works mentioned above, it is observed an increase in the number of strong Lewis sites with increasing Cl loading, with a loss of weak sites, as the total amount of Lewis sites remains more or less constant for all four Cl contents studied (from none to 1,4%<sub>w/w</sub>Cl or 1,3 Cl/nm<sup>2</sup>). The total number of Brønsted sites clearly increases with increasing Cl content, being more than double the value for non-doped alumina at 1,4%Cl. The proportion of strong Brønsted sites also increases with Cl loading. In additions, these results confirm that new hydroxyls are formed during chlorination.

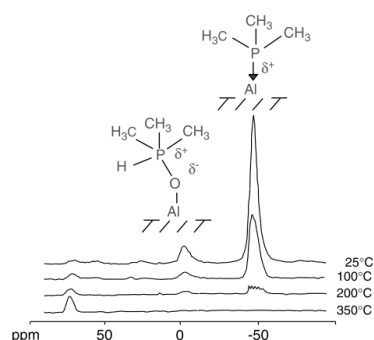


**Figure 1-18** -  $^{31}\text{P}$  MAS NMR spectra of  $(\text{CH}_3)_3\text{P}$  adsorbed on  $\gamma$ -alumina pre-treated at  $530^\circ\text{C}$  illustrating effect of desorption temperature [86].

The activity in skeletal isomerization of 3,3-dimethyl-1-butene was used as an indicative of Brønsted acidity in Pt/ $\gamma$ - $\text{Al}_2\text{O}_3$ -Cl catalysts, since this reaction occurs exclusively through a pure protonic mechanism on these sites [87]. Again, a higher chlorine loading translated into higher Brønsted acidity.

### 1.4.3 Conclusion

Chlorination of  $\gamma$ -alumina occurs firstly through exchange of the most basic  $\mu_1$  hydroxyls on the (110) surface and (110)/(100) edge, and eventually of more acidic  $\mu_2$ -OH, forming Al-Cl. The formation of new hydroxyls and the breaking of Al-O-Al surface bridges is also reported in the literature upon dissociation of chlorination agent HCl.

Upon chlorination an increase of acidity is revealed experimentally for both Lewis and Brønsted sites. For Lewis acid sites this is explained by the electron withdrawing effect of Cl on an adjacent CUS  $\text{Al}^{3+}$ . For Brønsted sites their increased acidity is attributed to either the electron withdrawing effect of the Cl atom on an adjacent hydroxyl or to the disturbance of the hydrogen bond network upon chlorination.

## 1.5 Supported Platinum

Highly dispersed noble metal nanoparticles supported on an oxide support are used for various catalytic applications, from refinery processes to exhaust gas depollution, and have thus been largely studied. In the case of catalytic naphtha reforming, the low metal loadings and its dispersed nature limit the characterization techniques that can be used to study the Pt phase. Generally the model systems studied have considerably higher Pt content (to

overcome sensitivity issues) and do not consider the doping of the alumina support or of the platinum particles.

The following sections summarize some of the work reported on the literature on relevant Pt/ $\gamma$ -Al<sub>2</sub>O<sub>3</sub> systems.

### 1.5.1 Supported Pt in oxide state

The metal oxide phase resulting from the drying and calcination operations that follow platinum impregnation appears to be in the form of ultra-dispersed oxide complexes.

HR-HAADF-STEM images of 0.35%<sub>w/w</sub>Pt/ $\gamma$ -Al<sub>2</sub>O<sub>3</sub> catalysts calcined at 500°C (Figure 1-19 a) [89] and of 0.3%<sub>w/w</sub>Pt or 0.5%<sub>w/w</sub>/ $\gamma$ -Al<sub>2</sub>O<sub>3</sub> catalysts calcined at 300°C (Figure 1-19 b) [90] shows mainly individual atoms distributed on the support, with occasional Pt dimers or trimers, in agreement with other works [91–94].

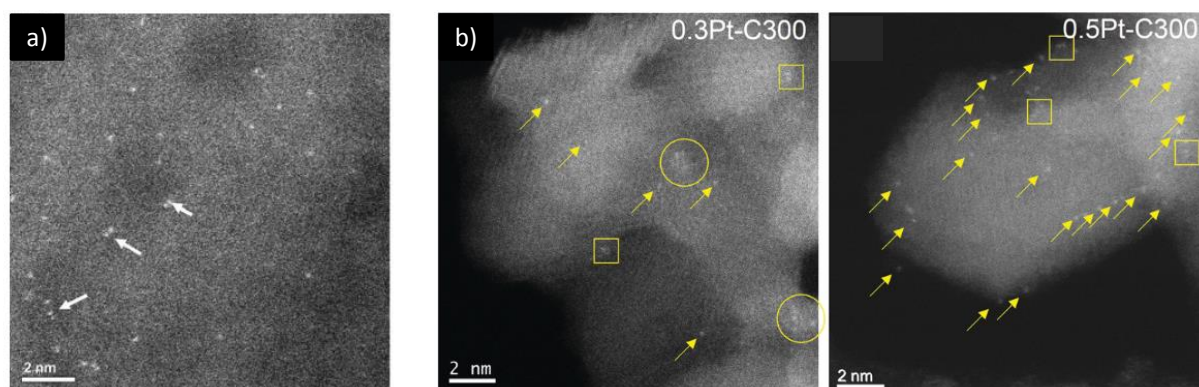


*Figure 1-19 – HR-HAADF-STEM images of calcined a) 0.35%<sub>w/w</sub>Pt/  $\gamma$ -Al<sub>2</sub>O<sub>3</sub> [89]; b) 0.3%<sub>w/w</sub>Pt and 0.5%<sub>w/w</sub>/ $\gamma$ -Al<sub>2</sub>O<sub>3</sub> [90].*

The study by Dessal et al. [90] also developed DFT models of oxide Pt complexes supported on the dehydrated (100) surface. Pt<sub>1</sub>O<sub>4</sub>/(100) and Pt<sub>2</sub>O<sub>4</sub>/(100) models (Figure 1-20) were found to be the most stable in calcination conditions. Also, the calculated “clustering” free energies showed that aggregation of Pt<sub>1</sub>O<sub>4</sub> into Pt<sub>2</sub>O<sub>x</sub> or Pt<sub>13</sub>O<sub>y</sub> oxide clusters is not favourable.

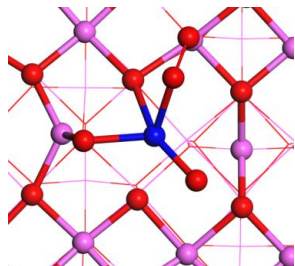
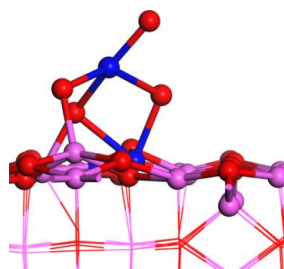
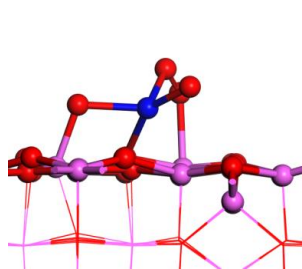
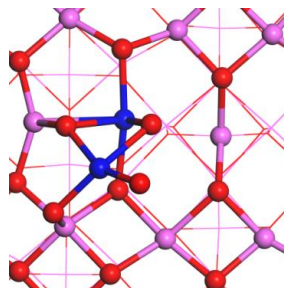
a)  $\text{Pt}_1\text{O}_4/(100)$ b)  $\text{Pt}_2\text{O}_4/(100)$ 

Figure 1-20 – Most stable Pt oxide structures supported on dehydrated (100) surface in calcination condition a)  $\text{Pt}_1\text{O}_4$  and b)  $\text{Pt}_2\text{O}_4$ [90]; top – top view, bottom – side view.

The monoatomic nature of the oxide complexes is supported by extended X-ray absorption fine structure spectroscopy (EXAFS) studies [90,94–97] for which a Pt-Pt distance is not found whereas the Pt-O contribution dominates the EXAFS spectra (Figure 1-21 a). For instance, the EXAFS spectrum of the sample featured in Figure 1-19 b ( $0.3\%_{\text{w/w}}/\gamma\text{-Al}_2\text{O}_3$ ) was fitted with a single Pt-O path with a coordination number of 5.5 (Figure 1-21 a). When chlorine species are used in the impregnation, a Pt-Cl distance is also found in EXAFS (Figure 1-21 b). Table 1-6 summarizes the EXAFS fitting results of those studies.

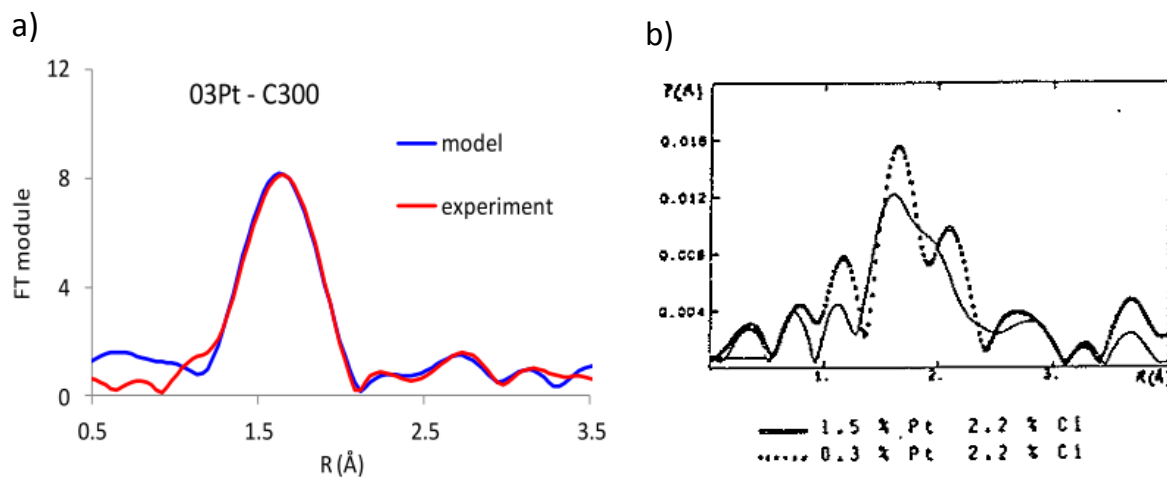


Figure 1-21 - Pt  $L_3$  edge EXAFS F.T. spectra of a) 0.3%<sub>w/w</sub>/γ- $Al_2O_3$  calcined at 300°C [90] and corresponding fitted model and of b) Pt/γ- $Al_2O_3$ -Cl catalysts calcined at 530°C [95,97].

Table 1-6 - EXAFS fitting results for oxidized Pt/ $Al_2O_3$ -Cl samples [95,96].

	Gracia <i>et al.</i> [96]			Berdala <i>et al.</i> [95]			
Catalyst	1.5%Pt/Al <sub>2</sub> O <sub>3</sub>	1.5%Pt/Al <sub>2</sub> O <sub>3</sub> -2.1%Cl		0.3%Pt/Al <sub>2</sub> O <sub>3</sub> -2.2%Cl		1.5%Pt/Al <sub>2</sub> O <sub>3</sub> -2.1%Cl	
Treatment	Calcined 250°C	Calcined 300°C		Calcined 530°C			
Path	Pt-O	Pt-O	Pt-Cl	Pt-O	Pt-Cl	Pt-O	Pt-Cl
R (Å)	2.06	2.03	2.31	2.04	2.34	2.03	2.32
CN*	5.9	3.5	2.5	5.5	1.7	5.5	1.7

\* Coordination Number

The supported metal oxide created by the calcination treatment after impregnation is then believed to consist of a  $PtO_x$  species ( $PtO_2$  is a common theoretical starting point and corresponds to the stoichiometry of the  $Pt_2O_4$  DFT model) or, when chlorine species are present, of a  $PtCl_xO_y$  ( $PtCl_4O_2$  having been suggested) [97,98].

These supported monoatomic oxides are actually single atoms catalysts (SAC), an emerging class of catalytic systems aiming at maximum metal use efficiency [99]. Indeed, platinum has been used in several studies looking to explore the potential of single atom catalysts, be it using alumina[90,92,94,100–102] or other supports such as nitrogen-doped microporous hierarchical carbon [103] or ceria [104–107]. Two challenges are common to all preparations: 1) the formation of nanoparticles upon activation and 2) the fact that the single atoms may not be intrinsically more active than NPs. SA sintering is particularly favourable upon reduction in the case of  $Pt_1/Al_2O_3$  [90,94], as discussed ahead. Nevertheless, single atom dispersion was maintained after reduction at 200°C under 5% $H_2$



and after hydrosilylation reaction test at 100°C when nano-rod alumina was used as a support [100].

Interestingly, re-oxidization of previously reduced Pt/Al<sub>2</sub>O<sub>3</sub> does not revert the metallic phase to its original monoatomic complex form, as Pt-Pt distances in EXAFS [96] are conserved. Indeed, DFT models (that do not consider Cl) show that re-oxidation of Pt<sub>13</sub>/(100) nanoparticles into Pt<sub>13</sub>O<sub>22</sub>/(100) oxide complexes is favourable under oxygen atmosphere, but this oxide complex is not expected to re-disperse into monoatomic complexes due to a strong interaction with the support through Pt-O and Pt-Al bonds [90].

### **1.5.2 Supported Pt in reduced state**

The active metallic phase capable of promoting de/hydrogenation is that of reduced platinum. Reduced supported Pt has been for long studied in order to clarify what is the shape and size of Pt entities and what is the impact of Pt-support and Pt-adsorbate interactions on the nanoparticles (NPs). As expected in complex systems, these factors are strongly interconnected.

#### **1.5.2.1 Shape, size and local structure of Pt nanoparticles**

After calcination, the metallic phase is mostly composed of single atoms dispersed on the support as oxide complexes. In a HR-HAADF-STEM study, Sinkler et al. [108] showed that Pt clusters and nanoparticles are successively created with increasing reduction temperature (from 250°C to 700°C) for a 0.35%<sub>w/w</sub>Pt/Al<sub>2</sub>O<sub>3</sub>-Cl catalyst (*S*<sub>BET</sub>=160m<sup>2</sup>/g) that can be considered representative of the ones industrially employed. These observations are in agreement with in situ reduction EXAFS results by Dessal et al. [90] showing the Pt-Pt contribution increase while the Pt-O one decreased with increasing temperature from room temperature to 300°C for a 0.3%Pt/Al<sub>2</sub>O<sub>3</sub> catalyst (note no Cl is present in this case).

After 700°C reduction the average nanoparticle size found by Sinkler et al. [108] is of 0.88 nm with around 8-18 Pt atoms per cluster (Figure 1-22). By plotting the number of atoms per cluster vs cluster size and comparing the experimental plot (reduction at 700°C) with theoretical curves for different particle morphologies, the cluster shape was found to be a flat bi-planar slab. This result was confirmed by HAADF intensity analysis that shows nanoparticles have a thickness of at most two Pt atom layers.

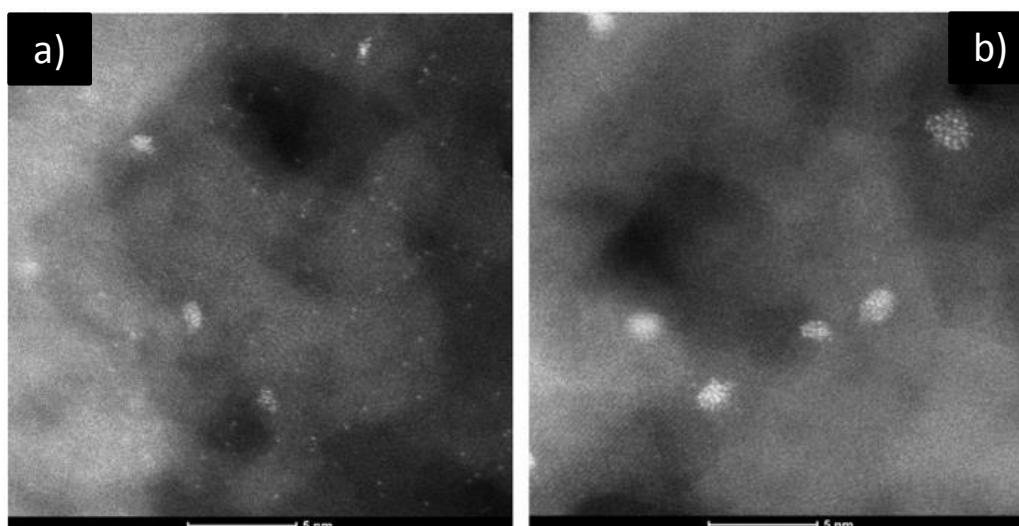


Figure 1-22 – HAADF-STEM images of a 0.35%<sub>w/w</sub>Pt/Al<sub>2</sub>O<sub>3</sub>-Cl catalyst reduced at a) 350°C and at b) 700°C, from [108].

These results are in good agreement with other HR-STEM observations [89] of 0.35%Pt/Al<sub>2</sub>O<sub>3</sub> reduced at 500°C showing 0.6-1 nm nanoparticles, as well as isolated atoms and occasional Pt dimers on the support, that are believed to be of a *raft-like* morphology consisting of two layers of atoms. It should be noted that such observations highlight the highly dispersed nature of the metallic phase. Table 1-7 offers a summary of reported or mean Pt particle size measured by electron microscopy for reduced catalysts in other studies. It can be seen that even for different supports and Pt loadings, the Pt NPs are of nanometric size around 1 nm.

Table 1-7 - Platinum particle sizes measured by STEM.

	Catalyst	Size (nm)
Gänzler et al.[109]	4%Pt/ Al <sub>2</sub> O <sub>3</sub>	1.5
Zhu et al.[110]	2%Pt/ Al <sub>2</sub> O <sub>3</sub>	2-4
Bus et al.[111]	2% Pt/ Al <sub>2</sub> O <sub>3</sub>	1
Ramallo-Lopez et al.[112]	1.6%Pt/ Al <sub>2</sub> O <sub>3</sub>	4.9
Li et al.[113]	1%Pt/SiO <sub>2</sub>	1.51
Dessal et al.[90]	0.5%/ Al <sub>2</sub> O <sub>3</sub>	≈1
Ramallo-Lopez et al.[112]	0.8%Pt/ Al <sub>2</sub> O <sub>3</sub>	2.8
El Assal et al.[114]	0.7%Pt/ Al <sub>2</sub> O <sub>3</sub>	1.2
Bradley et al.[89]	0.35%Pt/ Al <sub>2</sub> O <sub>3</sub>	0.6-1
Sinkler et al.[108]	0.35%Pt/ Al <sub>2</sub> O <sub>3</sub> -Cl	0.88
Gorczyca et al.[115]	0.3%Pt/Al <sub>2</sub> O <sub>3</sub>	0.5-1
Zhu et al.[110]	0.3%Pt/ Al <sub>2</sub> O <sub>3</sub>	0.5-1
Dessal et al.[90]	0.3%/ Al <sub>2</sub> O <sub>3</sub>	≈1
Sanchez et al.[39]	Pt-Re/ Al <sub>2</sub> O <sub>3</sub>	0.75
Small et al.[116]	10% Ir-Pt/ Al <sub>2</sub> O <sub>3</sub>	1.7

Other characterization methods have been used to evaluate Pt nanoparticle sizes such as Small-angle X-ray scattering (SAXS) and EXAFS. The study of Ramallo-Lopez et al. [112] aimed at comparing the results obtained by TEM, SAXS and EXAFS for the nanoparticle size evaluation. While their SAXS and EXAFS measurements for reduced 0.8 and 1.6%<sub>w/w</sub>Pt/Al<sub>2</sub>O<sub>3</sub> (1.20 and 1.44 nm, and, 1.5 and 1.6 nm, respectively) are in good agreement with the microscopy results by other authors, their own TEM analysis gives much larger metal particle average sizes (see Table 1-7). Their microscopy measurements were done in TEM mode, while nanoparticles of <1 nm are hardly visible in TEM. Such large Pt particles and resulting low metal dispersion (35% and 22% by H<sub>2</sub> chemisorption) must result from inadequate synthesis (in this case, incipient wetness impregnation with H<sub>2</sub>PtCl<sub>6</sub>). The fact that an averaging analysis like EXAFS still produces a size estimate under 2 nm can be indicative that only a small fraction of the Pt particles was observed by TEM, as the remaining fraction with sizes more characteristic of this system are too small to be observed.

Lee et al. [117] employed small angle X-ray spectroscopy (SAXS) to evaluate Pt nanoparticle size in contact with n-dodecane at different temperatures (room temperature to 600°C) with the goal of studying the effect of particle size on n-dodecane cracking. While the catalyst prepared by incipient wetness impregnation of SiO<sub>2</sub> with H<sub>2</sub>PtCl<sub>6</sub> (final content of 1.2%<sub>w/w</sub>Pt) maintained a size of 0.9-1 nm at all reaction temperatures, the catalyst prepared by ion exchange with a solution of Pt(NH<sub>3</sub>)<sub>4</sub>(NO<sub>3</sub>)<sub>2</sub> (1.88%<sub>w/w</sub>Pt/SiO<sub>2</sub>) presents a sudden increase in particle size at 300°C from 1.2 nm to 2.1 nm. These results are used to explain differences in n-dodecane cracking conversion and selectivity. However, the authors overlooked in their discussion that the catalyst prepared by impregnation may have residual amounts of Cl (possible impact on Lewis acidity of support) and that both catalysts show very different CO uptake values, suggesting that the amount of accessible Pt atoms is not the same in the two materials.

EXAFS results of reduced supported Pt by various authors [90,95,96,108,111,112,118–122] share a main common point: the Pt-Pt contribution is dominant, with lower coordination number (CN) and slightly contracted distances compared to bulk fcc Pt (CN=12 and R=2.77 Å). This smaller distance can be explained by an increased electron density between metal atoms (vs bulk), caused by the dehybridization of spd metal orbitals, resulting in contraction of the Pt-Pt distance [121,123]. Some studies [90,95,96,108,111,112,120,120,121] fit a Pt-O

distance ( $R \approx 2.0 \text{ \AA}$ ) that is attributed to oxygen atoms from the supports' surface. Others [108,113,120,122,123] also find a *long Pt-O* contribution ( $R \approx 2.5 \text{ \AA}$ ). In this case, a flat raft like Pt nanoparticle morphology is again evoked [122,123]. When Cl is present in the catalyst, no Pt-Cl contribution is detected [95,96], in contrast with the results in oxide state.

Despite STEM analysis hinting at a flat bi-planar nanoparticle morphology, the small amount of sample observed raises the question of how representative can those results be. Another approach at clarifying the particle morphology issue was undertaken by Hu et al. [124] with a DFT study of  $\text{Pt}_{13}$  nanoparticles that considered seven distinct morphologies (from 2D bi-planar to 3D) and two  $\gamma$ -alumina surfaces as starting point (dehydrated (100) and (110) with  $8.9 \text{ OH/nm}^2$ , from [51]). These authors found flat bi-planar nanoparticles to be the most stable on the dehydrated (100) surface (Figure 1-23), which exhibits strong deformation, once adsorbed, in comparison to their *gas phase* state. This morphology is most likely stabilized due to interaction with the support, as several Pt-O and Pt-Al bonds are formed. These nanoparticles are overall anionic due to charge transfer from the support (O atoms bonded to Pt are electronically depleted). On the contrary, 3D spherical NPs are stabilized on the hydrated (110) surface (Figure 1-23). There is less interaction with the support, that is made through Pt-O(H) bonds, preferably between  $\mu_1$ -OH that protrude outwards from the surface and low coordination corner Pt atoms. When migration of an H atom (from a  $\mu_2$  or  $\mu_3$  acidic hydroxyl) onto the cluster is considered, the cluster is stabilized and is overall cationic in charge (it is slightly anionic without H migration). This work suggests that 1)  $\text{Pt}_{13}$  nanoparticle morphology depends on the alumina surface and its hydration degree and 2) NPs are more stable on the dehydrated (100) surface, considered to account for 20% of the crystallites' surface.

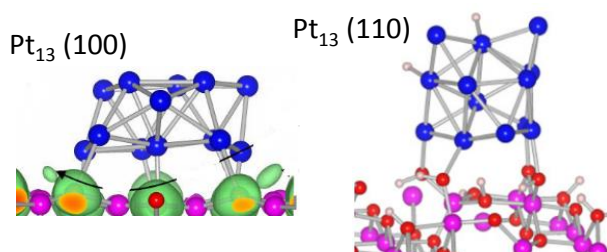


Figure 1-23 - Most stable Pt cluster morphology on the (100) and (110) alumina surfaces [124].

From the results described above one can see there is a relationship between nanoparticle shape, interaction with support and resulting charge transfer that impacts the electronic

properties of the metallic phase. XANES analysis is the tool of choice to probe electronic properties of the metal in such systems, however its interpretation is not straight forward and usually depends on the comparison of experimental spectra with the ones of references such as Pt foil or PtO<sub>2</sub>. In the case of nanoparticles those comparisons may induce erroneous conclusions, on the oxidation state of the metal for example, due to XANES effects inherent to cluster size [125].

The work of Behafarid et al. [126] tackles this issue by studying the XANES features of Pt nanoparticles synthesised by micellar encapsulation to have specific shapes and sizes (2D to 3D), Figure 1-24, deposited on  $\gamma$ -alumina. Crossing characterisation data from EXAFS (coordination numbers) and TEM (particle diameters) with a data base of fcc cluster shapes allowed for a suggested cluster shape for each sample and the calculation of *surface/total atoms* and *in contact with support/total atoms* ratios. They found that the XANES white line (WL) of nanoparticles is wider and is shifted to higher energy with respect to bulk Pt. The increase in WL width was found to be more pronounced for smaller particles in comparison with larger particles of the same shape, 2D. A linear correlation between energy shift (relative to bulk Pt) as well as edge peak area and particle size indicates that the smallest nanoparticles are the most affected by intrinsic size effects.



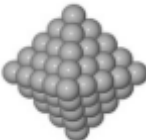

Model cluster shapes				
TEM diameter (nm)	$0.8 \pm 0.2$	$0.8 \pm 0.2$	$1.0 \pm 0.2$	$1.0 \pm 0.2$
Total # of atoms	22	44	85	33

Figure 1-24 - Pt nanoparticle shape, size by TEM and total number of atoms used in Behafarid's work [126]

### 1.5.2.2 Pt-support and Pt-adsorbate effects

It was already seen above that the shape of Pt nanoparticles relates with the interaction with the support. The same study by Behafarid [126] found that the XANES WL energy shift towards higher energies (vs bulk Pt) is more pronounced for flat 2D morphologies which have a higher portion of Pt atoms in contact with the support ( $\nearrow \Delta E_0 \rightarrow$  flat shape  $\rightarrow$

enhanced metal/support interaction). These findings were explained by considering that the alumina surface of the synthesized samples can be expected to be O-terminated and so there can be charge transfer from Pt towards the support. This was used by Lee *et al.* [117] (mentioned above) to deduce nanoparticle morphology from XANES data.

Pt-adsorbate effects are mostly studied using hydrogen, due to its relevance in de/hydrogenation reactions and in chemisorption characterization methods. Also, as reduced samples are often obtained by reduction with H<sub>2</sub>, the study of reduced catalysts may be performed in the presence of adsorbed hydrogen, even if this is not often considered to be the case. XAS experiments have overall shown that upon hydrogen adsorption: 1) the Pt-Pt distance measured by EXAFS increases to bulk-like values, [111,121,123,127,128]; 2) XANES WL is shifted to higher energies [115,126,127,129] and WL intensity decreases [115,123,126,127]. The Pt-Pt bond length expansion is explained by the electron-withdrawing properties of H chemisorbed on Pt that leads to a decrease in electronic density [115,121,123]. This can be accompanied by a decrease in the density of electronic states near the Fermi level that relates to the positive WL energy shift [126]. The decrease in WL intensity indicates a reduction in the number of unoccupied d states of Pt [127] that may be explained by the formation of less discrete Pt-H orbitals.

Theoretical DFT molecular dynamics calculations by Mager-Maury *et al.* [130] suggest a change in nanoparticle morphology (on the dehydrated alumina (100) surface) upon H adsorption, from flat bi-planar to 3D cuboctahedral for H/Pt>1.4, accompanied by a loss of metallic character of the Pt atoms. In catalytic reforming reaction conditions with moderate H/Pt ratios below 1.4 [131] the particles retain their flat shape and metallic character. Follow up experimental work by Gorczyca *et al.* [115] with *in situ* XANES and spectral simulation based on Pt<sub>13</sub> nanoparticle models incorporating different H contents on both (100) and (110) alumina surfaces. Cluster models used in the best spectral simulation are illustrated in Figure 1-25. It was found that, for the conditions used, the nanoparticle morphology on the (100) surface remains mostly bi-planar in the presence of hydrogen. Nanoparticles on the (110) surface do evolve from their initial (no H) 3D shape [124] to a distorted cuboctahedron with increasing hydrogen adsorption. Indeed, another EXAFS study [123] concluded that Pt NP morphology for reduced 1%Pt/ $\gamma$ -Al<sub>2</sub>O<sub>3</sub>-Cl is flat raft-like whether

H<sub>2</sub> is chemisorbed or not, in contrast with a reduced 1%Pt/ $\gamma$ -Al<sub>2</sub>O<sub>3</sub>-Rb sample for which the NP morphology is “flattened” upon H<sub>2</sub> desorption.

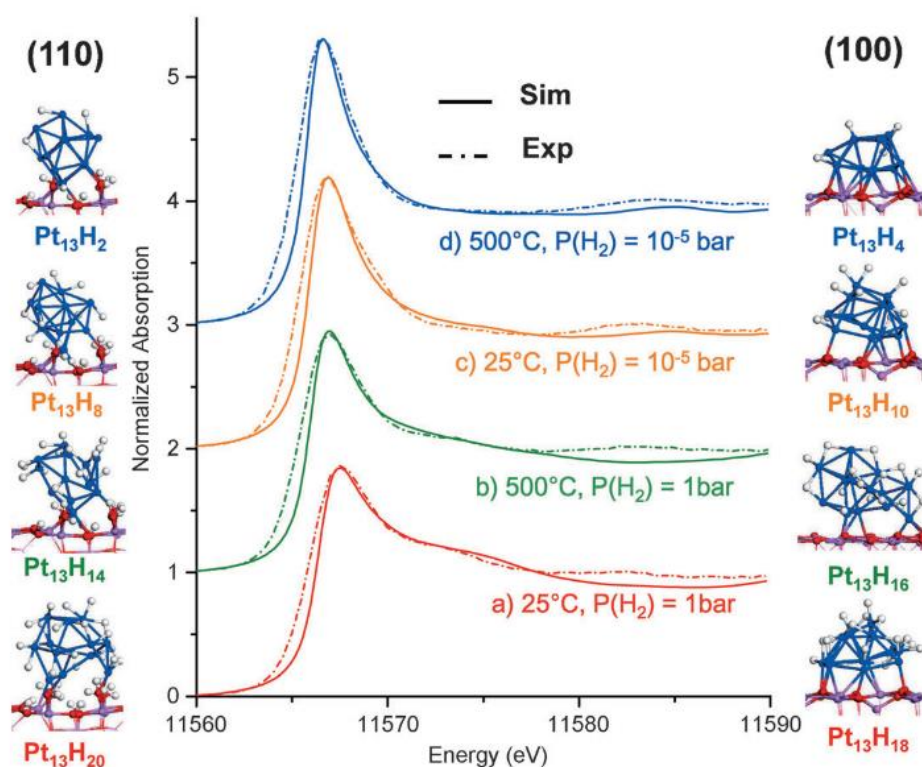


Figure 1-25 – Pt-L<sub>3</sub> edge HERFD–XANES spectra recorded in different operating conditions (dashed line) and best simulated XANES spectra (full lines) combining models on the (100) face (right side) and on the (110) face (left side) reported in the work of Gorczyca et al. [115].

In a work that correlates with most of the aspects so far discussed, Mager-Maury [132] also studied by DFT the stability of Pt<sub>n</sub> clusters (1 ≤ n ≤ 5, n = 13) on dehydrated (100) and (110) with varying hydration levels and Cl content surfaces considering H, OH or Cl migration onto the clusters. On the *bare* (100) surface the clusters are stabilized by Pt-Al and Pt-O bonds and there are no species available for migration. On the (110) surface, without considering species migration, small clusters (n = 1–3) are more stable when a high surface chlorination of 5.9 Cl/nm<sup>2</sup> is used, already showing the effect of chlorination on the metallic phase. The migration of an H atom from surface hydroxyl groups, reverse spill-over, stabilizes clusters (mainly the smaller ones) due to its affinity to the metal and to the newly formed bond with the deprotonated O atom (this is accompanied by cluster deformation). Only one migrated H atom stabilizes the Pt<sub>13</sub> cluster since this structure cannot deform sufficiently to accommodate additional Pt-O bonds. The migration of an OH group (most likely a  $\mu_1$ ) only stabilizes Pt<sub>2</sub> and Pt<sub>3</sub> clusters, in agreement with previous work [124]. On the other hand, the

migration of a Cl atom (most likely a  $\mu_1$ -Cl) stabilizes all clusters, Pt<sub>13</sub> nanoparticles in particular for the slightly chlorinated (110) surface, and favours interaction with CUS Al<sub>III</sub>. The combined migration of H and Cl is even more favourable than the sum of their separate effects, originating a stronger interaction with the support leading to a flatter morphology of the Pt<sub>13</sub> cluster on the highly chlorinated (110) surface. To be noted the stabilizing effect of chlorine, not only on small clusters, but also on Pt<sub>13</sub> that was found to adopt a 3D morphology on the hydrated (110) surface in the absence of Cl [124]. In agreement with already discussed results, the migration of these species was found to expand the clusters. An electronic charge analysis showed that clusters on the dehydrated (100) surface are negatively charged, as seen before [124]. On the (110) surface, H only migration renders the cluster positively charged by being electronically depleted through then newly formed Pt-O bond. Migration of Cl renders the clusters more negatively charged due to a greater interaction with surface Al. The combined migration of H and Cl ends up producing a compensating effect leading to more or less neutral clusters, Figure 1-26. Overall, Pt clusters are more stable on the chlorinated (110) surface and a local energy minimum was found for the Pt<sub>3</sub> cluster.



Figure 1-26 - Schematic illustration of the charge transfers induced by surface species migration [132].

Even without evoking Cl migration onto the Pt NP, Cl doping can have an impact on Pt-support interactions. In the XAS study by Stakheev et al. [123], it was found, by studying 1%Pt/ $\gamma$ -Al<sub>2</sub>O<sub>3</sub>-Cl and 1%Pt/ $\gamma$ -Al<sub>2</sub>O<sub>3</sub>-Rb, that the increase in acidity of the support with Cl doping (decreasing basicity) is directly correlated with a decrease in electron charge on the support oxygen atoms. This results in a shift of the Pt 5d valence band to higher energy leading to strong Pt-O<sub>support</sub> bonds that explain the Pt nanoparticle's flat raft morphology.

Further on the stabilizing effect of chlorine on Pt nanoparticles, EXAFS studies [95,97] showed the Pt-Pt coordination number is lower for higher Cl loading of the reduced samples, indicating increased metal dispersion. Calcination at 500°C of samples without chlorine



results in sintering with the appearance of Pt-Pt contributions in the EXAFS spectra, which are not present for Cl doped catalysts submitted to the same thermal treatment. This is evidence that sintering at high temperatures is reduced in the presence of chlorine.

### 1.5.2.3 Location of Pt on the support

The question of the location of the nanoparticles, in terms of possibly preferred anchoring alumina facet, is important to evaluate its proximity and relative location to the acidic function of the catalyst.

Kovarík et al. [56] studied 5%<sub>w/w</sub>Pt/ $\gamma$ -Al<sub>2</sub>O<sub>3</sub> reduced at 300°C and prepared by incipient wetness impregnation with Pt(NH<sub>3</sub>)<sub>4</sub>(NO<sub>3</sub>)<sub>2</sub> of an alumina with platelet like crystallites exposing (110) and (111) type surfaces by electron tomography. Of the two segmented support crystallites, Pt was found to be mostly on the (110) surface for one and more or less on both (110) and (111) surfaces for the other. Pt particles were also found to be in the open pores of the alumina. This technique is of great interest to assess the position of Pt on the alumina crystallites, despite the results being hardly representative of the whole material, as this cannot be inferred from 2D STEM images. Unfortunately, such a high metal loading, leading to particles of 2 or 3 nm, does not reflect the high metal dispersion present in industrial catalysts such as catalytic naphtha reforming.

A <sup>27</sup>Al SS MAS NMR study [92] of 10%<sub>w/w</sub>Pt/ $\gamma$ -Al<sub>2</sub>O<sub>3</sub> calcined at 300°C shows a decrease of the peak corresponding to Al<sub>V</sub> accompanied by an increase of the Al<sub>VI</sub> contribution in comparison with the spectra of the support (Figure 1-27). It is concluded that the supported metal oxide, assumed to be PtO, is bonded to the support's Al<sub>V</sub> surface sites, which convert to Al<sub>VI</sub>. Unsaturated Al<sub>V</sub> sites are formed on the surface by dehydration during high temperature treatments. Since for usual calcination temperatures, the (100) surface is considered to be dehydrated [82] and thus exposing more Al<sub>V</sub> sites, Pt is expected to be preferentially located in this surface. By quantitatively calculating a *Pt/Al<sub>V</sub> site* ratio and confirming the results obtained by HR-HAADF-STEM for a set of catalysts with varying Pt loadings (from 1 to 10%<sub>w/w</sub>) it was found, in agreement with previous works [91], that for the lowest loading the metal phase is atomically dispersed (*Pt/Al<sub>V</sub> ≈ 1*) and for the highest loading 1 nm 2D raft like aggregates are observed as well as isolated metal atoms (*Pt/Al<sub>V</sub> ≈ 4*). A complementary study [133] of the same samples, this time calcined also at 600°C, confirms the bimodal

distribution of Pt oxide for high loadings (atomically dispersed and aggregated) by HR-HAADF-STEM and EXAFS spectroscopy. DFT calculations on the dehydrated (100) surface show that the aggregation of isolated Pt or PtO is not favourable due to the interactions with surface  $\text{Al}_\text{V}$  sites. However, other works, described above, indicate that (reduced) nanoparticles are more stable on the (100) surface [124] in the absence of Cl. When H and Cl migration are considered, nanoparticles are more stable on the (110) surface [132]. Also,  $\text{PtO}_4$  and  $\text{PtO}_2$  oxide stoichiometries (and not PtO) were found to be the most stable on the (100) dehydrated surface [90]. It should also be considered that even the lowest Pt loading used ( $1\%_{\text{w/w}}$ ) in this set of studies [92,133] is relatively high in comparison of the  $0.3\%_{\text{w/w}}$  of industrial catalysts and the impact of chlorine was not studied.

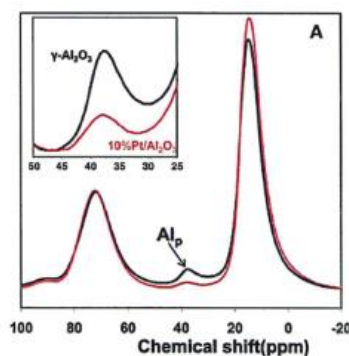


Figure 1-27 -  $^{27}\text{Al}$  MAS NMR spectra of  $\gamma\text{-Al}_2\text{O}_3$  in black and  $10\%_{\text{w/w}}\text{Pt}/\gamma\text{-Al}_2\text{O}_3$  in red, after calcination at  $300^\circ\text{C}$  [92].

In both works, the authors affirm Pt is located on the (100) surface, anchored to  $\text{Al}_\text{V}$  sites. The empirical NMR evidence supports the claim that  $\text{Al}_\text{V}$  is impacted upon Pt introduction, yet such experiments may fail at detecting low coordination sites that are very distorted [59] and are considered by some authors to provide an incomplete picture of the  $\gamma$ -alumina structure [76].

The same group proposed that temperature programmed desorption (TPD) of ethanol could be used to quantify the (100) surface  $\text{Al}_\text{V}$  sites [60,134,134], as they were found to be the active sites in alcohol dehydration [135]. Based on this, another investigation focused on the impact on the number of (100)  $\text{Al}_\text{V}$  sites on platinum dispersion [136]. A series of  $\gamma$ -alumina supports of different surface areas ( $S_{\text{BET}}$  from 79 to  $143\text{ m}^2/\text{g}$ ) with varying quantity of those sites measured by ethanol TPD ( $\text{mol/g}$ ) and then a pair with the same quantity (in  $\text{mol/g}$ ), but of different strength (also measured by ethanol TPD), were used to prepare catalysts with varying Pt loadings varying from  $0.5\%_{\text{w/w}}$  up to  $10\%_{\text{w/w}}$ . Up to  $1\%_{\text{Pt}}$  loading, after

reduction at 500°C for 1h, platinum is well dispersed for all supports, exhibiting NPs with an average size of 1 nm (STEM). For higher loadings, in particular for 10%Pt, a bimodal distribution of Pt entities is again evoked, as NPs < 3 nm and > 10nm agglomerates are observed by STEM. In this case, a higher dispersion (meaning, higher proportion of NPs < 3 nm) is achieved when supports with higher number of (100) Al<sub>v</sub> sites or with stronger such sites are used. Note that the authors insist in comparing the absolute number of anchoring sites obtained by ethanol TPD in mol/g which was found to vary up to 50% for a set of alumina supports with very different surface areas. Instead, if the surface density of anchoring sites is considered, in mol/m<sup>2</sup>, the chosen aluminas are actually very similar, with those values varying less than 5%. Also, no impact of the supposed (100) Al<sub>v</sub> anchoring sites' quantity or strength was found in the platinum loading range of industrial interest (up to 1%), suggesting these two parameters are not correlated with platinum dispersion at low loadings.

### 1.5.3 Conclusion

Supported oxidized Pt is atomically dispersed on the γ-Al<sub>2</sub>O<sub>3</sub> support, after calcination, whether the support is chlorinated or not. After reduction of the catalyst at an adequate temperature, for metal loadings characteristic of industrial catalysts, nanoparticles of around 1 nm are formed and some isolated atoms can also be observed. This is indicative of the ultra-dispersed nature of the metallic phase in active catalysts.

In several investigations, the nanoparticles seem to have a flat bi-planar morphology. Theoretical calculations showed that this is the case on the dehydrated (100) surface of alumina by allowing a maximization of the interaction with the support. On the (110) surface, while a 3D morphology is favoured, it can be flattened when surface species migration is considered. The interaction of Pt nanoparticles with hydrogen leads to a relaxation of Pt-Pt distances and a decrease of the WL intensity in XANES. The presence of chlorine on the catalyst stabilizes the metallic phase and reduces sintering at high temperatures.

There is no clear evidence of a preferred location of Pt on the alumina surface, with both most exposed surfaces (100) and (110) being strong candidates.

Although supported Pt systems have been for long the subject of research, some points remain relatively unstudied: 1) the influence of edges or corners on Pt location; 2) the influence of Cl on the metallic phase; 3) are previous findings valid for low metal loading industrial catalysts.

## 1.6 Conclusion and strategy

Catalytic reforming is a key process in petroleum refineries that produces high-octane number reformat for the production of gasoline, aromatics for BTX plants and hydrogen for hydrotreatment units. Catalytic reforming relies on isomerization, dehydrogenation and (dehydro)cyclization reactions. These are promoted by a bifunctional catalyst composed of a metallic phase of platinum and other metals (Re, Sn) dispersed over an oxide support of  $\gamma$ -alumina doped with chlorine to enhance its Brønsted acidity. These reactions occur through bifunctional mechanisms that demand diffusion of intermediates from one type of site to the other. Even when Weisz's intimacy criterion is respected, in terms of distance between sites, intermediates can be *intercepted* to undergo undesired reactions, lowering process selectivity. This makes the relative location of the sites another important factor for catalytic performance enhancement.

The catalysts acid Brønsted sites are surface hydroxyl groups that for  $\gamma$ -alumina have been studied by IR and  $^1\text{H}$  NMR for which there are several signal attribution suggestions. The chlorination of  $\gamma$ -alumina is mainly done by exchange of basic hydroxyls with chlorine resulting in an increase in acidity attributed to either the electron withdrawing effect of Cl atoms or the disturbance of the H bond network caused by Cl introduction. Despite the large amount of studies concerning  $\gamma$ -alumina hydroxyls and chlorinated  $\gamma$ -alumina, there is little information on the exposed edges and corners of alumina platelets.

Supported Pt nanoparticles of around 1 nm and flat bi-planar morphology are formed during catalyst reduction. The nanoparticles are stabilized by the presence of Cl, which also reduces sintering at high temperatures. Although these effects of Cl are well known, there are not many experimental studies that look into the impact of Cl on platinum nanoparticles and its electronic state. In fact, most alumina supported Pt studies use samples without chlorine. There is little information concerning platinum location, but (100) facet has been suggested to harbour preferential anchoring sites. Again, the impact of the edges and corners of alumina crystallites on the Pt nanoparticles or their location is not considered. Also, most studies use platinum loadings greatly superior to those used in commercial catalysts ( $\approx 0.3\%_{\text{w/wPt}}$ ) due to sensibility issues. The question remains, however, if their findings are still valid for lower Pt loadings.

The present work proposes to go beyond the current knowledge on the Pt/ $\gamma$ -alumina-Cl catalytic system by studying catalysts representative of the industrial materials to evaluate active site location and proximity, considering the edges of the support crystallites, as well as the impact of Cl on the metallic phase.

To do so a multi-technique approach, including HR-HAADF-STEM, electron tomography, high field MAS NMR, HERFD-XANES, EXAFS, and DFT calculations, will be applied to investigate the location of the metallic and acidic sites on the  $\text{Al}_2\text{O}_3$  support crystallites for Pt/ $\gamma$ - $\text{Al}_2\text{O}_3$ -Cl catalysts, and to estimate the distance between such sites. Two series of samples, representative of the industrial materials, will be synthesized so as to vary the distance between the two types of sites as a function of key parameters: %Pt, %Cl and  $\text{Al}_2\text{O}_3$  crystallite size and shape.

First, the two alumina supports will be studied as well as their chlorination, to establish the location of the Cl atoms on the alumina crystallites (Chapter 3). Then the metallic phase will be characterised both in oxide and reduced state so as to establish in which form it is supported and its location on the support, as well to search for an impact of chlorine on platinum's electronic state and dispersion (Chapter 4). Finally, with the information gathered by these atomic scale studies, a geometric model of the Pt/ $\gamma$ -alumina-Cl catalyst will be built so as to estimate the distance between the platinum nanoparticles and chlorine atoms (Chapter 5). Before presenting these results, the detailed methodology that will be used is described in the following chapter.



# **Chapter 2**

## **Methodology and Standard characterization of materials**



In this chapter the methodology and protocols used in the synthesis, characterization and modelling of the studied materials is presented, as well as the standard characterization results obtained for those materials.

## ***2.1 Catalyst preparation methods***

The synthesis of the supported heterogeneous catalysts considered here comprises the following main steps [6]: 1) support preparation, 2) impregnation of support with active species' precursors, 3) activation. They are detailed after a summary of the samples prepared for this work.

### **2.1.1 Strategy for catalyst formulations**

Commercial boehmites were preferred to lab samples for easy access and quality uniformity. PuralSB3 and TH100, high-purity boehmites synthesised by the aluminium alkoxide route from Sasol® were chosen for their textural properties, resulting in alumina supports with significantly different crystallite size and morphology. These two commercial boehmite powders were used to prepare two types of materials: catalysts (Pt/alumina-Cl) and chlorinated (or acidified) aluminas (alumina-Cl). The latter were prepared in order to study in solely the effect of chlorine on  $\gamma$ -alumina. All chlorinated aluminas were subjected to a thermal treatment equivalent to that of catalyst reduction prior to characterization.

Two sets of catalysts were prepared using the two commercial boehmites mentioned. For each set, three platinum loadings were targeted: 0.3%<sub>w/w</sub> Pt, 0.6%<sub>w/w</sub> Pt and 1%<sub>w/w</sub> Pt. The upper value reflects approximately the maximum quantity of platinum that can be deposited on  $\gamma$ -alumina using diffusional impregnation of  $\text{H}_2\text{PtCl}_6$ . The lowest value is very representative of the metal loadings used in industrial catalysts. One of the difficulties of studying commercial reforming catalysts is precisely such low noble metal loadings. For each metal loading, four chlorine contents were targeted: 1.4%<sub>w/w</sub> Cl; 1%<sub>w/w</sub> Cl; 0.5%<sub>w/w</sub> Cl and 0.1%<sub>w/w</sub> Cl. Commercial catalysts have a Cl loading of about 1 to 1.1%<sub>w/w</sub>. A slightly higher upper bound was chosen, due to sensitivity issues and to ensure a larger difference between the highest and lowest loadings. The lower bound is the lowest chlorine content that can be obtained by the dechlorination method used, already requiring at least around 70 h of water injection (see ahead).

Since the two supports do not have exactly the same surface area, more important than mass content is the surface coverage (atom/nm<sup>2</sup>) in platinum and chlorine to allow consistent comparisons. The *real* mass content in each compound varies slightly around these target values to ensure the same surface coverage between the two supports (and due

to limitations of the synthesis method to achieve a given target loading). Support surface area, measured mass contents and calculated surface coverages are reported later in the text, in section 2.3. For simplicity and clarity of the text, the catalysts (or chlorinated aluminas) are referred to using the theoretical target mass loadings of platinum and chlorine and the commercial name of the support: x%Pt/alumina-y%Cl (example: 1%Pt/PuralSB3-1.4%Cl). This name is followed by the mention “oxide” or “reduced” to clarify which was the last thermal treatment applied to the material in question. As will be evident in the next chapters, particularly for the catalysts, not all prepared samples could be studied by all advanced methods due to practical constraints, so catalysts with extreme Pt and Cl loadings were prioritized.

The materials synthesized to date are listed in Table 2-1 and Table 2-2.

*Table 2-1 – List of chlorinated aluminas prepared with PuralSB3 and TH100 and their nomenclature.*

PuralSB3 alumina		TH100 alumina	
Target %Cl	Nomenclature	Target %Cl	Nomenclature
0.5	PuralSB3-0.5%Cl	0.5	TH100-0.5%Cl
1.4	PuralSB3-1.4%Cl	1.4	TH100-1.4%Cl

*Table 2-2 – List of catalysts prepared with PuralSB3 and TH100 alumina supports and their nomenclature.*

PuralSB3 alumina			TH100 alumina		
Target %Pt	Target %Cl	Nomenclature	Target %Pt	Target %Cl	Nomenclature
0.3	1.4	0.3%Pt/PuralSB3-1.4%Cl	0.3	1.4	0.3%Pt/TH100-1.4%Cl
	1	0.3%Pt/PuralSB3-1%Cl		1	0.3%Pt/TH100-1%Cl
	0.5	0.3%Pt/PuralSB3-0.5%Cl		0.5	0.3%Pt/TH100-0.5%Cl
	0.1	0.3%Pt/PuralSB3-0.1%Cl		0.1	0.3%Pt/TH100-0.1%Cl
0.6	1.4	0.6%Pt/PuralSB3-1.4%Cl	0.6	1.4	0.6%Pt/TH100-1.4%Cl
	1	0.6%Pt/PuralSB3-1%Cl		1	0.6%Pt/TH100-1%Cl
	0.5	0.6%Pt/PuralSB3-0.5%Cl		0.1	0.6%Pt/TH100-0.1%Cl
	0.1	0.6%Pt/PuralSB3-0.1%Cl			
1	1.4	1%Pt/PuralSB3-1.4%Cl	1	1.4	1%Pt/TH100-1.4%Cl
	1	1%Pt/PuralSB3-1%Cl		1	1%Pt/TH100-1%Cl
	0.5	1%Pt/PuralSB3-0.5%Cl		0.5	1%Pt/TH100-0.5%Cl
	0.1	1%Pt/PuralSB3-0.1%Cl		0.1	1%Pt/TH100-0.1%Cl

### 2.1.2 Alumina support preparation

Extruded  $\gamma$ -alumina pellets prepared from two commercial boehmite powders produced by Sasol GmbH® (PuralSB3™ and TH100™) were used as oxide support for the catalysts.

The pellets are prepared by subjecting the boehmite powder to a shaping process in which a paste of adequate rheological properties is formed by adding water in combination with inorganic (acids/bases) and/or organic compounds.

The paste that is extruded to make the catalyst support is made by a process named mixing, kneading or mulling, which aims at dispersing the boehmite powder and deals with the different possible textural entities of boehmite. Those are ( $d_p$  being the mean particle diameter) [137]:

- Primary Particles/Crystallites: smallest entity;  $2 < d_p < 50$  nm
- Aggregates/Primary aggregates: assembly of primary particles chemically connected by Al-O-Al bridges;  $30 < d_p < 500$  nm
- Agglomerates: assembly of aggregates held together by physical and electrostatic forces (van der Waals, hydrogen bonds);  $5\mu\text{m} < d_p < 10\mu\text{m}$
- Powder: assembly of agglomerates;  $d_p \approx 40\mu\text{m}$

The powder particles and agglomerates can be “broken down” or crumbled into aggregates by mechanical force provided by a mixer. Mechanical force is not enough to break the chemical bonds that hold the aggregates together electrostatically. For complete disaggregation, a chemical attack is mandatory. Mixing with an acid solution will bring forth crumbling and peptization of the resulting primary particles.

Peptization by acids, in a general way, consists of creating a positive net charge on the surface of the boehmite crystallites preventing them from coalescing or settling by electrostatic repulsion. The process of peptization is still not totally clear, nor is the relationship between the mixing conditions and the final texture of the support produced. However, it is accepted that peptization reduces larger pores due to deaggregation and that the smaller particles thus obtained rearrange in some sort of long range order. So, a higher peptization degree may be expected to eliminate macroporosity and provide a narrow pore size distribution in the mesoporous area [138,139].

The thus obtained paste is then extruded into the desired shape (cylindrical, multilobal) and size. After drying, the resulting boehmite extrudates are calcined, transforming into  $\gamma$ -alumina. The experimental parameters are described below.

Mixing took place in a Battagion mixer. After filling the mixing bowl with the adequate amount of boehmite powder, a nitric acid aqueous solution is added in two minutes. The resulting paste is mixed for 30 minutes, this being called the “acid mixing” stage.

When the acid mixing ends, an aqueous solution of ammonia is added at once. The paste is mixed for 15 minutes more at 50 rpm, this being called the “neutralization stage”. After recovering the paste from the mixing bowl, it is extruded using a Retma extruder using a cylindrical die plate with a 2 mm diameter. The extrudates are dried in a Binder® oven at 80°C for at least 12h, typically overnight, and then calcined in either a Thermconcept or a Cera-therm muffle furnace to transform the boehmite into  $\gamma$ -alumina. The calcination parameters were different for each of the two supports used: 700°C for 2h for PuralSB3 and 560°C for 4h for TH100 and were adjusted to obtain the targeted surface area.

The alumina supports were prepared by Emanuel Rosati from IFPEN.

### **2.1.3 Catalyst preparation**

Sample preparation was performed with the support of Carine Guégan and Clara Mancia from IFPEN.

#### **2.1.3.1 Support chlorination and platinum impregnation**

In the case of catalytic reforming, the impregnation of the support includes the deposition of the metallic phase, Pt, and the acidification of the support through Cl doping. While the target quantity of Pt to be impregnated is controlled during the impregnation via the precursor solution, the loading in Cl is tuned only after impregnation.

The alumina extrudates issued from the synthesis described above are calcined in a fixed bed cylindrical reactor under dry air flow at 520°C for 2h. The calcined support is saturated in water by adding it drop by drop to the pellets in a rotating bowl until all the pellets are uniformly wet but not sticking to the container’s walls (around 0.6 mL H<sub>2</sub>O/g<sub>supp</sub> for the supports used).

The wet extrudates are loaded onto a fluidized bed for acidification and impregnation (diffusional impregnation). The same impregnation can be done using a laboratory shaking table. The volume of water circulating in the fluidized bed (in mL) is of 4.5 times the mass of dry support (in g) and its flow rate is maintained at 1.7 mL/min. Hexachloroplatinic acid ( $\text{H}_2\text{PtCl}_6 \cdot 6\text{H}_2\text{O}$ , MM=517.90 g/mol, Sigma-Aldrich) is used as platinum precursor. A solution of this precursor and hydrochloric acid is prepared considering the targeted Pt loading. For example, if the target is 0.3%<sub>w</sub> Pt per gram of catalyst, the solution should have around 0.35%<sub>w</sub> Pt per gram of dry support. A little excess of precursor is used due to losses during the preparation and to the metal fixation ratio not being 100%. The HCl in the platinum solution is added in the proportion of 0.5%<sub>w</sub> Cl per gram of dry support. Its purpose is to guarantee a homogeneous distribution of Pt though the support pellet. A competitive adsorption effect of chloride ions with  $\text{PtCl}_6^{2-}$  anions has been suggested [32].

The Pt impregnation solution is added to the circuit in 45 minutes. The solution is left in circulation for at least 4h. The circuit is then purged.

As mentioned in the previous chapter, the point of zero charge of alumina is at around pH 9 and this can have an influence in the bulk pH of the impregnation solution along with adsorption of solution species onto the support. Furthermore, the platinum species in solution depend on the bulk pH. For one of the impregnations performed (0.6%<sub>w/w</sub> Pt/TH100), the pH of the impregnation solution, of the circuit solution at the end of the 45 minutes of injection of the impregnation solution and of the circuit solution after 24h of circulation was measured using a Thermo Orian 250A+ pH meter (Table 2-3).

*Table 2-3 - pH and temperature of impregnation solution and circuit solution after addition of impregnation solution, for the 0.6%<sub>w/w</sub> Pt/TH100 preparation.*

	pH	T (°C)
$\text{H}_2\text{PtCl}_6 + \text{HCl}$ solution	0.26	24.4
Circuit solution t=45min	2.40	32.9
Circuit solution t=45 min + 24h	3.52	32.3

First it is observed that the circuit solution is not at room temperature: the passing of the liquid through the pump that assures the flow in the circuit causes its heating and no cooling system is used. Secondly, the increase in pH after 24h of circulation should be a combined expression of the buffer effect of alumina and of the adsorption of solution species. The pH

being always below 4, the main species in solution are expected to be  $\text{PtCl}_6^{2-}$  and  $\text{PtCl}_5(\text{H}_2\text{O})^-$  [7].

After Pt impregnation, the pellets are dried at 120°C overnight in a Memmert oven and then calcined in a fixed bed cylindrical reactor under dry air flow at 520°C for 2h. The resulting materials are referred to in the text as “Impregnated and Calcined” or “Impreg+Calc”.

The synthesis of the chlorinated aluminas diverges from the methodology described above in that there is no  $\text{H}_2\text{PtCl}_6$  impregnation step.

### **2.1.3.2 Tuning of chlorine loading**

At this point the chlorine loading is tuned. As described previously, four final chlorine contents were targeted. For a given platinum loading, impregnated and calcined pellets were divided in four batches. Each batch underwent the necessary treatment to reach the targeted chlorine loading.

The highest Cl loading desired is often not achieved during the acidification in fluidized bed. In that case, a dry oxychlorination treatment is used, consisting of heating the impregnated and calcined pellets in a cylindrical reactor under dry air flow up to 520°C and then injecting a short chain chloroalkane for 2h by means of a syringe pump. At such a temperature, it decomposes into HCl. This injection is followed by a plateau at 520°C for another 2h under dry air.

The remaining three Cl targets were prepared by dechlorination of the impregnated and calcined pellets. This is done by injecting 8000 ppm of water into a dry air flow (1 L/min/ $g_{\text{cata.}}$ ) of a cylindrical reactor at 520°C, charged with the extrudates. The time during which the injection is performed must be adjusted to the target Cl loading (lower %Cl, more time).

The materials obtained after Cl loading adjustment thermal treatment (dry oxychlorination or dechlorination) are referred to in the text as “oxide catalysts” and have the mention “oxide” after their name. Oxide catalysts are stored in flasks under Ar and shielded from light.

### 2.1.3.3 Reduction treatment

Activation of these catalysts is accomplished by reduction under hydrogen of 2-3 g of oxide catalyst. The pellets are crushed to a powder of  $< 100\ \mu\text{m}$  particles: a powder sample is mandatory or more practical for most of the analysis. The oxide catalyst powder is loaded in a dedicated glass cell. The reduction treatment consists of a pre-calcination step at  $520^\circ\text{C}$  under dry air flow ( $1\ \text{L/min/g}_{\text{cata.}}$ ) for 30 minutes, after which temperature decreases to  $500^\circ\text{C}$  for a 10 minutes purge of the circuit with  $\text{N}_2$  and finally reduction under  $\text{H}_2$  flow ( $1\ \text{L/min/g}_{\text{cata.}}$ ) at  $500^\circ\text{C}$  for two hours. The cell is then cooled to room temperature under hydrogen, purged with nitrogen and put under vacuum. The pre-calcination dries the catalyst of physisorbed water that can cause sintering of the metal if present during the reduction step. A dedicated part of the cell is sectioned off leaving the catalyst in a sealed glass ampoule under vacuum. The resulting material is referred to as “reduced catalyst” and have the mention “reduced” after their name.

The chlorinated aluminas also undergo a thermal treatment as described for the reduction step in order to have the same surface hydration state as the reduced catalysts and thus be comparable to them. Unless specified in the text, the mention of chlorinated aluminas refers to the material after this “reduction-like” thermal treatment.



## ***2.2 Characterization techniques and modelling methods***

This section describes the various characterization techniques used to study the prepared materials and the methods used for molecular modelling. The characterization techniques are divided in two groups: standard and advanced characterization. The first group is composed of the techniques that are routinely performed at IFPEN laboratories to confirm the result of material synthesis. In the second group are the sophisticated techniques chosen to achieve the objectives of the present work.

### **2.2.1 Standard techniques**

#### **2.2.1.1 Nitrogen Physisorption**

Nitrogen Physisorption ( $N_2$  Phys.) is a textural analysis method based on the physical adsorption of  $N_2$  at normal boiling point (77 K) on the surface of the sample. It can be used to evaluate micro ( $d_{\text{pore}} < 2$  nm) and mesoporosity ( $2 < d_{\text{pore}} < 50$  nm) and surface areas superior to  $1 \text{ m}^2/\text{g}$ [140]. It is used in this work to evaluate the surface area, namely  $S_{\text{BET}}$ , of the alumina supports, obtained by applying the Brunauer-Emmett-Teller (BET) equation [141] to the points in the relative pressure ( $P/P_0$ ) interval of 0.05 to 0.15.

The samples were pre-treated at  $350^\circ\text{C}$  for 3 h under vacuum and the equipment used was a Micromeritics ASAP 2420.

#### **2.2.1.2 Mercury porosimetry**

Mercury porosimetry (Hg poro.) is another textural analysis, often used in addition to  $N_2$  Phys., and is based on the behaviour of non-wetting liquids, like mercury, that require pressure to be applied in order to penetrate inside a pore. This pressure is related to the pore diameter when the pore is assumed to have a circular cross section. This analysis can evaluate pore size from 3.7 to 7000 nm (values superior to this are attributed to rugosity or powder compaction)[140].

The mesoporous volume ( $V_{\text{meso}}$ ) is given by the difference between the injected volume at 3.7 nm and at 50 nm. The macroporous volume ( $V_{\text{macro}}$ ) is calculated as the difference between the injected volume at 50 nm and at 7000 nm. These volumes are especially important when there is macroporosity, which is not assessed by the Nitrogen Physisorption.

The diameter at half of the mesoporous volume ( $D_{V_{\text{meso}}/2}$ ) is used as an average pore diameter for the alumina supports.

The analyses were performed in a Micromeritics Autopore IV equipment and the samples were pre-treated for at least 3 h at 250°C.

### **2.2.1.3 Powder X-ray diffraction (XRD)**

X-ray Diffraction (XRD) is a technique used for phase identification of crystalline materials based on the diffraction of X-rays, following Bragg's Law [142], and was used to confirm the alumina polymorph obtained at the end of support preparation. An average crystallite size was also measured by applying the Scherrer formula [71] to the 400 peak.

The samples are ground into powder and compacted in a sample carrier. A angle range of 5° to 72° 2 $\theta$  was scanned. The reference pattern for  $\gamma$ -Al<sub>2</sub>O<sub>3</sub> was ICDD n° 00-010-0425. The equipment used was a PANalytical X'Pert Pro diffractometer with a copper anode ( $K\alpha = 0.15402$  nm) and a X'célator detector.

### **2.2.1.4 X-ray Fluorescence Spectrometry (XRF)**

X-ray Fluorescence Spectrometry (XRF) is an elemental analysis technique that can be applied to both solids and liquids. When an atom is excited by an X-ray photon, an electron will be expelled from its core shells creating a vacancy that is filled by another electron of a higher energy shell, releasing energy in the form of X-ray photons (or Auger electrons), this phenomenon being called fluorescence. The energy of the emitted X-rays is characteristic for each element, allowing for its identification, and the intensity of the peak measured by wavelength dispersive spectrometry (WDS) permits quantification down to some ppm, using a calibration curve [143].

A Thermo scientific ARL Perform'X wavelength dispersive device was used.

This analysis was used to evaluate platinum and chlorine content of the samples. To be noted that reduced samples were loaded to a flask that was tightly closed under ambient air, and stayed in the flask for varying amounts of time (from a couple of days to more than a week) between the moment they were delivered to the team in charge of the analysis and the moment they were in fact analysed. Previous studies at IFPEN showed no significant change of the loss in ignition for samples delivered in such manner.

### 2.2.1.5 Electron Probe Microanalyser (Castaing microprobe)

The Electron Probe Microanalyser (EPMA) is a tool to determine the local chemical composition of samples, at the  $\mu\text{m}$  scale. The sample is bombarded with a focused and accelerated electron beam that causes the emission of X-rays, heat and electrons, allowing for imaging and composition determination [143].

This analysis was used to check the repartition of platinum through the interior of the catalyst extrudate. The samples are embedded in an epoxy resin and polished with heptane to expose a cross section in the middle of the extrudate. The concentration of the components of interest is measured for five extrudates on points along a straight line passing along a diameter of the extrudate, the points are  $50\ \mu\text{m}$  apart taking into account the beam size is approximately  $5\ \mu\text{m}$ . The five lines are averaged for the final result. The resulting concentration profile shows if the components are homogeneously distributed (straight profile), concentrated on the edges (bowl shaped profile, called egg-shell distribution in the worst case) or concentrated on the centre (dome shaped profile). A repartition coefficient (R, Equation 2-1) is also reported, being 1 (straight),  $<1$  (bowl) or  $>1$  (dome) for the respective cases. It is known that exposure to the electron beam results in loss of chlorine, so this method does not evaluate chlorine concentration accurately, but the distribution profile is still correct.

$$R = \frac{C_{\text{average of local measurements}}}{C_{\text{global}}} \quad \text{Equation 2-1}$$

The equipment used was a JEOL Microsonde 8800R, equipped with 5 WDS, and operated at 20kV.

### 2.2.1.6 Static chemisorption of $\text{H}_2$

Selective chemisorption techniques rely on the chemisorption (interaction between substrate and adsorbate caused by sharing of electrons) [144] of an adsorbate resulting in monolayer coverage of the metal. The adsorbed amount of gas can be quantified to calculate the dispersion of the metallic active phase, meaning the ratio between accessible metal atoms and total metal atoms, considering an adsorption stoichiometry [140].

Knowing the quantity of H<sub>2</sub> chemisorbed ( $Q$  in mol/g<sub>sample</sub>), the quantity of Pt in the sample ( $q$  in mol/g<sub>sample</sub>, obtained by XRF for example) and assuming an adsorption stoichiometry ( $n$ ), metal dispersion can be calculated as (Equation 2-2):

$$\text{Disp}(\%) = \frac{Q}{q \cdot n} \quad \text{Equation 2-2}$$

In the case of H<sub>2</sub> chemisorption on platinum dispersed over alumina, the stoichiometry is taken to be ½ (Equation 2-3) [140]:



For ultra-dispersed catalysts such as the one considered here, such an adsorption stoichiometry is likely underestimated [115,130]. However due to compensation of errors as mentioned below, the overall quantification likely remains valid. Figure 2-1 illustrates the temperature and gas program used.

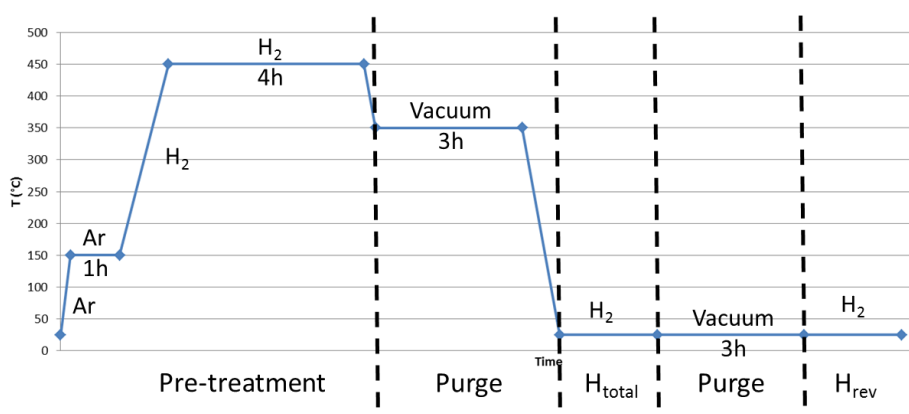


Figure 2-1 – Temperature and gas program used for H<sub>2</sub> chemisorption with discrimination of the different stages

The sample, that would be an oxide catalyst, is first reduced at 450°C under pure H<sub>2</sub> (pre-treatment step). Remaining hydrogen is purged under vacuum (pressure < 10<sup>-5</sup> mbar) to ensure a *bare* metallic surface and the sample is brought down to room temperature before the hydrogen chemisorption. The “total” quantity of adsorbed hydrogen is thus quantified. For ultra-dispersed catalysts, the bare character of the surface can be questioned [115,130], but the difference between the saturated state (with H/Pt > 1)<sup>1</sup> and the state under vacuum (with H/Pt > 0) effectively leads to ½ being a reasonable choice for adsorption stoichiometry [130]. After purge under vacuum (still at room temperature), another hydrogen

<sup>1</sup> For Pt single atoms, a H/Pt ratio of 2 was found, for example [90].

chemisorption is performed. The quantity of “reversibly adsorbed” hydrogen is quantified: the hydrogen adsorbed the second time corresponds to the hydrogen desorbed during the purge. The metallic dispersion can then be calculated using the “total” or “reversible” hydrogen absorption.

The equipment used was a Bel Japan Belsorp-max.

### 2.2.1.7 H<sub>2</sub> / O<sub>2</sub> titration

This is another chemisorption technique used to quantify the dispersion of the metallic active phase, this time a dynamic method (pulses of adsorbate injected on neutral carrier gas flow) consisting of the titration of chemisorbed hydrogen with gaseous oxygen. In this case the adsorption equations, and thus stoichiometry, are different (Equation 2-4, Equation 2-5, Equation 2-6 and Equation 2-7) [145,146].



In these equations the starting state of platinum is assumed to be PtO<sub>2</sub>. This seems to be true for oxide clusters that were found to have an overall stoichiometry close to PtO<sub>2</sub> [147], but for monoatomic oxides (single atoms) O/Pt>2 [90]. Also, the intermediate state of platinum is supposed to be PtO. This is even more of an approximation when chlorine is present, given that the supported oxide platinum species on the catalysts may be a chlorinated species.

The temperature and gas program used is shown in Figure 2-2.

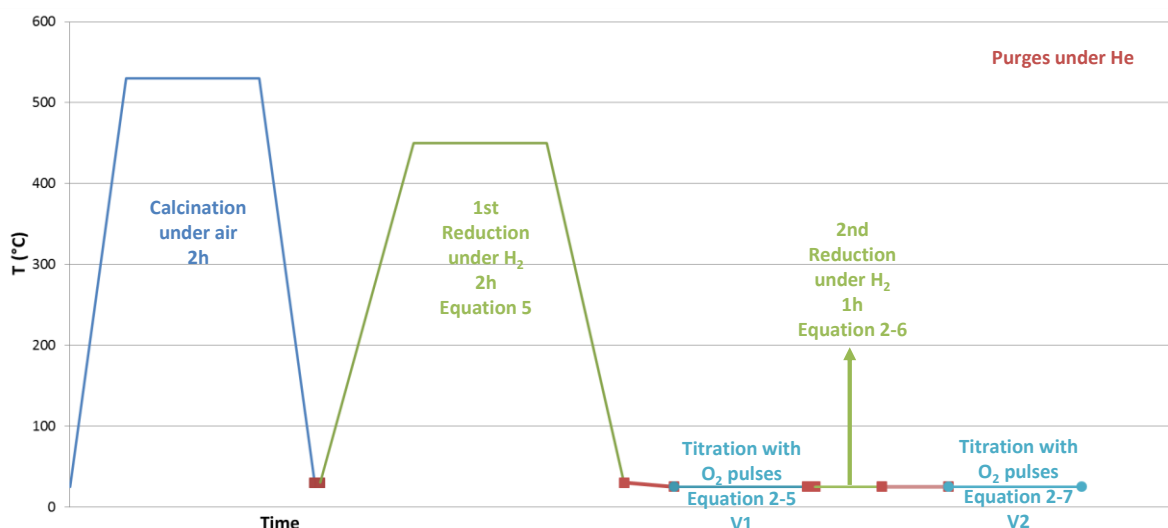


Figure 2-2 – Temperature and gas program used for  $H_2 / O_2$  titration with discrimination of the different stages.

In fact, two titrations (at room temperature) of adsorbed hydrogen with  $O_2$  are performed resulting in two *consumed* oxygen volumes, V1 and V2. When multi-metallic (promoted) catalysts are tested, these volumes are not equal. The difference between the two titrations is the temperature of the preceding reduction step. After the first reduction at high temperature, eventual promoters such as tin or rhenium are expected to be partially reduced and also consume oxygen during the first titration. Only platinum is believed to be reduced during the second reduction step, performed at room temperature. Thus, only (accessible) platinum is responsible for oxygen consumption during the second titration. V1 is indicative of Pt-promoter interactions and V2 is used to calculate platinum dispersion using Equation 2-8 in which  $MM_{Pt}$  is the molar mass of platinum,  $V_m$  is the molar volume at 25°C and  $n$  is the stoichiometry coefficient of  $O_2$  consumed per Pt ( $n=3/4$  from Equation 2-5 and Equation 2-7).

$$Disp(\%) = \frac{MM_{Pt} \cdot V2}{\%_{w/w}Pt \cdot V_m \cdot n} \quad \text{Equation 2-8}$$

The equipment used was a  $\chi$ -sorb GIRA (developed at IFPEN).

### 2.2.1.8 2.4.1.8 Temperature programmed reduction (TPR)

TPR analysis monitors hydrogen consumption as a function of temperature, qualitatively informing on the reducibility of the metal (temperature of peak consumption) and its degree of oxidation ( $H_2$ /metal ratio can be calculated from total  $H_2$  consumption).

The oxide catalyst sample (less than 1g) is dried at room temperature for 2h under argon, calcined under air at 450°C for 2h and cooled to room temperature. After this pre-treatment, the TPR is recorded. Diluted H<sub>2</sub> is used (5% H<sub>2</sub> in Ar) and the temperature is increased from RT to 1000°C at 10°C/min. The consumption of H<sub>2</sub> is measured by a thermal conductivity detector (TCD). The equipment used was a Micromeritics Autochem II 2920.

## 2.2.2 Advanced techniques

Three advanced characterization techniques were chosen for this study. They are believed to be able to overcome the challenges of low Pt and Cl loadings as well as high platinum dispersion. These are: BF-TEM and HR-HAADF-STEM, high-field solid state MAS NMR, and XAS (HERFD-XANES and EXAFS) (see below for abbreviations).

### 2.2.2.1 Transmission electron microscopy / Scanning transmission electron microscopy (TEM/STEM)

#### 2.2.2.1.1 Principle

Electron microscopy is based on the principle of the wave-particle duality of electrons which dictates moving particles exhibit properties of both waves and particulate matter [148]. So to sufficiently accelerated electrons will correspond sufficiently small wavelengths ( $\lambda$ ) [149] as *Equation 2-9* shows, where  $h$  is Plank's constant,  $m$  is the electron mass and  $E$  is the electrons' kinetic energy.

$$\lambda = \frac{h}{p} = \frac{h}{\sqrt{2mE}} \quad \text{Equation 2-9}$$

Moreover, being charged particles, electrons can be deflected and focused by electromagnetic fields, just like physical lenses can focus visible light. Various technological advances in the 30's allowed the application of this principle for the creation of transmission electron microscopes (TEM) offering unprecedented resolutions [140,150].

The image obtained in TEM is dependent on electron-matter interactions. Some electrons will be adsorbed or diffused by the sample and others will be transmitted. The diffused and transmitted electrons are then used to form the image by passing through different lenses

below the sample holder (Figure 2-3). The microscope column is thus kept in high vacuum ( $< 10^{-5}$  Pa) to minimize electron beam interaction with air molecules.

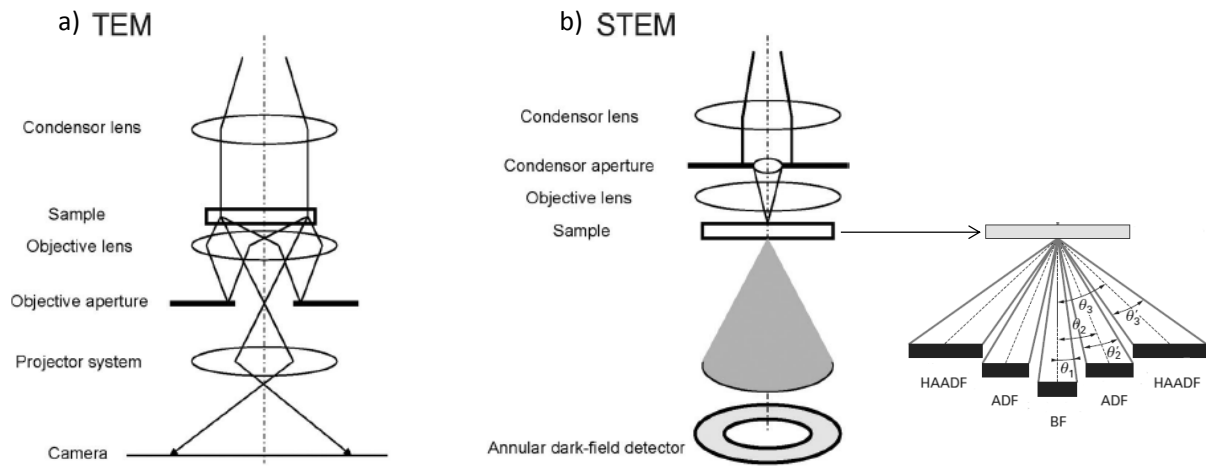


*Figure 2-3 – Microscope configuration in a) TEM mode and in b) STEM mode with the different available detectors, adapted from [151].*

Bright-field (BF) TEM imaging is obtained using the transmitted electron beam. Resolution in TEM ( $\delta$ ), given by the Rayleigh criterion in Equation 2-10 in which  $\lambda$  is the beam's wavelength,  $\mu$  is the medium's diffraction index and  $\beta$  is the lenses' half-angle of collection, depends on the acceleration of the electron beam and the aberrations induced by the lenses, which are today the limiting factor. Sub-nanometre resolution can be achieved.

$$\delta = \frac{0.61 * \lambda}{\mu * \sin\beta} \quad \text{Equation 2-10}$$

The intensity is dependent on the thickness, atomic number and crystallinity of the sample. There are three types of image contrast in TEM:

- Thickness contrast: thicker zones appear darker as the electron beam is either more absorbed or scattered at higher angles outside the lens's acceptance
- Diffraction contrast: for a crystalline sample in Bragg's condition will also scatter more electrons by diffraction and its contrast will not depend only on its thickness
- Phase contrast: diffraction and propagation of the electron wave through the microscope generate modifications of the electron phase that result in this complex contrast.



As can be deduced, TEM instruments can also be used for electron diffraction, a particular case of elastic scattering. Due to the electron beam's wave-particle duality, the formalism that describes the phenomenon is the same as for X-rays. The condition for diffraction to occur for an incident wave of wavelength  $\lambda$  with incidence angle  $\theta$  with respect to a set of (hkl) planes equidistant by  $d_{hkl}$  is expressed as Bragg's law (Equation 2-11) [142] where  $n$  is the diffraction order.

$$2d_{hkl}\sin\theta = n\lambda \quad \text{Equation 2-11}$$

Three main modes are available for diffraction pattern acquisition: parallel beam high-energy electron diffraction; low-energy electron diffraction and convergent beam electron diffraction (CBD). In CBD the incident beam is cone-shaped and the convergent beam diameter can be reduced to a few nanometres, called a nanoprobe or nanoarea diffraction. The diffraction patterns obtained, which are a section of the diffraction reciprocal space, can be more easily interpreted when the sample is oriented in a zone axis. Its reflections are distributed in Laue zones [143].

Hybrid microscopes allow for two utilization modes, TEM and Scanning TEM (STEM) (Figure 2-3). In TEM mode, the sample is put under a parallel electron beam. In scanning mode, a convergent electron probe of small diameter is rastered at the sample surface. Under the sample in the microscope column, a beam electron diffraction pattern is obtained for each point, which is integrated by a detector point by point [152]. The information contained in this pattern depends on probe diameter, and thus so does STEM resolution [153]. Chemical mapping images can also be obtained point by point thanks to, for example, the detection of X-rays emitted due to electron-matter interactions.

In STEM, different types of imaging modes are possible depending on the range of scattering angles over which the electron flux is integrated. High Annular Angle Dark Field detectors (HAADF) produce a directly interpretable image from electrons elastically scattered at high angles. This scattering is incoherent, it does not depend on the sample's crystallinity and is in accordance with Rutherford's law. The intensity of each point in the image is linked to sample thickness and to atomic number  $Z$  (proportional to  $Z^2$  in a first approximation [93]). HAADF mode is also called Z-contrast mode for that reason and is particularly useful for the study of metals over light supports.

The focusing power of round STEM electron lenses, and thus STEM resolution, is limited by their spherical aberration that causes electrons further from the lenses' centre to be incorrectly focused onto a different point along the optical axis. This increases the electron probe diameter and its minimum size ( $d_{min}$ ) can be defined through Equation 2-12 where  $C_s$  is the third-order spherical aberration coefficient [152].

$$d_{min} = 0.43 \cdot \lambda^{3/4} C_s^{1/4} \quad \text{Equation 2-12}$$

In aberration-corrected instruments, non-rotationally symmetric electron lenses change the trajectory of the electrons off the optical axis in such a way that the deviations induced by the round lenses are cancelled out [154,155].

#### **2.2.2.1.2 TEM protocol**

BF-TEM was used to observe the morphology and size of the alumina platelets forming the supports. Experiments were performed with the participation of Anne-Lise Taleb on a JEOL JEM 2100F microscope at IFPEN, equipped with a FEG (field emission gun) electron gun, operated at 200 kV. The grinded materials were suspended in ethanol and a drop was deposited on a 300 mesh holey carbon copper grid and allowed to dry.

#### **2.2.2.1.3 HR-HAADF-STEM protocol**

High resolution (HR) HAADF STEM was used to observe supported Pt entities of the catalysts. Experiments were carried out on a  $C_s$ -corrected JEOL JEM 2100F microscope, operated at 200 kV at the Institut de Physique et Chimie des Matériaux de Strasbourg (IPCMS). Its resolution in STEM mode (probe size) is of 0.11 nm. The HAADF detector is JEOL and a Gatan Bright Field detector allows simultaneous acquisition of BF and HAADF images. For HAADF-STEM observations, the camera length used in the HAADF mode was 10 cm, corresponding to inner and outer diameters of the annular detector of 60 and 160 mrad, respectively. The experiments were devised in cooperation with Ovidiu Ersen, Walid Baaziz from IPCMS and Anne-Sophie Gay from IFPEN and with the participation of Anne-Lise Taleb from IFPEN.

The crushed materials were rubbed between two glass slabs and scraped onto a 300 mesh holey carbon copper grid (dry deposition). Since there is no way of introducing the sample holder in the microscope column without air exposure, even the reduced samples were deposited on the grid on table top. It is accepted a certain degree of passivation by oxygen

of the platinum nanoparticles is unavoidable and assumed it will not change nanoparticle size and morphology. (STEM studies at IFPEN on similar catalysts, performed after temperature programmed desorption of O<sub>2</sub>, show an average particle diameter equivalent to that of our reduced samples and very distinct from what is observed for oxide catalysts).

The nanoparticle (NP) size histograms and average size were obtained from at least 200 measurements from images taken at the same magnification. Nanoparticle morphology and shape was studied measuring HAADF intensity to estimate the number of Pt atoms stacked perpendicularly to the electron beam ( $n$ ) from the intensity of atomic column ( $I$ ), given that the image intensity is roughly proportional to the square of the mean atomic number of the analysed area [93]. As the measurements were performed on thin areas, alumina contribution to intensity was neglected in first approximation. The intensity of several single atoms (SA) were measured, to estimate the proportionality factor between  $I_{SA}$  and  $Z_{SA}^2$ . Starting from the assumption that the atomic number of a column composed of  $n$  Pt atoms is equal to  $nZ_{SA}$ , by measuring intensity  $I$  in nanoparticles,  $n \propto \sqrt{I}/I_{SA}$ . Single atom population was quantified through a number of SA to number of NP ratio calculated for several images at the same magnification.

#### ***2.2.2.1.4 Electron tomography experiments and protocol***

Tomography is a technique used to retrieve the 3D structure of an object from 2D images of the same object. The mathematic formalism that reconstructs a 3D volume from 2D projections was first developed by Radon [156]. This reconstruction is possible if the 2D images respect the projection requirement: intensity must correspond to a monotonic measurement of some property of the object [157]. In HAADF-STEM acquisition mode this requirement is fully met, as there is no diffraction contrast.

In practice, a series of 2D images (tilt series) of the object is collected by tilting the object in relation to the electron beam and acquiring an image at each tilt step while correcting for specimen movement, focus and astigmatism changes. The most straight forward method is that of single-axis tilting, in which the object is tilted about the rotation axis of the microscope goniometer. The tilt range is mechanically limited by the goniometer and by the appearance of shadow effects at high angles from the sample's particles, from the grid or from the sample holder and will typically be  $\pm 70^\circ$ . The tilt series is aligned with respect to

the tilt axis and then the object can be reconstructed using dedicated algorithms. Assuming a perfect alignment, the resolution along the rotation axis ( $x$ ) is equal to that of the original 2D images. The resolution in the direction perpendicular to the sample holder and to the electron beam axis ( $y$ ) depends on the number of projections ( $N$ ) and the diameter of the reconstructed volume ( $D$ ) according to Equation 2-13 [157], valid when the tilt range is  $\pm 90^\circ$ .

$$d_y = \frac{\pi D}{N} \quad \text{Equation 2-13}$$

The resolution in the electron beam direction ( $z$ ) depends on the tilt range. The missing wedge, lack of information for the unexplored high tilt angles (Figure 2-4 a), causes the elongation of features along this axis by an elongation factor  $e_{yz}$  [158]. Thus, reconstructed volume resolution is anisotropic. Resolution estimation for reconstructed objects is not straightforward, as it is affected by other factors such as microscope stability, drift, sample thickness or alignment quality. Along with tilt range (Figure 2-4 b) and increment, electron dose is an important acquisition parameter, as electron beam induced damage defeats the purpose of 3D structure reconstruction.

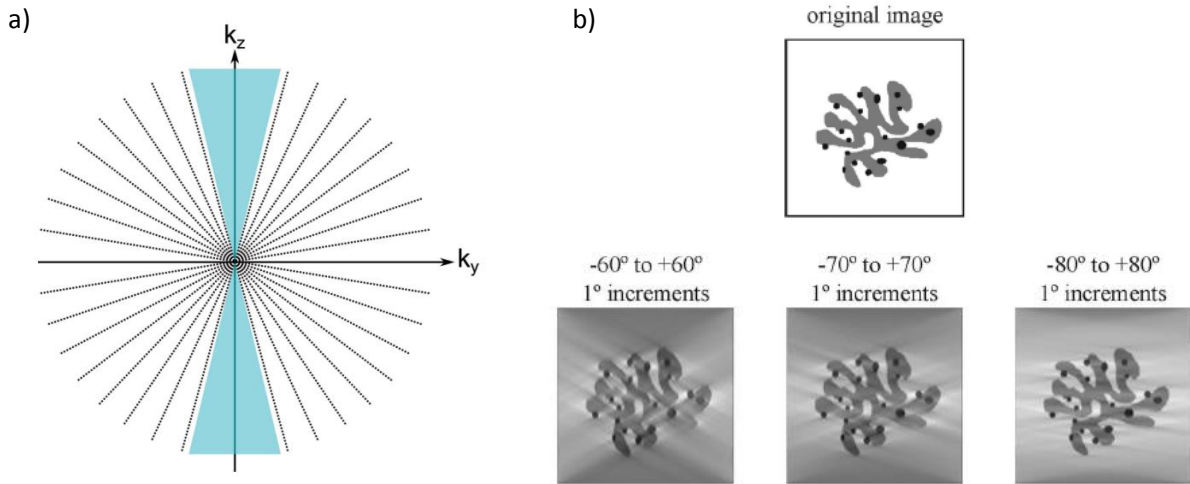


*Figure 2-4 – a) illustration of object sampling by a tilt series from  $\pm 70^\circ$  with blue zones indicating the missing wedge between  $70^\circ$  and  $90^\circ$  [152] and b) effect of maximum tilt angle on the reconstruction quality [151].*

Tilt series acquisition was performed on a  $C_s$ -corrected JEOL JEM 2100F microscope, operated at 200 kV at IPCMS. The tilt series were acquired in HAADF mode using  $2.5^\circ$  increments by using the tomography plug-in of the Digital Micrograph software (it controls the specimen tilt, the defocusing and the specimen drift). The powdered samples were again deposited without solvent on a 200 mesh holey carbon grid. The grid was plasma cleaned

before sample deposition. A tomographic single-tilt sample holder was used. Image alignment was performed through fiducial-less methods: a combination of cross-correlation and centre of mass methods using the IMOD software [159]. The reconstructed 3D volumes were obtained using the algebraic reconstruction technique (ART)[160] implemented in the TomoJ plugin [161] in the ImageJ software. Segmented 3D models were constructed using the displaying capabilities and the isosurface rendering method on the Slicer software [162,163].

Tilt series acquisition, alignment, reconstruction and segmentation were performed at IPCMS by Walid Baaziz, PhD.

#### ***2.2.2.1.5 In situ reduction experiments and protocol***

Investigation of materials' behaviour under real-world conditions other than vacuum is essential for several systems. Important insights can be gained from studying gas–solid interactions with atomic resolution in S/TEM at ambient pressures. This is possible thanks to the development of dedicated equipment for in situ TEM experiments, such as sample holders with a windowed gas cell that enclose the sample and the gas within a tiny space [164–166].

Such a setup is commercialized by Protochips under the name *Atmosphere* that can withstand up to 1 bar and includes integrated heating up to 1000°C. It consists of a cell formed by two *E-chips* with electron transparent windows between which gas can flow (up to atmospheric pressure), Figure 2-6. The sample is deposited on one of the chips that also has the heating components. The sample containing area is made of a SiC chip with six holes covered by an electron transparent thin SiN over which the sample can be imaged. The chips are assembled on a sample holder that is inserted in the microscope column.

In situ reduction of an oxide catalyst was performed on a  $C_s$ -corrected JEOL JEM 2100F microscope, operated at 200 kV at IPCMS using an *Atmosphere* set up (in situ holder, gas manifold, heating system). An ethanol suspension of powdered sample (1  $\mu$ L) was deposited on the sample supporting chip. After insertion of the holder in the microscope column and checking for leaks, the system is purged 3 times with Ar (back fill pressure 300 torr) then left overnight under Ar flow (0.2  $\text{cm}^3/\text{min}$  and pressure of 50 torr) in order to remove the residual  $\text{H}_2\text{O}$ /air content.

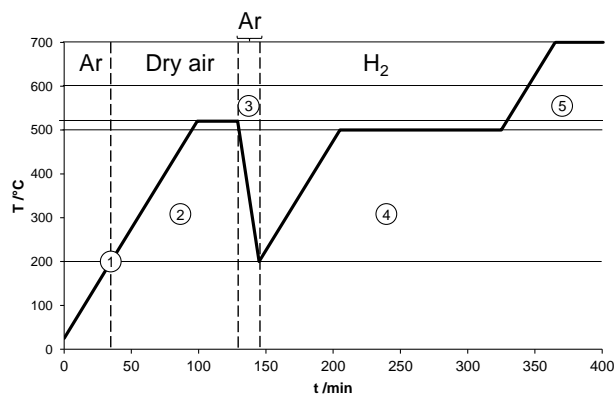


*Figure 2-5 – Treatment sequence used during the in situ reduction experiments. Numbers 1 to 5 indicate the stages described in the text.*

The reduction treatment is realized under atmospheric pressure (760 torr) with a gas flow of  $0.1 \text{ cm}^3/\text{min}$  as follows (Figure 2-5): heating to  $200^\circ\text{C}$  at  $5^\circ\text{C}/\text{min}$  under Ar to choose the zones for imaging (1); heating to  $520^\circ\text{C}$  at  $5^\circ\text{C}/\text{min}$  under dry air and left for 30 min (pre-calcination, 2); cooling to  $200^\circ\text{C}$  under Ar (3); heating to  $500^\circ\text{C}$  at  $5^\circ\text{C}/\text{min}$  under  $\text{H}_2$  and left for 120 min (reduction, 4); further heating to  $600^\circ\text{C}$  and to  $700^\circ\text{C}$  to check nanoparticle stability (5). These different steps aim at mimicking the ex situ catalysts reduction procedure. Non imaged zones during the in situ treatment were also analysed at the end of the treatment to check that identical states are recovered which confirms that no beam effect has occurred.

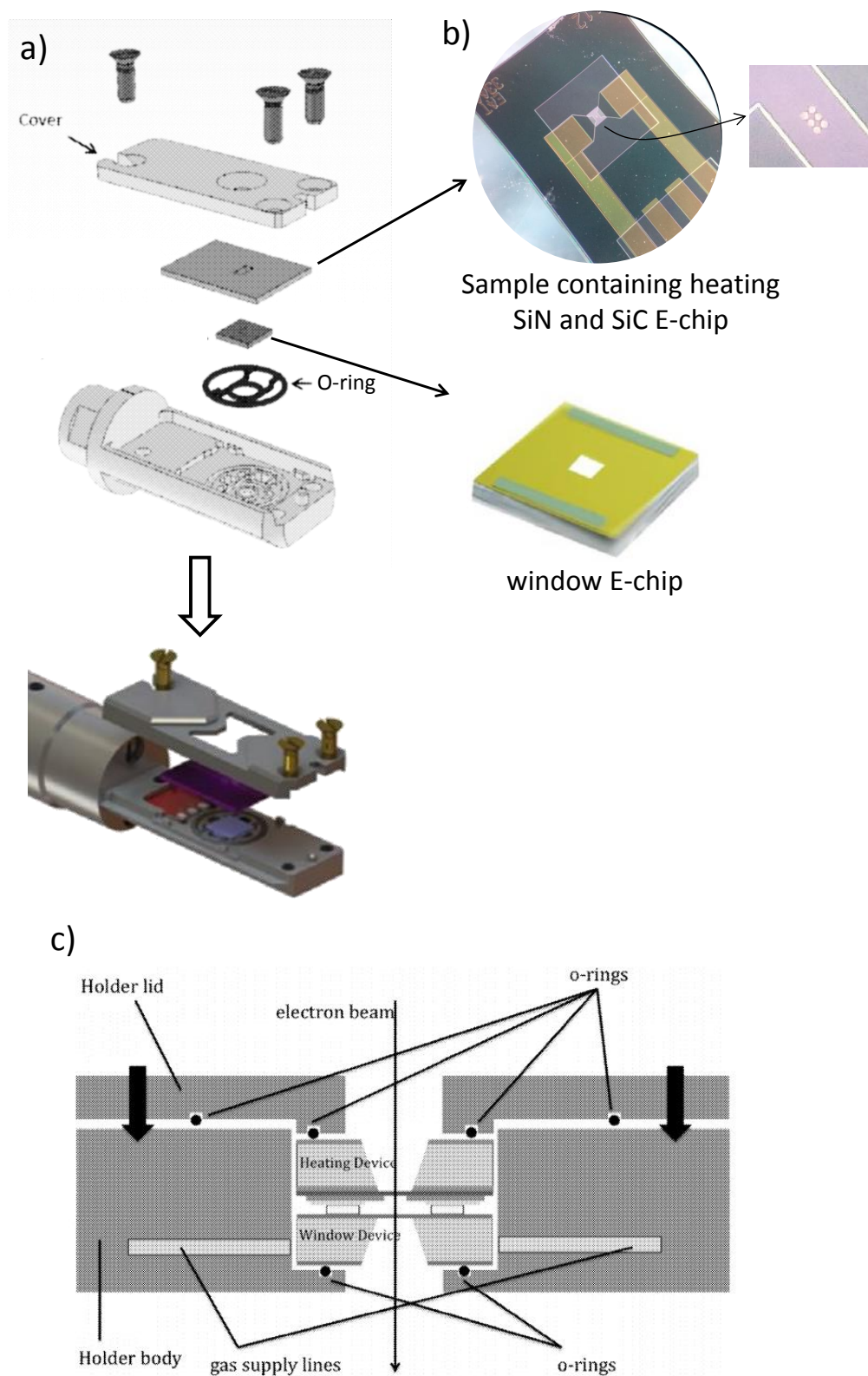


Figure 2-6 – Protochips Atmosphere sample holder: a) main components and assembly [167], b) E-chips and detail of SiN holes and c) sample holder cross section [168].

In situ experiments were performed at IPCMS by Walid Baaziz, PhD.

## 2.2.2.2 Solid State Magic-Angle-spinning Nuclear Resonance spectroscopy (MAS NMR)

### 2.2.2.2.1 Principle

NMR spectroscopy is used across various fields in science and medicine for a range of applications from structural elucidation of molecules in organic synthesis to the calculation of diffusion coefficients.

It is based on these simplified principles here exemplified for nuclei of spin  $\frac{1}{2}$  [140,169]:

- Atomic nuclei possess a magnetic moment and an angular momentum, as if spinning around a self-centred axis. So a nucleus can be thought of as a small spinning magnet.
- In the ground state, the magnetic moments of the various nuclei in a given sample are disordered, *pointing* in whatever direction, with no energy difference between them (Figure 2-7, a).
- When an external magnetic field  $B_0$  is applied, the nuclear magnetic moments become ordered. Some will be aligned with  $B_0$  and others will be aligned against  $B_0$  (Figure 2-7 b).
- There is now an energy difference between the nuclei depending on whether they are aligned with (lower energy level,  $\alpha$ ) or against (higher energy level,  $\beta$ )  $B_0$ . This is called the Zeeman effect. The population of these levels ( $N_x$ ) is not the same and follows the Boltzmann distribution (Equation 2-14 where  $k$  is the Boltzmann constant), being dependent on the energy difference between the two levels ( $\Delta E$ ) and on the temperature ( $T$ ). This difference is proportional to the field  $B_0$  (hence why high field spectrometers have higher sensitivity) and to the gyromagnetic ratio ( $\gamma$ ), a parameter characteristic of the type of nucleus (Equation 2-15).

$$N_{\alpha}/N_{\beta} = e^{\Delta E/kT} \quad \text{Equation 2-14}$$

$$\Delta E = \gamma h B_0 / 2\pi \quad \text{Equation 2-15}$$

- The nuclei under the influence of  $B_0$ , that let's say follows the  $z$  axis, are being pulled towards the  $z$  axis due to their magnetic moment while still spinning due to their



angular momentum, so they end up precessing around  $B_0$  at a certain frequency, called Larmor frequency.

- Since there are slightly more nuclei aligned with  $B_0$  than against, the macroscopic magnetization of the sample  $M_0$  is aligned with  $B_0$  on the z axis (Figure 2-7 b).
- To make a measurement, the system needs to be disturbed, namely to modify the population on the two energy levels so that the system can be observed going back to equilibrium. If the system is subjected to an oscillating field  $B_1$  (frequency  $\approx$  Larmor) for a certain duration, the macroscopic magnetization rotates to the xy plane ( $M_{xy}$ ). In the absence of  $B_1$ ,  $M$  will *rotate* around z to go back to  $M_0$  and restore equilibrium (relaxation) (Figure 2-7 c). This movement of  $M$  creates a fluctuating magnetic field that generates current in a coil, creating the NMR signal called FID (free induction decay).
- So far, this would *only* allow the measurement of the difference in energy between the two states which being characteristic of the type of nucleus, leads to its identification. An interesting phenomenon renders NMR much more useful: electrons moving around the nucleus create a secondary magnetic field that opposes  $B_0$ , *shielding* the nucleus. The nuclei of atoms of the same type but on different electronic environments will feel a magnetic field  $B_{\text{eff}}$  that is different between them, and so will be their Larmor frequency. This displacement of frequency (relative to a chosen reference) is called chemical shift (Equation 2-16). Also, the greater  $B_0$  the greater the displacement of frequency, so high field spectrometers also have better resolution.

$$\delta = 10^6(f - f_{\text{ref}})/f_{\text{ref}}$$

Equation 2-16

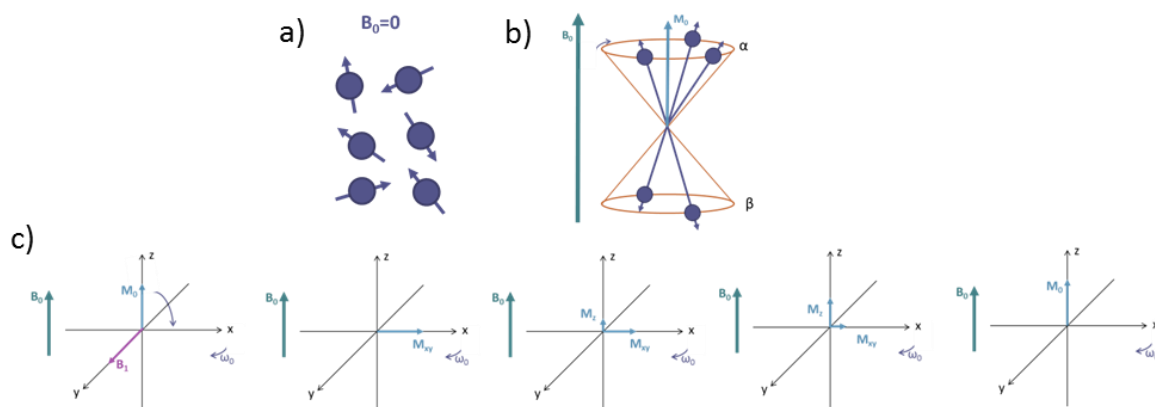


*Figure 2-7 - Schematic representation of nucleus magnetic moment a) in the absence of  $B_0$ ; b) in the presence of  $B_0$  with creation of two states ( $\alpha$ ,  $\beta$ ) and of the samples macroscopic magnetization  $M_0$ ; and c) impact of oscillating field  $B_1$  on  $M_0$  and consequential relaxation in the absence of  $B_1$ , represented in the laboratory frame*

Although the principle is the same, in practice NMR spectroscopy of samples in liquid or solid state (SS) is quite different. Some interactions in NMR, namely chemical shielding and homo and heteronuclear dipolar couplings and quadrupolar interactions are anisotropic, they depend on the orientation of species in space. In solution, Brownian motion ensures a random movement of species, averaging out these space dependent components. This does not happen for solid state samples, resulting in very broad spectra. The introduction of an artificial motion of the sample (at the macroscopic scale) can suppress some anisotropic interactions that cause broadening, by spinning the sample about an axis oriented at  $54.74^\circ$  with respect to  $B_0$  (Magic-Angle Spinning, MAS). MAS removes the broadening effects of chemical shift anisotropy, dipolar coupling effects and to certain extent of the quadrupolar interactions [140,170].

#### **2.2.2.2 Protocol and sequences**

Proton and aluminium-27 NMR spectra were obtained using the following sequences:

- One-dimensional proton DEPTH experiment [171]:

This experiment filters out probe background signals by removing the contributions of nuclei outside the rotor. It consists of a  $90^\circ$  pulse followed by two  $180^\circ$  pulses of different phases and then signal acquisition. The corresponding spectra are quantitative.

- Two-dimensional (2D) proton-proton BABA experiment [172]:

The BABA experiment yields 2D double-quantum (DQ) single-quantum (SQ) correlations and uses the following general scheme: excitation of DQ coherences with BACK-to-BACK pulses (BABA),  $t_1$  evolution, reconversion of these coherences into observable magnetization, Z-filter, and detection. The corresponding 2D map yields correlations between pairs of dipolar coupled (spatially close) protons. The DQ frequency in the indirect dimension corresponds to the sum of the two SQ frequencies of the two coupled protons and correlates with the two individual proton resonances. The observation of a DQ peak reveals a close proximity between the two protons. Thus, two equivalent protons will give an autocorrelation peak located on the  $\omega_1 / 2\omega_2$  line of the 2D map. Conversely, single spins will not give rise to diagonal peaks.

As the proton content is extremely low in the studied samples, the proton single-pulse spectra were dominated by the probe background. Several strategies were envisaged to suppress this probe background. A common strategy is to subtract the NMR signal of the empty probe (with possibly an empty static rotor) but it did not work in this case to suppress all background. The second most common background removal technique, a spin-echo sequence, does not allow for quantitative calculations and the corresponding data are not reported here. The DEPTH sequence appeared to be the most adequate experiment for the samples and work objectives at hand. Note that background signals come from protonated elements inside the probe that surround the coil and the rotor, and that are experiencing the radio-frequency pulses ( $B_1$ ).

$^1\text{H}$  DEPTH and  $^1\text{H}$ - $^1\text{H}$  Single Quantum-Double Quantum (BABA) solid state MAS NMR spectra were obtained on a Bruker Avance III 800 SB 800 MHz spectrometer at the Centre de RMN à Très Hauts Champs (CRMN) in Villeurbanne, Lyon, using a zirconia 2.5 mm rotor with Vespel<sup>®</sup> caps and 30 kHz MAS. Proton chemical shifts were referenced relative to adamantane.

Proton  $\pi/2$  pulses were usually set to 2.5  $\mu\text{s}$  in all experiments. Proton decoupling was always carried out using SPINAL-64 at 100 kHz radio frequency. Spectral deconvolution was performed using DMFit [173].

All samples were subjected to a reduction thermal treatment prior to acquisition, even for alumina samples. The sample containing ampoules were opened in a glove box where the rotor was filled ( $<0.5$  ppm  $\text{H}_2\text{O}$ ,  $<0.5$  ppm  $\text{O}_2$ ).

The NMR studies were performed with the participation of Dorothea Wisser, PhD, in cooperation with Anne Lesage and David Gajan from CRMN and with Mickael Rivallan and Leonor Duarte from IFPEN.

### **2.2.2.3 X-ray absorption spectroscopy (XAS)**

#### ***2.2.2.3.1 Principle***

XAS is an analysis technique that informs on the electronic state and local environment of a given type of absorbing atom. It consists in exposing the sample of interest to a monochromatic X-ray beam over a given energy range to measure the variation of the absorption coefficient (given by Beer-Lambert's law) as a function of incident X-ray energy [143].

The absorption of X-rays deals with core level electrons. Considering the targeted absorbing atom (ex. Pt), to each of this atom's core levels (K, L, M...) corresponds a binding energy that has to be provided in order to *extract* an electron from that respective level[143]. Also, the transition of a core electron to a higher partially occupied or unoccupied level by excitation follows a selection rule: electrons jumping out of a given core level are expected to land on certain available orbitals [174]. A core level of the considered target atom is chosen to be of interest (ex. L<sub>3</sub> shell of Pt) for which the electron binding energy is known.

A sample containing the atom of interest is illuminated by a monochromatic X-ray beam. Let us consider all the electronic transitions when the energy of the incident beam photon is increased (Figure 2-8). To start, the beam can have an energy lower than the binding energy of the electrons in the chosen core level. There is very little absorption, which is due to other atoms in the sample or other electronic levels of the target element, resulting in an almost flat, slightly decreasing, line in the spectrum (Figure 2-8). This zone of the spectrum is called pre-edge. Pre-edge peaks can also appear, due to transitions of electrons from the core level to partially occupied valence levels [174,175].

When increasing the beam energy very close to the binding energy (within a few eV) a great jump in absorption occurs: the absorption edge is attained (Figure 2-8). This leads to a sharp increase in absorption coefficient in the spectrum called edge. A sharp feature may appear at the top of the edge called white line for historical reasons. In this incident energy range, electrons on the chosen core level of the atoms of interest are excited and transitioned to

higher partially occupied or unoccupied levels. The energy at which the white line appears varies (around the binding energy) depending on the oxidation state of the absorbing atom. The intensity of the edge is representative of the probability of that transition: the more vacancies in the valence band (*arrival* level of the absorption process) there are, the more electrons from the core can make the transition, the more X-ray photons are absorbed. Measuring the probability of transition means measuring electronic density of the final state of the transition that depends on the electronic and geometric surroundings of the absorbing atom [174].

When beam energy is slightly over the edge several peaks and shoulders can appear on the spectrum. Now the core electrons are ejected to the continuum with a low kinetic energy and thus a large mean free path. The ejected electrons are photoelectron, and either the particle or the associated wave (wave-particle duality) can be considered to describe the process. Due to its large mean free path the photoelectron can *probe* a distance of several Ångströms (roughly 10 to 20 Å) around the absorbing atom and can be involved in multiple scattering with neighbouring atoms (multiple scattering demands longer travelled distances), providing information on the 3D geometry around the absorbing atom [174].

Increasing incident beam energy results in photoelectrons being ejected with increasingly higher kinetic energy and shorter mean free path. These photoelectrons probe mostly the neighbouring atoms closest to the absorbing atom, up to 5 Å. The wave associated with the photoelectron can be scattered by the electronic potential of the neighbouring atoms. The interaction between the incident and scattered waves induces modulations, oscillations, of the absorption cross-section. Due to the limited mean-free-path, the more important process to consider are single backscattering events. Oscillations observed in the spectrum become more spaced out for higher beam energies[143,176]. They are mainly characteristic the nature of the neighbouring atoms and distance between them and the absorbing atom. This is the EXAFS region.

The phenomena described lead to the typical XAS spectrum depicted in Figure 2-8.

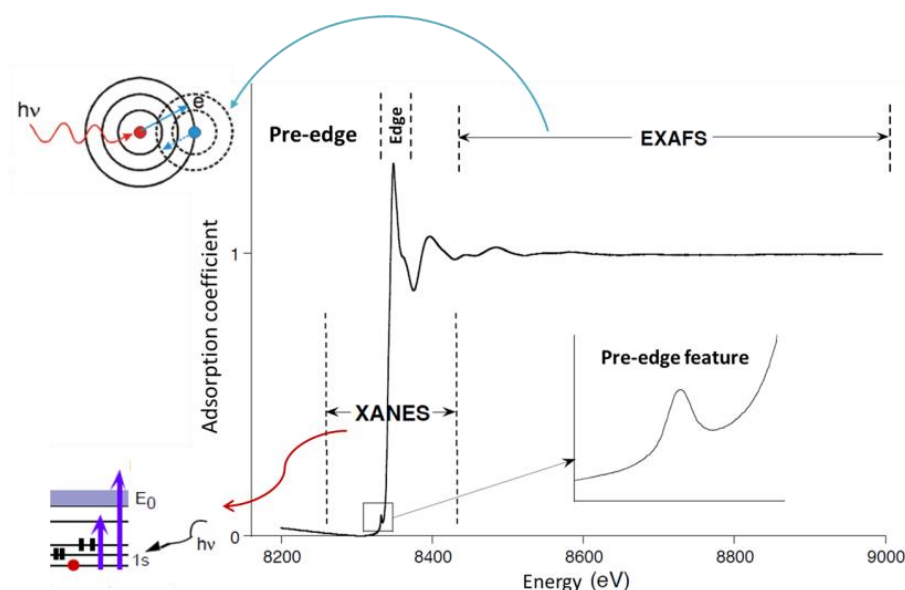


Figure 2-8 – Different zones of the XAS spectrum exemplified on a Ni K edge spectrum accompanied by schematic representations of the phenomena at play in the XANES and the EXAFS zones, adapted from [175,177].

It is now clear why XAS is said to be:

- A selective probe: a particular element and electronic transition can be targeted by the choice of edge and energy range of incident beam.
- A local probe: not only does the edge depend on the local environment of the absorbing atom, but also ejected photoelectron scattering provides information on neighbouring atoms at a short distance.

The X-ray Absorption Near Edge Structure (XANES) part of the spectrum (the edge part) provides information on the electronic structure and local geometry and symmetry of the absorbing atom [178]. The interpretation of the spectra is commonly done by comparison with known reference compounds or by ab initio simulation of spectra from theoretical models [174].

The Extended X-ray Absorption Fine Structure (EXAFS) part of the spectrum (the oscillation part) can be fitted to a structure model to identify the closest neighbours and quantify their number and distance to the absorbing atoms. The ejected photoelectron can be thought of as a spherical wave that interacts with neighbouring atoms. Upon this interaction, the neighbouring atoms emit scattering waves. The scattering waves interact with the absorbing atom, interfering with its emitted wave. The result of this interference between the scattered and emitted waves depends on the number of neighbouring atoms and the

distance between them and the absorbing atom. The interference between the scattered and emitted waves also depends on the kinetic energy of the photoelectron, and thus on incident beam energy, causing the oscillations observed in the spectrum [143,176]. The EXAFS region is usually represented as  $\chi(k)$  as a function of the photoelectron wavenumber  $k$  given by Equation 2-17 in which  $\hbar$  is the reduced Plank's constant,  $m_{\text{electron}}$  is the mass of an electron and  $E_0$  may be defined as the edge energy and  $E$  is the X-ray energy.

$$k = \frac{2\pi}{\lambda} = \sqrt{\frac{2m_{\text{electron}}(E - E_0)}{\hbar^2}} \quad \text{Equation 2-17}$$

This part of the spectrum can be modelled by the EXAFS equation (Equation 2-18), admitting a few approximations. This equation represents the sum of different possible scattering events for each neighbouring atom  $i$  [176,179].

$$\chi(k) = S_0^2 \sum_i N_i \frac{f_i(k)}{kR_i^2} e^{-\frac{2R_i}{\lambda(k)}} e^{-2k^2\sigma_i^2} \sin(2kR_i + \delta_i(k)) \quad \text{Equation 2-18}$$

The main approximations made to establish this formula are: 1) only one electron is considered (mono-electronic approximation), 2) the electronic potential of the absorbing atom has a spherical symmetry, 3) the incident photoelectron wave is considered to be plane close to the neighbouring atoms (plane wave approximation), 4) only single scattering events are considered and 5) the disorder is small, the bond length distribution can be described as a Gaussian function (harmonic approximation) [176].

In the EXAFS equation, for a given neighbour  $i$ :

- $R_i$  is the half-path length which can be the absorbed-scattered distance for single-scattering paths
- $N_i$  is the path degeneracy also called coordination number for single-scattering paths
- $\sigma_i^2$  is the square of the standard deviation of the half path length called the pseudo-Debye-Waller factor that represents the disorder in the path distance
- $f_i(k)$  is the photoelectron scattering amplitude and  $\delta_i(k)$  is the corresponding scattering phase shift.

Two other parameters are:

- $S_0^2$ , the amplitude reduction factor that is an approximation of intrinsic losses related to the formation of the core hole (incomplete overlap)
- $\lambda(k)$ , mean free path of the photoelectron that accounts for extrinsic losses such as the photoelectron doing anything other than scattering elastically off neighbouring atoms.

It should be kept in mind that XAS results represent an average of all the absorbing atoms in the sample that can be in different environments, with different numbers and types of neighbouring atoms [176].

XAS experiments require synchrotron source X-rays due to three main reasons [180]:

- 1) A good signal to noise ratio can only be obtained with a high X-ray flux, not provided by conventional laboratory sources,
- 2) Such high flux needs to be available over a broad and tunable energy range,
- 3) The X-ray beam has to be very stable over long periods of time in flux, energy range and position.

Absorption can be detected by comparing the intensity of the incident and transmitted beams (transmission mode) or by measuring the fluorescence X-ray radiation given off by relaxation (filling core hole) of the excited atoms (fluorescence mode). Fluorescence mode is indicated for dilute samples and allows high resolution XANES spectra to be obtained when an adequate detector is used.

#### ***2.2.2.3.2 Beamline presentation and acquisition conditions***

XAS analysis were conducted at the European Synchrotron Radiation Facility (ESRF) in Grenoble, France, over the course of three experimental runs at the two French Absorption spectroscopy beamlines in Material and Environmental science (FAME): BM30 (2016) and BM16 (2017, 2018). Experiments were devised with the help of beamline staff Antonio Aguilar-Tapia, Olivier Proux, Isabelle Kieffer and Jean-Louis Hazemann from the CNRS and of Christèle Legens from IFPEN.

BM16 was opened to users in January 2017 and is dedicated to the analysis of highly diluted samples thanks to optimized optics and the use of a multi-crystal analyser fluorescence detector (Figure 2-9) that allows high resolution measurement of the fluorescence photons (bandwidth around 1-3 eV compared to the 150-250 eV bandwidth of a conventional solid



state fluorescence detector) allowing High Energy Resolved Fluorescence Detection-XANES (HERFD-XANES). Before BM16 was available, HERFD-XANES data could be acquired on the original FAME beamline, BM30, equipped with the same crystal analyser [181].

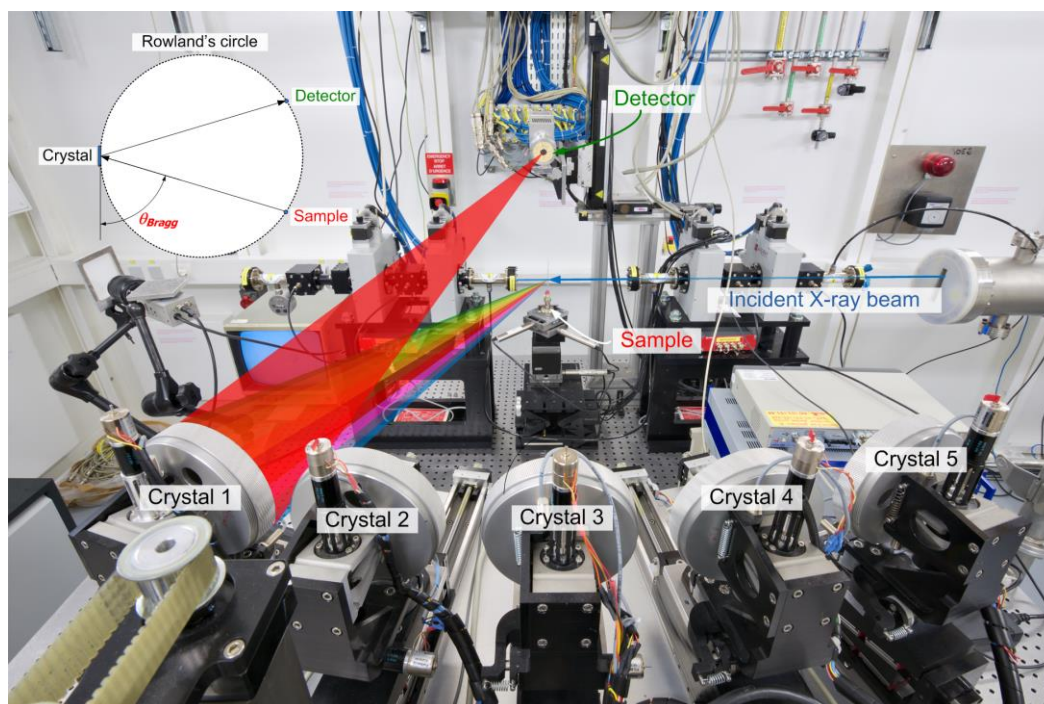
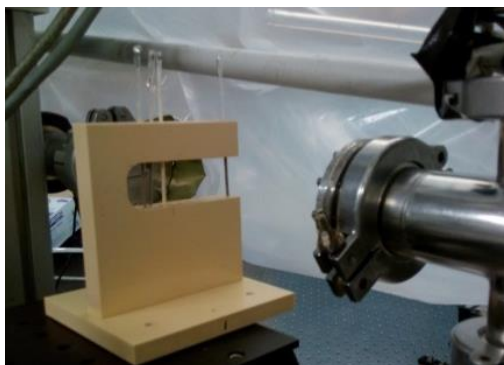


Figure 2-9 - Scheme of crystal analyser geometry [182].

At both beamlines, experiments were performed at the Pt  $L_3$  edge (11564 eV) on fluorescence mode using a multi-crystal analyser composed of Ge (110) crystals and a mono-element silicon drift detector (Figure 2-11, a). A Helium bag was placed between the sample, the crystals and the detector to prevent signal intensity loss by absorption of the (fluorescence emitted) X-rays by air molecules (not shown in Figure 2-11 for clarity). The beam energy was calibrated with Pt foil (first maximum of the first derivative XANES spectrum of the Pt metallic foil was set to 11564 eV). These beamlines use a double crystal Si(220) monochromator (to have a monochromatic beam) surrounded by two Rh-coated Si mirrors (to remove high energy harmonics from the monochromatic beam). Both HERFD-XANES and EXAFS data were acquired.

For the experiments at BM30 in 2016, five Ge(110) crystals were used. The grinded catalyst samples (oxide and reduced) were packed in Mark-tubes (Figure 2-10). The reduced samples were reduced ex situ and packed into the tubes in a glove box, where they were sealed with an epoxy glue. Unfortunately, the first data obtained in BM30 showed that the glue did not

completely prevent re-oxidation of the reduced samples, making its exploitation impossible, but the references' and oxide catalysts' data were of adequate quality.



*Figure 2-10 – Mark-tubes packed with powdered catalysts mounted on a support for analysis.*

The re-oxidation problem led to the use of a dedicated reactor [183] to perform in situ re-reduction of the catalysts for the experiments at BM16. These were again performed on the Pt  $L_3$  edge in fluorescence mode using a multi-crystal analyser composed of three (in 2017) or eight (in 2018) Ge (110) crystals, a Vortex Silicon drift solid detector (Figure 2-11, b) and a He bag or glove box (inset Figure 2-11, b). References and oxide catalysts were again analysed packed into Mark-tubes.

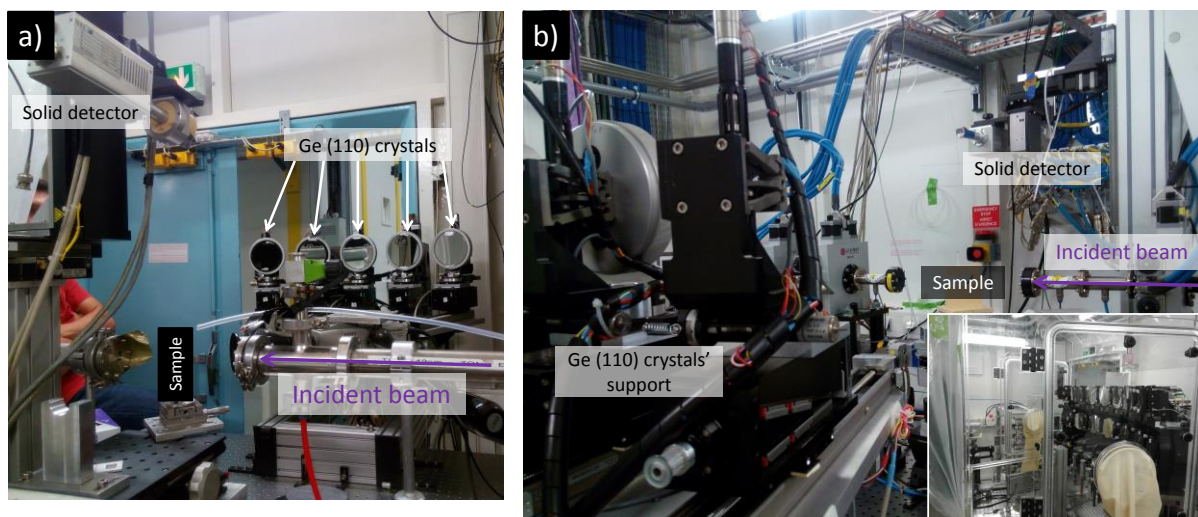


*Figure 2-11 - Experimental set-up on beamlines a) BM30 and b) BM16 as it stood in 2017, inset in b) showing the He glove box at BM16 installed in 2018.*

The scan settings used for data acquisition are detailed in Table 2-4 and were the same for both beamlines.

*Table 2-4 - Scan setting used for data acquisition of HERFD-XANES and EXAFS spectra and the HERFD-XANES scans used to follow the thermal treatment of re-reduced samples.*

	HERFD-XANES + EXAFS scan			HERFD-XANES scan		
	Before edge	Edge	After edge	Before edge	Edge	After edge
Ei (eV)	11450	11550	11586	11510	11550	11586
Ef (eV)	11550	11586	12413	11550	11586	11700
Step (eV)	2	0.5	2	2	0.5	2

### **2.2.2.3.3 Acquisition strategy and in situ re-reduction protocols**

For oxide catalysts and references, the grinded samples were packed in Mark-tubes of quartz or borosilicate glass (80mm length, 2mm diameter, 10  $\mu$ m wall thickness, Figure 2-10). Reference compounds were platinum oxide PtO<sub>2</sub> (Sigma-Aldrich, purity >99.9%, CAS Number 52785-06-5) and metallic platinum powder (Strem Chemicals, purity >99.9%, CAS Number 7440-06-4). These pure compounds were diluted in boron nitride with a mortar and pestle so as to have a Pt concentration of 3%<sub>w/w</sub>.

Catalysts previously reduced at IFPEN and transported on sealed ampoules under vacuum were re-reduced in a dedicated reactor developed at Néel Institute (CNRS) [183] in cooperation with the beamline team. This is a plug-flow reactor heated with a resistive molybdenum metallic wire (thermocouple inside the reactor regulates temperature). It was built specifically for use in the beamline, as the internal reactor is made of vitreous carbon and three window arrangement with Kapton windows to allow acquisition in transmission and fluorescence mode. Figure 2-12 depicts a scheme of the reactor cross section and a photo. In the version of the reactor used in 2017, its windows limited the span of the emitted fluorescence, so only three crystals were used. In 2018, the reactor had been upgraded with a larger window, so eight crystals were used.

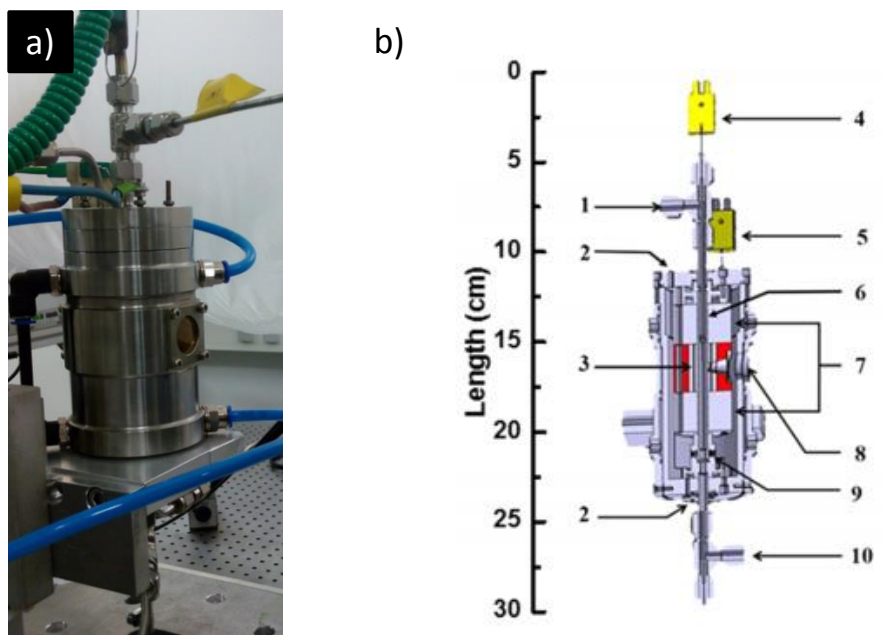
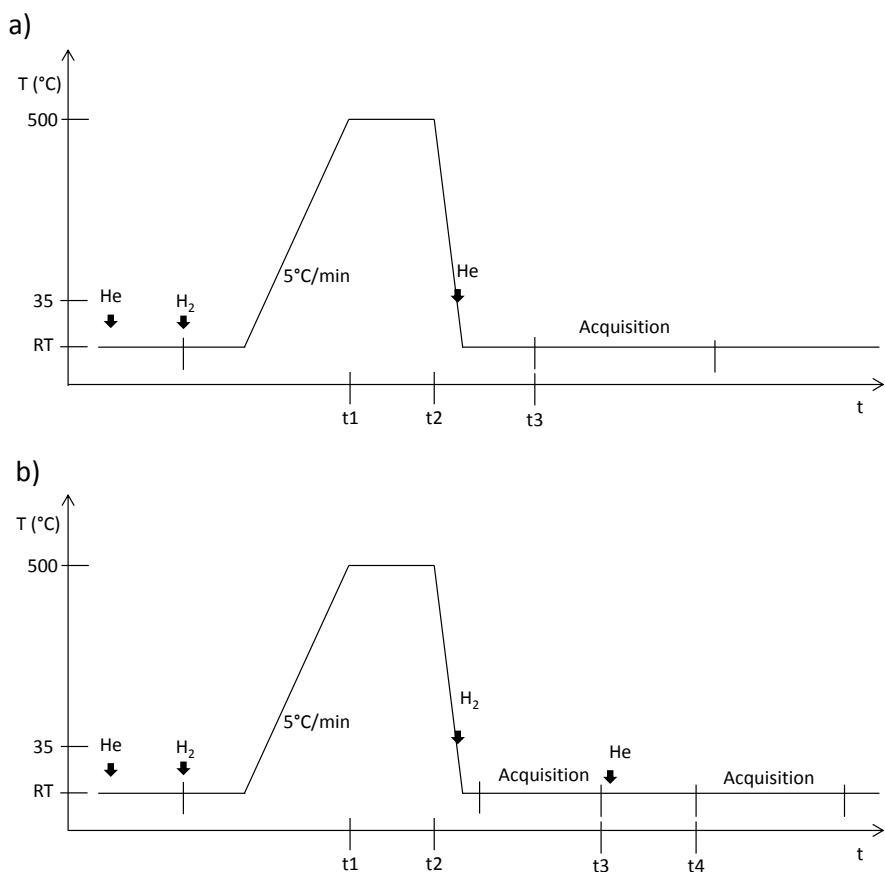


Figure 2-12 – Picture of the operando reactor used at BM16 a) and scheme of its cross section b) [183].

Gas flow is controlled before the inlet and effluents were analysed with a mass spectrometer (MS). The sample ampoules were opened on table top and 40 mg of catalyst was charged in the reactor. The re-reduction treatment used is presented in Figure 2-13 and XANES scans (10 minutes long) were used to follow the thermal treatment.

After charging, the reactor is purged of air with a He flow of 30 mL/min until the MS spectrum shows no  $N_2$ . The gas flow is changed to  $H_2$  at 10 mL/min and when no more He is detected by MS the temperature is increased to 500°C at 5°C/min, which takes about 2h. Once at 500°C, the plateau duration  $t_2-t_1$  is determined by comparing XANES scans: when two consecutive scans are equal the re-reduction is considered complete. The reactor is brought down to room temperature under  $H_2$  which takes about 15 minutes.



**Figure 2-13 – Re-reduction sequence applied prior to acquisition at room temperature a) under He (He@RT) or b) under H<sub>2</sub> (H<sub>2</sub>+He@RT).**

For all catalysts except one, the scheme in Figure 2-14 a) was followed. When the reactor cooled to about 35 °C the gas was changed back to He 50 mL/min. The full HERFD-XANES + EXAFS acquisition is carried out at room temperature under He flow. Total acquisition time takes from 4 to 8h, the number of scans depending on Pt loading (each scan is 45 minutes long). The full acquisition is launched when no more H<sub>2</sub> is detected in the MS (t<sub>3</sub>).

The goal was to acquire the full scans in absence of H<sub>2</sub>. However, the descending portion of the edge evolved during the long acquisition time and this could only be noticed after a few hours. A feature at 11572 eV progressively disappears while another at 11569 eV appears (Figure 2-14). It seems, despite H<sub>2</sub> not being detected in the MS, residual H<sub>2</sub> desorption occurred during acquisition under He, post-edge features at about the same position as the disappearing 11572 eV feature have been associated with adsorbed hydrogen [115,118,129]. This effect in particular was not interpreted nor exploited, as varying t<sub>3</sub> and acquisition times mean the conditions for desorption were not the same for each sample.

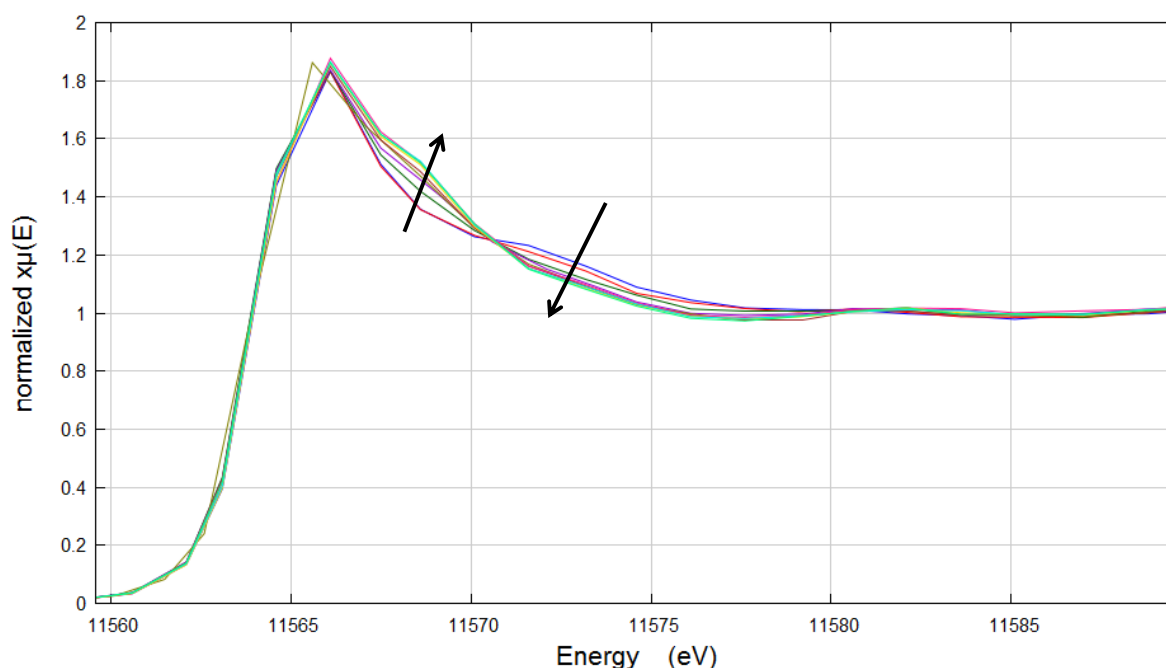


*Figure 2-14 - Pt  $L_3$  edge HERD-XANES region of scans of 0.3%Pt/PuraISB3-1.4%Cl showing the post-edge evolution during acquisition under He at room temperature along black arrows (each scan takes about 45 min).*

In a subsequent run (2018) there was an attempt to avoid this undesired desorption by waiting at least 3h under He flow after re-reduction before starting acquisition. This resulted in yet another unexpected effect: after about 2h under He the white line increased in intensity. As Figure 2-15 illustrates, the first scans show the same changes attributed to  $H_2$  desorption shown in Figure 2-14, and after 2h the white line intensity progressively increases and post-edge features change considerably in a way that resembles oxidation.

The reactor and overall system were extensively checked for leaks, the He bottle used was changed from one with  $< 1 \text{ O}_2 \text{ ppm}$  to one with  $< 10 \text{ ppb}$ , and no  $\text{O}_2$  or  $\text{N}_2$  were detected at that point by MS. This phenomenon was observed for several catalysts and the data thus obtained was not exploited. As this waiting period did not help in getting better quality data, it was abandoned and the acquisition conditions used in 2017 were used for the 2018 run as well.

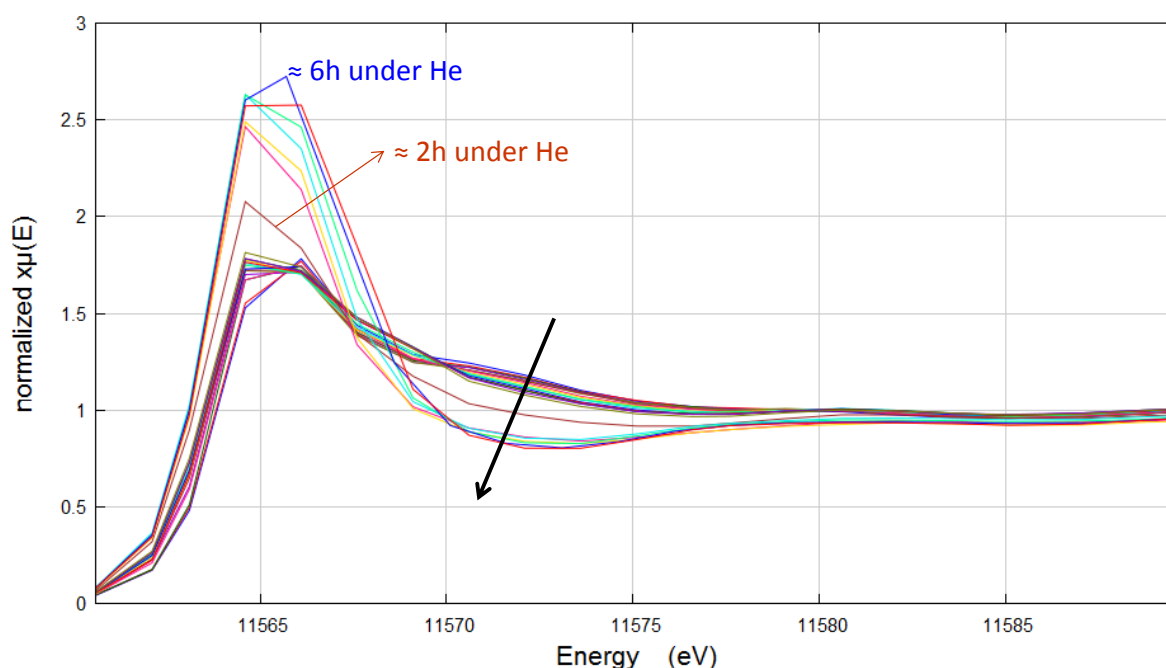


*Figure 2-15 - Pt  $L_3$  edge HERD-XANES region of consecutive scans of 1%Pt/PuralSB3-1.4%Cl acquired under He at room temperature. Black arrow indicates evolution with time. Up to the yellow line, scans are 10 minutes apart and the last four scans are 45 minutes apart.*

For one catalyst, the scheme in Figure 2-13 b) was followed. After re-reduction at 500°C, full XANES+EXAFS acquisition was performed at room temperature under  $H_2$ . The reactor was then put under He for a period of time  $t_4-t_3$  defined by the absence of  $H_2$  in the MS spectrum and full XANES+EXAFS acquisition was launched again. The goal here was to have spectra acquired at RT under  $H_2$  and under He for comparison.

Table 2-5 summarizes, for each analysed sample, at which beamline and with which protocol the exploited and presented data was acquired.



*Table 2-5 – Summary of analysed catalysts and on which beamline and year the discussed data was acquired.*

	Oxide		Re-reduced		
	BM30 (2016)	BM16 (2017)	BM16 (2017)		BM16 (2018)
			He@RT	H <sub>2</sub> + He@RT	He@RT
0.3%Pt/PuralSB3-1.4%Cl	x				x
0.3%Pt/PuralSB3-0.1%Cl	x		x		
1%Pt/PuralSB3-1.4%Cl	x		x		
1%Pt/PuralSB3-0.1%Cl	x		x		
0.3%Pt/TH100-1.4%Cl		x		x	
0.3%Pt/TH100-0.1%Cl		x	x		x
1%Pt/TH100-1.4%Cl		x	x		
1%Pt/TH100-0.1%Cl		x	x		

#### **2.2.2.3.4 Data processing and EXAFS fitting methodology**

Data were processed using Athena from the Demeter 0.9.26 software package [184]. The HERFD-XANES+EXAFS scans obtained for each sample were merged equally weighted. In the case of the re-reduced samples, for which the post-edge region evolved during acquisition due to undesired hydrogen desorption, not all acquired scans were merged. Only the last scans that have little difference between them were merged and the total number of merged scans used was tuned to minimize noise in the EXAFS region of the merged spectra while avoiding the first scans that have a large variation in the post-edge.

Normalization and background subtraction were applied to the merged spectra. In Athena's *Normalization and background removal parameters*,  $E_0$  was set to 11566.1 eV for all samples (a value between that of the maximum of the white line of reduced and oxide catalysts, to later homogenise the  $\Delta E_0$  obtained by EXAFS fitting) and the *Rbkg* cut-off parameter was set to 1.1. For the forward Fourier transform, a Kaiser-Bessel window was used. The k-range was tuned for each sample.

The wavelet transform analysis [185] was performed for the EXAFS spectra by calculating the Continuous Cauchy Wavelet Transform modulus (continuous decomposition of the EXAFS amplitude terms) using the available Matlab script [186].

The EXAFS spectra were fitted using Artemis from the Demeter 0.9.26 software package [184]. The EXAFS spectra of references PtO<sub>2</sub> and Pt powder, acquired at BM16 in 2017 and 2018, were fitted using paths obtained from crystallographic data (CIF files) sourced from



the literature (Pt – COD ID 4334349 [187] and PtO<sub>2</sub> – COD ID 1530633 [188] and 1537410 [189]) to obtain  $S_0^2$  and  $\Delta E_0$  (Appendix A). The values thus obtained for the reference data sets of 2017 and 2018 were averaged for each reference. The  $S_0^2$  and  $\Delta E_0$  values obtained for PtO<sub>2</sub> were used in the fitting of oxide catalysts and those obtained for Pt powder were used in the fitting of reduced compounds, as summarized in Table 2-6.

*Table 2-6 – Fitted amplitude reduction factor and energy shift  $\Delta E_0$  to the references Pt powder and PtO<sub>2</sub>.*

	Pt Powder	PtO <sub>2</sub>
$S_0^2$	0.79±0.05	0.88±0.03
$\Delta E_0$	4.49±0.58	9.28±0.62

For the oxide catalysts the k-range chosen for the FT transform was from about 4 to 12 Å<sup>-1</sup>, varying slightly for each sample in order to select “zero values” on the spectra and so limit the truncation effects. For reduced catalysts, the k-range had to be reduced to about 4 – 8.3 Å<sup>-1</sup> because noise at  $k > 8$  Å<sup>-1</sup> introduced parasitic signals in the FT transform  $|\chi(k)|$ . To be sure that no valuable information was being incorrectly disregarded by this window, the EXAFS spectrum of re-reduced 1%Pt/TH100-1.4%Cl was fitted using that range with fitting k-weights either 1, 2 or 3. As the fitted parameters did not drift outside the ranges define by their uncertainties, this k-range was considered valid [190].

Overall, EXAFS spectra of oxide and reduced catalysts were fitted in all three k-weights by the following procedure:

- The Artemis N parameter was set to 1
- The Artemis  $S_0^2$  parameter was equalled to  $N_i \cdot \text{amp}$ , in which  $N_x$  is the coordination number/degeneracy of path i and amp is the  $S_0^2$  value obtained from the adequate reference [191]. In this way the Artemis  $S_0^2$  parameter actually represents the “ $S_0^2 N_i$ ” multiplying factor of the EXAFS equation (Equation 2-18).
- The Artemis  $\Delta E_0$  parameter was initially set to the energy shift  $\Delta E_0$  obtained from the adequate reference.
- The other fitted parameters are the half-path length variation  $\Delta R_i$  and the pseudo-Debye-Waller factor  $\sigma_i^2$ .
- For a given path i,  $\Delta R_i$  and  $\Delta E_0$  are first allowed to vary. The obtained values are set as constants for the subsequent fit, in which  $N_i$  varies. All parameters are set as

constants except for  $\sigma_i^2$  that is then evaluated. Lastly, all parameters are set as constants except for  $\Delta E_0$  that is again evaluated.

- This procedure is repeated for each path and for all paths.

The paths used to fit the data were sourced from reference crystallographic data or obtained using the Quick First Shell Path tool available in Artemis, as detailed later in the text. The paths obtained from crystallographic data are summarized in Table 2-7.

*Table 2-7 – Paths obtained from published crystallographic data of reference compounds used in the fitting, in which @ symbolises the absorbing atom.*

Compound	ID	Paths	
PtO <sub>2</sub>	1530633*	@ O @	R=1.999 Å
PtCl <sub>4</sub> 5H <sub>2</sub> O [192]	1214146†	@ Cl @	R=2.266 Å
Pt	4334349*	@ Pt @	R=2.773 Å

\* COD; † Pearson's Crystal Structure Database

The fitted parameters are presented with the corresponding uncertainties as given by Artemis, except for the coordination number. This parameter  $N_x$  is fitted whilst in a mathematical function of  $\text{amp}$ , so the coordination number uncertainty is obtained by error propagation using the reference-sourced  $S_0^2$  value uncertainty and the  $N_x$  uncertainty [193].

#### **2.2.2.3.5 FDMNES XANES simulation**

The XANES spectra is a measurement of the electronic density of the final state of the transition of an excited core electron towards a valence band. To simulate this spectra relativistic calculations are necessary. Here XANES spectra were simulated for several supported Pt models using the FDMNES code [194] which is based on density functional theory (DFT) with the Local Spin Density Approximation (the generalization of LDA to spin-polarized systems) (see section 2.2.3). The code calculates the electronic structure for all atoms located inside a sphere of a defined radius. The X-ray absorption is obtained by calculating the absorption cross section for the transition between two states. For this work, the final state was calculated using the Finite Difference Method (FDM) technique to solve the Schrödinger equation. The calculations were performed by Yves Joly (Néel Institute, Grenoble).

The calculation results are given as the absorption cross section in megabarn in function of the photoelectron energy in eV, relative to a calculated XANES Pt bulk edge so that the Pt bulk edge position is at 0 eV. The FDMNES code calculates XANES up to about 60 eV past the edge. To compare the XANES spectra calculated for different supported platinum models, the absorption cross section must be divided by the number of Pt atoms in each model so as to have megabarn/atom. Then it is useful to compare the calculated XANES with the experimental XANES spectra. For this, the experimental non-normalized  $\mu(E)$  is used. First, the calculated spectra are aligned in energy with the experimental ones by shifting them by the experimental Pt bulk edge energy (Pt powder reference). Secondly, the calculated spectra are normalized in intensity in relation to the experimental spectra by multiplying the absorption cross section by a constant factor for which its post-edge region is aligned at the same intensity as the experimental spectra's post-edge. As this results in odd values of intensity on the ordinates axis, the maximum of the experimental spectrum's white line was set to 1 a.u..

## 2.2.3 DFT molecular modelling

### 2.2.3.1 Methods

Molecular modelling of the  $\gamma\text{-Al}_2\text{O}_3$  surface terminations and of supported Pt clusters was used throughout this work to complement or interpret experimental results. As these systems are of sub-nanometric nature, they have to be resolved by quantum mechanical methods. The calculations performed in the present work are based on the Density Functional Theory (DFT) which is an ab initio method (does not require fitting of external data).

The goal is, for a given system with M nuclei and N electrons, to solve the Schrödinger equation (Equation 2-19) which is a force balance on the electrons and nuclei of the system, in which  $\Psi$  is the wavefunction of the multielectronic system depends on atom position and on the spin of each electron, E the system energy and H the Hamiltonian operator.

$$H\Psi = E\Psi$$

*Equation 2-19*

The Hamiltonian operator is in turn comprised of kinetic and potential energy operators (Equation 2-20): kinetic energy terms for electrons ( $T_e$ ) and for nuclei ( $T_n$ ), potential energy terms for electron-electron ( $V_{ee}$ ), electron-nuclei ( $V_{en}$ ) and nuclei-nuclei ( $V_{nn}$ ) interactions.

$$H = T_e + T_n + V_{ee} + V_{en} + V_{nn} \quad \text{Equation 2-20}$$

The Born-Oppenheimer approximation states that electronic motion can be decoupled from nuclear motion, due to the large difference of their respective masses, so that the electronic wavefunction can be solved separately for a set of fixed nuclear positions. The problem becomes an electronic one since the Hamiltonian operator can be simplified by neglecting the kinetic energy of nuclei  $T_n$  and the  $V_{nn}$  component is constant for a given set of nuclei positions. There is no exact solution for systems with  $N > 1$  due to the electron-electron repulsion term in the electronic Hamiltonian.

DFT is one method developed to solve this multielectronic problem using reasonable approximations and it is based on two exact Hohenberg and Kohn theorems [195]. The first Hohenberg and Kohn theorem states that an arbitrary external local potential  $v(r)$ , which can be in place of  $V_{en}(r)$ , can be determined up to an arbitrary additive constant by the ground state electronic density  $\rho(r)$ . The electronic density  $\rho(r)$  of a  $N$  electron system is the number of electrons per volume on the point given by coordinate  $r$ . This means that all the systems' properties at ground state (0 K) can be defined by the electronic density. This is valid for the total energy of the system in particular that can now be written as in Equation 2-21 in which  $F_{HK}$  is the universal density functional (independent from the external potential  $v(r)$ ).

$$E[\rho] = T_e[\rho] + V_{en}[\rho] + V_{ee}[\rho] = \int \rho(r)v(r)dr + F_{HK}[\rho] \quad \text{Equation 2-21}$$

The second Hohenberg and Kohn theorem showed that  $E[\rho]$  is minimal when the electron density is equal to that of the ground state, thus the ground state can be found by minimizing the electronic energy.

Since there is no exact expression for  $F_{HK}[\rho]$ , in particular for its kinetic energy component, Kohn and Sham proposed an indirect expression based on a mono-electronic formalism [196]. The electronic system energy is thus written as in Equation 2-22 in which  $T_{ni}$  is the kinetic energy of non-interacting electrons,  $V_{ee, classical}$  the classical component of Coulombian

interaction  $V_{ee}$  and  $E_{xc}$  is the exchange-correlation energy that contains corrections to the kinetic energy and to the non-classical part of  $V_{ee}$ .

$$E[\rho] = T_{ni}[\rho] + V_{ee,classical}[\rho] + \int \rho(r)v(r)dr + E_{xc}[\rho] \quad \text{Equation 2-22}$$

It was demonstrated that the problem can be solved self-consistently using the Kohn-Sham equations, Equation 2-23 and Equation 2-24, where  $\psi_i$  is the wavefunction and  $\varepsilon_i$  is the eigenvalue.

$$\hat{H}[\rho(r)]\psi_i(r) = \varepsilon_i\psi_i(r) \quad \text{Equation 2-23}$$

$$\rho(r) = \sum_i |\psi_i|^2 \quad \text{Equation 2-24}$$

There is no exact formulation for the exchange-correlation component so it has to be necessarily approximated. Two approaches are here of interest: the Local Density Approximation (LDA) considers that exchange-correlation per electron is equivalent to the exchange-correlation per electron in a homogeneous electron gas which has the same electron density at a specific point  $r$ ; and the Generalized Gradient Approximation that corrects for the fact that real electron systems are not homogeneous. The latter was used in this work, in particular the PBE functional, and in order to account for the van der Waals dispersion forces, the PBE-dDsC functional was used [197,198].

Having settled the issue of the exchange-correlation component, the wavefunction in the Kohn-Sham equations has to be defined in order to solve them. When bulk solid systems and surfaces are being studied, the periodic approach is the most adequate. In this case, an elementary cell is periodically replicated in three directions. In such periodic systems, Bloch's theorem applies and the wavefunction is defined by a basis set. In the case of the Vienna Ab initio Simulation Package (VASP) [199,200], used in this work, a plane-wave basis set is used. This means, in practice, that the wavefunction is expressed as the sum of plane-waves expanded out to a chosen cut off energy. Increasing the cut off energy increases the accuracy by allowing a more expansive wavefunction. The system is described in reciprocal space where the first Brillouin zone is divided and described by a number of  $k$ -points that describe the sampling of the wavefunction. The plane-wave basis is efficient if used together

with the pseudopotential approach, in which the core electrons are substituted with a pseudopotential that acts upon the valence electrons. In this work projector-augmented wave (PAW) pseudopotentials were used [201].

### **2.2.3.2 Types of calculations performed**

In practice, for a given model built in a elementary cell with an initial geometry (determined by the atomic positions), the wavefunction of the system is solved by an iterative scheme (self-consistent field cycle). Once the wavefunction is determined the electronic structure of the system with the given atomic positions is solved. There are two iterative loops: the inner loop requires the convergence of the electronic structure for a set of atomic positions and the outer loop moves the atoms so that the forces upon each atom are minimized and the lowest energy structure is found. In the inner loop, with the initial geometry and basis functions as input, the initial electron density, initial wavefunction and the initial system energy are determined. The wavefunction is calculated again using the Kohn-Sham equations as well as a “new system energy”. The inner loop stops when the difference between two energies at two successive steps is inferior to the convergence electronic energy criterion. The calculation moves then on to the outer loop and the forces acting upon each atom are determined. Based on the result, the atomic positions are changed so as to minimize the forces down to the second convergence criterion related to the geometry. If the criterion is not met, the inner loop is repeated using this new geometry, and so on. This is the principle of geometry optimization calculations used in this work with a convergence criterion for electronic energy of  $10^{-7}$  eV and a convergence criterion on forces of 0.01 eV/Å.

To correct the energy calculated at 0 K for thermal and pressure effects, the chemical potential approach was employed, which allows to include the vibrational entropy and enthalpy contributions as well as the partial pressure of water in close to experimental conditions. This aspect is detailed in the corresponding chapter 3.

The optimized geometries of the most relevant models were used to calculate NMR chemical shifts using the linear response method [202,203]. Linear response provides an analytical way of computing the second derivative of the total energy with respect to a perturbation, which in this case will be a perturbation in magnetic field.

Atomistic models of  $\gamma\text{-Al}_2\text{O}_3$  (110), (100) and (111) surfaces and of  $\gamma\text{-Al}_2\text{O}_3$  supported Pt entities previously developed at IFPEN and published in the literature were used throughout this work [50,51,82,90,115,124,132,204]. When specific models were re-optimized that is made explicit in the text.

In particular, new models of  $\gamma\text{-Al}_2\text{O}_3$  (110)-(100) crystallite edges and of Pt nanoparticles supported on those edges were built. The details are given in the corresponding sections of chapters 3 and 4. The construction of the edge model and the study of its hydration were performed by Thomas Pigeon during his gap year internship of CPE (Lyon) co-supervised by Céline Chizallet and Pascal Raybaud at IFPEN.

## 2.3 Standard characterization of prepared materials

The alumina pellets, acidified aluminas and catalyst samples were characterized by what are here called “standard” methods.

### 2.3.1 Alumina supports and acidified aluminas

The textural properties of the two alumina supports, analysed after extrusion and calcination, are summarized in Table 2-8. In terms of texture, both supports are mesoporous. One main difference between these aluminas relates to their crystallite size, larger for TH100, which is consistent with its lower surface area.

*Table 2-8 – Calcination conditions and properties of PuralSB3 and TH100 aluminas given by N<sub>2</sub> physisorption\*, Hg porosimetry† and XRD‡ (diffractograms available in Appendix B).*

	Pural SB3	TH100
$S_{\text{BET}}$ (m <sup>2</sup> /g)*	183 ± 9	149 ± 7
$D_{\text{Vmeso}/2}$ (nm)†	9.8 ± 0.2	15.1 ± 0.3
$V_{\text{meso}}$ †	0.49 ± 0.02	0.60 ± 0.03
Alumina polymorph‡	γ	γ
Average crystallite size (400 peak) (nm)‡	5.7	7.3

Chlorinated or acidified aluminas were analysed by XRF before and after the thermal treatment they underwent before NMR analysis which is equivalent to the catalysts’ reduction treatment. Measured values are very close to target values. A slight loss of chlorine is observed after reduction as discussed below for catalyst samples.

*Table 2-9 – Chlorine mass loadings measured by XRF and calculated surface coverages for acidified PuralSB3 and TH100 aluminas.*

Sample	Before final T. T.	After final T. T.	
	% <sub>w/w</sub> Cl	% <sub>w/w</sub> Cl	Cl/nm <sup>2</sup>
PuralSB3-0.5%Cl	0.58 ± 0.02	0.55 ± 0.02	0.52 ± 0.03
PuralSB3-1.4%Cl	1.37 ± 0.03	1.19 ± 0.03	1.11 ± 0.02
TH100-0.5%Cl	0.47 ± 0.03	0.48 ± 0.03	0.55 ± 0.04
TH100-1.4%Cl	1.16 ± 0.06	1.04 ± 0.05	1.19 ± 0.08



## 2.3.2 Pt/alumina-Cl catalysts

Several standard techniques were applied to verify the quality of the catalyst synthesis performed in terms of target loading, uniform repartition of species on the support and metallic dispersion.

### 2.3.2.1 Pt and Cl loadings

The platinum mass content was quantified by XRF for the impregnated and calcined materials (before Cl tuning) of both catalysts series (PuralSB3 and TH100) and was used to calculate platinum surface coverages (Table 2-10).

*Table 2-10 – Platinum mass content and surface coverage of impregnated and calcined materials*

PuralSB3 – Impregnated+calcined			
	0.3%Pt	0.6%Pt	1%Pt
% <sub>w/w</sub> Pt	0.307 ± 0.007	0.66 ± 0.01	1.04 ± 0.03
Pt/nm <sup>2</sup>	0.053 ± 0.003	0.114 ± 0.006	0.18 ± 0.01
TH100 – Impregnated+calcined			
	0.3%Pt	0.6%Pt	1%Pt
% <sub>w/w</sub> Pt	0.292 ± 0.007	0.64 ± 0.01	0.97 ± 0.02
Pt/nm <sup>2</sup>	0.061 ± 0.003	0.135 ± 0.007	0.21 ± 0.01

The measured platinum loadings correspond to the targets. As mentioned previously, the mass content in platinum is not identical for both sets to allow for identical surface coverages, as the two aluminas have different surface area. The TH100 set has slightly higher platinum surface coverages, but they are still considered comparable to those of the PuralSB3 set.

Chlorine mass content was quantified by XRF for impregnated and calcined materials, oxide catalysts after tuning of chlorine loading (by oxychlorination for the highest target and dechlorination for the remaining), and for reduced catalysts. Surface coverages were also calculated. The data are available in Table 2-11 and Table 2-12.

Note that the chlorine coverage is still non-negligible for the lower chlorine loadings. As for platinum, the mass content in chlorine is not identical for both sets (but still very close) with

the aim of achieving identical surface coverages. The TH100 samples still present higher chlorine surface coverages than the PuralSB3 samples.

As for the acidified aluminas, chlorine content (and thus surface coverage) of catalysts decreases after the reduction treatment. The Cl loss is less pronounced for low Cl loading, as shown in Figure 2-16. It is expected that weakly attached chlorine is lost during the calcination or reduction stages of the reduction thermal treatment, presuming that with increasing Cl loading the most favourable sites for chlorine become saturated and less favourable sites start being occupied.

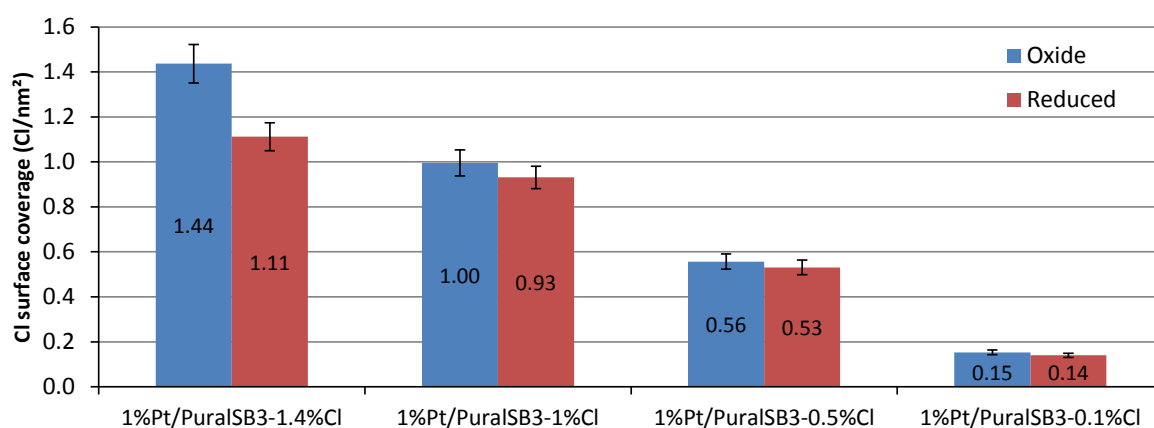


Figure 2-16 - Chlorine surface coverage of PuralSB3 oxide and reduced catalysts.

Table 2-11 – Chlorine loading evaluated by XRF and calculated surface coverage of PuralSB3 and TH100 impregnated and calcined materials.

	PuralSB3 - Impregnated + calcined	
	% <sub>w/w</sub> Cl	Cl/nm <sup>2</sup>
0.3%Pt/PuralSB3	1.37 ± 0.03	1.29 ± 0.07
0.6%Pt/PuralSB3	1.35 ± 0.03	1.28 ± 0.07
1%Pt/PuralSB3	1.41 ± 0.03	1.34 ± 0.07
	TH100 - Impregnated + calcined	
	% <sub>w/w</sub> Cl	Cl/nm <sup>2</sup>
0.3%Pt/TH100	1.18 ± 0.03	1.37 ± 0.08
0.6%Pt/TH100	1.25 ± 0.03	1.45 ± 0.08
1%Pt/TH100	1.12 ± 0.03	1.30 ± 0.07

**Table 2-12 –Chlorine loading measured by XRF and calculated surface coverage of oxide and reduced PuralSB3 and TH100 catalysts.**

PuralSB3				
	Oxide		Reduced	
	% <sub>w/w</sub> Cl	Cl/nm <sup>2</sup>	% <sub>w/w</sub> Cl	Cl/nm <sup>2</sup>
<b>0.3%Pt/PuralSB3-1.4%Cl</b>	1.50 ± 0.04	1.42 ± 0.08	1.25 ± 0.03	1.18 ± 0.07
<b>0.3%Pt/PuralSB3-1%Cl</b>	1.02 ± 0.03	0.96 ± 0.06	0.89 ± 0.02	0.84 ± 0.05
<b>0.3%Pt/PuralSB3-0.5%Cl</b>	0.52 ± 0.01	0.49 ± 0.03	0.58 ± 0.02	0.54 ± 0.03
<b>0.3%Pt/PuralSB3-0.1%Cl</b>	0.108 ± 0.006	0.101 ± 0.008	0.107 ± 0.006	0.10 ± 0.01
<b>0.6%Pt/PuralSB3-1.4%Cl</b>	1.48 ± 0.04	1.40 ± 0.08	1.22 ± 0.03	1.15 ± 0.06
<b>0.6%Pt/PuralSB3-1%Cl</b>	1.10 ± 0.03	1.04 ± 0.06	1.04 ± 0.03	0.98 ± 0.06
<b>0.6%Pt/PuralSB3-0.5%Cl</b>	0.59 ± 0.02	0.55 ± 0.03	0.59 ± 0.02	0.55 ± 0.03
<b>0.6%Pt/PuralSB3-0.1%Cl</b>	0.119 ± 0.006	0.111 ± 0.008	0.12 ± 0.006	0.112 ± 0.007
<b>1%Pt/PuralSB3-1.4%Cl</b>	1.51 ± 0.04	1.44 ± 0.09	1.18 ± 0.03	1.11 ± 0.06
<b>1%Pt/PuralSB3-1%Cl</b>	1.05 ± 0.03	1.00 ± 0.06	0.99 ± 0.02	0.93 ± 0.05
<b>1%Pt/PuralSB3-0.5%Cl</b>	0.59 ± 0.02	0.56 ± 0.03	0.57 ± 0.02	0.53 ± 0.03
<b>1%Pt/PuralSB3-0.1%Cl</b>	0.163 ± 0.007	0.15 ± 0.01	0.150 ± 0.007	0.14 ± 0.01
TH100				
	Oxide		Reduced	
	% <sub>w/w</sub> Cl	Cl/nm <sup>2</sup>	% <sub>w/w</sub> Cl	Cl/nm <sup>2</sup>
<b>0.3%Pt/TH100-1.4%Cl</b>	1.33 ± 0.03	1.54 ± 0.08	1.08 ± 0.03	1.25 ± 0.07
<b>0.3%Pt/TH100-1%Cl</b>	0.98 ± 0.02	1.13 ± 0.06	-	-
<b>0.3%Pt/TH100-0.5%Cl</b>	0.52 ± 0.02	0.60 ± 0.04	-	-
<b>0.3%Pt/TH100-0.1%Cl</b>	0.132 ± 0.006	0.15 ± 0.01	0.132 ± 0.006	0.15 ± 0.01
<b>0.6%Pt/TH100-1.4%Cl</b>	1.31 ± 0.03	1.52 ± 0.08	1.09 ± 0.03	1.26 ± 0.07
<b>0.6%Pt/TH100-1%Cl</b>	0.90 ± 0.02	1.04 ± 0.06	-	-
<b>0.6%Pt/TH100-0.1%Cl</b>	0.161 ± 0.007	0.19 ± 0.01	0.159 ± 0.007	0.18 ± 0.01
<b>1%Pt/TH100-1.4%Cl</b>	1.27 ± 0.03	1.48 ± 0.08	1.02 ± 0.03	1.18 ± 0.07
<b>1%Pt/TH100-1%Cl</b>	1.01 ± 0.02	1.17 ± 0.06	-	-
<b>1%Pt/TH100-0.5%Cl</b>	0.52 ± 0.03	0.60 ± 0.05	0.52 ± 0.03	0.60 ± 0.05
<b>1%Pt/TH100-0.1%Cl</b>	0.212 ± 0.008	0.24 ± 0.02	0.214 ± 0.008	0.25 ± 0.02

### 2.3.2.2 Repartition of Pt and Cl through the support pellet

Platinum and chlorine distribution through the interior of the impregnated and calcined materials extrudates was evaluated by electron microprobe analyser (EPMA), which showed an homogeneous profile and a repartition coefficient close to 1 for both elements (Figure

2-17). This distribution was considered not to vary with subsequent chlorine content tuning and reduction thermal treatments.

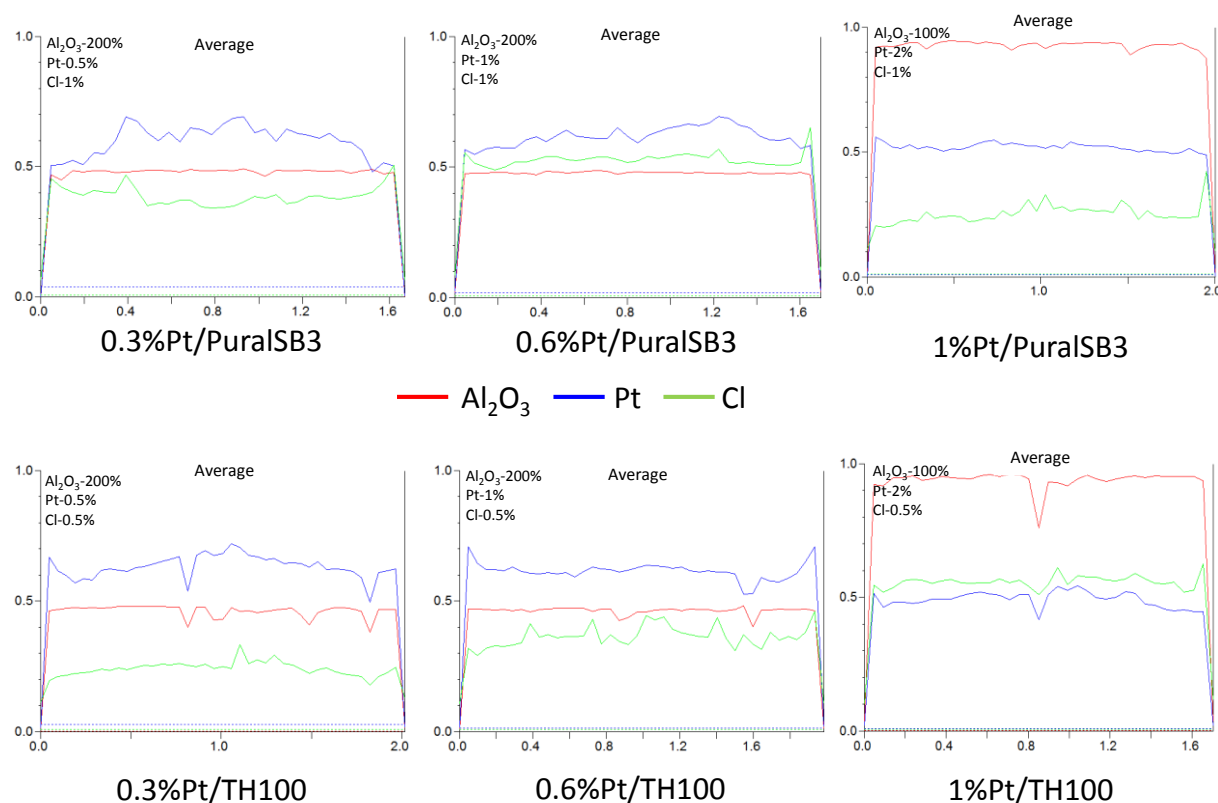


Figure 2-17 – Platinum, chlorine and alumina concentration profiles through the pellets given by EPMA.

### 2.3.2.3 Platinum dispersion

Platinum metallic dispersion (accessible Pt atoms vs total) was evaluated for impregnated and calcined materials by static chemisorption of  $H_2$  and by  $H_2/O_2$  titration (Table 2-13). Note that for both kinds of experiments, the Impregnated and calcined samples are fact reduced during the pre-treatment prior to the chemisorption experiments. The dispersion given by total adsorption of  $H_2$  being superior to 100% indicates adsorption of more than one hydrogen atom per exposed platinum in those conditions, contrary to the stoichiometry coefficient assumed for calculation. The phenomenon at the origin of such deviation could be the existence of single atoms, as for these species a H/Pt ratio of 2 is predicted [90].

**Table 2-13 - Platinum dispersion (in percentage) of PuralSB3 and TH100 impregnated and calcined materials according to  $H_2/O_2$  titration and static  $H_2$  chemisorption.**

Dispersion (%) for Pural SB3 - Impregnated+Calcined materials			
		Static chemisorption of $H_2$	
Pt loading	$H_2 / O_2$ titration	Irreversible Adsorption	Total Adsorption
0.3% Pt	$87 \pm 7$	$78 \pm 10$	$141 \pm 17$
0.6% Pt	$83 \pm 7$	$76 \pm 9$	$135 \pm 17$
1% Pt	$84 \pm 7$	$65 \pm 8$	$121 \pm 15$
Dispersion (%) for TH100 - Impregnated+Calcined materials			
		Static chemisorption of $H_2$	
Pt loading	$H_2 / O_2$ titration	Irreversible Adsorption	Total Adsorption
0.3% Pt	$83 \pm 7$	$65 \pm 8$	$125 \pm 15$
0.6% Pt	$91 \pm 7$	$78 \pm 10$	$142 \pm 17$
1% Pt	$89 \pm 7$	$73 \pm 9$	$130 \pm 16$

The use of two different techniques can be discussed, as that practice is more useful for bimetallic catalysts. For these monometallic catalysts the dispersion measured by  $H_2 / O_2$  titration would have sufficed but the traditional static chemisorption of  $H_2$  was also performed to allow for comparison of the overall evolution trend of metallic dispersion between loadings and between supports. Indeed the results of both analysis follow the same trends. The high dispersion values characteristic of Pt/ $\gamma$ -alumina systems were achieved and the dispersion (given by the same analysis) is equivalent for all samples within the measurement uncertainty.

#### **2.3.2.4 Reducibility of supported platinum**

TPR analysis was performed on PuralSB3 impregnated and calcined materials and PuralSB3 oxide catalysts, and on TH100 impregnated and calcined materials. From the resulting curves, the temperature of maximum  $H_2$  consumption and consumed  $H_2$  volume were determined. The uncertainty of measurement of these parameters was previously evaluated at IFPEN for the methodology and equipment used for the analysis and catalytic reforming type catalysts (low metal loadings leading to low  $H_2$  consumption volumes) and is used to present the results.

### 2.3.2.4.1 Effect of chlorine loading

The TPR profiles of the impregnated and calcined materials and oxide catalysts were compared for each platinum loading, as exemplified for 1%Pt/PuralSB3 in Figure 2-18. Consumed  $H_2$  volume and temperature of maximum  $H_2$  consumption are summarized in Appendix C. The volume was obtained by integration of the first consumption peak, up to the temperature signalled by the blue line, not of the whole curve, due to the presence of a baseline that is not negligible.

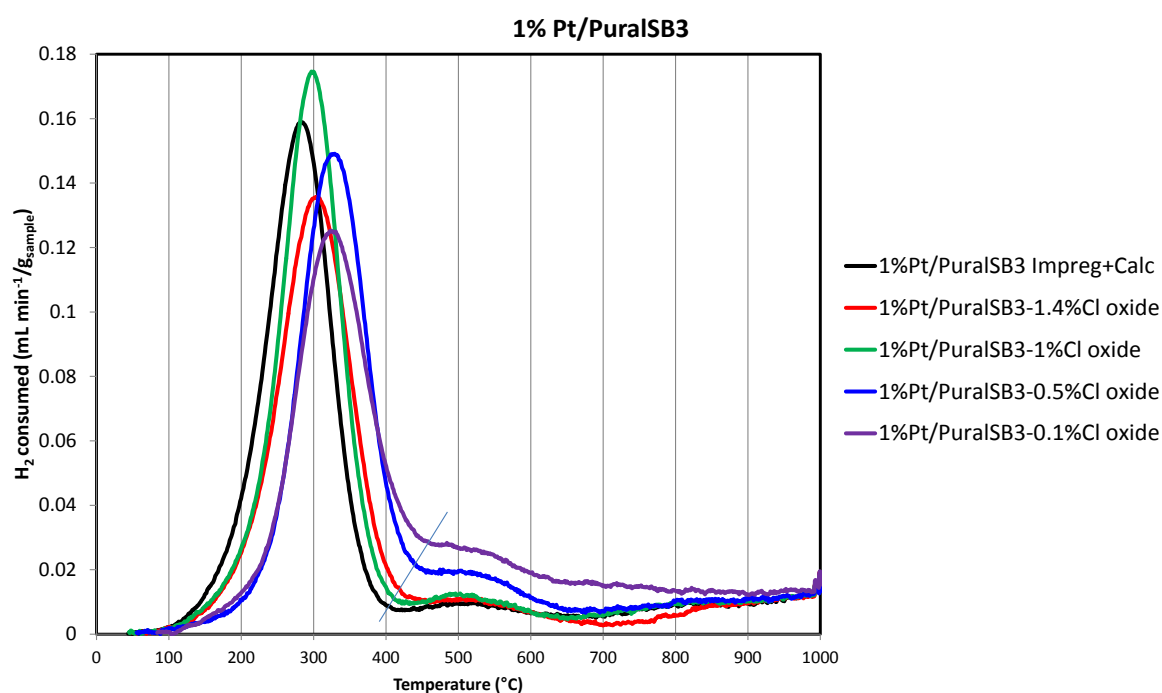


Figure 2-18 – TPR profile of PuralSB3 impregnated and calcined materials and oxide catalysts at 1%Pt loading and variable chlorine loadings, the thin blue line indicates the upper limit of peak integration.

As Figure 2-19 illustrates, no trend was found going from impregnated+calcined to oxide catalysts or with change in chlorine loading for either platinum loading. Moreover, the observable differences in peak maximum temperature and peak intensity, for each platinum loading, are within measurement uncertainty and thus not significant, as Figure 2-19 shows. The impact of chlorine (if there is one) cannot be evaluated by TPR (as performed at IFPEN) due to measurement uncertainty.

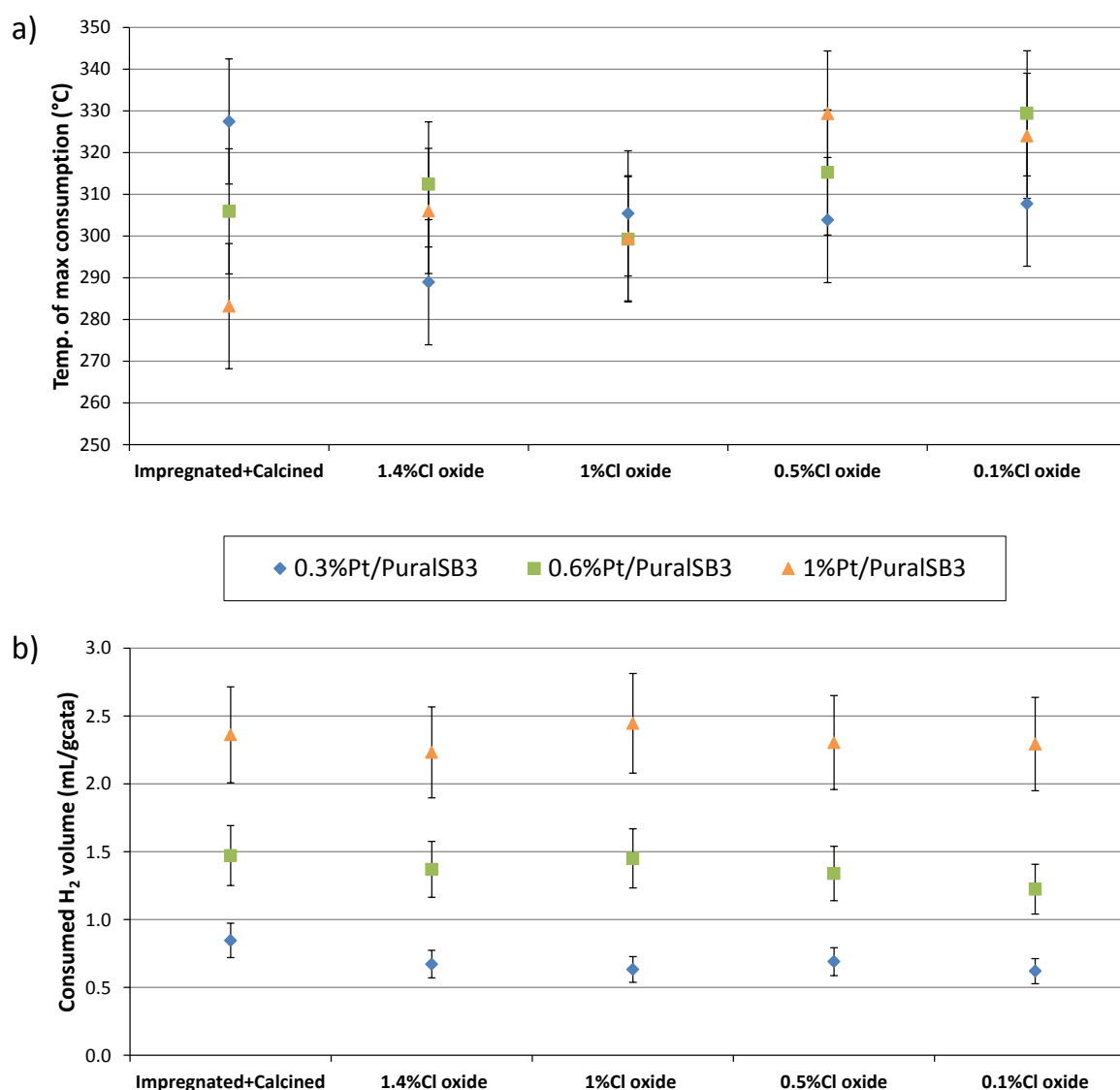


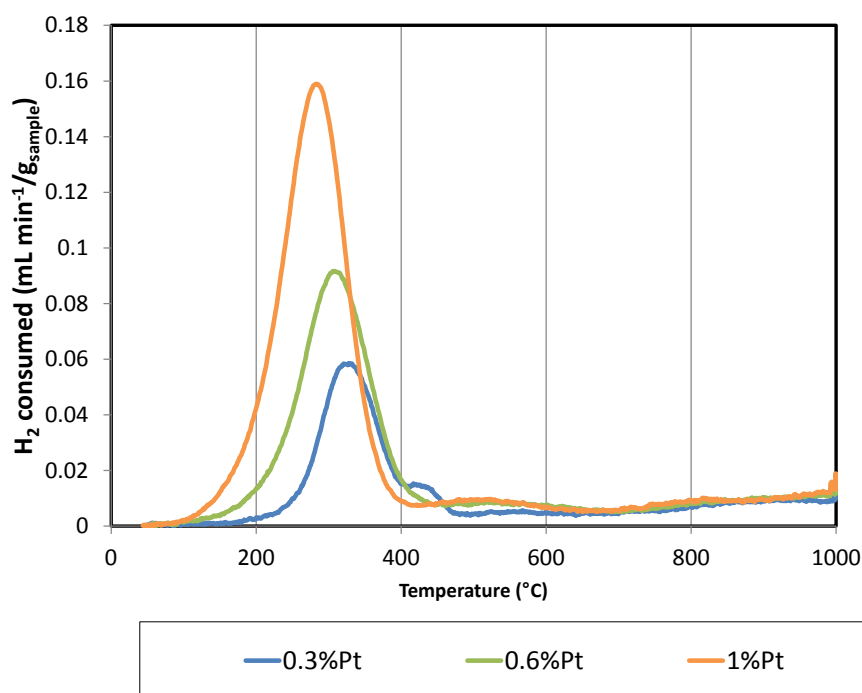
Figure 2-19 – Temperature of maximum H<sub>2</sub> consumption a) and consumed H<sub>2</sub> volume b) obtained for PuralSB3 impregnated and calcined materials and oxide catalysts by TPR.

#### 2.3.2.4.2 Effect of platinum loading

So, to investigate the effect of platinum loading, it was decided to use the TPR of impregnated and calcined PuralSB3 and TH100 materials for interpretation, as the impregnation and calcination steps are common for all catalysts (while there are two types of Cl tuning treatments) and those materials, of the same support, have similar chlorine contents.

The TPR profiles obtained for PuralSB3 and TH100 impregnated and calcined are shown in Figure 2-20.

a) PuralSB3 Impreg+Calc



b) TH100 Impreg+Calc

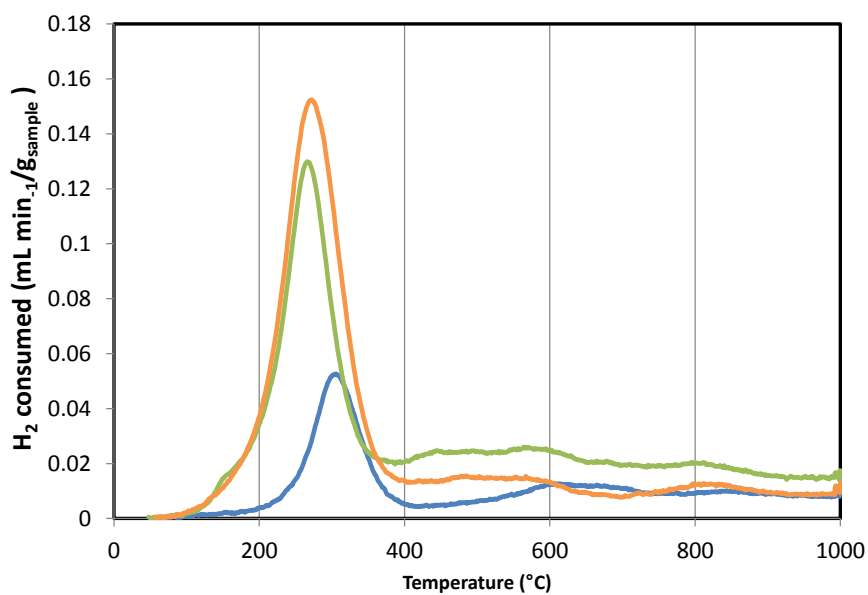


Figure 2-20 - TPR profiles of a) PuralSB3 and b) TH100 supported materials for the various platinum loadings investigated after impregnation and calcination.

For PuralSB3, a shoulder appears for 0.3%Pt/PuralSB3 Impreg+Calc, suggesting a bi-population of platinum nanoparticles with different sizes. This shoulder is not present in the TPR of 0.3%Pt/PuralSB3 oxides so it is not certain if it is relevant.



Consumed  $H_2$  volume, temperature of maximum  $H_2$  consumption and molar  $H_2$ /Pt ratio (calculated from the consumed volume) are represented in Figure 2-21. The values can be found in Table 2-14.

*Table 2-14 - Consumed  $H_2$  volume, temperature of maximum  $H_2$  consumption and molar  $H_2$ /Pt ratio of PuralSB3 and TH100 impregnated and calcined materials from TPR.*

Impreg+Calc	Consumed $H_2$ vol. (mL/g <sub>cata</sub> )	T. of max consumption (°C)	$H_2$ /Pt (molar)
0.3%Pt/PuralSB3	0.8±0.1	327±15	2.4±0.3
0.6%Pt/PuralSB3	1.5±0.2	306±15	1.9±0.3
1%Pt/PuralSB3	2.4±0.4	283±15	2.0±0.3
0.3%Pt/TH100	0.55±0.08	306±15	1.6±0.4
0.6%Pt/TH100	1.5±0.2	267±15	2.0±0.3
1%Pt/TH100	2.0±0.3	272±15	1.8±0.3

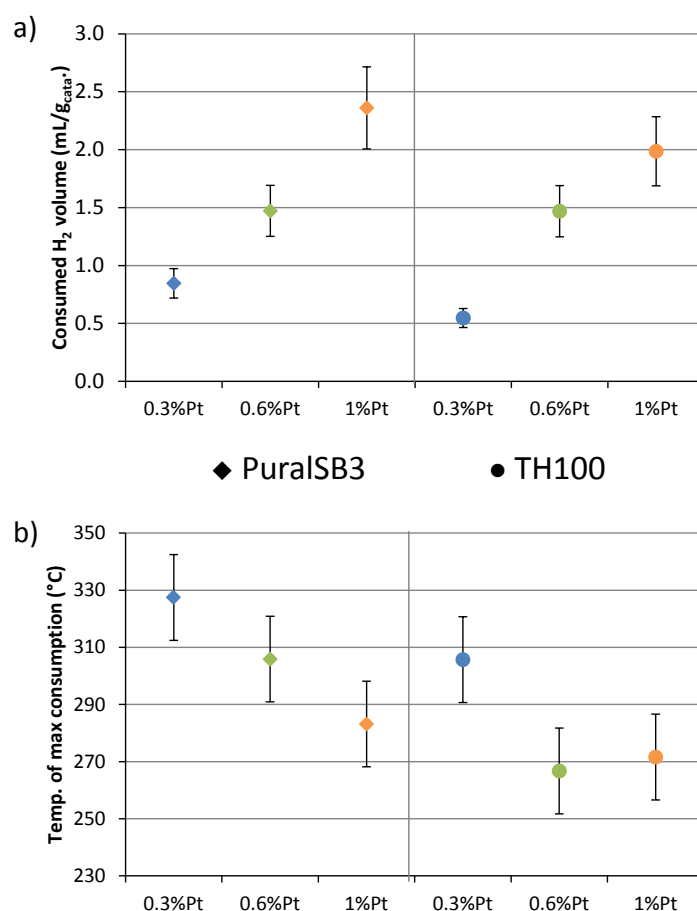


*Figure 2-21 - Consumed  $H_2$  volume a) and temperature of maximum  $H_2$  consumption b) of PuralSB3 and TH100 impregnated and calcined materials from TPR.*

Consumed  $H_2$  volume (per gram of catalyst) increases with platinum loading and the trend is similar for both supports. The slightly lower values for TH100 can be explained by these having slightly lower Pt content per gram of catalyst.

The temperature of maximum consumption decreases continuously with increasing platinum loading for PuralSB3. For TH100, that temperature decreases for 0.6 and 1%Pt and seems to reach a plateau at those loadings. Usually, higher reduction temperature, and thus lower reducibility, is associated with smaller platinum oxide particles' size with stronger metal-support interactions [205–207]. However, one can also invoke another effect such as the different anchoring strength of the alumina sites involved in the interaction with Pt, as discussed below.

One way to look at the results is to consider all anchoring sites are equal for each alumina and that Pt oxide particles can have different sizes. For TH100 the particles would be smaller at 0.3%Pt than at 0.6% and 1%Pt. At those higher loadings the anchoring sites are already saturated and further Pt aggregates on the sites forming larger particles that are more easily reduced. For PuralSB3, at 0.6%Pt the sites are not completely saturated but some aggregation starts to occur and for 1%Pt (assuming saturation at that point) larger particles are formed by aggregation of the *extra* deposited platinum. The saturation of sites occurring at lower Pt loading for TH100 indicates they are less numerous in this support.

Another is to assume that the size of the Pt oxide particles is similar for all systems. Thus these results could be interpreted as anchoring sites with decreasing interaction strength (probed by the temperature of maximum consumed H<sub>2</sub>) being progressively occupied with increasing platinum loading. For PuralSB3, the anchoring sites would be stronger than those of TH100 (according to the temperature of max. consumption). They are also more numerous on PuralSB3. For TH100, the stronger sites are saturated at 0.6%Pt and the *extra* platinum introduced then occupies weaker surface sites. For PuralSB3 the strong sites are not yet saturated at 0.6%Pt.

Either way, interpretation is complex because the resulting data do not depend only on the initial metal oxide species. As H<sub>2</sub> consumption is measured over a temperature range while platinum is being reduced, the technique concerns all the intermediate states between the initial oxide and the final reduced metal.

The morphology of the two alumina supports (section 3.1.1) may result in different amounts of “anchoring sites”/nm<sup>2</sup>, with TH100 having less. PuralSB3's crystallites are expected to expose more edges, corners and possibly facets with higher Miller plane index (stepped and/or kinked surfaces) than TH100. Such edges, corners and facets are expected to have

stronger defective aluminium sites with higher unsaturated coordination [42] which may strongly stabilize the platinum oxide particles. The role of such edges on chlorine exchange and reduced Pt nanoparticles will be studied in detail in the next chapters. Nevertheless, it cannot be excluded that they already play a key role on the oxide complexes.

#### **2.3.2.4.3 Oxide stoichiometry**

The last piece of information TPR can provide is the  $H_2/Pt$  ratio that can be used to infer on the nature of the supported metal oxide when compared to the stoichiometry of the reduction reaction of a given metal oxide.

On the choice of “model” reaction for comparison of stoichiometry, chlorinated platinum oxide species are not considered for the moment for simplicity sake. A classical choice for initial oxide is  $PtO_2$  or  $PtO$ , leading to Equation 2-25 and Equation 2-27 presuming adsorption of hydrogen on the reduced platinum at the end of the reduction process, and Equation 2-26 and Equation 2-28 if there is no adsorption.



Looking at Table 2-14, the experimental  $H_2/Pt$  ratios fall mostly between 1.5 and 2. For 0.3%Pt/PuralSB3 impreg+calc the ratio is closer to 2.5 as the peak shoulder was included in the peak integration. Except for that sample, the  $H_2/Pt$  ratios are mostly equivalent, within uncertainty. By comparison with the equations above,  $PtO_2$  seems a reasonable oxide model with or without hydrogen adsorption.

# **Chapter 3**

## **Location and environment of $\gamma$ -alumina hydroxyl groups and chlorine**

In this chapter the alumina supports and acidified alumina samples are studied with the goal of characterizing the alumina crystallite's morphology and its surface hydroxyl groups so as to infer on the chlorination mechanism and on the preferred location of chlorine atoms on the alumina surface.

These results were the object of a published priority communication and are presented here in the pre-print version of the publication followed by the respective supporting information. The references herein are listed at the end of the article.

Batista, A. T. F.; Wisser, D.; Pigeon, T.; Gajan, D.; Diehl, F.; Rivallan, M.; Catita, L.; Gay, A.-S.; Lesage, A.; Chizallet, C.; Raybaud, P. *Beyond  $\gamma$ -Al<sub>2</sub>O<sub>3</sub> crystallite surfaces: the hidden features of edges revealed by Solid-State <sup>1</sup>H NMR and DFT calculations*. *Journal of Catalysis* 378 (2019), 140-143 (DOI: 10.1016/j.jcat.2019.08.009)

# Beyond $\gamma$ -Al<sub>2</sub>O<sub>3</sub> Crystallite Surfaces: the Hidden Features of Edges Revealed by Solid-State <sup>1</sup>H NMR and DFT Calculations

Ana T. F. Batista<sup>a</sup>, Dorothea Wisser<sup>a,b</sup>, Thomas Pigeon<sup>a</sup>, David Gajan<sup>b</sup>, Fabrice Diehl<sup>a</sup>, Mickael Rivallan<sup>a</sup>, Leonor Catita<sup>a</sup>, Anne-Sophie Gay<sup>a</sup>, Anne Lesage<sup>b</sup>, Céline Chizallet<sup>a</sup>, and Pascal Raybaud<sup>a,\*</sup>

<sup>a</sup> IFP Energies nouvelles, Rond-point de l'échangeur de Solaize, 69360 Solaize (France)

<sup>b</sup> Centre de RMN à Très Hauts Champs, Université de Lyon (CNRS/ENS Lyon/UCB Lyon 1), 69100 Villeurbanne (France)

Corresponding author: Pascal Raybaud

## Abstract

Elucidating the nature of high surface area gamma alumina sites is of great interest for numerous catalytic applications. In this work, the structural and spectroscopic features of edge sites are unravelled thanks to density functional theory (DFT) calculations combined with high field <sup>1</sup>H MAS NMR of two high surface area alumina samples exhibiting distinct morphologies. DFT chemical shift calculations were carried out for relevant surface models with different hydration degrees. However, the best assignment is achieved by considering the first DFT model representing the hydroxylated edges located at the intersection of (110) and (100) alumina facets. The sharp <sup>1</sup>H NMR peak at 0 ppm corresponds to  $\mu_1$ -OH groups which are located on this edge and are free from hydrogen bonding. Moreover, we show that these edge sites are the most reactive with respect to chlorine exchange.

**Keywords:** alumina, density functional theory, edge, hydroxyls, NMR spectroscopy

## 1. Introduction

The gamma polymorph of  $\text{Al}_2\text{O}_3$  is used in numerous industrial applications thanks to its remarkable catalytic and adsorptive properties[1] which have been extensively studied by experimental and theoretical approaches.[2–9] In particular, surface hydroxyl groups, responsible for Brønsted acidity, have been characterized by infra-red (IR) spectroscopy [2,3,10–12] and by  $^1\text{H}$  solid-state nuclear magnetic resonance (NMR) spectroscopy.[12–16] Moreover, DFT calculations[5] enabled the refinement of the empirical assignment of the main IR bands thanks to the determination of the hydration of the three main exposed  $\gamma$ - $\text{Al}_2\text{O}_3$  surfaces:[17] (110), (100) and (111). In  $^1\text{H}$  NMR work, the use of high fields and fast magic angle spinning (MAS) provided improved spectral resolution, revealing various, partially resolved,  $^1\text{H}$  signals. Three main spectral regions were identified at around 0 ppm, 1-3 ppm and 3-5 ppm, respectively assigned to non-H-bonded  $\mu_1\text{-OH}$ ,  $\mu_2\text{-OH}$  and  $\mu_3\text{-OH}$ . These hydroxyls are connected to one, two or three Al atoms exhibiting different coordination ( $\text{Al}_{\text{IV}}$ ,  $\text{Al}_{\text{V}}$ ,  $\text{Al}_{\text{VI}}$ ).[15,16] Also, broad signals above 5 ppm were associated with hydrogen bond donor species.[16]

However, to go beyond the current knowledge of high surface aluminas, atomic scale insights into the nature and location of the hydroxyls that originate each signal are required. In particular, considering extended surfaces only to interpret NMR data overlooks that  $\gamma$ - $\text{Al}_2\text{O}_3$  crystallites are finite nano-objects exhibiting various morphologies. Like metallic nanoparticles with stepped surfaces and edges that provide low coordination sites active in catalysis,[18–21] edge architectures present on alumina crystallites should harbour original hydroxyl and Al sites distinct from those on such surfaces. In recent reviews, Busca points to the likely role of edges and corners on alumina's reactivity, which are suspected to be the location of the strongest Lewis acid sites bearing hydroxyl groups more resistant to dehydration.[8,22]

Here, the interpretation of the proton NMR spectra of  $\gamma\text{-Al}_2\text{O}_3$  is revisited, providing new insights into the nature and location of the hydroxyls in order to refine our current structural knowledge of high surface area aluminas.  $^1\text{H}$  NMR spectra were recorded for two  $\text{Al}_2\text{O}_3$  samples of different morphologies, and it is shown by chemical shift DFT calculations that considering alumina facets only leads to an incomplete description of the spectra. This

challenge is solved by establishing edge models highlighting the selective chlorination of the edge sites.

## 2. Materials and methods

Two relevant high surface alumina samples prepared from two commercial boehmites are considered, PuralSB3 and TH100 (Sasol), labelled *P-egg* and *T-flat* respectively, exhibiting different high BET surfaces (S.I.S1). Their characterization by high-resolution transmission electron microscopy (HR-TEM) suggests that T-flat crystallites are larger and have a better defined and more parallelepipedic platelet-like morphology than P-egg's, which appear to have a round shape (S.I.S1). Chlorinated alumina samples were prepared by exposing alumina to an HCl solution (3.5%<sub>w</sub>Cl/g<sub>dry alumina</sub>) for 45 minutes, followed by drying and calcination under dry air at 520°C. After thermal treatment under H<sub>2</sub> for 2h at 500°C (ramp 5°C/min) and rotor packing under inert atmosphere, quantitative solid-state <sup>1</sup>H NMR spectra were acquired. NMR spectra were obtained on a SB Bruker Avance III 800 (800 MHz <sup>1</sup>H resonance frequency, 18.8 T) spectrometer using a zirconia 2.5 mm rotor at 30 kHz MAS. To ensure a quantitative analysis <sup>1</sup>H NMR spectra were recorded using a DEPTH[23–25] sequence for probe background suppression and pre-scan delays were set to five times the <sup>1</sup>H longitudinal relaxation time (T<sub>1</sub>). Chemical shifts were referenced relative to adamantane. Spectral deconvolution was done using DMFit[26]. These spectra recorded at high magnetic field and relatively fast MAS reveal the surface OH signals and subtle changes in chemical shifts between the two different types of alumina (Figure 1 a).

To help for the interpretation of NMR experiments, chemical shifts (S.I.S2.3.) were calculated by using the linear response approach[27,28] within the PBE-dDsC exchange correlation functional[29,30] and PAW pseudopotentials[31] with an energy cut off of 400 eV as implemented in the VASP code.[32,33] The average of the isotropic chemical shielding (σ) of each proton on a TMS (tetramethylsilane) model (a single molecule surrounded by vacuum) was used as reference to calculate the isotropic chemical shift (δ) of the protons of the various hydroxyls of the alumina surfaces or at the edges.

$$\delta_{iso} = \sigma_{iso} - \sigma_{ref} \quad (1)$$



For that purpose, relevant periodic models of alumina (110), (100) and (111) surfaces and (110)-(100) edges have been constructed and optimized for various thermodynamically relevant hydration coverages depending on the experimental (T, p) analytical conditions (S.I.S2.). Geometry optimizations were performed using a conjugate-gradient algorithm and convergence criterion on forces of  $0.01 \text{ eV } \text{\AA}^{-1}$ .

### 3. Results and Discussion

$^1\text{H}$  NMR spectra of P-egg and of T-flat (Figure 1 a) present the main features expected for  $\gamma\text{-Al}_2\text{O}_3$ : a resolved signal at around 0 ppm, intense and well-defined peaks in the 1-3 ppm range and broad components ranging from 3-7 ppm. Moreover, the spectra of the two aluminas are clearly distinguished. The most remarkable difference is that the higher-field signal (at respectively -0.1 and -0.4 ppm) is much more intense for P-egg than for T-flat (12% vs 4% of the total  $^1\text{H}$  signal from spectral deconvolution, Table S2). The 1-3 ppm region is also distinguishable: for P-egg two main signals (1.6 and 2.2 ppm) are observed while for T-flat only one is (1.2 ppm), albeit some shoulders indicating other contributions. Lastly, the contribution of the broad signals ranging from 3-7 ppm is significantly more intense in the T-flat spectrum.

In order to rationalize these experimental results, chemical shifts were calculated (Figure 1 b and S.I.S2.3) for hydrated surface models of the three main exposed  $\gamma\text{-Al}_2\text{O}_3$  surfaces[17] (110), (100) and (111) as defined in previous DFT works [4,5,7] For each surface, several hydration degrees were considered (S.I.S2.1.) in order to better represent the alumina samples after thermal treatment, (Figure S8). In the experimental conditions,  $10^{-4} < P(\text{H}_2\text{O}) < 10^{-6}$  bar and  $700\text{K} < T < 800\text{K}$ , the (110) surface exhibits 3.0 OH/nm<sup>2</sup> and 9.0 OH/nm<sup>2</sup>, the (111) surface 12.3 OH/nm<sup>2</sup>, while the (100) surface is dehydrated.

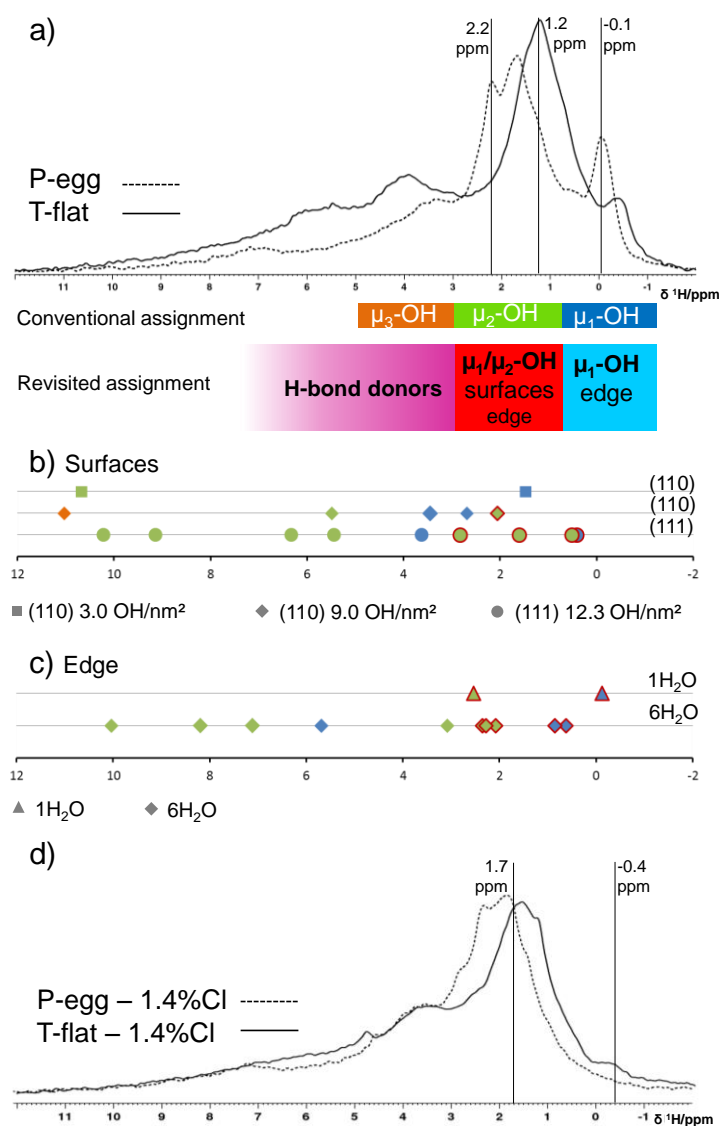


**Figure 1.** a)  $^1\text{H}$  MAS NMR spectra of two aluminas with different morphologies, P-egg and T-flat (800 MHz, 30 kHz MAS). The conventional assignment and the revisited one are represented below. b)  $^1\text{H}$  chemical shifts calculated by DFT for hydroxyls, colour coded according to the type of OH group given in the conventional assignment, for three surface models; non H-bond donor hydroxyls are highlighted by red outline. c)  $^1\text{H}$  chemical shifts calculated by DFT for hydroxyls for the (110)-(100) edge model at two hydration degrees. d)  $^1\text{H}$  MAS NMR spectra (800 MHz, 30 kHz MAS) of chlorinated samples.

First, it can be noted that most of the hydroxyls on these surfaces are involved in hydrogen bonding (Tables S9, S10, S11). Almost half of them are H-bond donors, resulting in high chemical shifts such as several  $\mu_2\text{-OH}$  appearing at  $>5$  ppm. In this case, the chemical shift correlates with hydrogen bond length (Figures S11 and S12), [16,34–36] leading to large variations in  $\delta$ . Experimentally, H-bond donors are not expected to provide well defined signals such as the ones observed up to 3 ppm. [36]

Thus, we observe a poor correspondence between the previously proposed range and the simulated  $^1\text{H}$  chemical shifts which do not explain the signal below 0 ppm, expected to correspond to  $\mu_1\text{-OH}$ . [14,15] Contributions calculated at 0.4 and 0.8 ppm from  $\mu_1\text{-OH}$  and  $\mu_2\text{-OH}$  (respectively) of the (111) surface are found, while the classical assignment does not expect  $\mu_2\text{-OH}$  in this range. In addition, no  $\mu_3\text{-OH}$  are predicted in the 3-5 ppm region. Overall, these results show that the resonances observed in the experimental  $^1\text{H}$  NMR spectra of these  $\gamma\text{-Al}_2\text{O}_3$  samples cannot be fully interpreted by considering only their crystalline surfaces. This trend holds true for any hydration degree (S.I.S2.3).

To go beyond, another site architecture must be conceived. Apart from the empirical model proposed by Busca,[8] no atomistic model of alumina edge was previously reported in the literature. Thus, a novel model for the (110)-(100) edge was determined (Figure 2 a) based on a nano-rod structure (S.I.S2.2) resulting from the cleavage of the alumina bulk[37] in the two directions perpendicular to the (110) and (100) surfaces. This induces two edge-terminations, one exposing Al atoms (here called Al-edge) and the other exposing O atoms (O-edge). The Al-edge is constituted of one upper row of  $\text{Al}_{\text{III}}$  atoms (also three-fold coordinated on the (110) surface) and one lower row of  $\text{Al}_{\text{III}}$  atoms that correspond to  $\text{Al}_{\text{IV}}$  on the (110) surface. The O-edge exhibits a row of alternating  $\text{O}_{\text{II}}$  and  $\text{O}_{\text{III}}$ , both formally  $\text{O}_{\text{III}}$  on the (110) surface. These rows of atoms on both edges will be referenced to as edge sites.

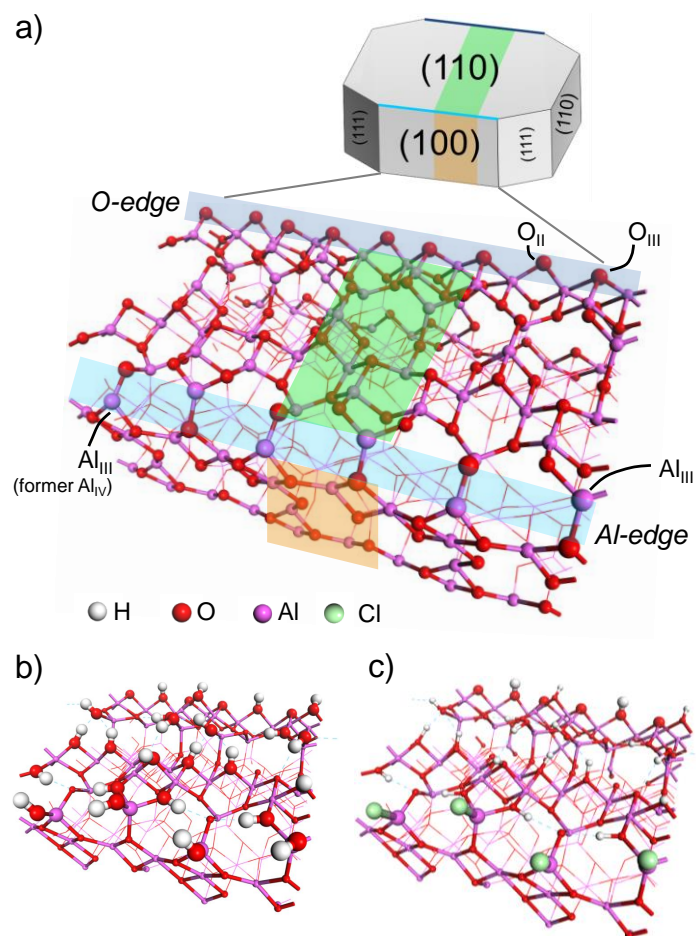


*Figure 2. a) Alumina platelet scheme[5] and dehydrated edge model corresponding to two possible edge terminations (blue) between the (110) (green, top) and the (100) (orange, sides) surfaces. Edge sites are depicted by bigger balls. b) hydrated edge model with 6H<sub>2</sub>O and c) chlorinated edge model constructed from the 6H<sub>2</sub>O hydrated model by exchanging Al-side  $\mu_1$ -OH. Blue dashed lines indicate hydrogen-bonds (bond length's threshold of 2.5 Å).*

The systematic study of the hydration state of the nano-rod (and the corresponding edges) shows that water is most strongly stabilized at the edge sites, rather than on the facet sites. For the adsorption of the first water molecule per unit cell of simulation, this leads to the formation of one  $\mu_2$ -OH, the H<sup>+</sup> bonding to the O<sub>II</sub> atom on the O-edge, and of one  $\mu_1$ -OH, the OH<sup>-</sup> bonding to the Al<sub>III</sub> on the lower row on the Al-edge that relaxes into a tetragonal geometry (Table S7). Both these hydroxyls are not involved in hydrogen bonding. The corresponding adsorption energy is -436 kJ.mol<sup>-1</sup>, which is far greater than usual adsorption energies reported on the alumina surfaces,[4] and is consistent with the chemical intuition that the reactivity of Lewis Al edge sites should be greater.[8] Such a configuration is a priori striking when thinking in terms of water dissociation, because the hydroxyl and the corresponding proton are not lying on the same kind of edge. However, one should consider

that experimentally, such low hydration states are obtained upon dehydration of the surface sites, making it possible to leave at the surface distant OH and H groups in the end, after recombination of other OH and H pairs. When more than two water molecules are adsorbed per unit cell of simulation, all the “edge sites” are saturated and the near edge sites on the (110) top surface of the nano-rod start being occupied (Figure 2 b), while the (100) facet of the rod remains dehydrated. These “near edge” sites exhibit a H-bond network identical to that of the surface models. In the conditions of thermal treatment ( $10^{-4} < P(\text{H}_2\text{O}) < 10^{-6}$  bar and  $700\text{K} < T < 800\text{K}$ ), among the multiple equally stable hydration degrees (S.I. Figure S10), we choose two relevant cases: one and six adsorbed water molecules per pair of edges.

The calculated  $^1\text{H}$  chemical shifts for the (110)-(100) edge with one and six adsorbed water molecules are represented in Figure 1 c).  $\mu_1$  and  $\mu_2$  hydroxyls on edge sites appear in the expected  $\delta$  range:  $\approx 0$  ppm and  $\approx 2$  ppm respectively. These OH are not only free from hydrogen bonding, but also isolated from other neighbouring hydroxyls. For 6  $\text{H}_2\text{O}$  molecules, hydroxyls with  $\delta > 3$  ppm are located on near edge sites and are H-bond donors, as the red outline indicates.

With this edge model a significantly improved correlation between experimental and calculated chemical shifts is achieved, especially for the sharp peak at  $\approx 0$  ppm. Thus, this peak corresponds mostly to isolated  $\mu_1$ -OH located on the edges of alumina crystallites, which are free from hydrogen bonding. While the contribution of some free and H-bond acceptor species on the (111) surface cannot be ruled out, their contribution to the signal is minor, as discussed ahead. The 1-3 ppm region is expected to result from non-isolated  $\mu_1$ -OH and  $\mu_2$ -OH that are free from H-bonds or H-bond acceptors located on the edges and on the surfaces of the crystallites. The fact that in average, the  $\mu_2$ -OH sites are much more represented in this region with respect to the 0-1 ppm region, is in agreement with  $^1\text{H}$ - $^{27}\text{Al}$  RESPDOR experiments by Taoufik et al..[15] While not much insight was gained into the 3-5 ppm broad signal, its empirical assignment to  $\mu_3$ -OH is strongly questioned. Indeed, for the hydration degree of our samples, only two  $\mu_3$ -OH were found in the models of interest (one for (110) 12.0 OH/nm<sup>2</sup> and other for edge 6 $\text{H}_2\text{O}$ ) and both are hydrogen bond donors with  $\delta > 5$  ppm (7.9 and 14.2 ppm, respectively). Moreover,  $\mu_1$ -OH and  $\mu_2$ -OH species acting as hydrogen bond donors are impact the 3-5 ppm broad signal. Lastly, broad signals with  $\delta > 5$

ppm are thought to correspond to hydroxyls involved in the hydrogen bond network of the surfaces as hydrogen bond donors.

With this improved assignment, it is now possible to rationalize the impact the of alumina nano-crystallite morphology on the  $^1\text{H}$  NMR spectra. As mentioned above, P-egg crystallites are rounded and smaller than those of T-flat, which are more parallelepipedic. Thus, P-egg presents a higher edge to surface ratio than T-flat, which explains the relative intensities of the  $\approx 0$  ppm peaks of edge  $\mu_1\text{-OH}$ : 12% and 4% of  $^1\text{H}$  signal intensity for P-egg and T-flat respectively (Table S2). In the 1-3 ppm region, the  $\delta$  value of the most intense peak depends on the sample which is a strong indication of different proportions of exposed surface types for each alumina. Indeed, the electron diffraction analysis (Figure S4) suggests that the (111) termination is more exposed in T-flat crystallites than in P-egg's. Finally, the large signal for  $\delta > 3$  ppm is more intense for T-flat, which is explained by a H-bond network between hydroxyls that is more developed on the extended surface planes of T-flat than on P-egg.

To get further insights into the surface structure of P-egg and T-flat, the reactivity of the alumina hydroxyls were probed with chlorine. Chlorinated aluminas are used in many catalytic processes[38] but Cl can also be used as a probe for  $\mu_1\text{-OH}$ . [12,14,39] Chlorinated samples were prepared so as to have 0.5 and 1.4%<sub>w/w</sub>Cl deposited on each alumina (referred as P-egg-x%Cl and T-flat-x%Cl with x=0.5, 1.4). The effect of chlorine on the  $^1\text{H}$  NMR spectra is clearly different for both aluminas (Figure 1 d and Figure S6). For P-egg-1.4%Cl, the 0 ppm signal disappears completely, as previously reported,[12,14] while the remaining part of the spectrum is less perturbed. For T-flat-1.4%Cl, not only does the 0 ppm signal not disappear completely, but also an intensity increase is observed in the 3-5 ppm region, associated to a significant intensity decrease for  $\delta > 5$  ppm (Table S2). For T-flat-0.5%Cl only the 0 ppm signal decreased, while the remaining part of the spectrum is unchanged.

According to the DFT OH/Cl exchange energies (S.I. S2.5, Figure 2 c), the edge  $\mu_1\text{-OH}$  sites are predominantly exchanged with chlorine out of all the considered hydroxyls. The subsequent exchanged hydroxyls would be the  $\mu_1\text{-OH}$  of the (110) surface and after that only the  $\mu_1\text{-OH}$  and  $\mu_2\text{-OH}$  sites of the (111) surface. Since the  $\approx 0$  ppm peak completely disappears for P-egg-1.4%Cl, and no impact is observed on the remaining parts of the spectrum, it is believed that only the  $\mu_1\text{-OH}$  located on the edges are exchanged with chlorine at 1.4%Cl and not those of the surfaces. For T-flat-1.4%Cl, since the peak at  $\approx 0$  ppm does not fully disappear while the

3-5 ppm and  $\delta > 5$  ppm regions are perturbed, not only the edge  $\mu_1$ -OH are exchanged but also surface hydroxyls (most likely on the (110)), disturbing the H-bond network. The small signal remaining at  $\approx 0$  ppm after chlorination should correspond to the (111) surface  $\mu_1$  and  $\mu_2$  hydroxyls. Just as the electron diffraction analysis, the NMR results also suggest that the (111) surface is relatively more exposed in T-flat crystallites than in P-egg's. However, for T-flat-0.5%Cl, chlorine exchange occurs mainly on the edges because the spectral region at  $\delta > 3$  ppm is unchanged (Table S2). This implies that the number of edge  $\mu_1$ -OH of T-flat is not sufficient to exchange 1.4% Cl. By contrast, on P-egg the number of edge sites is enough since the spectral regions at  $\delta > 3$  ppm are weakly perturbed.

#### 4. Conclusion

The construction of the first DFT model of  $\gamma$ -Al<sub>2</sub>O<sub>3</sub> crystallite (110)-(100) edge has allowed a refined <sup>1</sup>H NMR peak assignment. It was found that the sharp peak at 0 ppm corresponds mostly to  $\mu_1$ -OH located on the edges of the crystallites that are isolated and free from hydrogen bonding. These hydroxyls are also the most favourably exchanged with chlorine, which can be considered as a selective probe of alumina edges. Overcoming the simple empirical assignment, the 1-3 ppm region corresponds to signals from not only  $\mu_2$ -OH but also from  $\mu_1$ -OH located either on the surfaces or on the edge, and that are either H-bond acceptors or free hydroxyls. Moreover, hydroxyls that are hydrogen bond donors are abundant on the surfaces and contribute to the high chemical shift broad signals. Hopefully, this novel alumina edge model and the improved assignment open new perspectives to further explore the potential of the edge sites present in industrially relevant high surface alumina crystallites.

#### Acknowledgements

A.T.F.B. thanks A.-L. Taleb for her collaboration in HR-TEM analysis and E. Rosati, C. Guegan and C. Mancina for their contribution to sample preparation. M. Marsman (University of Vienna) is acknowledged for advice with respect to chemical shift calculations, and K. Larmier for preliminary computational investigations. Calculations were performed using HPC resources from GENCI-CINES (Grant A0020806134) and from IFP Energies nouvelles. TGIR RMN THC (FR3050 CNRS) is acknowledged for the NMR characterizations.

This work was funded by IFPEN and financial support from Equipex contract ANR-10-EQPX-47-01 is acknowledged. This work was supported by the LCR "CARactérisation des Matériaux pour l'Energie" (CARMEN), IFPEN/CNRS/UCBL/ENS Lyon/UNISTRA/Sorbonne Université, and is part of the "RatiOnAl Design for CATalysis" (ROAD4CAT) industrial chair, project IDEXLYON funded by the French National Research Agency (ANR-16-IDEX-0005).

## References

- [1] P. Euzen, P. Raybaud, X. Krokidis, H. Toulhoat, J.-L. Le Loarer, J.-P. Jolivet, C. Froidefond, in: F. Schuth, K. S. W. Sing, J. Weitkamp (Eds.), Handbook of Porous Solids, Wiley-VCH Verlag GmbH, Weinheim, Germany, 2002, p. 1591.
- [2] H. Knözinger, P. Ratnasamy, Catal. Rev. - SCI. Eng. 17 (1978) 31.
- [3] G. Busca, V. Lorenzelli, G. Ramis, R.J. Willey, Langmuir 9 (1993) 1492.
- [4] M. Digne, P. Sautet, P. Raybaud, P. Euzen, H. Toulhoat, J. Catal. 211 (2002) 1.
- [5] M. Digne, P. Sautet, P. Raybaud, P. Euzen, H. Toulhoat, J. Catal. 226 (2004) 54.
- [6] J.H. Kwak, J. Hu, D. Mei, C.-W. Yi, D.H. Kim, C.H.F. Peden, L.F. Allard, J. Szanyi, Science 325 (2009) 1670.
- [7] R. Wischert, C. Copéret, F. Delbecq, P. Sautet, Angew. Chem. Int. Ed. 50 (2011) 3202.
- [8] G. Busca, Catal. Today 226 (2014) 2.
- [9] M. Lagache, K. Larmier, E. Jolimaitre, K. Barthelet, C. Chizallet, L. Favergeon, M. Pijolat, J. Phys. Chem. C 121 (2017) 16770.
- [10] C. Morterra, G. Magnacca, Catal. Today 27 (1996) 497.
- [11] A. Zecchina, E. Escalona Platero, C. Otero Arean, Inorg. Chem. 27 (1988) 102.
- [12] A. Kytokivi, M. Lindblad, J. Chem. Soc. Faraday Trans. 91 (1995) 941.
- [13] E. C. DeCanio, J. C. Edwards, J. W. Bruno, J. Catal. 148 (1994) 76.
- [14] J. Hietala, A. Root, P. Knuuttila, J. Catal. 150 (1994) 46.
- [15] M. Taoufik, K.C. Szeto, N. Merle, I. Del Rosal, L. Maron, J. Trebosc, G. Tricot, R.M. Gauvin, L. Delevoye, Chem. Eur. J. 20 (2014) 4038.



- [16] M. Delgado, F. Delbecq, C.C. Santini, F. Lefebvre, S. Norsic, P. Putaj, P. Sautet, J.-M. Basset, *J. Phys. Chem. C* 116 (2012) 834.
- [17] P. Nortier, P. Fourre, A.M. Saad, O. Saur, J.C. Lavalley, *Appl. Catal.* 61 (1990) 141.
- [18] M. Mavrikakis, P. Stoltze, J.K. Nørskov, *Catal. Lett.* 64 (2000) 101.
- [19] D.W. Blakely, G.A. Somorjai, *J. Catal.* 42 (1976) 181.
- [20] G. A. Somorjai, D. W. Blakely, *Nature* 258 (1975) 580.
- [21] R.A. van Santen, M. Neurock, S.G. Shetty, *Chem. Rev.* 110 (2010) 2005.
- [22] Guido Busca, *Progress in Materials Science* 104 (2019) 215.
- [23] M.R. Bendall, D.T. Pegg, *Magn. Reson. Med.* 2 (1985) 91.
- [24] D.G Cory, W.M Ritchey, *J. Magn. Reson.* 80 (1988) 128.
- [25] M Robin Bendall, Roy E Gordon, *J. Magn. Reson.* 53 (1983) 365.
- [26] D. Massiot, F. Fayon, M. Capron, I. King, S. Le Calvé, B. Alonso, J.-O. Durand, B. Bujoli, Z. Gan, G. Hoatson, *Magn. Reson. Chem.* 40 (2002) 70.
- [27] C.J. Pickard, F. Mauri, *Phys. Rev. B* 63 (2001) 245101.
- [28] J.R. Yates, C.J. Pickard, F. Mauri, *Phys. Rev. B* 76 (2007) 24401.
- [29] J.P. Perdew, K. Burke, M. Ernzerhof, *Phys. Rev. Lett.* 77 (1996) 3865.
- [30] S.N. Steinmann, C. Corminboeuf, *J. Chem. Theory Comput.* 7 (2011) 3567.
- [31] G. Kresse, D. Joubert, *Phys. Rev. B* 59 (1999) 1758.
- [32] G. Kresse, J. Hafner, *Phys. Rev. B* 49 (1994) 14251.
- [33] G. Kresse, J. Furthmüller, *Comp. Mater. Sci.* 6 (1996) 15.
- [34] M. Hunger, *Catal. Rev. - SCI. Eng.* 39 (1997) 345.
- [35] V. M. Gun'ko, V. V. Turov, *Langmuir* 15 (1999) 6405.
- [36] C. Chizallet, G. Costentin, H. Lauron-Pernot, M. Che, C. Bonhomme, J. Maquet, F. Delbecq, P. Sautet, *J. Phys. Chem. C* 111 (2007) 18279.
- [37] X. Krokidis, P. Raybaud, A.-E. Gobichon, B. Rebours, P. Euzen, H. Toulhoat, *J. Phys. Chem. B* 105 (2001) 5121.

- [38] C. Marcilly, in: C. Marcilly (Ed.), *Acido-basic catalysis: Application to refining and petrochemistry*, Editions Technip, Paris, 2006, p. 101.
- [39] M. Digne, P. Raybaud, P. Sautet, D. Guillaume, H. Toulhoat, *J. Am. Chem. Soc.* 130 (2008) 11030.

## Supporting Information

### S1. Alumina samples characterization

X-ray diffraction was performed on a PANalytical X'Pert Pro diffractometer with a copper anode ( $K\alpha=0.15402$  nm) and a X'célerator detector, scanning an angle range of 5 to 72° 2 $\theta$  (Figure S1)

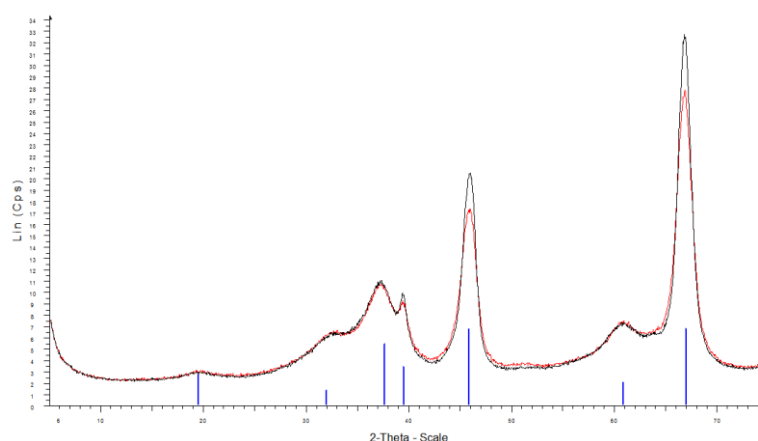


*Figure S1. XRD diffractograms of P-egg and T-flat (red-P-egg; black-T-flat; blue- $\gamma$ - $\text{Al}_2\text{O}_3$  reference ICDD n° 00-010-0425).*

$\text{N}_2$  physisorption was done using a Micromeritics ASAP 2420 equipment, samples were pre-treated at 350°C for 3h under vacuum.

Hg porosimetry was done using a Micromeritics Autopore IV equipment, samples were pre-treated at 250°C for 3h. The corresponding results, BET surface, mesoporous volume and mesopore diameter evaluated at half the mesoporous volume, are reported in Table S1.

*Table S1. Properties of P-egg and T-flat aluminas given by  $\text{N}_2$  physisorption and Hg porosimetry.*

	SBET ( $\text{m}^2\text{g}^{-1}$ )	DVmeso/2 (nm)	Vmeso ( $\text{mL/g}$ )
P-egg	183 $\pm$ 9	9.8 $\pm$ 0.2	0.49 $\pm$ 0.02
T-flat	149 $\pm$ 7	15.1 $\pm$ 0.3	0.60 $\pm$ 0.03

High resolution Transmission Electron Microscopy (HR-TEM) images in Bright field mode and nanoarea electron diffraction patterns were acquired on a JEOL JEM 2100F microscope.

For the P-egg sample (Figure S2), the following crystallite dimensions (from about 30 measurements) were measured:

- Length between 4 and 16 nm (average 12.5 nm)
- Width between 4 and 11 nm (average 6 nm)
- Thickness approximately between 4 and 6 nm

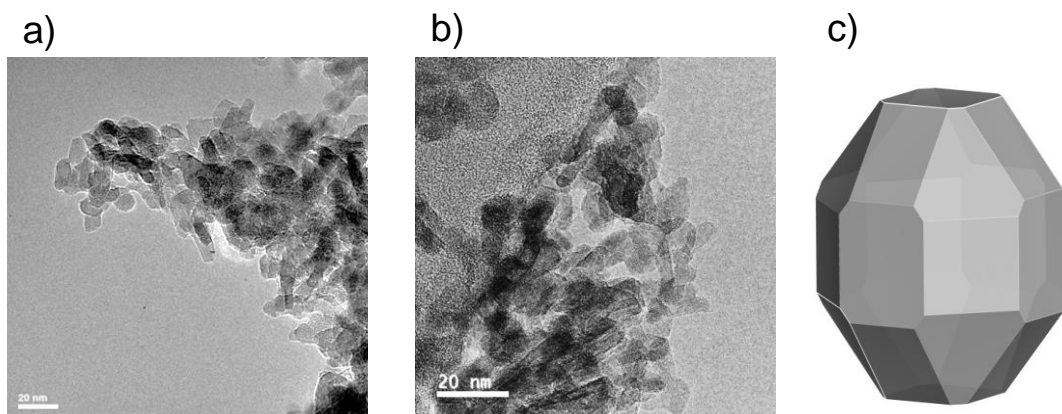


*Figure S2. a) and b) TEM images of P-egg alumina (scale: 20 nm), c) scheme of possible crystallite morphology.*

For the T-flat sample (Figure S3), the following crystallite dimensions (from about 30 measurements) were measured:

- Length between 7 and 27 nm (average 14.5 nm)
- Width between 5 and 16 nm (average 9 nm)
- Thickness approximately between 3 and 5 nm

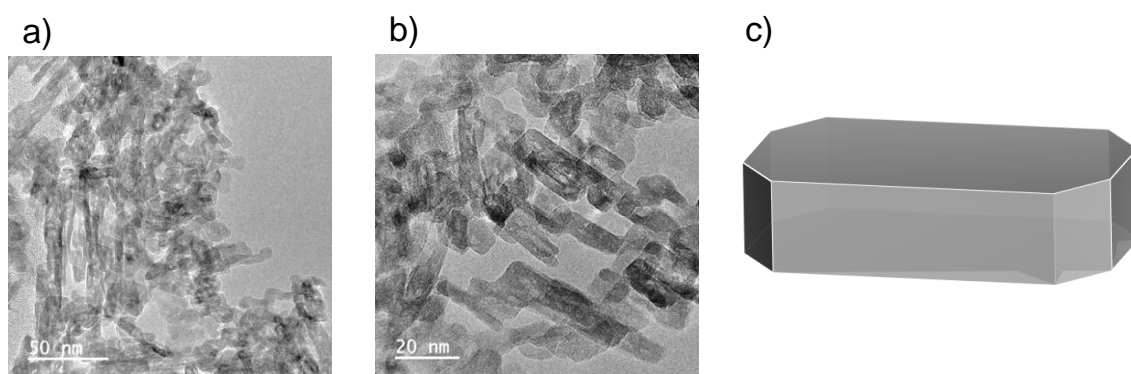


*Figure S3. TEM images of T-flat alumina (scale: a) 50 nm; b) 20 nm), and c) scheme of possible crystallite morphology.*

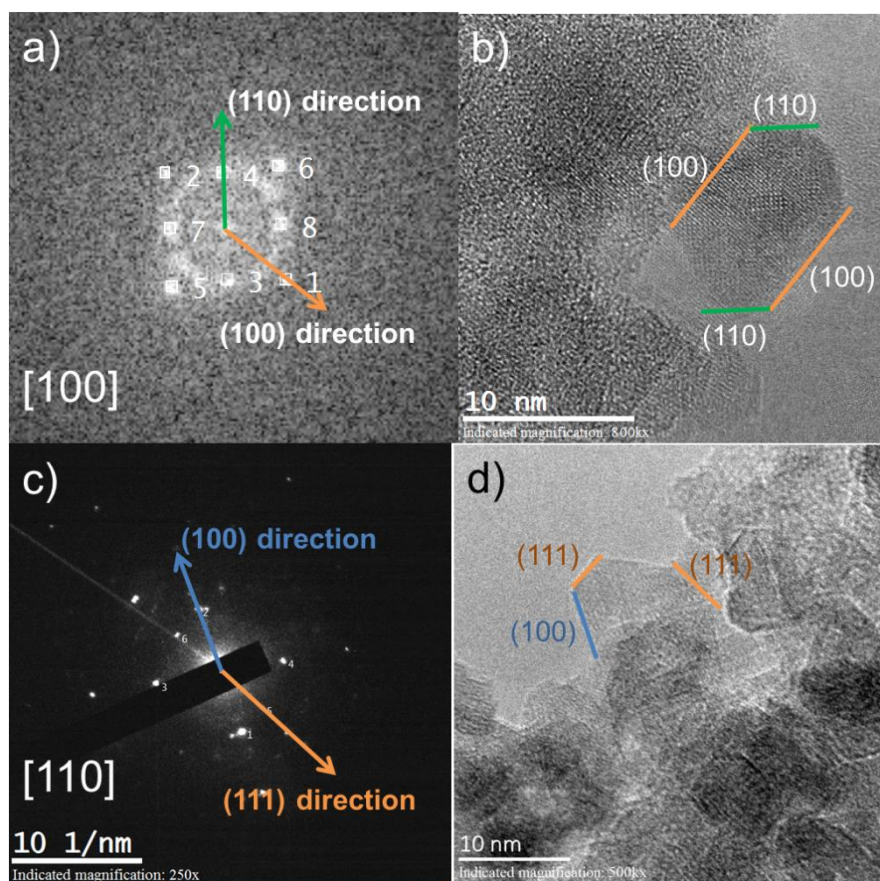


*Figure S4. Plane indexation of the illustrated crystallites (b) and c) performed by a) Fourier transform indexation from a HR-TEM image for P-egg sample (b) and by c) nanoarea electron diffraction pattern indexation for T-flat sample (d).*

$^1\text{H}$  NMR spectral deconvolution was done using DMFit[1] as illustrated in Figure S5. The results are reported in Table S2.

Samples with 0.5%<sub>w/w</sub> Cl were subjected to a thermal treatment at 500°C using a humid air flow after calcination to tune the chlorine content. All samples were treated under  $\text{H}_2$  for 2h at 500°C prior to NMR acquisition.

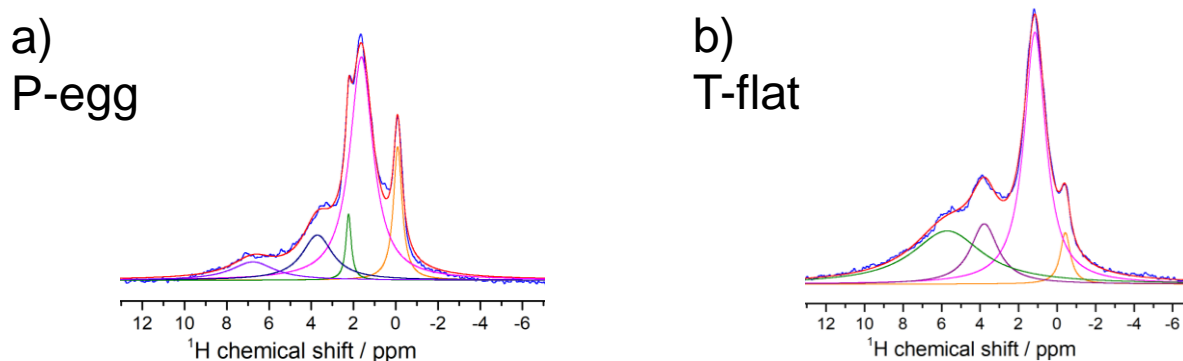


Figure S5. Relative peak intensity contributions obtained from fitting the  $^1\text{H}$  DEPTH spectra of both alumina samples without chlorine, blue – experimental spectrum, red – best fitted model. Note that for P-egg samples the central signals were fitted using two Gaussians while for T-flat samples only one Gaussian was used.

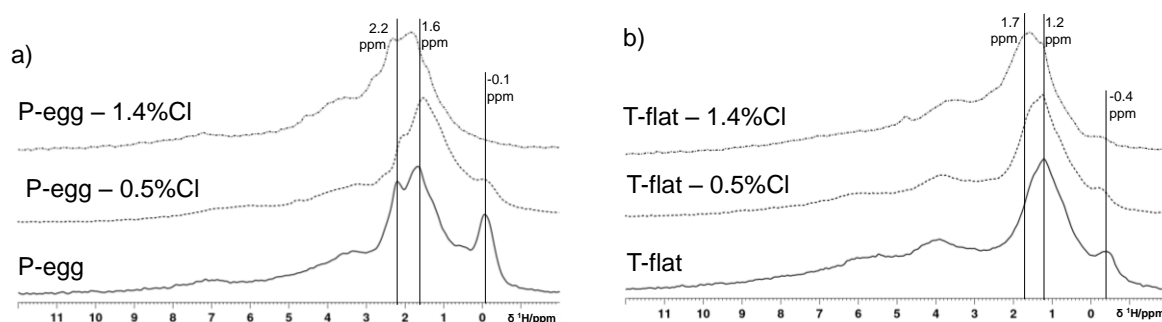


Figure S6.  $^1\text{H}$  MAS NMR spectra (800 MHz, MAS 30 kHz) of a) P-egg, P-egg – 0.5%Cl and P-egg – 1.4%Cl samples and of b) T-flat, T-flat – 0.5%Cl and T-flat – 1.4%Cl samples.

Table S2. Relative peak intensity contributions obtained from fitting the  $^1\text{H}$  DEPTH spectra. Note that these values have an estimated uncertainty of 10%; which is largely due to the impact of manual baseline correction. This impact is particularly relevant for signals above 5 ppm. Values below 5% are not precise.

P-egg		P-egg – 0.5%Cl		P-egg-1.4%Cl		T-flat		T-flat – 0.5%Cl		T-flat – 1.4%Cl	
Fit						Fit					
δ <sup>1</sup> H	Int. %	δ <sup>1</sup> H	Int. %	δ <sup>1</sup> H	Int. %	δ <sup>1</sup> H	Int. %	δ <sup>1</sup> H	Int. %	δ <sup>1</sup> H	Int. %
-0.1	12	-0.04	3	-		-0.4	4	-0.3	1	-0.3	0.1
1.6	56	1.5	64	1.7	46	1.2	48	1.4	51	1.5	40
2.2	5	2.1	3	2.3	22	3.8	15	3.7	17	3.5	44
3.7	19	3.6	23	3.9	25	5.7	33	6.0	31	6.9	17
6.8	8	6.2	7	7.1	7						

For T-flat, the intensity decrease for  $\delta > 5$  ppm is caused by the loss of H-bond donor species. This implies that the number of  $\mu_1$ -OH edge sites on the T-flat crystallites do not enable the exchange of all Cl atoms at 1.4%Cl, which is supported by the T-flat – 0.5%Cl sample (Table S2). Hence, some (110) surface  $\mu_1$ -OH are the next favourable sites to be exchanged (-28 to -

16 kJ.mol<sup>-1</sup>) at 1.4%Cl. With chlorine atoms in place of formally H-bonded hydroxyls, the H-bond network on the T-flat alumina surface is partially broken.[2] Some formally H-bond donor species may become free or H-bond acceptors. This effect is revealed in the increase in intensity of the 3-5 ppm region and of the shoulder at 1.7 ppm. By contrast, the number of edge sites of the P-egg crystallites seems to be high enough to be exchanged with 1.4%Cl since the spectral regions at  $\delta > 3$  ppm are weakly disturbed.

*Table S3. Total proton signal from spectral integration (range: 12 to -5 ppm), corrected for number of scans, receiver gain and mass and normalized to the highest value of the list (T-flat – 1.4%Cl). An uncertainty of 10%, due to the impact of manual baseline correction, must be considered.*

	<b>Spectra integral (normalized)</b>
P-egg	0.6
P-egg - 1.4%Cl	0.5
T-flat	1.0
T-flat - 1.4%Cl	1.0

Table S3 indicates that the total signal for T-flat is double that of P-egg. As the aluminas have distinct morphologies, they also have different proportions of exposed surfaces which have differing hydration degrees at a given T,P condition. Indeed, as the electron diffraction study suggests, TH100 seems to present a larger proportion of (111) surface, which is highly hydrated (see below). It is also observed that there is no impact of chlorine doping on the total signal as the loading used is quite small.

## S2. DFT calculations

Structures were re-optimized using PBE-dDsC exchange correlation functional[3,4] and PAW pseudopotentials[5] with an energy cut off of 400 eV using the VASP code[6,7].

### S2.1. DFT alumina surface models

The models used were taken from Digne et al.[8] and were re-optimized without major changes (except for the (110) surface, see below). The adsorbed water and the two upper atomic layers of the slab were allowed to relax for the (100) and (110) surface models, the full slab was relaxed for the (111) surface model. without major changes. With the exception of the (111) surface, the “slab” models used correspond to 2x2 supercells with respect to Digne’s unit cells (Figure S7). The (100) surface model used in the present study consists of a triperiodic cell, the size of which is  $16.8 \times 11.1 \times 28.0 \text{ \AA}^3$ , occupied by a  $6.0 \text{ \AA}$  wide alumina slab surmounted by a  $22 \text{ \AA}$  wide vacuum slab. The (110) surface model is  $16.1 \times 16.8 \times 28.0 \text{ \AA}^3$  wide, occupied by a  $6.0 \text{ \AA}$  thick alumina slab, surmounted by a  $22 \text{ \AA}$  wide vacuum slab. The (111) surface model is identical to that of Digne[8] with a  $9.7 \times 8.4 \times 21.5 \text{ \AA}^3$  wide cell occupied by a symmetric slab (hydroxylated on both sides) with a vacuum thickness of  $12 \text{ \AA}$ .

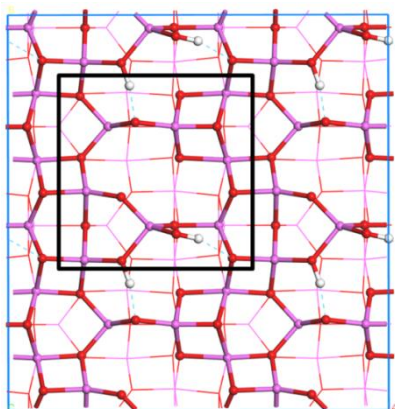


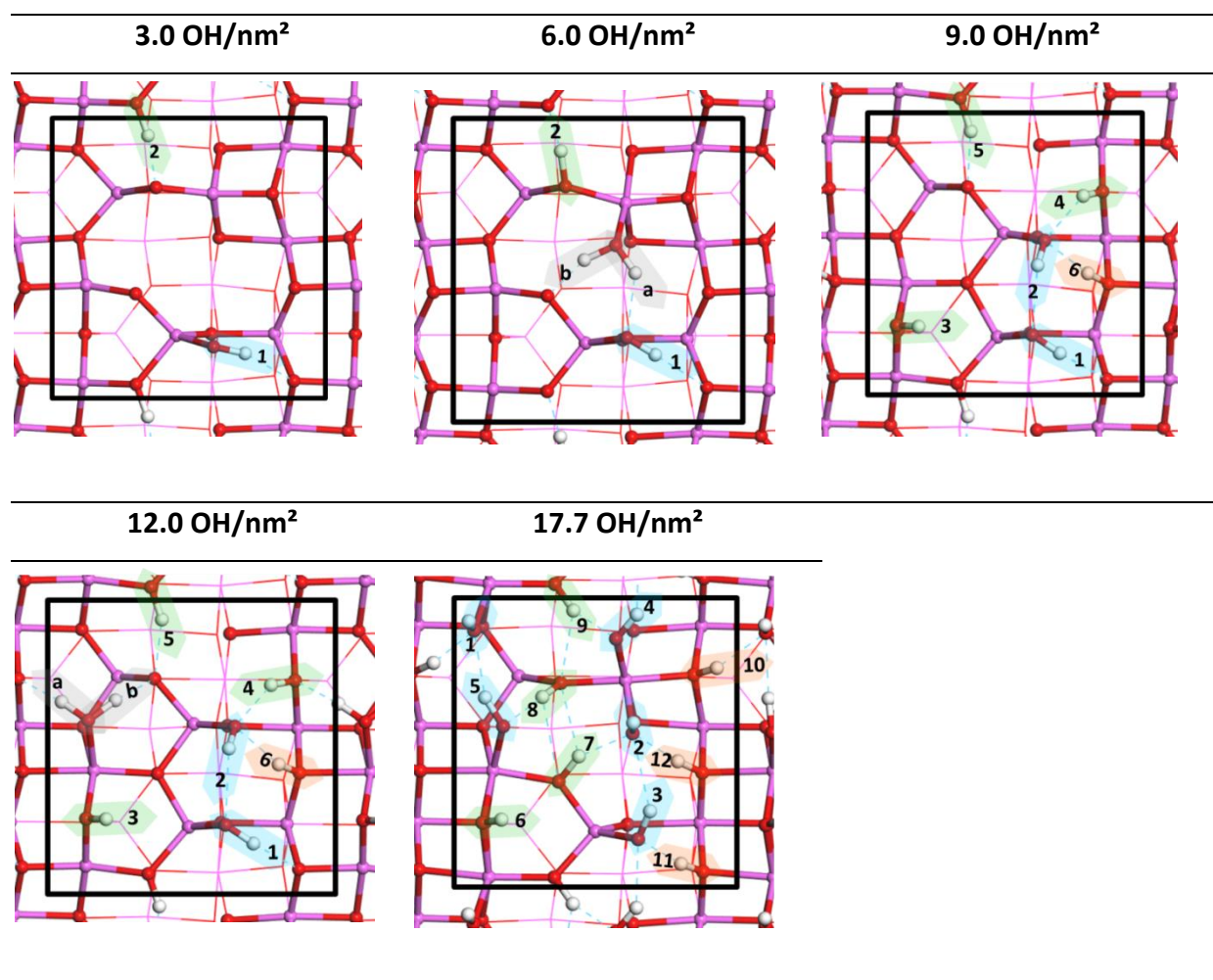
*Figure S7. Example of (110)  $3.0 \text{ OH/nm}^2$  surface slab in which Digne’s unit is highlighted by the black square and is repeated four times (2 by 2).*



### (110) surface

The surface reconstruction proposed by Wischert et al.[9] is here present for the surfaces at an OH coverage of 9.0 and 12.0 OH/nm<sup>2</sup>.

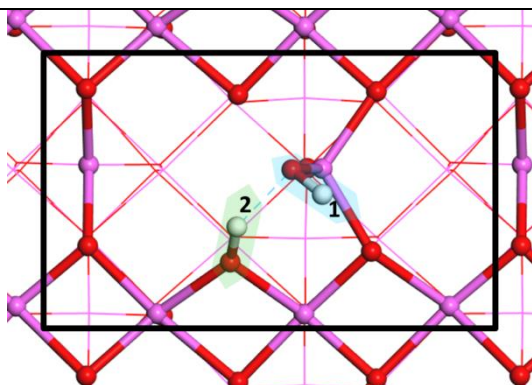
*Table S4. (110) models used, color coded as red-oxygen; purple-aluminium; white-hydrogen. Blue traced lines indicate hydrogen-bonds (bond length's threshold of 2.5 Å). Hydroxyls and adsorbed water identified by numbers and letters in each model, blue -  $\mu_1$ -OH; green -  $\mu_2$ -OH; orange -  $\mu_3$ -OH; grey - adsorbed water. Black square indicates Digne's surface unit.*



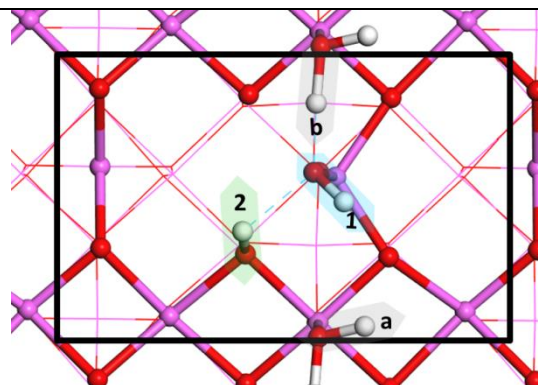
## (100) surface

Table S5. (100) models, colour coded as red-oxygen; purple-aluminium; white-hydrogen. Blue traced lines indicate hydrogen-bonds (bond length's threshold of  $2.5\text{\AA}$ ). Hydroxyls and adsorbed water identified by numbers and letters in each model, blue -  $\mu_1\text{-OH}$ ; green -  $\mu_2\text{-OH}$ ; orange -  $\mu_3\text{-OH}$ ; grey - adsorbed water. Black square indicates Digne's surface unit.

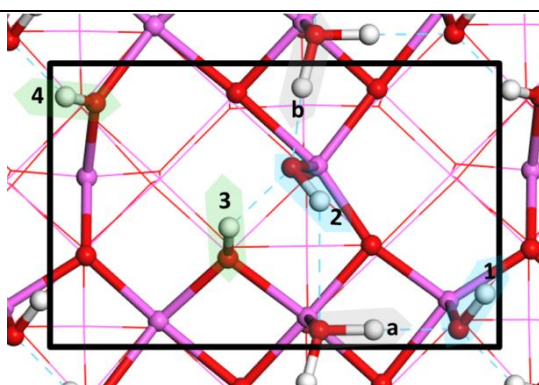
4.3 OH/nm<sup>2</sup>



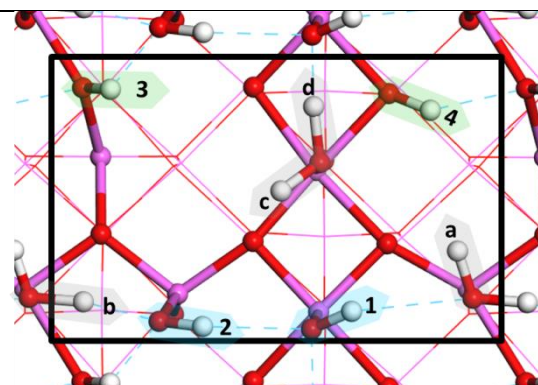
8.6 OH/nm<sup>2</sup>



13.0 OH/nm<sup>2</sup>



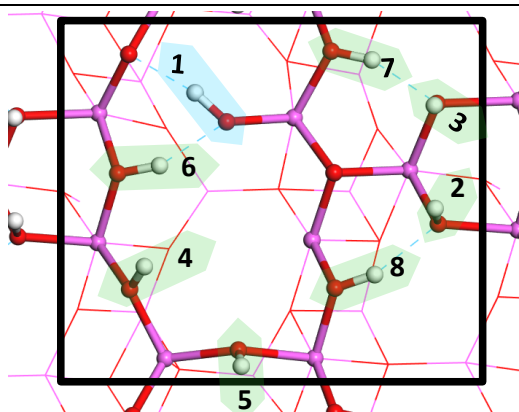
17.2 OH/nm<sup>2</sup>



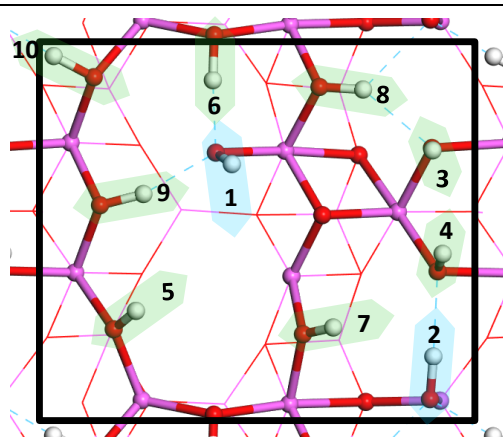
## (111) surface

Table S6. (111) models, colour coded as red-oxygen; purple-aluminium; white-hydrogen. Blue traced lines indicate hydrogen-bonds (bond length's threshold of  $2.5\text{\AA}$ ). Hydroxyls and adsorbed water identified by numbers and letters in each model, blue -  $\mu_1\text{-OH}$ ; green -  $\mu_2\text{-OH}$ ; orange -  $\mu_3\text{-OH}$ ; grey - adsorbed water. Black square indicates Digne's surface unit.

9.8 OH/nm<sup>2</sup>



12.3 OH/nm<sup>2</sup>



### *Thermodynamic diagrams*

The hydration state of each surface that would most likely correspond to that of our alumina samples after thermal treatment at 773.15 K was estimated thanks to thermodynamic calculations (without vibrational components, similar to ref.[8]). In Figure S8 are represented diagrams of water adsorption energy as a function of hydroxyl coverage and temperature for two given water pressure values ( $10^{-4}$  and  $10^{-6}$  bar) considered representative of experimental conditions (thermal treatment at 500°C). For each surface, the most stable hydrated model in the 700-800 K temperature range was chosen as representative of the hydration state of our samples.

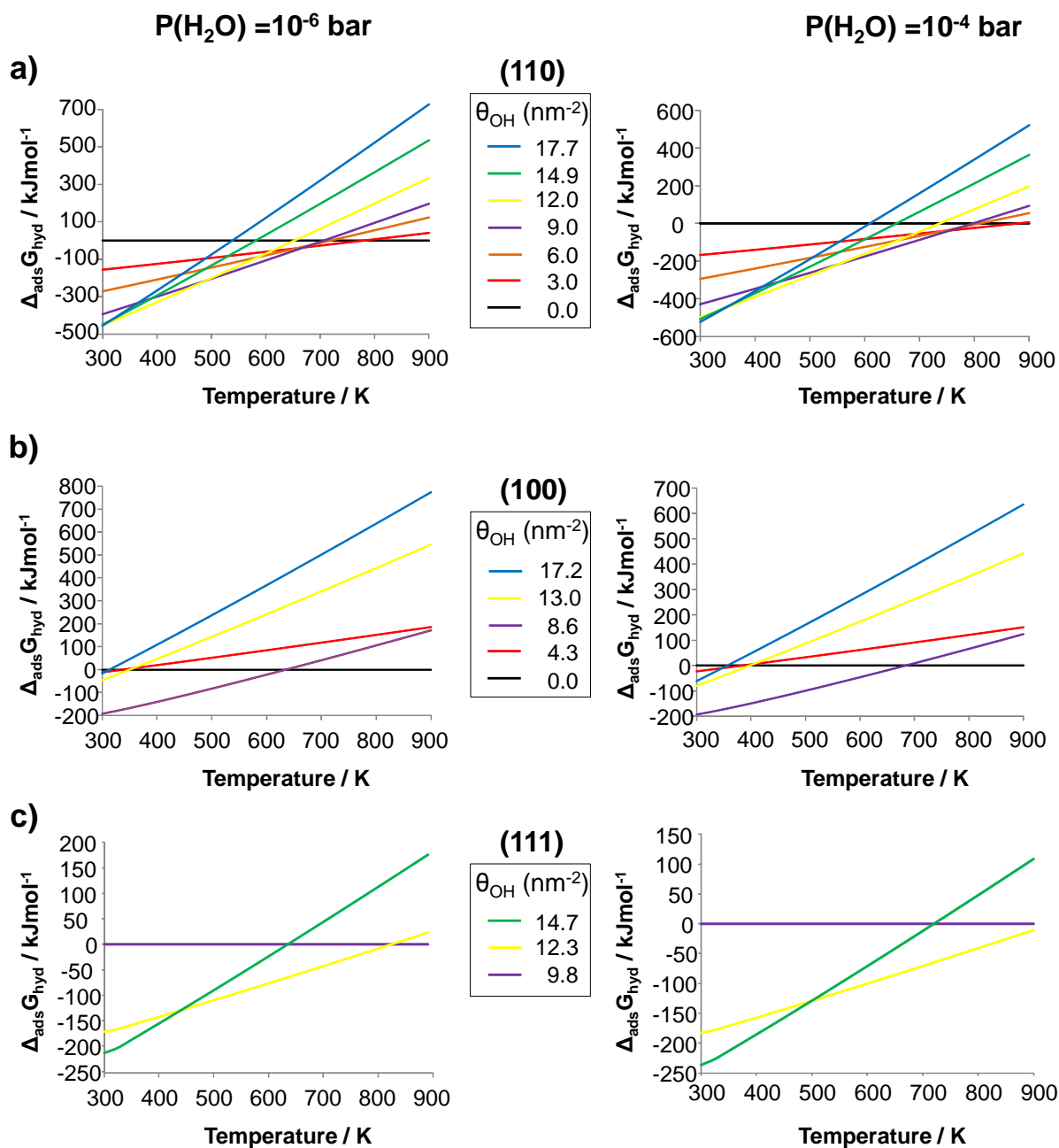
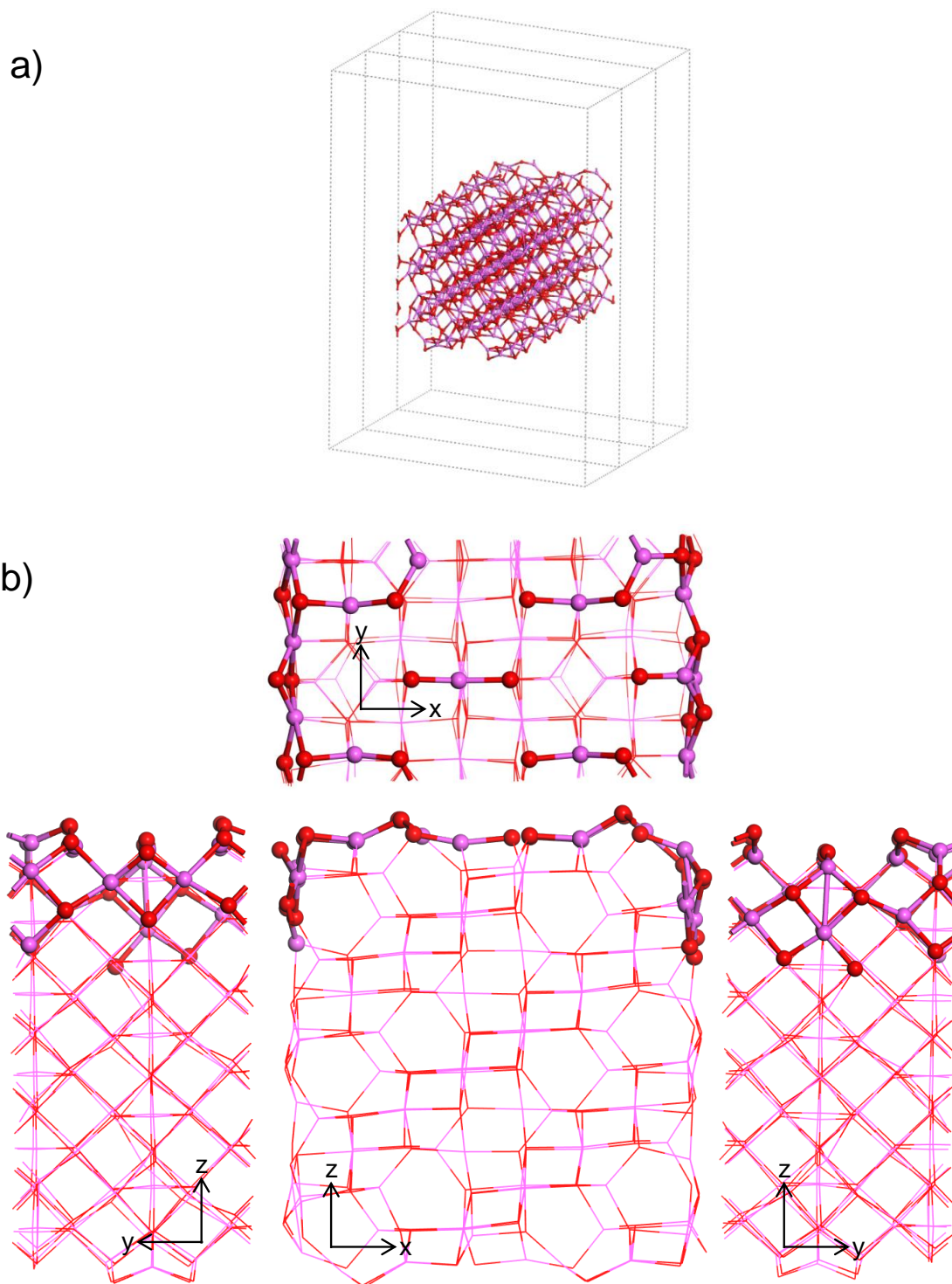


Figure S8. Water adsorption energy as a function of hydroxyl coverage and temperature for  $P(\text{H}_2\text{O})=10^{-4}$  and  $10^{-6}$  bar for a) (110), b) (100) and c) (111) surface models.

## S2.2. DFT alumina edge models

The (110)-(100) edge model was constructed as a nano-rod (Figure S9).



*Figure S9. a) Representation of the (110)-(100) nano-rod and b) detailed view of all rod sides: top (110) surface, side (100) surface and view perpendicular to edges.*



Table S7. Hydrated (110)-(100) edge model with one water molecule adsorbed colour coded as red-oxygen; purple-aluminium; white-hydrogen. Blue traced lines indicate hydrogen-bonds (bond length's threshold of 2.5Å). Hydroxyls and adsorbed water identified by numbers and letters in each model, blue -  $\mu_1$ -OH; green -  $\mu_2$ -OH; orange -  $\mu_3$ -OH; grey - adsorbed water.

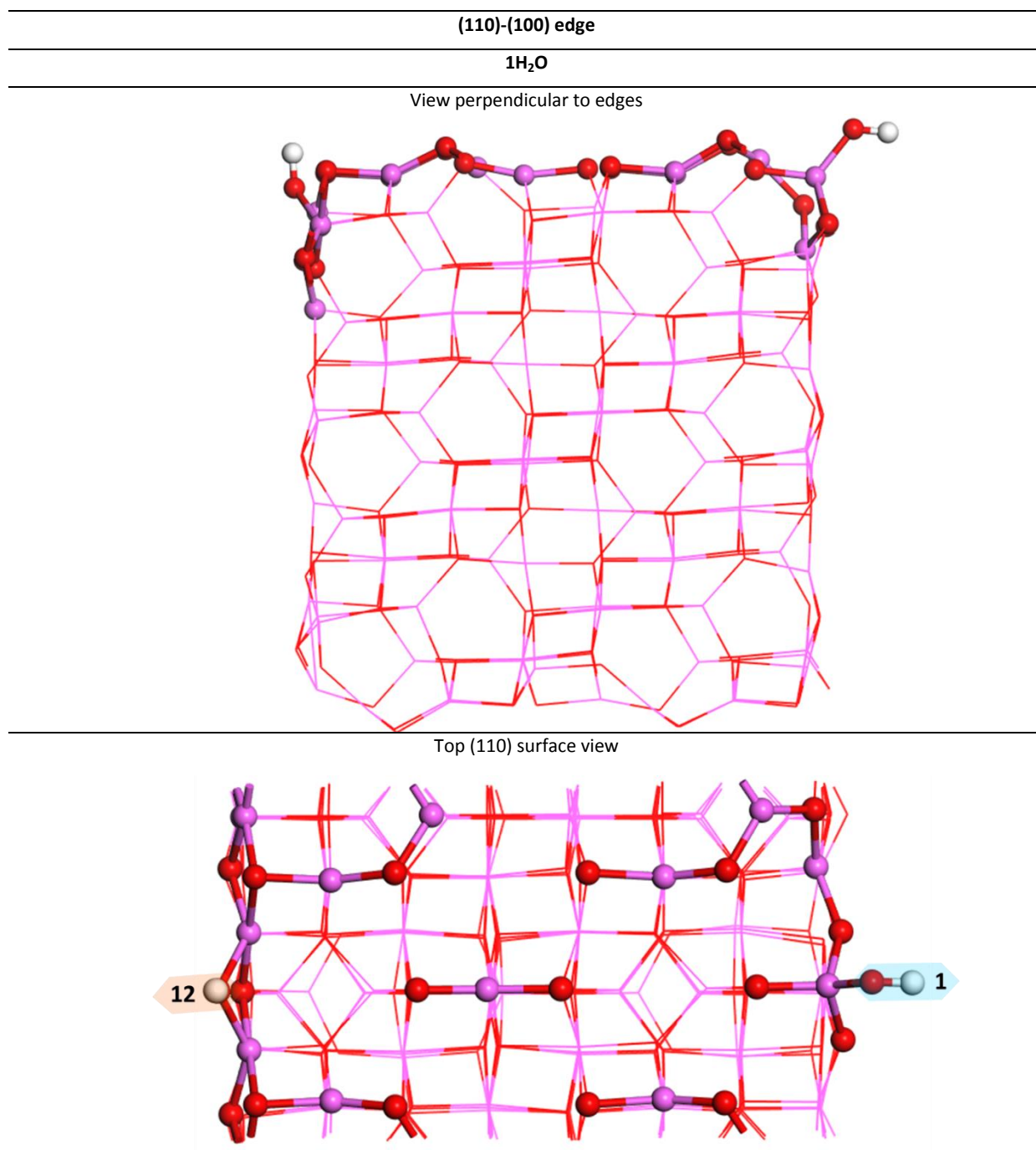
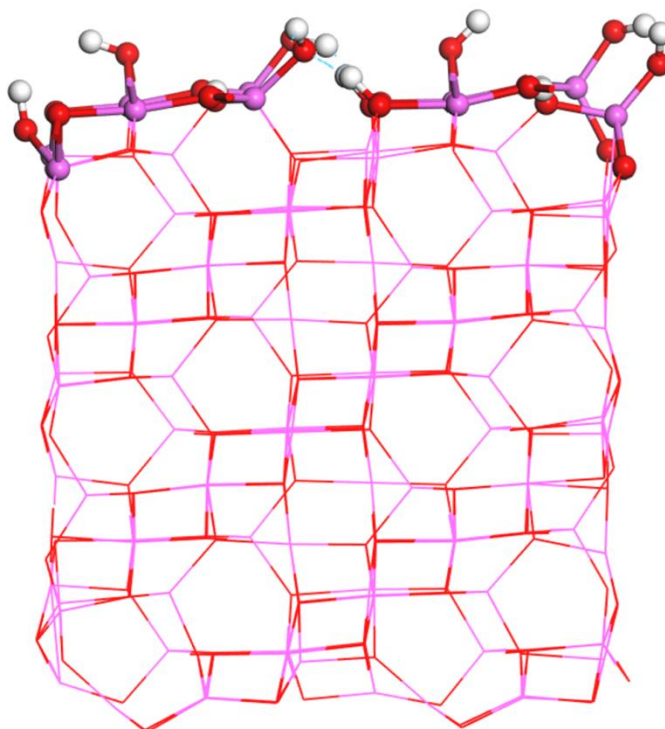


*Table S8. Hydrated (110)-(100) edge model with six water molecules adsorbed colour coded as red-oxygen; purple-aluminium; white-hydrogen. Blue traced lines indicate hydrogen-bonds (bond length's threshold of 2.5Å). Hydroxyls and adsorbed water identified by numbers and letters in each model, blue -  $\mu_1$ -OH; green -  $\mu_2$ -OH; orange -  $\mu_3$ -OH; grey - adsorbed water.*

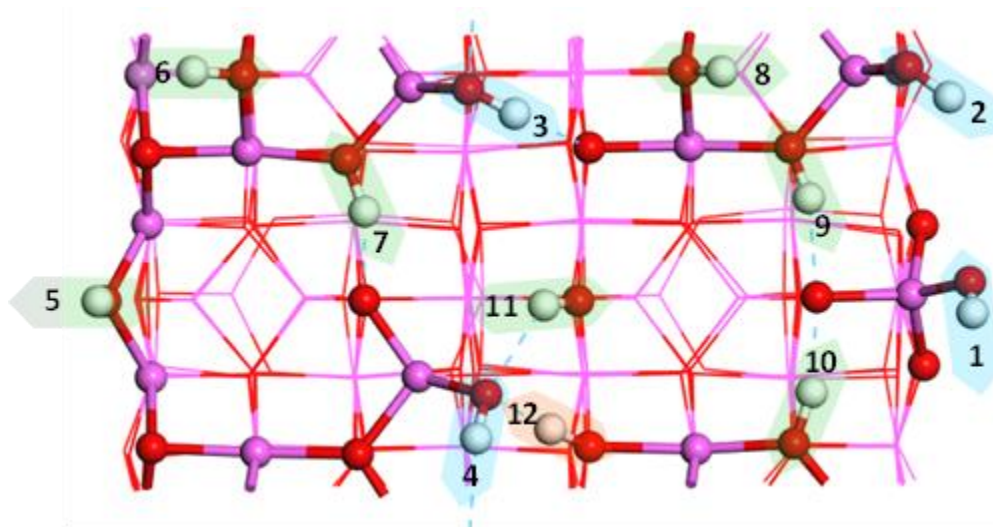
(110)-(100) edge

6H<sub>2</sub>O

View perpendicular to edge



Top (110) surface view





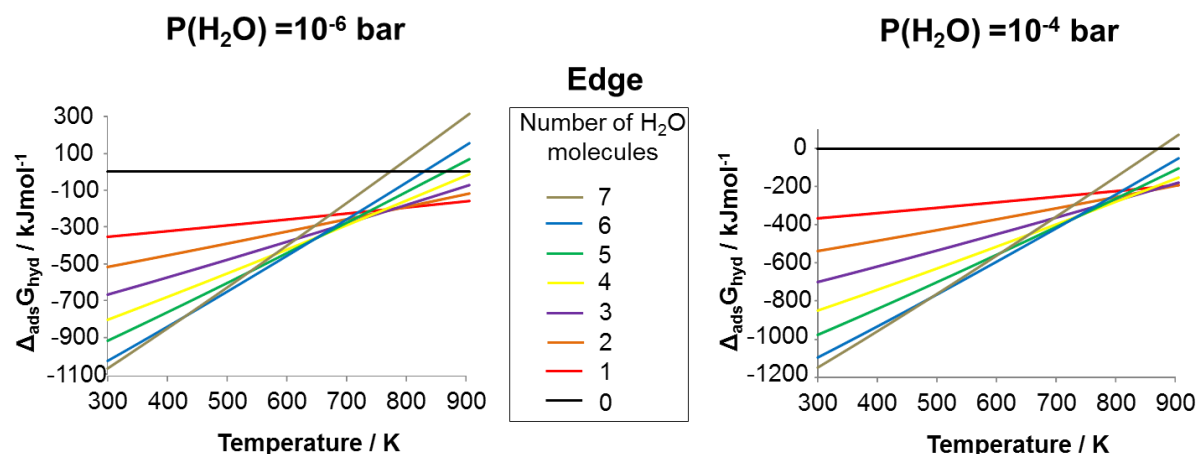


Figure S10. Water adsorption energy as a function of adsorbed water molecules per unit cell of simulation and temperature for  $P(\text{H}_2\text{O})=10^{-4}$  and  $10^{-6}$  bar for the (110)-(100) edge model.

### S2.3. Chemical shift calculation results

Chemical shifts were calculated by periodic DFT, with the linear response approach[10,11] as implemented in VASP. The step size for the finite difference k-space derivative was set to 0.003. First order of the finite difference stencil was used to calculate the magnetic susceptibility.

The calculations were performed at the gamma point for (110) and (100) models, and the k-points mesh was set to  $1 \times 3 \times 3$  for (111) models and to  $1 \times 2 \times 1$  for edge models (tests were performed with denser grids and show no significant deviation with a tolerance of less than 0.1 ppm). Also, the calculations were performed at various energy cutoff (400, 500, 600 and 700 eV), and for hydrogen-bond acceptors and isolated OH groups, the deviation was lower than 0.2 ppm. Finally, we also tested the influence of the exchange correlation functional on some relevant cases and found that with a cutoff of 400 eV, the proton chemical shifts differ by less than 0.3 ppm when using optPBE-vdW (most adapted for [12]) with respect to the ones obtained with the PBE dDsC functional.

Table S9. Calculated proton chemical shifts for (110) surface models at five hydration degrees.

(110) surface				
3.0 OH/nm <sup>2</sup>				
Hydroxyl				δ <sup>1</sup> H (ppm)
#	μ <sub>x</sub>	HO-Al <sub>n</sub>	H-bond type	
1	μ <sub>1</sub>	Al <sub>IV</sub>	Donor	1.5
2	μ <sub>2</sub>	Al <sub>IV</sub> ; Al <sub>IV</sub>	Donor	10.7
6.0 OH/nm <sup>2</sup>				
1	μ <sub>1</sub>	Al <sub>IV</sub>	Donor/acceptor	1.7
2	μ <sub>2</sub>	Al <sub>IV</sub> ; Al <sub>V</sub>	Donor	15.2
3	H <sub>2</sub> Oa	Al <sub>V</sub>	Donor	8.0
4	H <sub>2</sub> Ob		Donor	11.0
9.0 OH/nm <sup>2</sup>				
1	μ <sub>1</sub>	Al <sub>IV</sub>	Donor	2.7
2	μ <sub>1</sub>	Al <sub>IV</sub>	Donor/acceptor	3.4
3	μ <sub>2</sub>	Al <sub>V</sub> ; Al <sub>V</sub>	Free	2.1
4	μ <sub>2</sub>	Al <sub>VI</sub> ; Al <sub>VI</sub>	Donor	5.4
5	μ <sub>2</sub>	Al <sub>IV</sub> ; Al <sub>V</sub>	Donor	11.0
6	μ <sub>3</sub>	Al <sub>V</sub> ; Al <sub>V</sub> ; Al <sub>VI</sub>	Donor	9.6
12.0 OH/nm <sup>2</sup>				
1	μ <sub>1</sub>	Al <sub>IV</sub>	Donor/acceptor	2.8
2	μ <sub>1</sub>	Al <sub>IV</sub>	Donor/acceptor	3.1
3	μ <sub>2</sub>	Al <sub>V</sub> ; Al <sub>VI</sub>	Free	2.0
4	μ <sub>2</sub>	Al <sub>IV</sub> ; Al <sub>V</sub>	Donor/acceptor	7.0
5	μ <sub>2</sub>	Al <sub>IV</sub> ; Al <sub>V</sub>	Donor	9.2
6	μ <sub>3</sub>	Al <sub>VI</sub> ; Al <sub>VI</sub> ; Al <sub>VI</sub>	Donor	7.9
a	H <sub>2</sub> Oa	Al <sub>VI</sub>	Donor	7.5
b	H <sub>2</sub> Ob		Donor	9.6
17.7 OH/nm <sup>2</sup>				
1	μ <sub>1</sub>	Al <sub>VI</sub>	Acceptor	0.7
2	μ <sub>1</sub>	Al <sub>VI</sub>	Acceptor	1.6
3	μ <sub>1</sub>	Al <sub>IV</sub>	Donor/acceptor	2.2
4	μ <sub>1</sub>	Al <sub>V</sub>	Donor/acceptor	3.0
5	μ <sub>1</sub>	Al <sub>VI</sub>	Donor/acceptor	3.3
6	μ <sub>2</sub>	Al <sub>VI</sub> ; Al <sub>VI</sub>	Free	1.5
7	μ <sub>2</sub>	Al <sub>IV</sub> ; Al <sub>VI</sub>	Donor/acceptor	7.7
8	μ <sub>2</sub>	Al <sub>V</sub> ; Al <sub>V</sub>	Donor/acceptor	7.8
9	μ <sub>2</sub>	Al <sub>IV</sub> ; Al <sub>VI</sub>	Donor	11.8
10	μ <sub>3</sub>	Al <sub>V</sub> ; Al <sub>VI</sub> ; Al <sub>VI</sub>	Donor	9.4
11	μ <sub>3</sub>	Al <sub>VI</sub> ; Al <sub>VI</sub> ; Al <sub>VI</sub>	Donor	11.3
12	μ <sub>3</sub>	Al <sub>VI</sub> ; Al <sub>VI</sub> ; Al <sub>VI</sub>	Donor	11.7

Table S10. Calculated proton chemical shifts for (100) surface models at four hydration degrees.

(100) surface				
4.3 OH/nm <sup>2</sup>				
Hydroxyl				$\delta^1\text{H}$ (ppm)
#	$\mu_x$	HO-Al <sub>n</sub>	H-bond type	
1	$\mu_1$	Al <sub>VI</sub>	Acceptor	0.7
2	$\mu_2$	Al <sub>V</sub> ; Al <sub>V</sub>	Donor	10.7
8.6 OH/nm <sup>2</sup>				
1	$\mu_1$	Al <sub>VI</sub>	Acceptor	1.2
2	$\mu_2$	Al <sub>V</sub> ; Al <sub>VI</sub>	Donor	5.8
a	H <sub>2</sub> Oa	Al <sub>VI</sub>	Free	0.8
b	H <sub>2</sub> Ob		Donor	15.5
13.0 OH/nm <sup>2</sup>				
1	$\mu_1$	Al <sub>V</sub>	Acceptor	0.8
2	$\mu_1$	Al <sub>V</sub>	Acceptor	1.8
3	$\mu_2$	Al <sub>V</sub> ; Al <sub>VI</sub>	Donor	8.1
4	$\mu_2$	Al <sub>IV</sub> ; Al <sub>V</sub>	Donor	9.9
a	H <sub>2</sub> Oa	Al <sub>VI</sub>	Donor	9.5
b	H <sub>2</sub> Ob		Donor	11.0
17.2 OH/nm <sup>2</sup>				
1	$\mu_1$	Al <sub>V</sub>	Donor/acceptor	1.6
2	$\mu_1$	Al <sub>VI</sub>	Donor/acceptor	4.2
3	$\mu_2$	Al <sub>IV</sub> ; Al <sub>V</sub>	Donor/acceptor	8.6
4	$\mu_3$	Al <sub>VI</sub> ; Al <sub>VI</sub> ; Al <sub>V</sub>	Donor	6.2
a	H <sub>2</sub> Oa	Al <sub>V</sub>	Free	2.0
b	H <sub>2</sub> Ob		Donor	12.8
c	H <sub>2</sub> Oc	Al <sub>VI</sub>	Free	2.4
d	H <sub>2</sub> Od		Donor	16.2

Table S11. Calculated proton chemical shifts for (111) surface models at two hydration degrees.

(111) surface				
9.8 OH/nm <sup>2</sup>				
Hydroxy				$\delta^1\text{H}$ (ppm)
#	$\mu_x$	HO-Al <sub>n</sub>	H-bond type	
1	$\mu_1$	Al <sub>V</sub>	Donor/acceptor	5.5
2	$\mu_2$	Al <sub>VI</sub> ; Al <sub>VI</sub>	Acceptor	0.6
3	$\mu_2$	Al <sub>V</sub> ; Al <sub>VI</sub>	Acceptor	0.9
4	$\mu_2$	Al <sub>IV</sub> ; Al <sub>VI</sub>	Free	1.4
5	$\mu_2$	Al <sub>IV</sub> ; Al <sub>VI</sub>	Free	2.1
6	$\mu_2$	Al <sub>V</sub> ; Al <sub>VI</sub>	Donor	6.3
7	$\mu_2$	Al <sub>V</sub> ; Al <sub>VI</sub>	Donor	6.5
8	$\mu_2$	Al <sub>V</sub> ; Al <sub>VI</sub>	Donor	6.2
12.3 OH/nm <sup>2</sup>				
1	$\mu_1$	Al <sub>VI</sub>	Acceptor	0.4
2	$\mu_1$	Al <sub>IV</sub>	Donor/acceptor	3.6
3	$\mu_2$	Al <sub>VI</sub> ; Al <sub>VI</sub>	Acceptor	0.5
4	$\mu_2$	Al <sub>VI</sub> ; Al <sub>VI</sub>	Acceptor	0.5
5	$\mu_2$	Al <sub>IV</sub> ; Al <sub>VI</sub>	Free	1.6
6	$\mu_2$	Al <sub>IV</sub> ; Al <sub>VI</sub>	Donor	10.2
7	$\mu_2$	Al <sub>V</sub> ; Al <sub>VI</sub>	Free	2.8
8	$\mu_2$	Al <sub>VI</sub> ; Al <sub>VI</sub>	Donor	5.4
9	$\mu_2$	Al <sub>VI</sub> ; Al <sub>VI</sub>	Donor	6.3
10	$\mu_2$	Al <sub>IV</sub> ; Al <sub>VI</sub>	Donor	9.1

Table S12. Calculated proton chemical shifts for (110)-(100) edge models at two hydration degrees.

(110)-(100) edge				
1H <sub>2</sub> O				
#	$\mu_x$	Hydroxy	H-bond type	$\delta$ <sup>1</sup> H (ppm)
		HO-Al <sub>n</sub>		
1	$\mu_1$	Al <sub>IV</sub>	Free	-0.1
2	$\mu_2$	Al <sub>V</sub> ; Al <sub>V</sub>	Free	2.5
6H <sub>2</sub> O				
1	$\mu_1$	Al <sub>IV</sub>	Free	0.6
2	$\mu_1$	Al <sub>IV</sub>	Free	0.9
3	$\mu_1$	Al <sub>IV</sub>	Donor/acceptor	3.1
4	$\mu_1$	Al <sub>IV</sub>	Donor/acceptor	5.7
5	$\mu_2$	Al <sub>V</sub> ; Al <sub>V</sub>	Free	2.1
6	$\mu_2$	Al <sub>V</sub> ; Al <sub>V</sub>	Free	2.4
7	$\mu_2$	Al <sub>IV</sub> ; Al <sub>V</sub>	Donor	10.0
8	$\mu_2$	Al <sub>V</sub> ; Al <sub>V</sub>	Free	2.3
9	$\mu_2$	Al <sub>IV</sub> ; Al <sub>V</sub>	Donor	7.1
10	$\mu_2$	Al <sub>IV</sub> ; Al <sub>V</sub>	Donor	8.2
11	$\mu_2$	Al <sub>VI</sub> ; Al <sub>VI</sub>	Donor	3.3
12	$\mu_3$	Al <sub>V</sub> ; Al <sub>VI</sub>	Donor	14.2

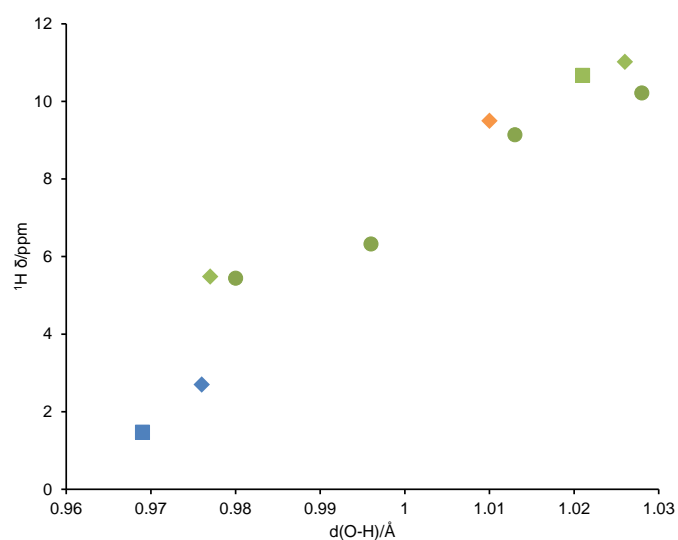
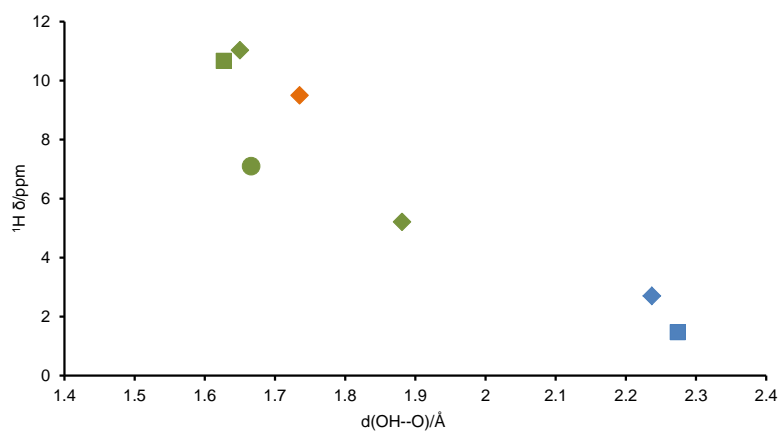


Figure S11. Correlation between length of hydroxyl O-H bond and <sup>1</sup>H chemical shift for H-bond donor surface hydroxyls represented as blue- $\mu_1$ -OH, green- $\mu_2$ -OH and orange  $\mu_3$ -OH and squares – (110) 3.0 OH/nm<sup>2</sup>; lozenges – (110) 9.0 OH/nm<sup>2</sup>; circles – (111) 12.3 OH/nm<sup>2</sup>.



*Figure S12. Correlation between H-bond length and <sup>1</sup>H chemical shift for H-bond donor surface hydroxyls blue-μ<sub>1</sub>-OH, green-μ<sub>2</sub>-OH and orange μ<sub>3</sub>-OH and squares – (110) 3.0 OH/nm<sup>2</sup>; lozenges – (110) 9.0 OH/nm<sup>2</sup>; circles – (111) 12.3 OH/nm<sup>2</sup>.*

## S2.5. Substitution of hydroxyl groups by chlorine

In order to find the most stable location of chlorine on each surface or edge model of interest, the exchange energy of each given hydroxyl with a Cl atom (as illustrated in Figure S13) was calculated as Equation S1

$$\text{Equation S1. } \Delta E_{\text{exch}} = E(-\text{Al}_n'(\text{Cl})-) + E(\text{H}_2\text{O}) - E(-\text{Al}_n(\text{OH})-) - E(\text{HCl})$$

assuming this exchange follows Equation S2



as in Digne et al.[13] For the (110)-(100) edge 6H<sub>2</sub>O model, both Al-edge  $\mu_1$ -OH (#1 and #2) have been simultaneously exchanged with chlorine.

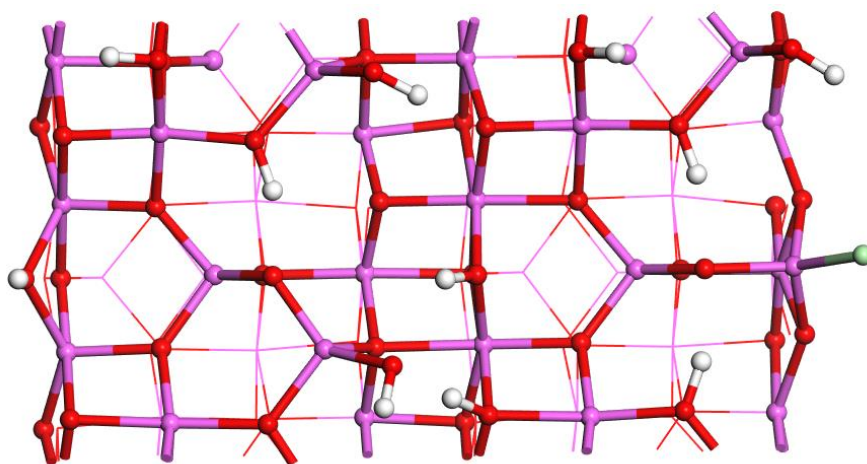


Figure S13. Top view of (110)-(100) edge 6H<sub>2</sub>O were edge  $\mu_1$ -OH (labelled #1) was exchanged with chlorine.

Table S13. Exchange energy of the given indicated hydroxyl with a chlorine atom for surface hydroxyls.

#	$\mu_x$	$\Delta E_{\text{exch}}$ (kJ mol <sup>-1</sup> )
(110) 3.0 OH/nm <sup>2</sup>		
1	$\mu_1$	-28
2	$\mu_2$	77
(110) 12.0 OH/nm <sup>2</sup>		
1	$\mu_1$	-16
2	$\mu_1$	-2
3	$\mu_2$	5
4	$\mu_2$	50
5	$\mu_2$	127
6	$\mu_3$	140
(111) 12.3 OH/nm <sup>2</sup>		
1	$\mu_1$	-3
2	$\mu_1$	-4
3	$\mu_2$	52
4	$\mu_2$	21
5	$\mu_2$	42
6	$\mu_2$	99
7	$\mu_2$	56
8	$\mu_2$	66
9	$\mu_2$	68
10	$\mu_2$	46

Table S14. Exchange energy of the given indicated hydroxyl with a chlorine atom for edge hydroxyls.

#	$\mu_x$	$\Delta E_{\text{exch}}$ (kJ mol <sup>-1</sup> )
(110)-(100) edge 1H <sub>2</sub> O		
1	$\mu_1$	-38
2	$\mu_2$	19
(110)-(100) edge 6H <sub>2</sub> O		
1	$\mu_1$	-31
2	$\mu_1$	-26
3	$\mu_1$	-9
4	$\mu_1$	1
5	$\mu_2$	12
6	$\mu_2$	27
7	$\mu_2$	139
8	$\mu_2$	23
9	$\mu_2$	39
10	$\mu_2$	55
11	$\mu_2$	26
12	$\mu_3$	149
1 and 2	both $\mu_1$	-58



*Table S15. Calculated proton chemical shifts for (110) 9.00 H/nm<sup>2</sup> surface model having exchanged the most favourable  $\mu_1$ -OH with Cl and for (110)-(100) edge 6H<sub>2</sub>O model having exchanged the two edge  $\mu_1$ -OH with Cl.*

(110) surface				
9.0 OH/nm <sup>2</sup>				
Hydroxyl			$\delta^1\text{H}$ (ppm)	
#	$\mu_x$	H-bond type	-	With Cl
1	$\mu_1$	Donor	2.7	-
2	$\mu_1$	Donor/acceptor	3.4	2.3
3	$\mu_2$	Free	2.1	2.0
4	$\mu_2$	Donor	5.4	5.3
5	$\mu_2$	Donor	11.0	11.0
6	$\mu_3$	Donor	9.6	9.6
(110)-(100) edge				
6H <sub>2</sub> O				
Hydroxyl			$\delta^1\text{H}$ (ppm)	
#	$\mu_x$	H-bond type	-	With Cl
1	$\mu_1$	Free	0.6	-
2	$\mu_1$	Free	0.9	-
3	$\mu_1$	Donor/acceptor	3.1	3.1
4	$\mu_1$	Donor/acceptor	5.7	5.9
5	$\mu_2$	Free	2.1	2.1
6	$\mu_2$	Free	2.4	2.4
7	$\mu_2$	Donor	10.0	10.0
8	$\mu_2$	Free	2.3	2.2
9	$\mu_2$	Donor	7.1	7.2
10	$\mu_2$	Donor	8.2	8.1
11	$\mu_2$	Donor	3.3	3.1
12	$\mu_3$	Donor	14.2	14.8

## References

- [1] D. Massiot, F. Fayon, M. Capron, I. King, S. Le Calvé, B. Alonso, J.-O. Durand, B. Bujoli, Z. Gan, G. Hoatson, Magn. Reson. Chem. 40 (2002) 70.
- [2] M. Digne, P. Sautet, P. Raybaud, P. Euzen, H. Toulhoat, J. Catal. 226 (2004) 54.
- [3] J.P. Perdew, K. Burke, M. Ernzerhof, Phys. Rev. Lett. 77 (1996) 3865.
- [4] S.N. Steinmann, C. Corminboeuf, J. Chem. Theory Comput. 7 (2011) 3567.
- [5] G. Kresse, D. Joubert, Phys. Rev. B 59 (1999) 1758.
- [6] G. Kresse, J. Hafner, Phys. Rev. B 49 (1994) 14251.
- [7] G. Kresse, J. Furthmüller, Comp. Mater. Sci. 6 (1996) 15.
- [8] M. Digne, P. Sautet, P. Raybaud, P. Euzen, H. Toulhoat, J. Catal. 211 (2002) 1.
- [9] R. Wischert, P. Laurent, C. Copéret, F. Delbecq, P. Sautet, J. Amer. Chem. Soc. 134 (2012) 14430.

- [10] J.R. Yates, C.J. Pickard, F. Mauri, Phys. Rev. B 76 (2007) 24401.
- [11] C.J. Pickard, F. Mauri, Phys. Rev. B 63 (2001) 245101.
- [12] J. Klimes, D. Bowler, A. Michaelides, Journal of Physics: Condensed Matter 22 (2010) 74203.
- [13] M. Digne, P. Raybaud, P. Sautet, D. Guillaume, H. Toulhoat, J. Amer. Chem. Soc. 130 (2008) 11030.



## **Chapter 4**

### **Platinum supported on $\gamma$ -Al<sub>2</sub>O<sub>3</sub>-Cl**

In the present chapter the fine characterization of the platinum catalysts with two extreme platinum and chlorine loadings is presented and discussed. The chapter is divided in two main sections dedicated respectively to the samples with low and high chlorine loading. Both oxide and reduced catalysts were analysed.

## ***4.1 Samples with 0.1%Cl loading***

In this section the characterization of the samples with the low chlorine loading of 0.1%Cl is presented and discussed, first for the catalysts in oxide form and then for the reduced ones. These were analysed by HR-HAADF-STEM, HERFD-XANES and EXAFS, with the exception of the oxide samples which were not imaged by STEM at this chlorine loading. Theoretical calculations of XANES spectra was moreover performed by Yves Joly (Institut Néel, Grenoble), starting from surface models built at IFPEN, and are reported in the present manuscript for the sake of the assignment of the spectra.

The catalysts discussed here are:

0.3%Pt/PuralSB3-0.1%Cl ; 1%Pt/PuralSB3-0.1%Cl

0.3%Pt/TH100-0.1%Cl ; 1%Pt/TH100-0.1%Cl

### **4.1.1 Oxide catalysts**

Both PuralSB3 and TH100 samples were analysed by XAS (Pt L<sub>3</sub> edge) on two different beamlines at the ESRF. PuralSB3 samples were analysed at BM30 and TH100 samples at BM16, in both cases spectra were acquired between 11450 eV and 12413 eV with a 2 eV step except for the edge region (11550 to 11586 eV) in which a 0.5 eV step was used, as detailed in section 2.2.2.3.2.

#### **4.1.1.1 X-ray absorption spectroscopy (XAS)**

##### ***4.1.1.1.1 HERFD-XANES***

The HERFD-XANES spectra are presented in Figure 4-1. The spectra were normalized using Athena from the Demeter 0.9.26 software package [184].

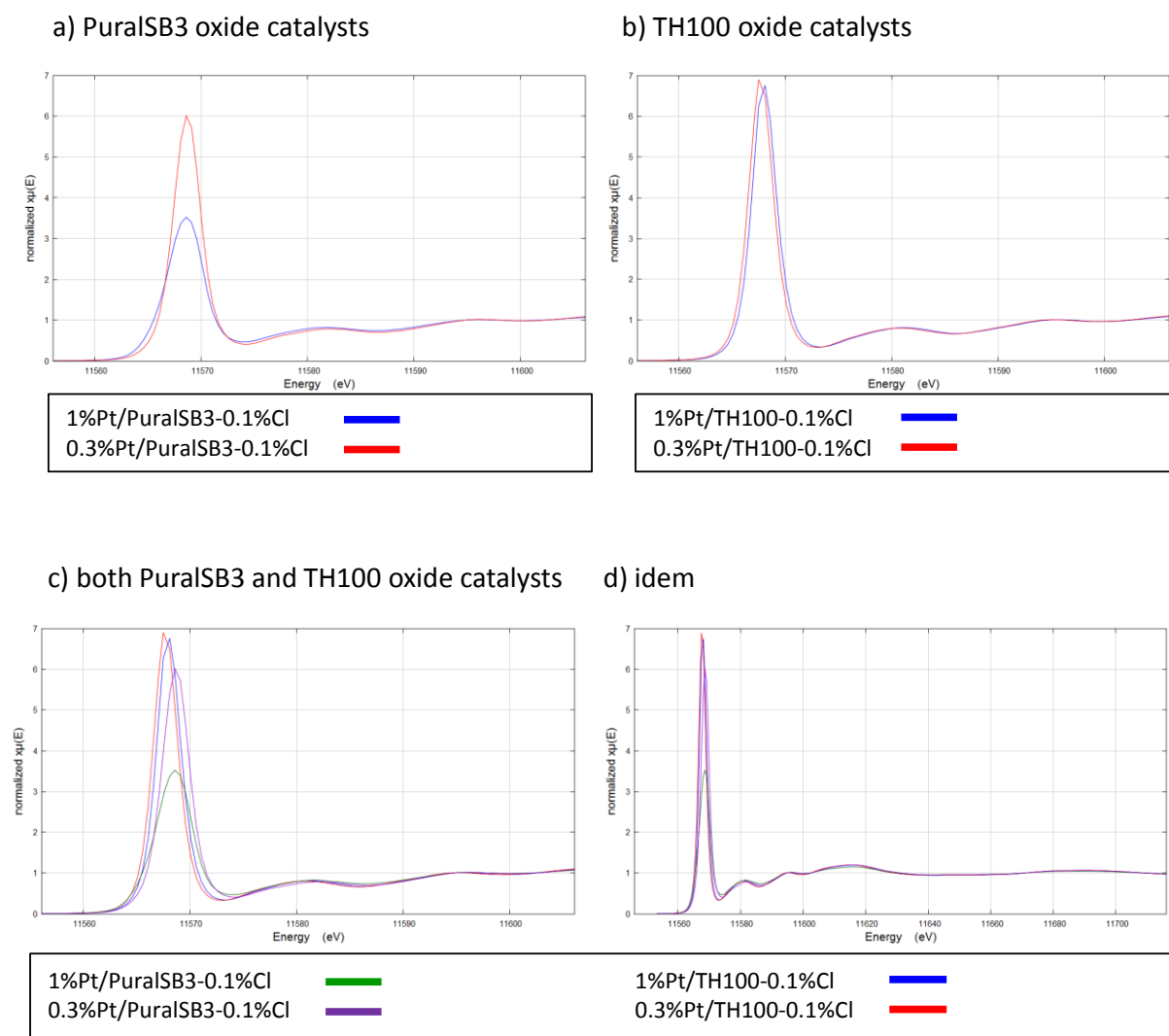


**Figure 4-1 - Pt  $L_3$  edge HERFD-XANES spectra of oxide catalysts at 0.1%Cl loading: a) supported on PuralSB3, b) supported on TH100 and c) and d) comparison of catalysts on both supports.**

The four samples display the same post-edge features but are distinct in edge energy and white line (WL) intensity. Overall the edge energy corresponds to that of the  $\text{PtO}_2$  reference (11568 eV, Appendix D). For PuralSB3, both catalysts share the same edge energy, 11568 eV (here defined as the peak of the white line) but exhibit very different WL intensity: with increased Pt loading, WL intensity decreases, indicating a more metallic state of platinum. The TH100 spectra, however, are essentially identical and are not impacted by changes in metal loading.

To help with the interpretation, let's consider the STEM imaging of oxide catalysts with 1.4%Cl presented ahead in section 4.2.1.1. For both alumina supports it was found that platinum is atomically dispersed as single atoms at 0.3%Pt loading while for 1%Pt loading several clusters with more than 5 atoms are also observed.

Working on the hypothesis that these STEM observations are transferable to the low Cl loading samples, the impact of Pt loading on the XANES spectra of PuralSB3 samples can start to be rationalized. The aggregated Pt oxide clusters possibly present at 1%Pt loading have a more metallic nature than the monoatomic platinum oxides. When Pt is supported on TH100, its electronic state is little affected by its loading even if clusters are also possibly present at 1%Pt.

To clarify this observed trend, experimental spectra were compared to simulated XANES spectra of several DFT models of different oxide Pt species on the dehydrated (100) surface. These models were obtained previously [90,147] by simulating the preferred interaction of oxygen with supported  $\text{Pt}_{13}$  and  $\text{Pt}_1$  entities, up to saturation. The  $\text{Pt}_{13}\text{O}_{22}$  and  $\text{Pt}_1\text{O}_4$  stoichiometries are expected to be dominant after calcination. The spectra were simulated using the FDMNES code [194]. Those that are useful in interpreting the experimental data are displayed in Figure 4-2 and the ordinate scale was normalized to the maximum of the experimental spectrum with the most intense white line, 1%Pt/TH100-0.1%Cl.



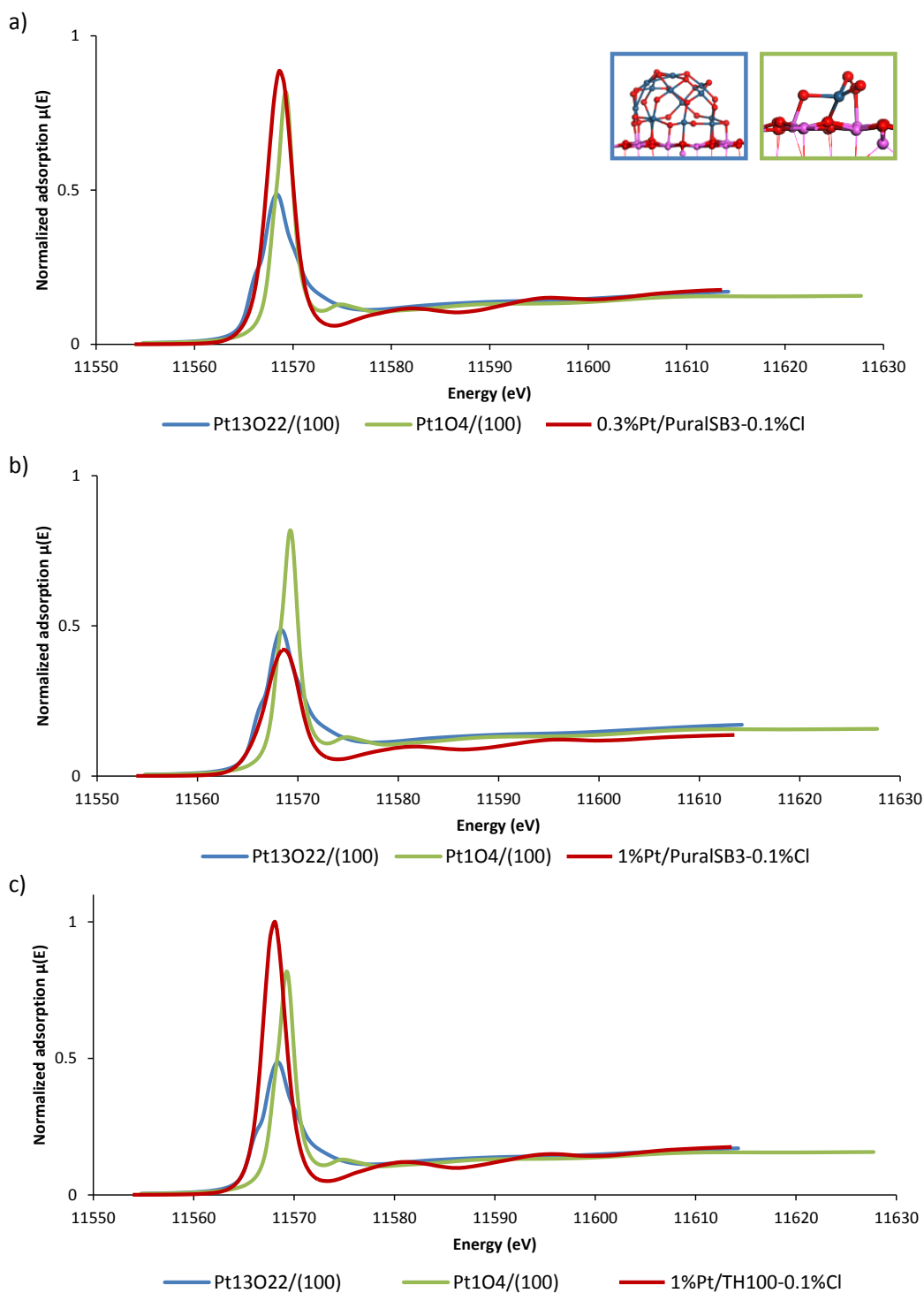


Figure 4-2 – Comparison between Pt  $L_3$  edge HERFD-XANES spectra of a) 0.3%Pt/PuralSB3-0.1%Cl, b) 1%Pt/PuralSB3-0.1%Cl and c) 1%Pt/TH100-0.1%Cl oxide catalysts in red and XANES spectra simulated from DFT models  $Pt_{13}O_{22}/(100)_{dehyd}$  in blue and  $Pt_1O_4/(100)_{dehyd}$  in green. Inset in a) illustrates the DFT models.

The simulated spectra of  $Pt_1O_4$  and  $Pt_{13}O_{22}$  are clearly distinct, despite both being oxide platinum complexes.  $Pt_{13}O_{22}$  has a more metallic character than  $Pt_1O_4$ , which is clearly demonstrated with by the edge energy shift of – 1 eV and white line intensity of half that of

Pt<sub>1</sub>O<sub>4</sub>. This same trend is observed for the PuraSB3 experimental spectra. Indeed, Figure 4-2 a and b reflect what is discussed in the previous paragraph, the XANES signature of 0.3%Pt supported on PuraSB3 corresponds to that of a Pt<sub>1</sub> oxide model and for 1%Pt it is closer to that of the Pt<sub>13</sub> oxide model, showing the impact of oxide cluster formation on the edge features. For TH100 oxide catalysts, Figure 4-2 c, the interpretation remains difficult: while for the experimental spectrum white line maximum corresponds to that of Pt<sub>1</sub>O<sub>4</sub>, the white line is even more intense than that of Pt<sub>13</sub>O<sub>22</sub>.

The XANES simulations thus confirm that PuraSB3 oxide complexes are mostly mononuclear at 0.3%Pt and aggregate into clusters with increased loading at 1%Pt. For TH100 there is no conclusive indication of which oxide complex aggregation mode is dominant or why there is no effect of metal loading. This is particularly intriguing because platinum surface coverage in the samples (Pt/nm<sup>2</sup>) is about 15% greater for TH100 catalysts than for PuraSB3's (section 2.3.2.1) and this slight "overpopulation" in Pt could be expected to potentiate aggregation in TH100 base samples.

It is important to note that even at 0.1%Cl the EXAFS analysis that follows reveals chlorine coordination but there are currently no DFT models of Pt oxide complexes that include chlorine. It seems the spectra of TH100 cannot be fully understood without considering the effect of Cl on the oxide complex.

#### **4.1.1.1.2 EXAFS**

The EXAFS spectra of the same samples were also acquired and were fitted following the method described in section 2.2.2.3.4 using Artemis from the Demeter software package [184]. The spectra ( $\chi(k)$  and FT) are presented in Figure 4-3, as well as the wavelet transform analysis and the best fit.

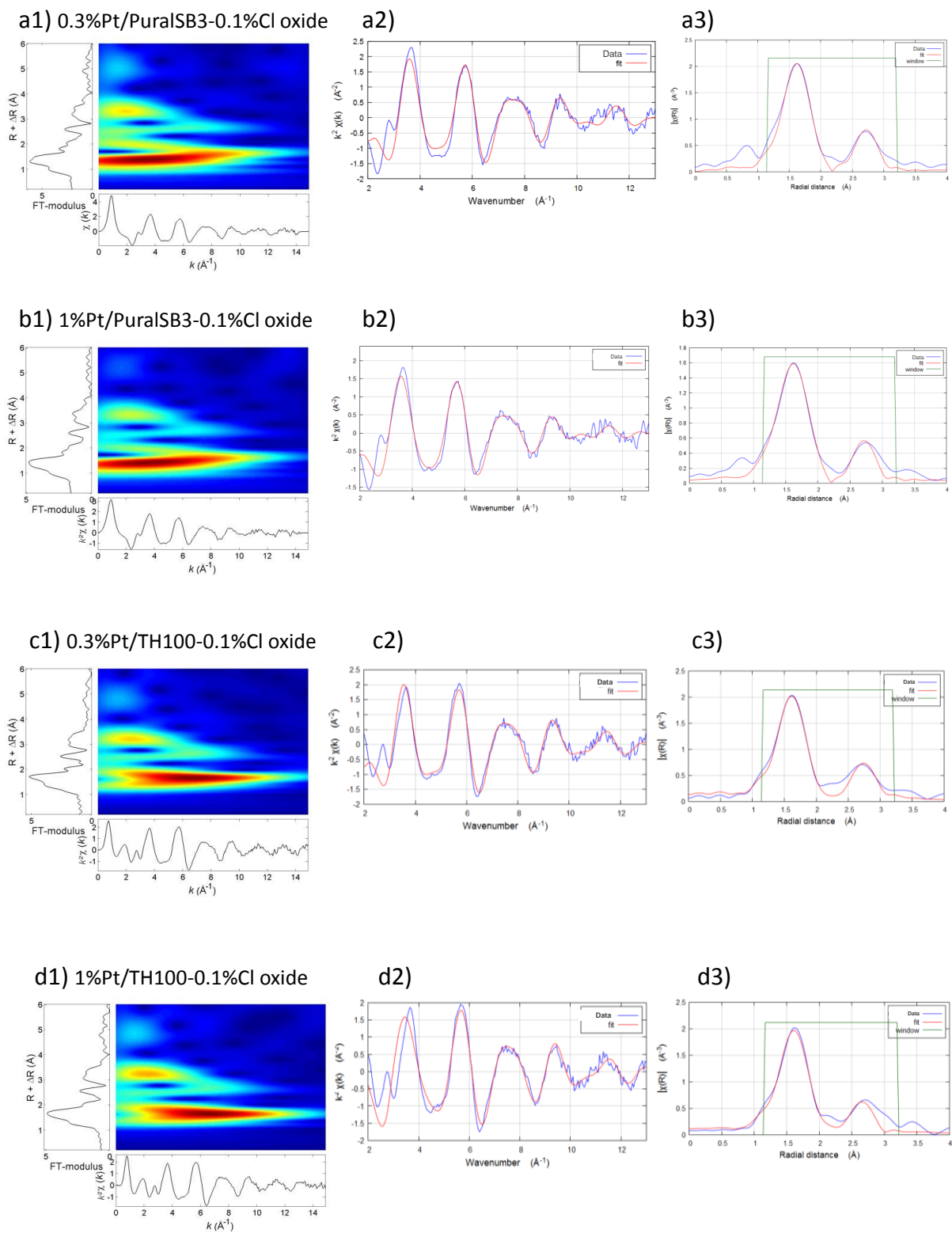


**Figure 4-3 – Wavelet transform analysis 1), EXAFS  $\chi(k)$  2) and magnitude of the Fourier transform  $|\chi(R)|$  (no phase correction) 3), all weighted by  $k^2$ . In 1) and 2), the red line represents the best fit. In 3), the fitting range is represented by the green line.**

It is observed that all spectra are similar and two main regions can be distinguished in the  $|\chi(R)|$  spectra (Figure 4-3 3): one from 1.3 to 2.3 Å and another from 2.3 to 3.3 Å. The

wavelet analysis suggests that the first region should correspond to one main light scatterer with possible contribution of a second. The position of the second region could be compatible with the signal from a Pt-Pt distance (at around 2.7 Å). Nevertheless the wavelet analysis does not indicate a heavy scatterer in this region (even when  $k^3$  weighted data is used) and indeed such a path could not be successfully fitted. The 2.3-3.3 Å signal was thus treated as a 2<sup>nd</sup> shell light scatterer. Two different light scatterers were successfully fitted at a distance of about 3 Å: either O or Al. The fitted parameters for the best fit shown in Figure 4-3 in red are detailed in Table 4-1.

*Table 4-1 – EXAFS fitting results for oxide catalysts at 0.1%Cl considering a 2<sub>nd</sub> shell Pt-O<sub>long</sub> coordination.  $E_0=11566.1$  eV;  $1.15 < R < 3.2$  Å;  $N_{ind}=12$ ;  $N_{var}=8$ .*

Oxide catalyst	k-range (Å <sup>-1</sup> )	Path	Coordination number	R (Å)	$\sigma^2$ (Å <sup>2</sup> )	$\Delta E_0$ (eV)	R-factor
0.3%Pt/PuralSB3-0.1%Cl	4.0 – 11.7	Pt-O	5.0±0.4	1.98±0.01	0.0021±0.0008	10.0±0.7	0.04
		Pt-Cl	0.9±0.3	2.29±0.03			
		Pt-O <sub>long</sub>	6±1	3.05±0.04			
1%Pt/PuralSB3-0.1%Cl	3.6 – 11.6	Pt-O	4.9±0.5	1.98±0.01	0.005±0.0008	8.6±0.6	0.03
		Pt-Cl	1.2±0.2	2.24±0.03			
		Pt-O <sub>long</sub>	4±1	3.07±0.02			
0.3%Pt/TH100-0.1%Cl	4.2 - 11.8	Pt-O	5.1±0.4	1.98±0.01	0.0013±0.0006	9.1±0.6	0.02
		Pt-Cl	0.9±0.3	2.23±0.03			
		Pt-O <sub>long</sub>	7±1	3.07±0.03			
1%Pt/TH100-0.1%Cl	4.2 - 12.3	Pt-O	5.1±0.7	1.97±0.03	0.002±0.001	7.58±0.7	0.03
		Pt-Cl	1±0.6	2.21±0.05			
		Pt-O <sub>long</sub>	5±1	3.03±0.02			

The 1.3-2.3 Å region can thus be fitted with a Pt-O path and a Pt-Cl path, with oxygen being the main neighbour in the 1<sup>st</sup> shell. Indeed, the dechlorination process removes the chlorine coordination and substitutes the attached Cl with O resulting in an oxygen rich PtCl<sub>x</sub>O<sub>y</sub> oxide complex. The contribution of the Pt-Cl path cannot be ignored. Even with a lengthy dechlorination protocol, the remaining chlorine stays in the oxide complex; leading to a neighbouring environment distinct from that found in Pt/Al<sub>2</sub>O<sub>3</sub> samples prepared from non-chlorinated precursors [90,96,121,208]. Both coordination number (CN) and atomic distances of both scatterers are not impacted by platinum loading, hinting that the platinum oxide is on average atomically dispersed.

Fitting the 2-3 Å region is less straight forward but without considering this region the fit would not correctly reproduce all the main features of  $\chi(k)$ . Pt-Pt paths from different reference structures were tried but none improved the fit, even for 1%Pt, in agreement with the wavelet analysis. This indicates again that oxide platinum complexes are atomically dispersed and that the clusters expected to be present at 1%Pt, particularly for PuralSB3 as seen above, are either very weakly aggregated or represent a only small proportion of the platinum.

As already mentioned, this region was fitted as a 2<sup>nd</sup> shell. Indeed, a second shell Pt-O contribution with a distance of 3.3 Å is reported in the literature [102] for 1%Pt and 10%Pt/ $\gamma$ -Al<sub>2</sub>O<sub>3</sub> catalysts calcined at 300°C. In a first investigation, paths obtained from DFT models<sup>2</sup> judged to provide a relevant and manageable list of paths generated by FEFF were used. Finally it was found that using paths obtained through the Quick First Shell (QFS) tool of Artemis, setting a path distance of 3.0 Å (here called Pt-O<sub>long</sub> or Pt-Al<sub>long</sub>), resulted in fits of the same quality and with equivalent results (within uncertainty) for the fitted parameters. Readers should be aware that, as the name indicates, the QFS tool was not created to deal with 2<sup>nd</sup> shell paths at large distances. It is used here to simplify the choice of path. Indeed, each DFT model provides several paths for O and Al at around 3 Å but all with slightly different distances. Moreover the main conclusions taken from the fits are the same using either QFS paths or DFT sourced paths. It was not possible to establish categorically which of these scatterers, O or Al originates this signal. Also, using both did not improve the fit.

---

<sup>2</sup> Those models were Pt<sub>1</sub>, Pt<sub>2</sub> and Pt<sub>5</sub> deposited on (100) [132] and Pt<sub>2</sub>O<sub>4</sub> deposited on (100) [90].

**Table 4-2 - EXAFS fitting results for oxide catalysts at 0.1%Cl considering a 2<sup>nd</sup> shell Pt-Al<sub>long</sub> coordination. E<sub>0</sub>=11566.1 eV; 1.15 < R < 3.2 Å; N<sub>ind</sub>=12; N<sub>var</sub>=8.**

Oxide catalyst	k-range (Å <sup>-1</sup> )	Path	Coordination number	R (Å)	σ <sup>2</sup> (Å <sup>2</sup> )	ΔE <sub>0</sub>	R-factor
0.3%Pt/PuralSB3-0.1%Cl	4.0 – 11.7	Pt-O	5.5±0.5	1.98±0.02	0.006±0.001	11.4±0.8	0.04
		Pt-Cl	0.5±0.4	2.26±0.04			
		Pt-Al <sub>long</sub>	3±0.8	2.91±0.03	0.002±0.003		
1%Pt/PuralSB3-0.1%Cl	3.6 – 11.6	Pt-O	5.3±0.5	1.99±0.01	0.002±0.001	9.97±0.7	0.04
		Pt-Cl	0.7±0.4	2.25±0.04			
		Pt-Al <sub>long</sub>	2.1±0.6	2.95±0.03	0.002±0.003		
0.3%Pt/TH100-0.1%Cl	4.2-11.8	Pt-O	5.5±0.4	1.98±0.02	0.0013±0.0006	8.8±0.6	0.03
		Pt-Cl	0.5±0.3	2.23±0.04			
		Pt-Al <sub>long</sub>	3.5±0.7	2.92±0.03	0.003±0.002		
1%Pt/TH100-0.1%Cl	4.2-12.3	Pt-O	5.1±0.7	1.97±0.03	0.002±0.001	6.99±1	0.04
		Pt-Cl	1±0.6	2.21±0.05			
		Pt-Al <sub>long</sub>	3±0.7	2.91±0.02	0.003±0.002		

The “best fit” shown in Figure 4-3 was in fact chosen arbitrarily as the fit using Pt-O<sub>long</sub>. The results obtained when Pt-Al<sub>long</sub> is used are presented in Table 4-2. Comparing both tables shows that the 2<sup>nd</sup> shell parameters vary depending on the scattering atom: CN is higher for Pt-O<sub>long</sub> and atomic distance is slightly shorter for Pt-Al<sub>long</sub>. Also, for the Pt<sub>1</sub>O<sub>4</sub> DFT model, considering only O or Al atoms belonging to the alumina support within 4 Å: CN(Pt-O)=5 and R(Pt-O)=3.3 Å; CN(Pt-Al)=6 and R(Pt-Al)=3.5 Å. This corresponds to the fitted values for Pt-O<sub>long</sub> but not for Pt-Al<sub>long</sub>, particularly the average distance which is quite longer than the fitted value. The 2<sup>nd</sup> shell scatterer, be it O or Al, is a part of the alumina and its impact on the EXAFS spectra indicates strong interactions with the support.

#### 4.1.1.2 Conclusion

The XAS study of the oxide samples at 0.1%Cl suggests that platinum is atomically dispersed in the form of an oxygen rich PtCl<sub>x</sub>O<sub>y</sub> complex (CN(Pt-O)≈5; CN(Pt-Cl)≈1) which is in strong interaction with the alumina support, as evidenced by a long distance 2<sup>nd</sup> shell EXAFS signal assigned to either O or Al. Such samples have been described as single atom catalysts in the literature [89,90,100,209]. No impact of platinum loading or of alumina support was found through EXAFS.

The XANES spectra confirm the oxidized state of platinum, being comparable to that of Pt(IV) in PtO<sub>2</sub> (Appendix A). An impact of platinum loading is here found for PuralSB3 supported samples: higher loading leads to a more metallic character which may be indicative of platinum aggregation. Indeed, FDMNES simulated XANES spectra of Pt<sub>1</sub>O<sub>4</sub> and Pt<sub>13</sub>O<sub>22</sub> correspond to the features of 0.3%Pt and 1%Pt PuralSB3 spectra, respectively. There is no clear impact of platinum loading on the XANES spectra of the TH100 samples. This may indicate a difference in interaction of these clusters with the support between the two aluminas, perhaps related to the nature of the anchoring sites where the clusters are formed or to their location relative to chlorine on the support's surface.

## 4.1.2 Reduced catalysts

The catalysts reduced ex situ as described in section 2.1.3.3 were analysed by HR-HAADF-STEM and by HERFD-XANES and EXAFS after in situ re-reduction as detailed in sections 2.2.2.1.3 and 2.2.2.3.3, respectively.

### 4.1.2.1 Electron microscopy: HR-HAADF-STEM

STEM images of the reduced catalysts discussed in this section are presented in Figure 4-4. After reduction well defined and well dispersed platinum nanoparticles (NPs) are formed. The NP size histograms and the corresponding average size for each sample are shown in Figure 4-4 and Table 4-3, respectively. These reveal the same average NP size for all catalysts of 0.9 nm, regardless of platinum loading and of alumina type. The histograms also show a narrow size distribution with the size of approximately 70% of the measured NPs being comprised between 0.6 and 1.2 nm. The synthesis and reduction protocols thus uniformly control NP size and guaranty high metal dispersion. This NP size is similar to those reported in previous works [108,136] for similar ranges of Pt loading.

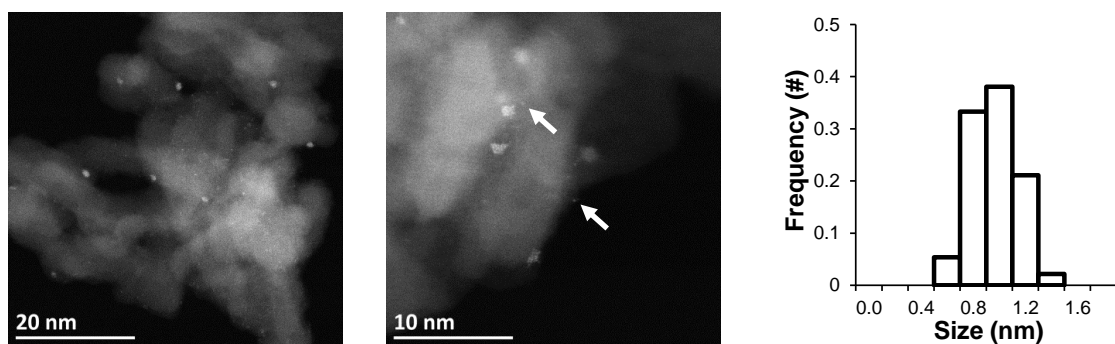
*Table 4-3 – Detailed results of nanoparticle size study, complementary to histograms of Figure 4-4.*

Sample	#measured NPS	Average NP size (nm)	Standard deviation (nm)	%[0.6; 1.2]nm
0.3%Pt/PuralSB3-0.1%Cl	171	0.87	0.16	75
1%Pt/PuralSB3-0.1%Cl	205	0.86	0.15	76
0.3%Pt/TH100-0.1%Cl	207	0.93	0.16	70
1%Pt/TH100-0.1%Cl	215	0.88	0.17	73

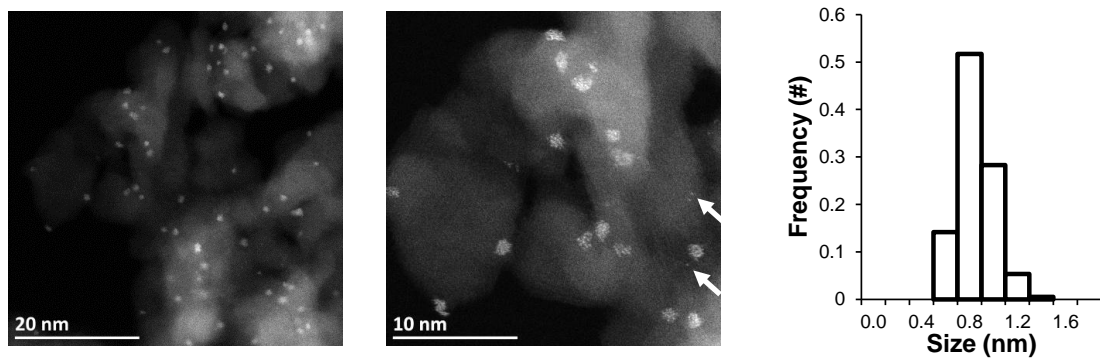
It can be discerned however that fewer NPs are present on the catalysts with 0.3%Pt loading. Indeed it seems logic that, at constant NP size, less impregnated platinum will result in less numerous nanoparticles. It can be thus easily deduced that the average distance between platinum NPs will be larger for catalysts with 0.3%Pt loading than for those with 1%Pt, assuming that the NP distribution on the support is homogeneous as it is qualitatively highlighted in STEM images of Figure 4-4.



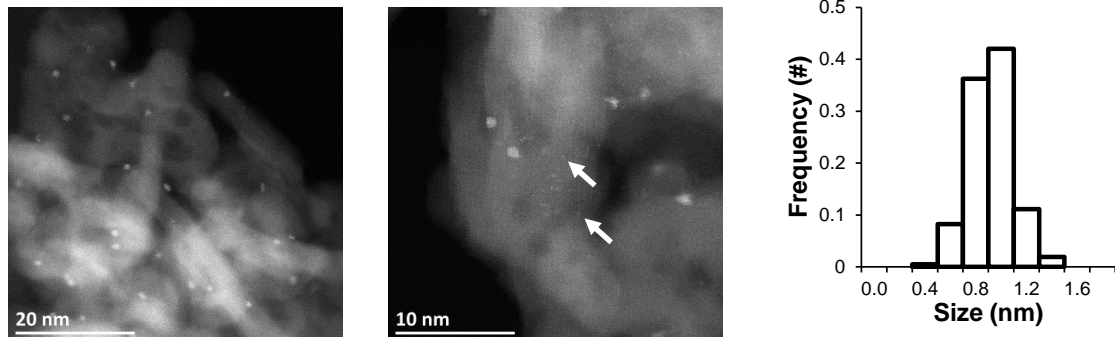
a) 0.3%Pt/PuralSB3-0.1%Cl reduced



b) 1%Pt/PuralSB3-0.1%Cl reduced



c) 0.3%Pt/TH100-0.1%Cl reduced



d) 1%Pt/TH100-0.1%Cl reduced

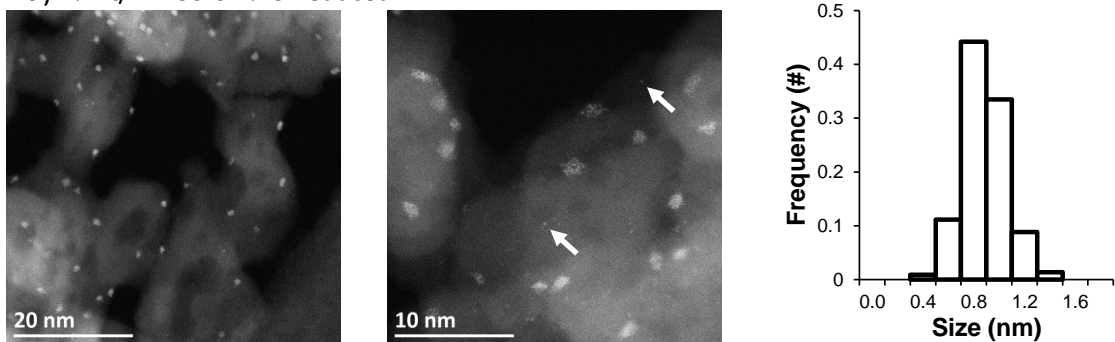
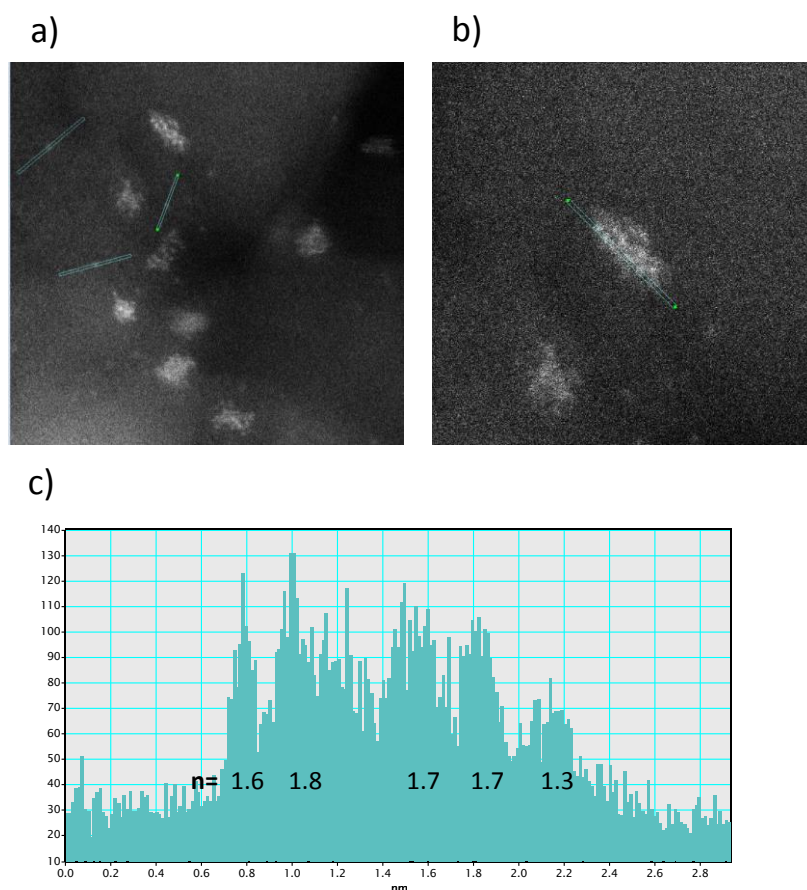


Figure 4-4 – HR-HAADF-STEM images and nanoparticle size histograms of four reduced catalysts a) 0.3%Pt/PuralSB3-0.1%Cl, b) 1%Pt/PuralSB3-0.1%Cl, c) 0.3%Pt/TH100-0.1%Cl, d) 1%Pt/TH100-0.1%Cl. White arrows highlight single atoms.



*Figure 4-5 – Detail of nanoparticle morphological study based on the analysis of the HAADF intensity for 1%Pt/PuralSB3-0.1%Cl reduced, a) three single atom reference paths, b) path through nanoparticle including five potential “stacks” of atoms, c) intensity graph for path of b) with the calculated  $n$  for each “stack”.*

Images acquired at higher magnification allow the platinum atoms that compose the nanoparticles to be observed. Nanoparticle morphology was studied measuring HAADF intensity to estimate the number of Pt atoms stacked perpendicular to the electron beam ( $n$ ) from the intensity of atomic column ( $I$ ), as the image intensity is roughly proportional to the square of the mean atomic number of the analysed area [93]. As measurements were performed on thin areas, alumina contribution to intensity can be neglected in first approximation. The intensity of three single atoms was measured, to estimate  $I_{SA}$  proportional to  $Z_{SA}^2$ . Stating that the atomic number of a column composed of  $n$  Pt atoms is equal to  $nZ_{SA}$ , by measuring intensity of nanoparticles the  $n$  parameter can be obtained as  $n \propto I/I_{SA}$ . An example of this analysis is given in Figure 4-5. At least one NP per sample was studied this way and it was consistently found that the NPs are composed of at most two layers of Pt atoms. This translates into a flat bi-planar morphology, often called “raft-like”, which had already been suggested for this type of samples from microscopic [89,108,122],

XAS [122] and ab initio studies [124,132]. Overall, NPs are composed of 10 to 20 Pt atoms, which is compatible with the Pt<sub>13</sub> nanoparticle model used in previous DFT studies [124,130,132]. DFT calculations [124] showed the bi-planar Pt<sub>13</sub> morphology is the most stable on the dehydrated (100) surface and a 3D morphology is the most stable on the (110) surface. Both the image intensity study and also a simple qualitative analysis by direct observation suggest 3D semi-spherical NPs are not present in our samples, their centre would appear with a higher intensity. Indeed, a follow up study [132] showed that the flat Pt<sub>13</sub> morphology is not exclusive to the (100) surface when it is stabilized by H and Cl migration.

It is also possible to observe the presence of several single atoms, highlighted by white arrows in Figure 4-4. The population of single atoms was quantified through a number of single atoms vs number of nanoparticles ratio (#SA/#NP). For each catalyst, the averaged ratios were estimated for three images taken at a high enough magnification to have an atomic resolution. For each image, single atoms and nanoparticles were counted in the region of the image judged to have optimal focus. Imaging in STEM mode on an aberration corrected microscope has a very small depth of field and the same image may include regions with different heights. The consequence is a less optimal focus in some regions that is enough to prevent single atoms from being observed, even if the resolution is good enough to identify the nanoparticles. The results are presented in Figure 4-6.

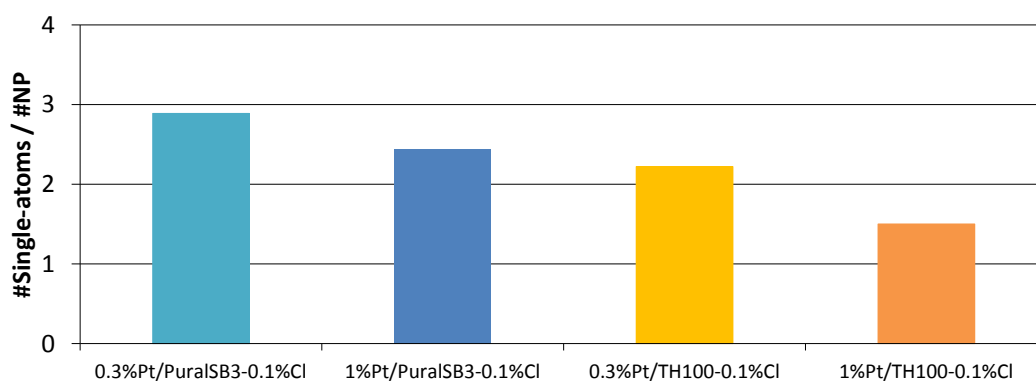


*Figure 4-6 – Quantification of single atom population through #Single atom/#NP ratio calculated for reduced catalysts 0.3%Pt/PuralSB3-0.1%Cl, 1%Pt/PuralSB3-0.1%Cl, 0.3%Pt/TH100-0.1%Cl and 1%Pt/TH100-0.1%Cl.*

Overall, it can be affirmed that about 15% of the deposited platinum atoms is present in the form of single atom, assuming that a NP is composed of 13 Pt atoms.

Two trends can be identified. Firstly, there seems to be an impact of platinum loading on the #SA/#NP ratio: the proportion of single atoms is smaller for the highest Pt loading on both supports. An explanation may be suggested by considering the work of Mager-Maury [132] showing that several small platinum clusters  $Pt_{1 < n < 13}$  are stabilized by H and Cl migration. Note that by dividing by #NP, the ratio is normalized and does not reflect the impact of %Pt in absolute quantity of metallic entities. However, at 0.1%Cl, there is very little chlorine left to stabilize the single atoms. For 1%Pt there is a higher absolute quantity of metallic entities for the same amount of chlorine ( $Pt/Cl \approx 1$  atom/atom), in comparison with the case at 0.3%Pt ( $Pt/Cl \approx 0.5$ ), resulting in a smaller proportion of single atoms.

This reasoning may seem a bit at odds with the results of section 4.1.1.1.2 showing that oxide catalysts' monoatomic complexes include one chlorine atom, even at the higher loading of 1%Pt. If there was one Cl atom per Pt for oxide catalysts at 1%Pt, why would there be less single atoms due to the Pt/Cl proportion after reduction? The reduction mechanism has not been elucidated in this work but something to be considered is that, for the oxide catalysts, two populations of chlorine atoms may be distinguished: those in oxychloride  $PtCl_xO_y$  complexes and those anchored on the surface of the support. The latter derived from the support acidification step of the synthesis procedure and are not expected to be affected by the reduction treatment, as this population should already correspond to the equilibrium state after calcination at 520°C. For the former it is not obvious that those Cl atoms will "stay put" on platinum atoms through a covalent bond as the complexes are reduced, lose oxygen and the nanoparticles form. A reasonable hypothesis would be that the Pt-Cl bond within the  $PtCl_xO_y$  complexes is broken after reacting with  $H_2$  leading to HCl formation, as the complex is being reduced. HCl is further exchanged with alumina surface hydroxyl groups, thus transforming into the second chlorine population. Chlorine migration would then have occurred uniquely from the support surface to the platinum entity, allowing for the explanation above.

Secondly, it was observed that the type of alumina also has an impact on the #SA/#NP ratio as the single atoms proportion is smaller for the catalysts supported on TH100. Two possible reasons can be explored, as this result is the expression of a differing stabilization of platinum between the two supports. On the one hand, this can be thought of in terms of

surface anchoring sites for platinum, either they are weaker (assuming equivalent sites) or there are fewer sites on TH100's surface.

On the other hand, it can be put down to Cl-to-Pt migration ability. It may be harder for chlorine on TH100's surface to migrate onto Pt entities than chlorine on PuralSB3's. This could be explained either by stronger anchoring of Cl on TH100's surface (which does not seem to be the case, see chapter 3) or by a difficult "access" of Cl to Pt due to distance/location. The former hypothesis is less likely, as it was shown in chapter 3 that chlorine is most favourably exchanged with hydroxyl groups in the crystallite edges and at this low loading of 0.1%Cl all Cl atoms should find their place in the edge sites on both aluminas. Nevertheless, both of these explanations are a reflection of the differing crystallite morphology of the supports (see chapter 3).

#### **4.1.2.2 X-ray absorption spectroscopy (XAS)**

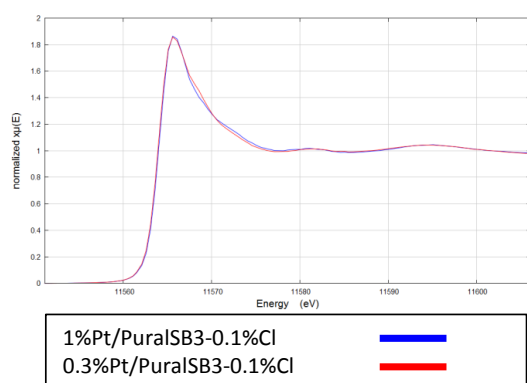
##### ***4.1.2.2.1 HERFD-XANES***

The HERFD-XANES spectra are presented in Figure 4-7. These are the spectra acquired at room temperature under He after in situ re-reduction. It is reminded that a poor control of hydrogen desorption during spectral acquisition has an impact on the descending portion of the post-edge, so small differences in this region of the spectra will not be interpreted. More details are available in section 2.2.2.3.3. The spectra were normalized using Athena from the Demeter 0.9.26 software package [184].

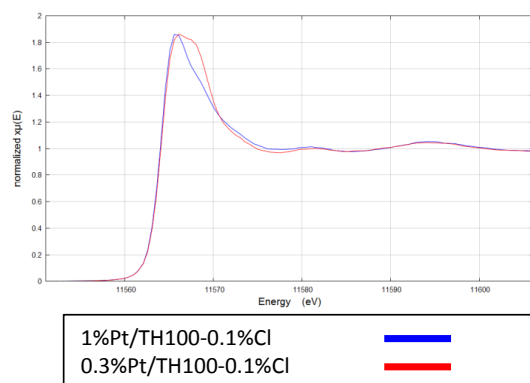
Comparison with spectra of the corresponding oxide catalysts (Figure 4-7, c and d), shown in section 4.1.1.1.1, shows clearly the impact of reduction on the white line: the intensity is two to three times lower than that of the oxides and the edge is shifted to lower energy by 3 eV.

Between the reduced samples, again they share the same post-edge features but now they present also the same white line intensity and edge energy. These results are coherent with the STEM observations of an homogeneous Pt nanoparticle size and shape, regardless of platinum loading or of type of alumina support. It can be concluded that this sub-nanometric homogeneity, indicative of the geometric surrounding of Pt atoms, indeed translates into an uniform electronic state.

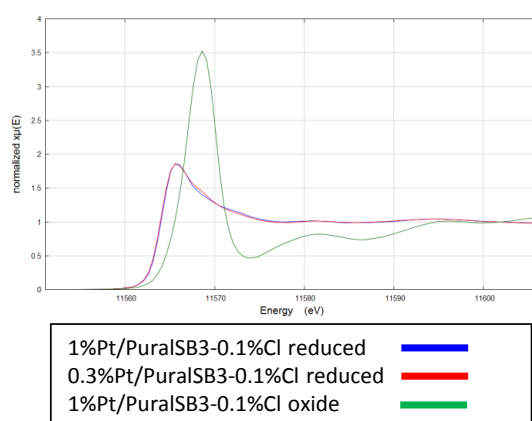
a) PuralSB3 reduced catalysts



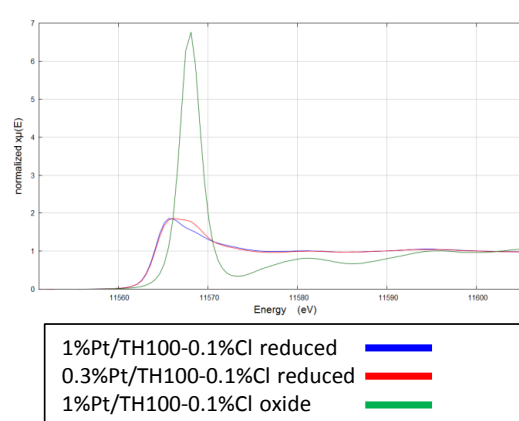
b) TH100 reduced catalysts



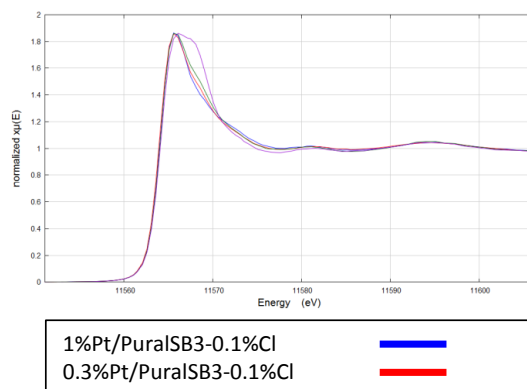
c) PuralSB3 reduced and oxide catalysts



d) TH100 reduced and oxide catalysts



e) Both PuralSB3 and TH100 reduced catalysts



f) idem

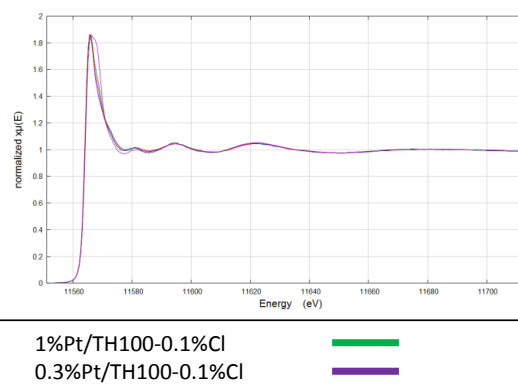


**Figure 4-7 – Pt  $L_3$  edge HERFD-XANES spectra of reduced catalysts at 0.1%Cl loading: a) supported on PuralSB3, b) supported on TH100, c) and d) compared with oxide counterpart, e) and f) catalysts of both supports.**

Nevertheless, one spectrum can clearly be distinguished, that of reduced 0.3%Pt/TH100-0.1%Cl. While the beginning of the white line follows that of the other samples, a large feature is present at 11567.8 eV, which will be referred to as “the unique feature”. As detailed in section 2.2.2.3.4, the spectra shown here are the result of a merger of several

scans. In Figure 4-8 those scans are shown, revealing the evolution of the unique feature with time. Each scan takes about 45 minutes, so approximately 8h passed between the first and the last scan. The unique feature gradually increases in intensity (black arrow) while at the same time the effect of the undesired hydrogen desorption that occurred during acquisition on the post-edge can also be observed (red arrow). It can be seen that the feature intensity variation had stabilized by the end of the acquisition, as the two last scans show no variation. This is reproducible, as the same catalyst was analysed during the successive synchrotron run and the same result was found (Appendix E).

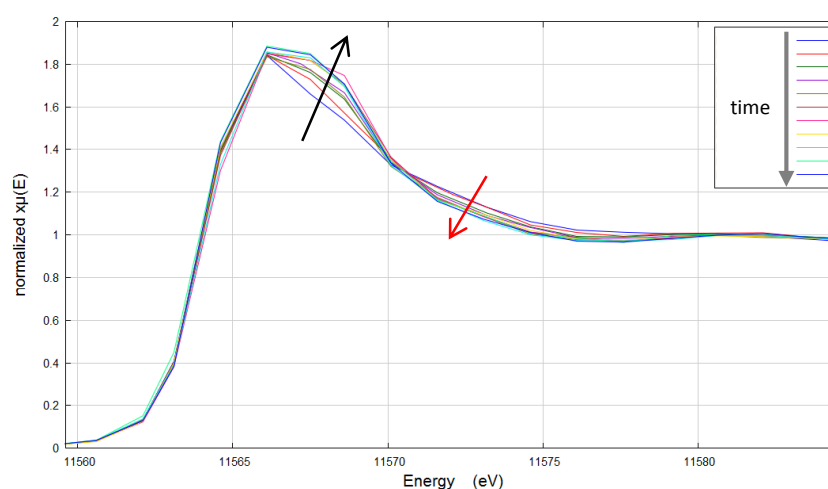


**Figure 4-8 – Pt L<sub>3</sub> edge HERFD-XANES scans of 0.3%Pt/TH100-0.1%Cl reduced illustrating their evolution during 8h of acquisition, namely the appearance of the unique feature (black arrow) and the impact of hydrogen desorption (red arrow).**

As Figure 4-9 shows, the unique feature on the descending portion of the WL of reduced 0.3%Pt/TH100-0.1%Cl appears at approximately the same energy, 11567.8 eV, as the edge of the corresponding oxide catalyst and of the PtO<sub>2</sub> reference, 11567.7 eV and 11567.9 eV respectively. However, the post-edge features of the oxides are very distinct from those of the reduced catalysts and such signature is not found on the post-edge of reduced 0.3%Pt/TH100-0.1%Cl, which is identical to that of the other reduced samples. Interestingly, Cui et al. [100] found the Pt L<sub>3</sub> edge XANES spectra of their single atom catalyst Pt/ $\gamma$ -Al<sub>2</sub>O<sub>3</sub>-nanorod after reduction at 200°C 2h under 5%H<sub>2</sub> to correspond precisely to that of their PtO<sub>2</sub> reference.

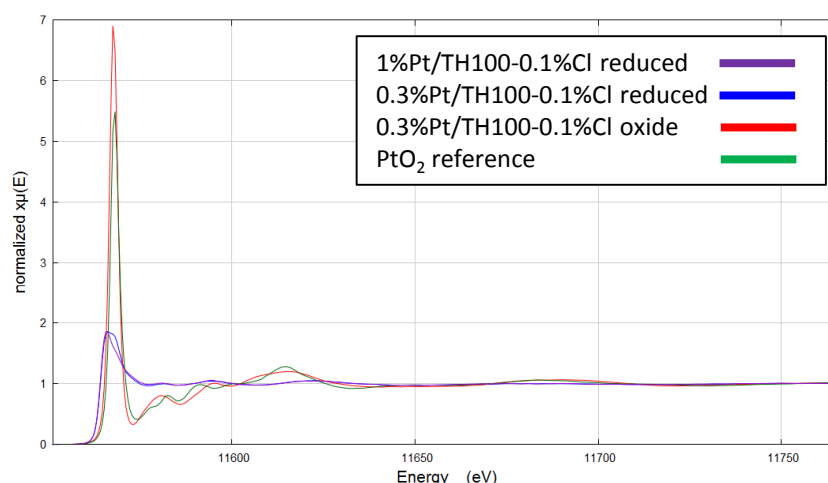


*Figure 4-9 – Pt  $L_3$  edge HERFD-XANES spectra of 1%Pt/TH100-0.1%Cl reduced, 0.3%Pt/TH100-0.1%Cl reduced, 0.3%Pt/TH100-0.1%Cl oxide and of  $PtO_2$  (reference).*

In an effort to better explain this “unique feature”, the experimental spectrum was compared to simulated XANES spectra of several DFT models of different Pt species supported on the dehydrated (100) surface using the FDMNES code [194]. Those that are the most relevant in interpreting the experimental data are displayed in Figure 4-10 and the ordinate scale was normalized to the maximum of the experimental spectrum with the most intense white line. The white line maximum of the oxide nanoparticle model  $Pt_{13}O_{22}$  (Figure 4-10 a) corresponds to that of the unique feature but the energy at which the edge starts is shifted by almost 2 eV and the white line intensity is almost two times larger than that of the experimental feature. Also, XANES scans of the in situ re-reduction under  $H_2$  at 500°C showed the successful reduction of the catalyst and the specifications of the He bottle used for the purge indicate the presence of less than 1 ppm of  $O_2$ . It is thus very unlikely that such an oxide complex would be formed in these conditions.



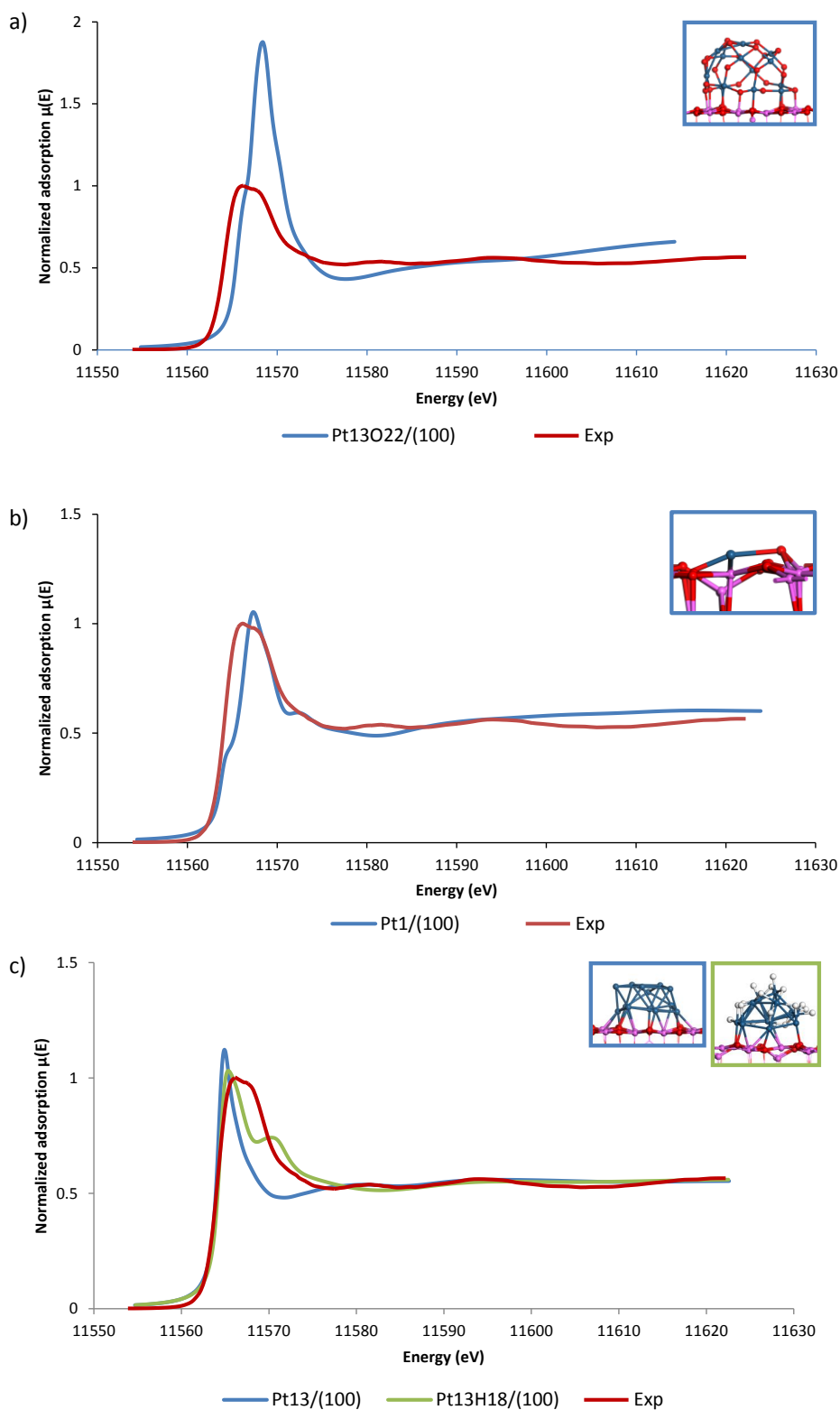


**Figure 4-10** –Comparison between Pt  $L_3$  edge HERFD-XANES spectrum of 0.3%Pt/TH100-0.1%Cl reduced, labelled “Exp”, and simulated XANES spectra of DFT models a)  $Pt_{13}O_{22}/(100)_{dehyd}$ , b)  $Pt_1/(100)_{dehyd}$ , c)  $Pt_{13}/(100)_{dehyd}$  and  $Pt_{13}H_{18}/(100)_{dehyd}$ . Insets contain illustrations of the DFT model used in the respective simulation.

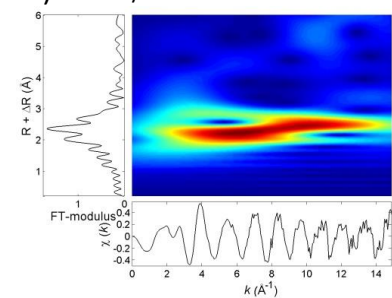
In contrast, the agreement with the reduced single atom model  $\text{Pt}_1$  simulated spectrum is notable (Figure 4-10 b). The white line energy maximum corresponds to that of the 11567.8 eV feature as well as the overall intensity. The simulated spectra of reduced  $\text{Pt}_{13}$  with and without adsorbed hydrogen (Figure 4-10 c) show that the initial part of the edge corresponds to Pt nanoparticles, which is equal to the edge of all the other catalysts. The unique feature can be clearly distinguished from the post-edge feature between 11570 eV and 11574 eV characteristic of H adsorption [115,129]. This suggests that: 1) the main XANES signal in the 0.3%Pt/TH100-0.1%Cl reduced sample and in the other catalysts corresponds to reduced nanoparticles that can be modelled as  $\text{Pt}_{13}$ , 2) the unique feature at 11567.8 eV in the 0.3%Pt/TH100-0.1%Cl reduced spectrum corresponds best to a single atom signature and cannot be associated with hydrogen adsorption on nanoparticles.

However, at this stage, it remains unclear why this signature would increase in intensity with time under He and parallel  $\text{H}_2$  desorption nor why it is detected on this catalyst only as the #SA/#NP ratio difference to other samples was of 9% at maximum. It is also intriguing that a single atom signature is found only at low chlorine loading, as chlorine is believed to stabilize such entities [132]. It could be useful to also calculate the XANES spectra of eventual  $\text{Pt}_1/(110)$  and  $\text{Pt}_1/(110)-(100)$  edge models to check whether the single-atom signature is always the same.

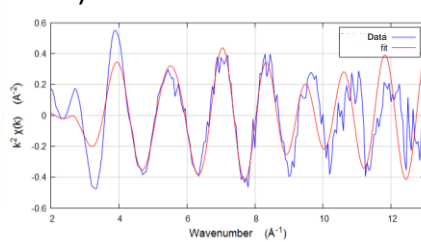
#### **4.1.2.2.2 EXAFS**

As previously, the EXAFS spectra were acquired and fitted following the method described in section 2.2.2.3.4 using Artemis from the Demeter software package [184]. The spectra ( $\chi(k)$  and FT) are presented in Figure 4-11, as well as the wavelet transform analysis and the best fit.

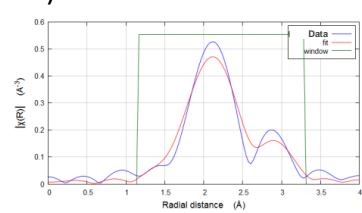
a1) 0.3%Pt/PuralSB3-0.1%Cl reduced



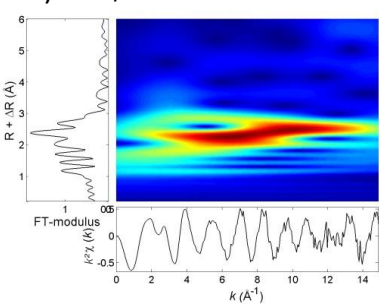
a2)



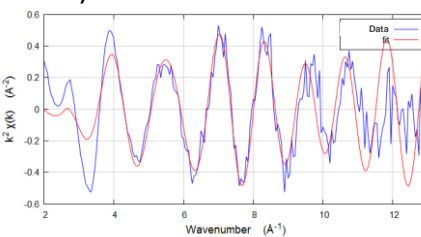
a3)



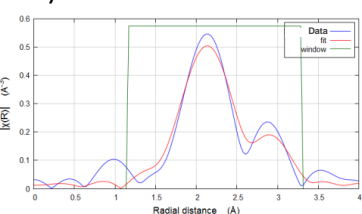
b1) 1%Pt/PuralSB3-0.1%Cl reduced



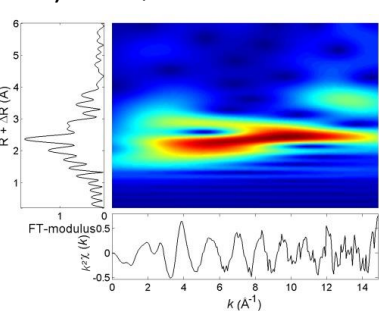
b2)



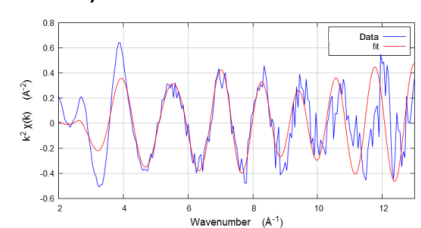
b3)



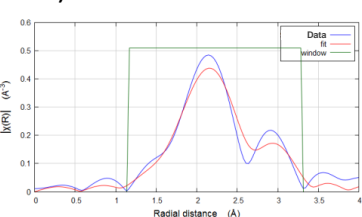
c1) 0.3%Pt/TH100-0.1%Cl reduced



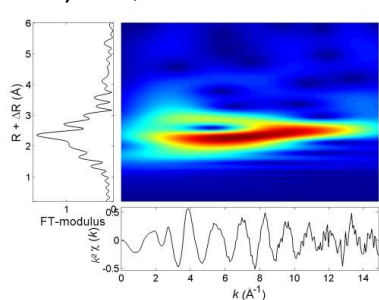
c2)



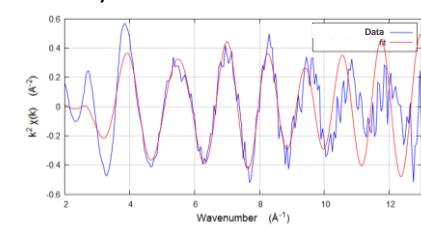
c3)



d1) 1%Pt/TH100-0.1%Cl reduced



d2)



d3)

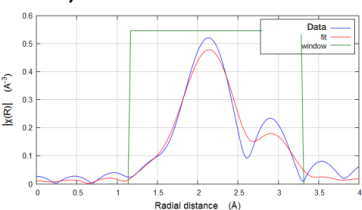


**Figure 4-11 - Wavelet transform analysis 1), EXAFS  $\chi(k)$  2) and magnitude of the Fourier transform  $|\chi(R)|$  (no phase correction) 3), all weighted by  $k^2$ . In 1) and 2), the red line represents the best fit. In 3), the fitting range is represented by the green line.**

Comparing these EXAFS  $\chi(k)$  spectra with those of the oxide catalysts in Figure 4-3, the difference is significant as the reduced catalysts show a greater signal amplitude at high wavenumbers, indicative of a heavy scatterer (Appendix F).

Again, the spectra are very similar between samples. The magnitude of the Fourier transform reveals two signals, one between 2 and 2.8 Å and another between 2.8 and 3.3 Å, which the wavelet transform analysis indicates would correspond to a light scatterer and a heavy scatterer, respectively. The heavy scatterer was successfully fitted as Pt, as would be expected.

For the light scatterer, the fitting was less straight forward. Oxygen at an approximate distance of 2 Å has been reported in the literature for similar samples [95,96,108,112,118] but it could not be fitted here. The lower limit of the k-range for the Fourier transform was lowered to different values to ensure this contribution was not being filtered out of the FT, however a Pt-O path at 2 Å could not be fitted in any case. Another probable scatterer would be chlorine, as it was the case for the oxide samples. Unfortunately a Pt-Cl distance at about 2.3 Å (both from reference CIF files and from QFS) could not be fitted either, in line with previous reports for reduced chlorinated catalysts in which a Pt-Cl distance was never found [95,96]. Note that this does not rule out the possibility of Cl migration onto platinum proposed by Mager-Maury et al. [132], it only means that a Pt-Cl distance is not detected. Imagining that one Cl atom migrates onto Pt<sub>13</sub>, CN(Pt-Cl) would be very low (<0.1) and so would be the contribution of this path to the  $\chi(k)$  spectra, as path degeneracy is a multiplying factor in the EXAFS equation.

The FT magnitude peak seems to be centred at about 2.5 Å. Such a distance is reported in two previous works: Vaarkamp et al. [122] found a Pt-O<sub>long</sub> distance at 2.7 Å (CN=1.2) and at 2.3 Å (CN=1.5) for 1%Pt/Al<sub>2</sub>O<sub>3</sub>-Cl reduced at 300°C and 450°C respectively, Sinkler et al. [108] found a Pt-O<sub>long</sub> distance at 2.5 Å (CN=1.9) for a 0.35%Pt/Al<sub>2</sub>O<sub>3</sub>-Cl catalyst reduced at 700°C in H<sub>2</sub>, Li et al. [113] found a long Pt-O/C distance at 2.55 Å (CN=1.8) for 1%Pt/SiO<sub>2</sub> after ethylene hydrogenation and under H<sub>2</sub>, and Stakheev et al. found a Pt-O<sub>long</sub> distance at 2.5 Å (CN=0.7) for a reduced 1%Pt/ Al<sub>2</sub>O<sub>3</sub>-Cl catalyst, but only in the presence of hydrogen. Computational work [132] on the effect of H and Cl migration on Pt<sub>1<n<13</sub> NPs supported on the (110) and (100) surfaces described several most stable structure models which exhibit

mean Pt-Al distances between 2.31 and 2.67 Å and mean Pt-O distances between 2.02 and 2.54 Å. Thus, Pt-O<sub>long</sub> or Pt-Al distances at 2.5 Å were considered.

Paths obtained from Pt<sub>1</sub> and Pt<sub>13</sub> supported on (100) [90,147] as well as from the QFS tool were tested for both O and Al scatterers. As the results were equivalent, for consistency sake the results obtained using the QFS tool are presented. The parameters obtained for the best fit presented in Figure 4-11 are detailed in Table 4-4 showing that in this case a Pt-Al distance was fitted. The fit parameters for when Pt-O<sub>long</sub> was used are presented in Table 4-5.

**Table 4-4 - EXAFS fitting results for reduced catalysts considering Pt-Al coordination for the light scatterer.  $E_0=11566.1$  eV;  $1.15 < R < 3.3$  Å;  $N_{ind}=8$ ;  $N_{var}=7$ .**

Reduced catalyst	k-range (Å <sup>-1</sup> )	Path	Coordination number	R (Å)	σ <sup>2</sup> (Å <sup>2</sup> )	ΔE <sub>0</sub> (eV)	R-factor
0.3%Pt/PuralSB3-0.1%Cl	4.2 – 8.3	Pt-Al	1.1±0.4	2.40±0.06	0.004±0.005	5±1	0.06
		Pt-Pt	3±1	2.72±0.03	0.004±0.003		
1%Pt/PuralSB3-0.1%Cl	4 – 8.3	Pt-Al	1.0±0.4	2.42±0.06	0.004±0.005	5±1	0.04
		Pt-Pt	3.4±0.9	2.72±0.03	0.003±0.002		
0.3%Pt/TH100-0.1%Cl	4 – 8.3	Pt-Al	1.1±0.4	2.39±0.06	0.005±0.004	5±1	0.05
		Pt-Pt	3.2±0.8	2.73±0.04	0.003±0.002		
1%Pt/TH100-0.1%Cl	3.9 – 8.3	Pt-Al	1.2±0.4	2.40±0.06	0.006±0.004	5±1	0.05
		Pt-Pt	3.2±0.8	2.73±0.03	0.003±0.002		

**Table 4-5 - EXAFS fitting results for reduced catalysts considering Pt-O<sub>long</sub> coordination for the light scatterer.  $E_0=11566.1$  eV;  $1.15 < R < 3.3$  Å;  $N_{ind}=8$ ;  $N_{var}=7$ .**

Reduced catalyst	k-range (Å <sup>-1</sup> )	Path	Coordination number	R (Å)	σ <sup>2</sup> (Å <sup>2</sup> )	ΔE <sub>0</sub> (eV)	R-factor
0.3%Pt/PuralSB3-0.1%Cl	4.2 – 8.3	Pt-O <sub>long</sub>	2.6±0.5	2.59±0.06	0.003±0.001	2.9±0.6	0.01
		Pt-Pt	2.9±0.5	2.68±0.02	0.007±0.003		
1%Pt/PuralSB3-0.1%Cl	4 – 8.3	Pt-O <sub>long</sub>	2.2±0.5	2.61±0.03	0.0029±0.0008	3.1±0.7	0.02
		Pt-Pt	3.0±0.5	2.68±0.02			
0.3%Pt/TH100-0.1%Cl	4 – 8.3	Pt-O <sub>long</sub>	2.8±0.8	2.59±0.03	0.008±0.005	3.4±0.9	0.03
		Pt-Pt	2.4±0.7	2.70±0.02	0.002±0.002		
1%Pt/TH100-0.1%Cl	3.9 – 8.3	Pt-O <sub>long</sub>	2.7±0.6	2.61±0.02	0.006±0.004	3.6±0.7	0.02
		Pt-Pt	2.6±0.6	2.70±0.02	0.002±0.002		

When using Pt-O<sub>long</sub>, the coordination number for this scatterer is around 3, which was considered high, knowing that about 75% of Pt is in the form of NPs. When Pt-Al is fitted, the

light scatterer has a coordination of 1 and this seems much more reasonable. Indeed, average coordination numbers calculated for the Pt<sub>13</sub> supported on a dehydrated (100) model [147], considering the covalent bonds only, are CN(Pt-Pt)=4.7; CN(Pt-O)=CN(Pt-Al)=0.54. Using both O<sub>long</sub> and Al paths to fit the signal centred on 2.5 Å was also tried (Appendix G) and resulted in CN(Pt-O<sub>long</sub>)+CN(Pt-Al) between 2 and 3. It could still be discussed that this Pt-Al path may correspond to a Pt-O-Al structure, but a “short” Pt-O distance ( $\approx 2\text{\AA}$ ) could not be successfully fitted, as explained previously. Between these three cases there is no clear improvement on how the fit reproduces the  $\chi(k)$  spectral features. The fit in which Pt-Al is used is presented here as “best fit” on the basis of this coordination number discussion. In fact, it was not possible to assess definitively if the light scatterer signal corresponds to oxygen, aluminium or to both.

The light scatterer evidences that, as was the case for the oxide catalysts, platinum is in strong interaction with the support. This significant contribution of the light scatterer may correspond to the contribution of the single atoms, that will only exhibit coordination to support atoms, to the EXAFS signal. Note also that in recent investigations [90] of 0.3%Pt/Al<sub>2</sub>O<sub>3</sub> in both oxide and reduced state, prepared using a non-chlorinated precursor, such distances revealing of metal-support interactions were not found, despite their STEM characterization revealing results identical to those of this report (NPs and SA present, same NP size). Perhaps even at the low loading of 0.1% chlorine has an impact on the metallic phase, especially considering the migration of only one Cl atom onto a NP may be sufficient to increase stability of the smallest objects [132].

Regarding the fitted Pt-Pt path, as Table 4-4 shows, a coordination number between 3 and 3.4 is found in agreement of previous reports also using chlorinated aluminas [95,108]. Other works report Pt-Pt coordination numbers from 4 up to 8, even for low Pt loadings between 0.3 and 0.8% [95,96,111,112,118,122]. As mentioned above, for the DFT Pt<sub>13</sub>/(100)<sub>dehyd</sub> model the Pt-Pt coordination number would be 4.7. The fact that the experimental CN(Pt-Pt) is slightly lower may be explained either by the natural heterogeneity of the number of Pt atoms and exact morphology of the NPs or by the averaging of the signal of the Pt single atoms that have no Pt-Pt coordination. A distance of 2.72 Å was consistently fitted for this path, which is inferior to the bulk distance of 2.773 Å, a characteristic of metal nanoparticles [121]. This is in line with the same studies cited above

that found distances between 2.68 and 2.76 Å. Interestingly, Bus's study [111] of hydrogen adsorption onto reduced Pt/Al<sub>2</sub>O<sub>3</sub> found differing Pt-Pt distances for the same sample exposed to H<sub>2</sub> or under vacuum, 2.72 and 2.68 Å respectively. The impact of hydrogen adsorption on Pt-Pt distance is also revealed by DFT calculations considering the average bond length for Pt<sub>13</sub>H<sub>18</sub>/(100)<sub>dehyd</sub> and Pt<sub>13</sub>/(100)<sub>dehyd</sub> which is respectively 2.75 and 2.68 Å [130]. As the evolution of the post-edge during data acquisition suggested, it is likely that there are still hydrogen traces adsorbed onto platinum even after evacuation and under He.

Overall, the EXAFS analysis reveals no significant difference between the samples, regardless of Pt loading and of the type of alumina support, having found a strong interaction with O or Al atoms from the support.

#### **4.1.2.3 Conclusion**

After reduction the metallic phase is mostly in the form of well-defined nanoparticles with a consistent average size of 0.9 nm and a flat morphology and of single atoms that are estimated to make up 15% of the overall deposited platinum atoms. Pt loading and the type of support were found to have a slight impact on this single atom population.

The XANES study confirms the reduced state of platinum and all catalysts have identical spectra with the exception of 1%Pt/TH100-0.1%Cl reduced for which a post-edge feature by 11567.8 eV appeared during the 8h long acquisition under He. Simulated XANES spectra from various DFT structural models suggest this unique feature corresponds to single atoms while the edge profile shared with all the other catalysts is comparable to the simulated spectrum of a Pt<sub>13</sub> model.

Fitting of the EXAFS portion of the spectra revealed strong interaction of Pt with the support through a long Pt-Al or Pt-O distance that dominates the FT magnitude spectra of all samples and may be the contribution of the single atoms to the signal. First shell Pt-Pt distance was found to be approximately 2.72 Å with a coordination number of about 3 for all samples. The EXAFS analysis showed no significant impact of metal loading nor of type of support on the fitted structural parameters.

## ***4.2 Samples with 1.4%Cl loading***

This section presents the characterization of the samples with the highest chlorine loading of 1.4%Cl in both oxide and reduced form. As previously, HR-HAADF-STEM, HERFD-XANES and EXAFS results are discussed.

The catalysts presented here are:

0.3%Pt/PuralSB3-1.4%Cl ; 1%Pt/PuralSB3-1.4%Cl

0.3%Pt/TH100-1.4%Cl ; 1%Pt/TH100-1.4%Cl

This section is then divided in three parts: one dedicated to the catalysts in oxide state including STEM results for PuralSB3 samples and XAS results for all samples; a second one devoted to the case of TH100 samples, for which a more detailed microscopic study was performed, including electron tomography and in situ reduction experiments, which is the object of a publication to be submitted and a third one in which the reduced catalysts STEM results for PuralSB3 samples and XAS results for all reduced samples are presented.

### **4.2.1 Oxide catalysts**

The oxide catalysts were analysed by HR-HAADF-STEM and XAS experiments, HERFD-XANES and EXAFS.

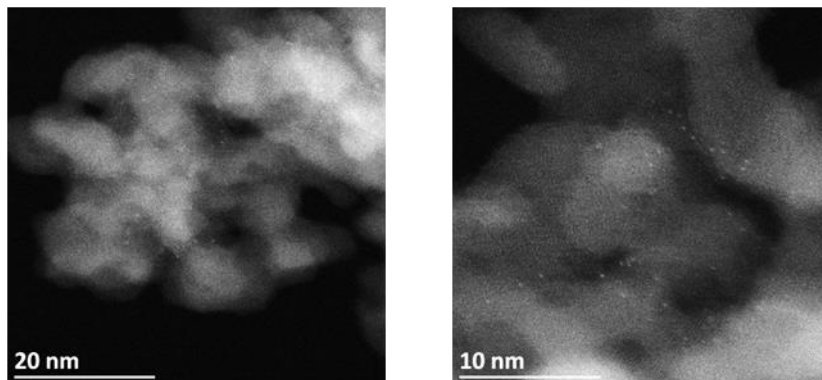
#### **4.2.1.1 Electron microscopy: HR-HAADF-STEM**

STEM images of the PuralSB3 samples are presented in Figure 4-12 and of TH100 samples are available in section 4.2.2. In both cases platinum is well dispersed and well distributed over the support. For the lower Pt loading there are mostly single atoms, some dimers and trimers are observed and clusters of more than 5 atoms are rare, in agreement with previous reports [89]. For the higher loading however, single atoms, small groups of atoms (dimers, trimers) and weakly bounded clusters with more than 5 atoms are discerned. These clusters do not present a clear structure and it is sometimes difficult to distinguish if a given atom is part of the cluster. Note that in oxide state these are oxide complexes where Pt is coordinated to O and Cl atoms (see ahead, section 4.2.1.2), which are not visible in STEM. Thus at 1%Pt there is a larger degree of platinum aggregation than at 0.3%Pt. This suggests



that at the higher loading, surface anchoring sites become saturated and the remaining platinum has to agglomerate.

a) 0.3%Pt/PuralSB3-1.4%Cl oxide



b) 1%Pt/PuralSB3-1.4%Cl oxide

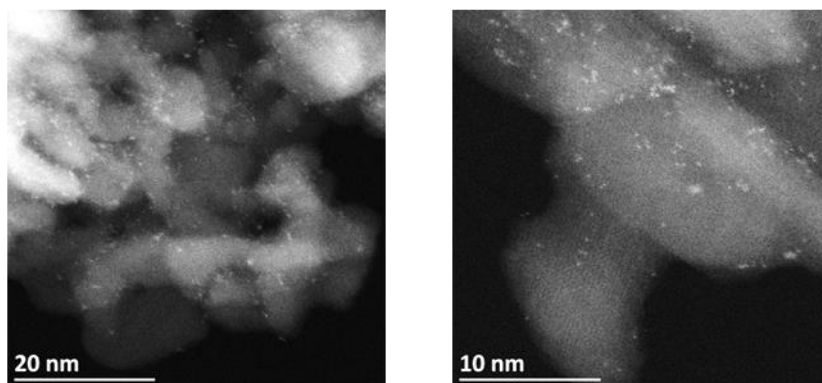


*Figure 4-12 – HR-HAADF-STEM images of PuralSB3 oxide catalysts a) 0.3%Pt/PuralSB3-1.4%Cl and b) 1%Pt/PuralSB3-1.4%Cl.*

#### 4.2.1.2 X-ray absorption spectroscopy (XAS)

The oxide catalysts were analysed by XAS (Pt  $L_3$  edge) at two beamlines at the ESRF: PuralSB3 samples were analysed at BM30 and TH100 samples at BM16.

##### 4.2.1.2.1 HERFD-XANES

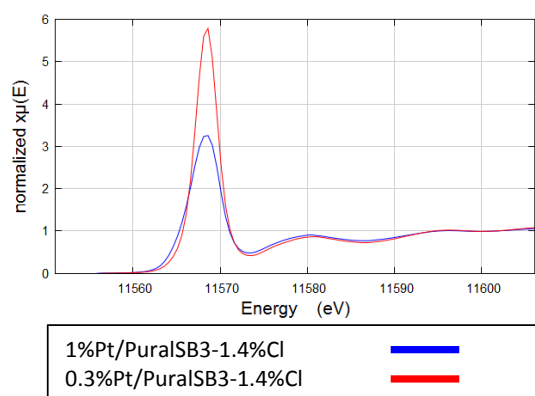
The HERFD-XANES spectra are presented in Figure 4-13. The spectra were normalized using Athena from the Demeter software package [184].

Overall the observations made for the catalysts at 0.1%Cl are reproduced here: the four catalysts have the same post-edge features (Figure 4-13 e), for PuralSB3 samples there is a

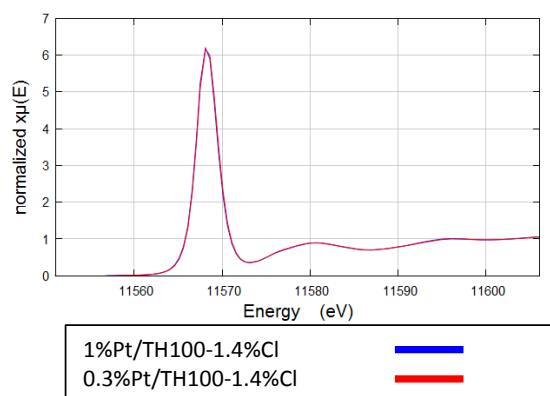
great effect of metal loading on white line intensity, for TH100 samples no impact of Pt loading is detected.

The same explanation as in section 4.1.1. is offered for the PuralSB3 spectra. As the STEM images show, at higher metal loading small clusters are present while at 0.3%Pt there are mostly single atoms, so at 1%Pt the XANES features reveal a more metallic character of Pt with a decreased WL intensity. The same trend was verified by comparison with XANES spectra simulated using the FDMNES code of  $\text{Pt}_1\text{O}_4/(\text{100})_{\text{dehyd}}$  and  $\text{Pt}_{13}\text{O}_{22}/(\text{100})_{\text{dehyd}}$  [90,147] in Figure 4-2 of section 4.1.1.1.

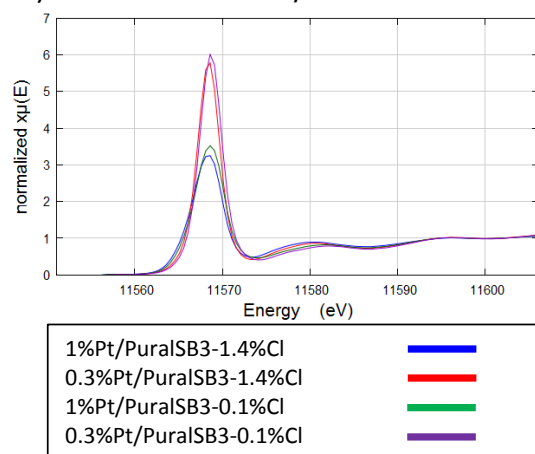
a) PuralSB3 oxide catalysts



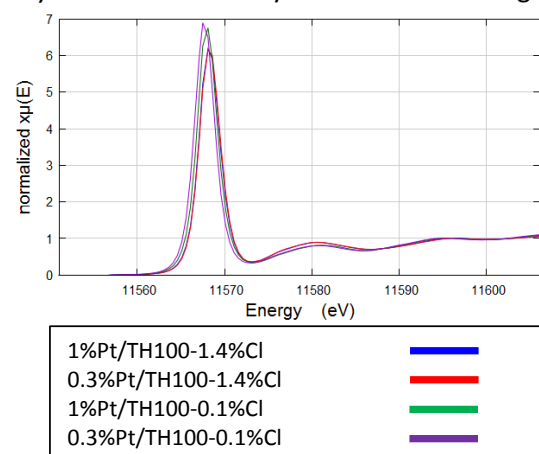
b) TH100 oxide catalysts



c) PuralSB3 oxide catalysts at both Cl loadings



d) TH100 oxide catalysts at both Cl loadings



e) both PuralSB3 and TH100 oxide catalysts

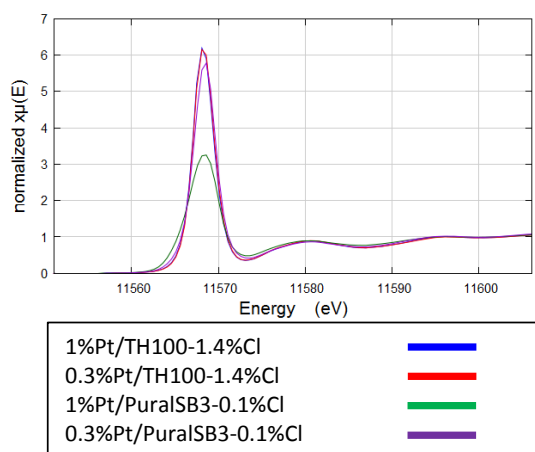


**Figure 4-13 – Pt  $L_3$  edge HERFD-XANES spectra of oxide catalysts at 1.4%Cl loading: a) supported on PuralSB3, b) supported on TH100, and comparison of c) all PuralSB3 oxide samples, d) all TH100 oxide samples and e) all oxide samples.**

However, the simulated spectra were not sufficient to interpret the experimental TH100 XANES spectra and it may be due to a more important impact of chlorine, as the current oxide

Pt DFT models do not include Cl. Indeed, Figure 4-13 d shows that the edge energy is slightly higher (by 0.5 eV) and WL intensity is lower for samples with 1.4%Cl. Again, these two trends seem contradictory. Also, the small impact of %Pt on the edge of samples at 0.1%Cl disappears completely for 1.4%Cl. For PuralSB3 catalysts the impact of Cl loading is less pronounced, with slightly higher WL intensity for 0.1%Cl samples.

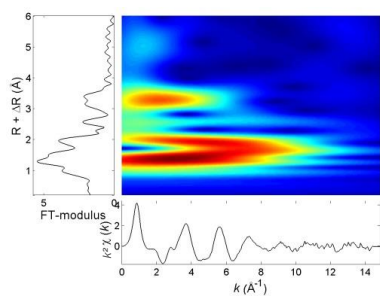
#### **4.2.1.2.2 EXAFS**

The EXAFS spectra of the same catalysts were fitted as described in section 2.2.2.3.4 using Artemis from the Demeter software package [184]. Figure 4-14 shows the  $\chi(k)$  and FT spectra, wavelet transform analysis and best fit.

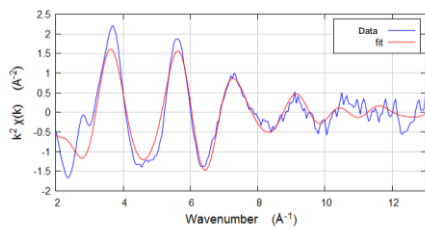
The  $\chi(k)$  spectra are all very similar between samples. Now at 1.4%Cl loading the wavelet analysis indicates clearly that there are two 1<sup>st</sup> shell light scatterers and in the magnitude spectra of the Fourier transform the signal between 1.3 and 2.3 Å is broad or even divided in two in the case of TH100. Indeed the  $\chi(k)$  is distinct from what was obtained for the catalysts with 0.1%Cl (Figure 4-3), particularly after 6 Å<sup>-1</sup>. The signal in the 2.3 – 3.3 Å region was treated as a 2<sup>nd</sup> shell with a light scatterer, all the considerations and reflections detailed in section 4.1.1.1 on this topic are valid here.

The fitted parameters are detailed in Table 4-6 and Table 4-7, Pt-O<sub>long</sub> (best fit of Figure 4-14) or Pt-Al<sub>long</sub> being used respectively. Figure 4-15 shows a comparison of coordination number of the fitted paths and of the Pt-Cl path distance in function of Pt and Cl loading and support type considering the fits in which the Pt-O<sub>long</sub> path was used. It is possible to see that there is little impact of the metal loading and of support type on the coordination numbers of all three paths for a given chlorine loading. At 1.4%Cl however the coordination number for the Pt-Cl path is between 2.1 and 2.7, indicating that the surface oxide complex PtCl<sub>x</sub>O<sub>y</sub> is enriched in chlorine at this loading. The distance obtained for the Pt-Cl path is somewhat larger for TH100 samples, which may explain the peak division in the FT magnitude spectra that is not observed for PuralSB3 samples. This distance is also slightly shorter (2 to 4%) for the samples at 0.1%Cl, perhaps to compensate the loss of Cl coordination during dechlorination. As the XANES spectra indicated, the high chlorine loading has a larger impact on TH100 supported catalysts rather than on PuralSB3 based catalysts.

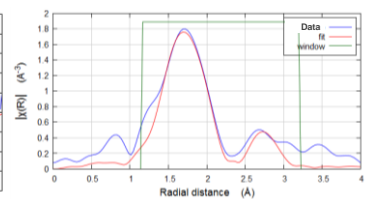
a1) 0.3%Pt/PuralSB3-1.4%Cl reduced



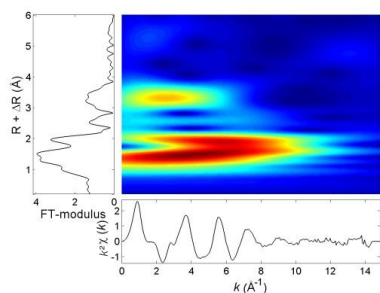
a2)



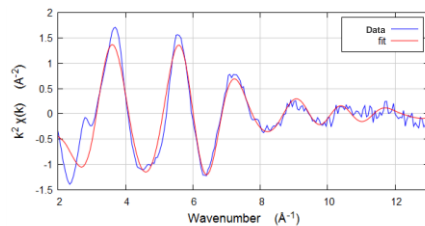
a3)



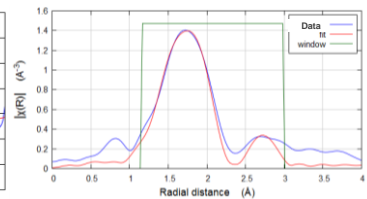
b1) 1%Pt/PuralSB3-1.4%Cl oxide



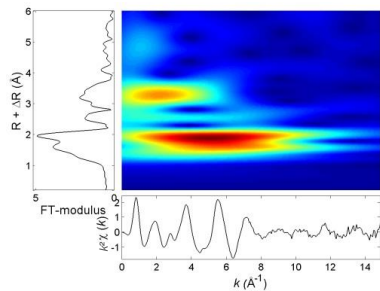
b2)



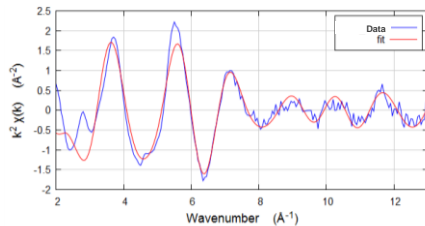
b3)



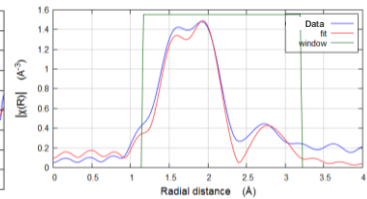
c1) 0.3%Pt/TH100-1.4%Cl oxide



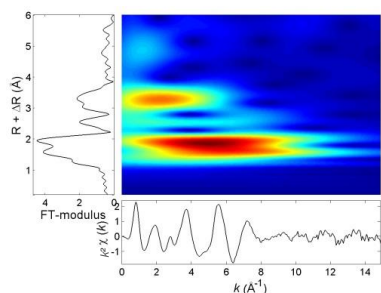
c2)



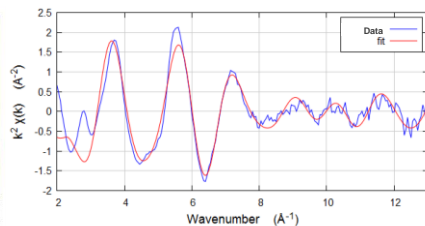
c3)



d1) 1%Pt/TH100-1.4%Cl oxide



d2)



d3)

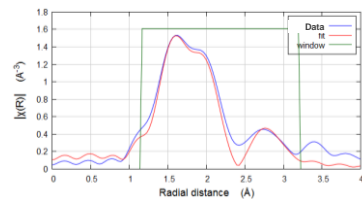


**Figure 4-14 – Wavelet transform analysis 1), EXAFS  $\chi(k)$  2) and magnitude of the Fourier transform  $|\chi(R)|$  (no phase correction) 3), all weighted by  $k^2$ , of oxide catalysts at 1.4%Cl loading. In 1) and 2) the red line represents the best fit. In 3), the fitting range is represented by the green line.**

**Table 4-6 – EXAFS fitting results for oxide catalysts at 1.4%Cl loading considering a 2<sup>nd</sup> shell Pt-O<sub>long</sub> coordination.**

$E_0=11566.1$  eV;  $1.15 < R < 3.2$  Å;  $N_{ind}=12$ ;  $N_{var}=8$ .

Oxide catalyst	k-range (Å <sup>-1</sup> )	Path	Coordination number	R (Å)	σ <sup>2</sup> (Å <sup>2</sup> )	ΔE <sub>0</sub>	R-factor
0.3%Pt/PuralSB3-1.4%Cl	3.6 – 11.8	Pt-O	3.9±0.3	2.00±0.02	0.003±0.001	10.7±0.7	0.04
		Pt-Cl	2.1±0.3	2.28±0.02			
		Pt-O <sub>long</sub>	4±1	3.09±0.05	0.002±0.004		
1%Pt/PuralSB3-1.4%Cl	3.6 – 12.3	Pt-O	3.4±0.2	1.99±0.01	0.005±0.001	8.6±0.6	0.03
		Pt-Cl	2.6±0.2	2.28±0.01			
		Pt-O <sub>long</sub>	2.5±0.7	3.08±0.02	0.002±0.003		
0.3%Pt/TH100-1.4%Cl	4.2 – 12	Pt-O	3.3±0.2	2.00±0.02	0.001±0.001	11.1±0.6	0.03
		Pt-Cl	2.7±0.2	2.31±0.01			
		Pt-O <sub>long</sub>	5±1	3.11±0.03	0.003±0.003		
1%Pt/TH100-1.4%Cl	4.2 – 11.8	Pt-O	3.8±0.4	2.00±0.03	0.001±0.001	11.1±0.5	0.02
		Pt-Cl	2.2±0.4	2.31±0.03			
		Pt-O <sub>long</sub>	4.6±0.9	3.10±0.02	0.003±0.002		

**Table 4-7 - EXAFS fitting results for oxide catalysts at 1.4%Cl loading considering a 2<sup>nd</sup> shell Pt-Al<sub>long</sub> coordination.**

$E_0=11566.1$  eV;  $1.15 < R < 3.2$  Å;  $N_{ind}=12$ ;  $N_{var}=8$ .

Oxide catalyst	k-range (Å <sup>-1</sup> )	Path	Coordination number	R (Å)	σ <sup>2</sup> (Å <sup>2</sup> )	ΔE <sub>0</sub>	R-factor
0.3%Pt/PuralSB3-1.4%Cl	3.6 – 11.8	Pt-O	4.1±0.3	2.01±0.02	0.002±0.001	11.4±0.8	0.04
		Pt-Cl	1.9±0.3	2.29±0.02			
		Pt-Al <sub>long</sub>	2.0±0.7	2.95±0.03	0.002±0.003		
1%Pt/PuralSB3-1.4%Cl	3.6 – 12.3	Pt-O	3.6±0.3	1.99±0.01	0.005±0.001	9.1±0.6	0.03
		Pt-Cl	2.4±0.3	2.29±0.01			
		Pt-Al <sub>long</sub>	1.5±0.5	2.93±0.02	0.004±0.003		
0.3%Pt/TH100-1.4%Cl	4.2 – 12	Pt-O	3.4±0.2	1.99±0.02	0.0012±0.0006	10.1±0.6	0.02
		Pt-Cl	2.6±0.2	2.31±0.02			
		Pt-Al <sub>long</sub>	2.4±0.6	2.95±0.03	0.004±0.002		
1%Pt/TH100-1.4%Cl	4.2 – 11.8	Pt-O	3.8±0.4	2.00±0.03	0.001±0.001	10.6±0.6	0.02
		Pt-Cl	2.3±0.4	2.31±0.03			
		Pt-Al <sub>long</sub>	2.7±0.5	2.94±0.02	0.004±0.002		

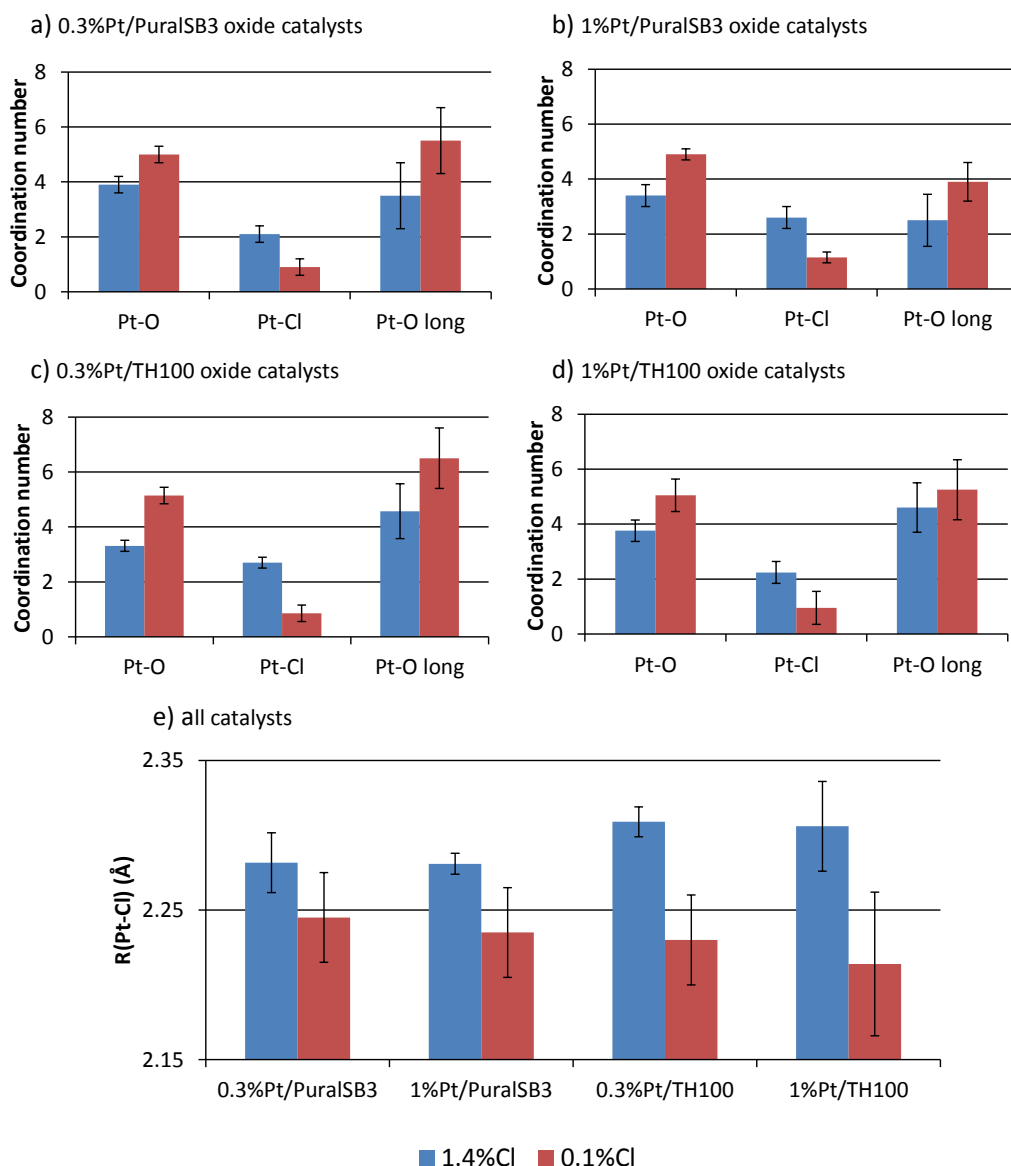


Figure 4-15 – Comparison of fitted parameters for each path between all oxide catalysts at two chlorine loadings, 0.1% in red and 1.4% in blue, namely coordination number a) to d) and distance fitted for the Pt-Cl path e).

#### 4.2.1.3 Conclusion

Oxide catalysts present highly dispersed platinum single atoms, with  $Pt_{n>5}$  clusters appearing at higher metal loading, fact confirmed by EXAFS analysis in which no Pt-Pt contribution is found. Those single atoms are in the form of a  $PtCl_xO_y$  oxide complex ( $CN(Pt-O) \approx 3.5$ ;  $CN(Pt-Cl) \approx 2.5$ ) in strong interaction with the support ( $2^{nd}$  shell Pt-O/Al). Interestingly the Pt-Cl distance in samples at 1.4%Cl was found to be larger than in samples at 0.1%Cl loading. This distance, at 1.4%Cl loading only, is also slightly longer for TH100 supported catalysts than for PuralSB3's.

The XANES spectra also revealed a larger impact of the high chlorine loading on TH100 than on PuralSB3 supported catalysts. For the former there is a shift in edge energy and white line intensity with increased Cl loading as well as the disappearance of the impact of metal loading in the spectra. In the latter the chlorine loading augmentation causes only a slight shift in white line intensity. However, there is always a great influence of platinum loading on the white line intensity of PuralSB3 catalysts, explained by the agglomeration of platinum into clusters at higher metal loading.



#### **4.2.2 Detailed microscopic study of TH100-1.4%Cl catalysts by advanced HAADF-STEM techniques**

The catalysts supported on TH100 with 1.4%Cl loading were the object of a detailed microscopy study including in situ experiments and electron tomography with the goal of deciphering the NP formation mechanism and of finding the location of the nanoparticles. These two samples were selected for such analysis because of three main factors: the TH100 support crystallites' morphology is more adequate for the study of NP location, this work is particularly focused on chlorinated samples, and both techniques are very time consuming and only a limited number of samples could be analysed. Those results are presented in the form of a publication draft that is to be submitted. The references herein are listed at the end of this section. The corresponding Supporting Information is available in Appendix H.

# Atomic resolution insight on the formation, size and distribution of platinum nanoparticles supported on $\gamma$ -alumina

Ana T. F. Batista<sup>†</sup>, Walid Baaziz<sup>‡</sup>, Johan Chaniot<sup>† §</sup>, Anne-Lise Taleb<sup>†</sup>, Ovidiu Ersen<sup>‡</sup>, Maxime Moreaud<sup>† Δ</sup>, Fabrice Diehl<sup>†</sup>, Céline Chizallet<sup>†</sup>, Anne-Sophie Gay<sup>†</sup> and Pascal Raybaud<sup>†\*</sup>

<sup>†</sup>IFP Energies nouvelles, Rond-point de l'échangeur de Solaize, BP 3-69360 Solaize, France

<sup>‡</sup>Institut de Physique et Chimie des Matériaux de Strasbourg, CNRS-Université de Strasbourg, 67034 Strasbourg, France

<sup>§</sup>Laboratoire Hubert Curien, CNRS-Université Jean Monnet de Saint-Etienne, 42000 Saint Etienne, France

<sup>Δ</sup>Centre for Mathematical Morphology, MINES ParisTech, 77305 Fontainebleau, France

*Keywords: Platinum, nanoparticles, alumina, electron microscopy, electron tomography, DFT*

**ABSTRACT:** The clear description of the morphology and location with respect to the support of metallic sub-nanometric particles remains a current experimental challenge. High resolution-HAADF-STEM coupled with in situ and tomographic analyses, was undertaken on industrial type chlorinated  $\gamma$ -Al<sub>2</sub>O<sub>3</sub> supported Pt active phase with 0.3 and 1%<sub>w/w</sub>Pt loading. The results highlight the formation of flat nanoparticles of 0.9 nm and Pt single atoms in the reduced state. While abundant single atoms and weakly cohesive clusters are observed in the oxide state, the relative population of single atoms and Pt nanoparticles in the reduced state is not affected by metal loading in contrary to the total number of NPs. Average geodesic distance between nanoparticles quantified by mathematical analysis was found to be controlled by Pt loading and to correspond to a statistic distribution. Evaluation of support tortuosity descriptors using the nanoparticle positions confirmed their uniform distribution on the support. For the first time, tomographic volumes revealed the vast majority of nanoparticles to be located on the edges or defects (steps, kinks) of the support crystallites. Density functional theory calculations show this edge position is energetically as favorable as the facets.

## INTRODUCTION

Noble-metal particles dispersed on oxide supports have several industrial applications from fine chemistry to petroleum refining, pollution abatement and biomass conversion.<sup>1,2</sup> This is the case for platinum supported on  $\gamma$ -Al<sub>2</sub>O<sub>3</sub>, which has been consistently studied in the literature with the advancement of characterization techniques, mostly using model systems.<sup>3–10</sup>

For many structure sensitive reactions,<sup>11</sup> the reactivity of metal active sites provided by Pt particles depends on their size and shape. Catalyst improvement thus depends on advancing knowledge of these features. Overall, for platinum loadings inferior to 1%<sub>w/w</sub> Pt, particles have a size of about 1 nm and are highly dispersed on the alumina support.<sup>12–17</sup> These nanoparticles (NPs) are formed during reduction,<sup>13,18</sup> as the catalysts in oxide state display mostly isolated Pt atoms.<sup>12</sup> The NPs of nanometric or even sub-nanometric sizes were described as having a bi-planar raft-like morphology.<sup>12,13,19</sup> In addition, single atoms (SA), binuclear and trinuclear Pt species were also observed in reduced catalysts.<sup>8,12,13</sup>

NP size and shape are inherently associated to the chemical interaction of NP with the support,<sup>20</sup> depending on the particle's location on the alumina nano-crystallite facets. Indeed, density functional (DFT) theory calculations suggested that the flat bi-planar morphology is the most stable for a Pt<sub>13</sub> NP on the dehydrated (100) alumina surface, whereas a 3D morphology is favored on hydrated (110) surface.<sup>21</sup> This modification of the NP shape as a function of the environment was recently assigned to a "ductility effect"<sup>22</sup> which implies the dynamic reconstruction of the Pt based NP<sup>23–27</sup> as a function of support surface,<sup>21</sup> reaction conditions<sup>7,28</sup> or chemical composition of NP<sup>22</sup> (when a second metallic element is added for instance).

Depending on the targeted applications, it is required to promote the acidity of the alumina support by chlorine doping.<sup>29,30</sup> In these cases, the catalyst belongs to the famous class of metal/acid bifunctional catalyst, for which the distance between metallic/acid sites is a known driver for selectivity variations<sup>31</sup> interpreted in light of the "intimacy criterion".<sup>32</sup> When both metallic and acid sites are deposited on the same support, the fine control of the distance between them requires their location to be determined. A preferred anchoring site on the alumina surface for Pt NPs has yet to be unequivocally found, especially for industry relevant samples. A <sup>27</sup>Al MAS NMR study by Kwak et al.<sup>5</sup> concluded that supported platinum oxide, assumed to be PtO, is bonded to Al<sub>v</sub> surface sites. These are considered to be mostly present on the alumina (100) surface after dehydration by thermal treatment at high temperatures. By electron microscopy<sup>33</sup> the morphology of a low surface area alumina with large 20x70 nm crystallites exposing (110) and (111) type surfaces was analyzed in detail. A sample containing 5%<sub>w/w</sub> Pt was found to exhibit large NPs to be equally present on both surface terminations. In both cases, these results can hardly be extrapolated to commercial catalysts in which significantly lower metal loadings (generally one order of magnitude smaller) are used, leading to highly dispersed NP on high surface area aluminas of smaller crystallites (d<20 nm).

Additionally, platinum has been used in several studies looking to explore the potential of single atom catalysts, be it using alumina<sup>3,5,18,34–36</sup> or other supports such as nitrogen-doped microporous hierarchical carbon<sup>37</sup> or ceria,<sup>38–41</sup> to name a few. Two challenges are common to all preparations, concerning the formation of nanoparticles upon activation and the fact that the SA may not be intrinsically more active than NPs. SA sintering is particularly

favorable upon reduction in the case of  $\text{Pt}_1/\text{Al}_2\text{O}_3$ ,<sup>18,34</sup> although single atom dispersion was maintained after reduction at 200°C under 5% $\text{H}_2$  and after hydrosilylation reaction test at 100°C when nano-rod alumina was used<sup>3</sup>. These are relatively mild activation and reaction conditions, but the remarkable SA stability is clearly associated with the alumina crystallites' morphology.

In the present work, the metallic Pt phase on a chlorinated alumina ( $\gamma\text{-Al}_2\text{O}_3$ ) support is comprehensively studied using microscopic methods with the goal of elucidating a) how the NP formation occurs during reduction, b) the size and morphology of NPs on the reduced catalyst, c) NP location on the alumina crystallites and of d) quantifying the distance between NPs.

Transmission electron microscopy is a key technique for characterizing the morphology of supported NPs. In particular, High-angle annular dark-field - Scanning transmission electron microscopy (HAADF-STEM) mode is widely used for morphological characterization at the nanoscale of supported noble metal particles and is one of the best tool for the objectives at hand. HAADF detection mode is based on the Rutherford scattering process, so image intensity is roughly proportional to the square of the atomic number of the material.<sup>8</sup> This means high Z elements such as metals appear with high contrast as opposed to the oxide support. Aberration-corrected instruments have allowed for high-resolutions in the range of 0.1 nm with a good signal to noise ratio.<sup>8,13</sup> Other techniques were coupled to the HAADF imaging: electron tomography provides spatial information through 3D reconstruction of an object<sup>42-45</sup> and recent technological advancements in electron microscopy have facilitated in situ experiments in which metal particles can be observed in real time during thermal treatments.<sup>46-49</sup>

Herein, we combine HR-HAADF-STEM with in situ and tomographic experiments to get unequaled level of information regarding the NP formation, size, morphology and most importantly, their location on the alumina support and their inter-particle distance. For this, two catalysts representative of commercial products were prepared with 0.3% and 1%<sub>w/w</sub> Pt loading supported on a high surface  $\gamma$ -alumina doped with 1.3%<sub>w/w</sub> chlorine. Tomographic segmented models are obtained and quantified geodesic distances evaluated thanks to mathematical analysis. Density functional theory calculations provide an atomistic

view of the local environment of the platinum particles at the locations identified experimentally

## EXPERIMENTAL SECTION AND METHODS

**Catalyst preparation.** Catalysts were prepared by diffusional impregnation of  $\gamma$ - $\text{Al}_2\text{O}_3$  extrudates prepared from TH100 commercial boehmite from Sasol ( $S_{\text{BET}}=149 \text{ m}^2/\text{g}$  by  $\text{N}_2$  physisorption) with a  $\text{H}_2\text{PtCl}_6$  and HCl solution, followed by drying overnight and calcination at  $520^\circ\text{C}$  for 2h under dry air (heating  $5^\circ\text{Cmin}^{-1}$ ,  $1\text{Lmin}^{-1}\text{g}_{\text{cat}}^{-1}$ ). The chlorine loading was increased by thermal treatment at  $520^\circ\text{C}$  adding a HCl organic precursor to the air flow. The catalyst obtained after this treatment is referred to as being “oxide”. The oxide catalysts were reduced ex situ under  $\text{H}_2$  flow at  $500^\circ\text{C}$  for 2h, after a 30 min pre-calcination at  $520^\circ\text{C}$  under dry air ((heating  $5^\circ\text{Cmin}^{-1}$ ,  $1\text{Lmin}^{-1}\text{g}_{\text{cat}}^{-1}$ ). Two catalysts were prepared so as to have a chlorine loading of  $1.3\%_{\text{w/w}}$  and platinum loading of  $0.3\%_{\text{w/w}}$  or  $1\%_{\text{w/w}}$  (measured for oxide samples by X-ray fluorescence). They are referred to as oxide or reduced  $0.3\%\text{Pt}/\gamma\text{-Al}_2\text{O}_3\text{-Cl}$  and  $1\%\text{Pt}/\gamma\text{-Al}_2\text{O}_3\text{-Cl}$ , respectively.

**Scanning transmission electron microscopy.** High resolution high angle annular dark field in scanning transmission electron microscopy (HR-HAADF-STEM) imaging, HAADF-STEM in situ reduction experiments and HAADF-STEM electron tomography analyses were carried out on a Cs-corrected JEOL JEM 2100F microscope, operated at 200kV, equipped with a JEOL HAADF detector. For the HR-STEM images, the camera length used in the HAADF mode was 10 cm, corresponding to inner and outer diameters of the annular detector of 60 and 160 mrad, respectively. The size of the electron probe in STEM mode is 0.11 nm. Before the STEM analyses, the powdered samples were deposited without solvent on a 300 mesh holey carbon copper grid. The nanoparticle size histograms and average size were obtained from at least 200 measurements from images taken at the same magnification. Nanoparticle morphology and shape was studied measuring HAADF intensity to estimate the number of Pt atoms stacked perpendicularly to the electron beam ( $n$ ) from the intensity of atomic column ( $I$ ), given that the image intensity is roughly proportional to the square of the mean atomic number of the analyzed area.<sup>8</sup> As the measurements were performed on thin areas, alumina contribution to intensity was neglected in first approximation. The intensity of several single atoms ( $\text{SA}$ ) were measured, to estimate the proportionality factor between  $I_{\text{SA}}$  and  $Z_{\text{SA}}^2$ . Starting from the assumption that the atomic number of a column composed of  $n$  Pt atoms is

equal to  $nZ_{SA}$ , by measuring intensity  $I$  in nanoparticles,  $n \propto VI/I_{SA}$ . Single atom (SA) population was quantified through a number of SA to number of NP ratio calculated for several images at the same magnification.

**Electron tomography.** The powdered samples were deposited without solvent on a previously plasma cleaned 200 mesh holey carbon grid which was mounted on a tomographic single-tilt sample holder. For the two reduced catalysts the tilt series were acquired in HAADF mode using  $2.5^\circ$  increments by using the tomography plug-in of the Digital Micrograph software, which controls the specimen tilt step by step, the defocusing and the specimen drift. Two series per sample of circa 200 nm large objects composed of less than 20 alumina crystallites were acquired. Image alignment was performed through fiducial-less methods, namely a combination of cross-correlation and center of mass methods using the IMOD software.<sup>50</sup> The reconstructed 3D volumes were obtained using the algebraic reconstruction technique (ART)<sup>51</sup> implemented in the TomoJ plugin<sup>52</sup> in the ImageJ software. Segmented 3D models were constructed using the displaying capabilities and the isosurface rendering method on the Slicer software.<sup>53,54</sup>

**Geometrical analysis of the segmented volume.** Inter-NP distance calculations and tortuosity assessments were conducted on the segmented volumes using the *M-tortuosity* algorithm<sup>55,56</sup> that combines geometric tortuosities between two points defined as the ratio of the geodesic distance (length of the shortest path following the support surface) and the Euclidean distance (length of the straight path) between them. This is a two-step calculation. First, M-coefficients are computed as the harmonic mean of the geometric tortuosities weighted by the inverse of the geodesic distances. Secondly, M-scalar, global tortuosity descriptor, is calculated as the harmonic mean of the M-coefficients weighted by the inverse of the Euclidean distance to the center of mass of the considered volume. An indicator of confidence in the M-scalar value is  $\sigma_c$  which is twice the standard deviation of the M-coefficients divided by the square root of the number of points. The set of points upon which these operators were calculated was either the segmented model's own NP positions or a set of up to 200 points with uniform density of points, called as stratified distribution.

**In situ experiments.** A *Protochips Atmosphere* set up (in situ holder, gas manifold, heating system) was used for the TEM in situ reduction experiments. A suspension of powdered sample in ethanol (1  $\mu$ L) was deposited on the sample supporting chip, consisting of a SiC

chip with six holes covered by an electron-transparent thin SiN membrane that is then mounted on the in situ holder. The cell is sealed by another chip. After insertion of the holder in the microscope column and checking for leaks, the system is purged 3 times with Ar (back fill pressure 300 torr) then left overnight under Ar flow ( $0.2 \text{ cm}^3/\text{min}$  and pressure of 50 torr) in order to remove the residual  $\text{H}_2\text{O}$  molecules and/or the residual air content. The reduction treatment is realized under atmospheric pressure (760 torr) with a gas flow of  $0.1 \text{ cm}^3/\text{min}$  as follows (Figure 1): heating to  $200^\circ\text{C}$  at  $5^\circ\text{C}/\text{min}$  under Ar to choose the zones for imaging (1); heating to  $520^\circ\text{C}$  at  $5^\circ\text{C}/\text{min}$  under dry air and left for 30 min (pre-calcination, 2); cooling to  $200^\circ\text{C}$  under Ar (3); heating to  $500^\circ\text{C}$  at  $5^\circ\text{C}/\text{min}$  under  $\text{H}_2$  and left for 120 min (reduction, 4); further heating to  $600^\circ\text{C}$  and to  $700^\circ\text{C}$  to check nanoparticle stability (5). These different steps aim at mimicking the ex situ catalysts reduction procedure. Non imaged zones during the in situ treatment were also analyzed at the end of the treatment to check that identical states are recovered which confirms that no beam effect has occurred.

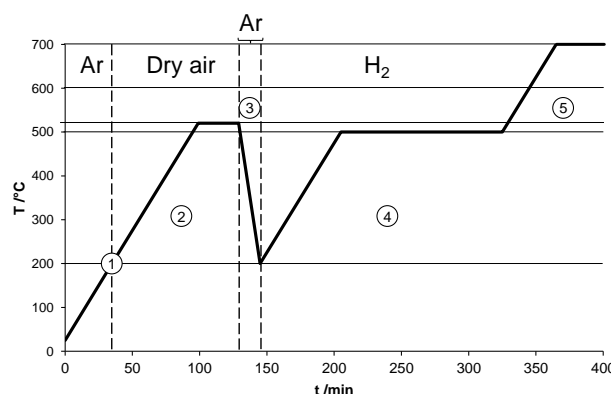


**Figure 1.** Treatment sequence used during the in situ reduction experiments. Numbers 1 to 5 indicate the stages described in the text.

**DFT calculations.**  $\text{Pt}_{13}$  supported on  $\gamma\text{-Al}_2\text{O}_3$  was modeled using the PBE-dDsC exchange correlation functional<sup>57,58</sup> and PAW pseudopotentials<sup>59</sup> with an energy cut off of 400 eV using the VASP code.<sup>60,61</sup> The criterion for the convergence of the self-consistent cycles was fixed to  $10^{-7}$  eV. Geometry optimizations were performed using a conjugate-gradient algorithm and convergence criterion on forces of  $0.01 \text{ eV } \text{\AA}^{-1}$ . The  $\text{Pt}_{13}/(100)$  (dehydrated) and  $\text{Pt}_{13}/(110)$  ( $11.8 \text{ OH}/\text{nm}^2$ ) models previously reported by Mager-Maury et al.<sup>62</sup> were considered as references and were re-optimized as described above.  $\text{Pt}_{13}$  nanoparticles with the same initial morphology as in the  $\text{Pt}_{13}/(100)_{\text{dehyd}}$  model were deposited in a similar position on the (100) side of the (110)-(100)  $\gamma\text{-Al}_2\text{O}_3$  hydrated or chlorinated edge model<sup>63</sup>

(Figure S1 of SI) and then optimized. This edge model is a nano-rod resulting from cleaving the alumina bulk<sup>64</sup> in the directions perpendicular to the (110) and the (100) surfaces. It includes two edge terminations, the Al-side exposing Al atoms and the O-side exposing O atoms. Here two hydration degrees were considered: 1H<sub>2</sub>O molecule per edge cell and 6H<sub>2</sub>O molecules per edge cell (saturated edge sites and hydrated (110) side). The chlorinated edge models are obtained by exchanging either one or both the terminal hydroxyls on the Al-side with Cl.<sup>63</sup> The binding energy ( $E_b$ ) of a nanoparticle ( $Pt_n$ ) on a given substrate ( $subs$  = surface or edge) in kJ/mol per Pt atom was calculated according to Equation 1, where  $E(Pt_1)$  is the energy of a single Pt atom in the center of a 20x20x20 Å<sup>3</sup> cell in vacuum.

$$E_b(Pt_n - subs) = [E(Pt_n - subs) - E(subs) - nE(Pt_1)]/n \quad \text{Eq. 1}$$

## RESULTS

**HR-HAADF-STEM imaging of oxide catalysts.** Typical HR-HAADF-STEM images of both oxide catalysts are shown in Figure 2. The supported metal oxide created during the calcination in the presence of chlorine is presumed to consist of a  $PtCl_xO_y$  species,  $PtCl_4O_2$  having been suggested.<sup>65,66</sup> Note that O and Cl atoms are not visible in STEM mode. Overall, platinum is well dispersed and uniformly distributed over the support. At 0.3%Pt loading, there are mostly single atoms and some dimers and trimers are also observed, as found previously.<sup>12,18</sup> On the observed regions, clusters of more than 5 atoms were rare. For the higher loading of 1%Pt however, single atoms, small groups of less than 5 Pt atoms and weakly cohesive clusters with more than 5 atoms are visible. These clusters often appear elongated and for some of them it is hard to determine if a given atom is part of the cluster or not. Since they do present ill-defined structures, the determination of size histogram for these oxide clusters was not possible.

Assuming that there is a given number of anchoring sites for the platinum precursor on the surface of the support, the presence of  $Pt_{n>5}$  clusters at higher loading suggests that for 0.3%Pt there is at most one Pt atom per occupied site, stabilized by Cl and O coordination, while for 1%Pt such sites should be saturated, causing subsequent Pt atoms to coalesce and form the observed oxide clusters.



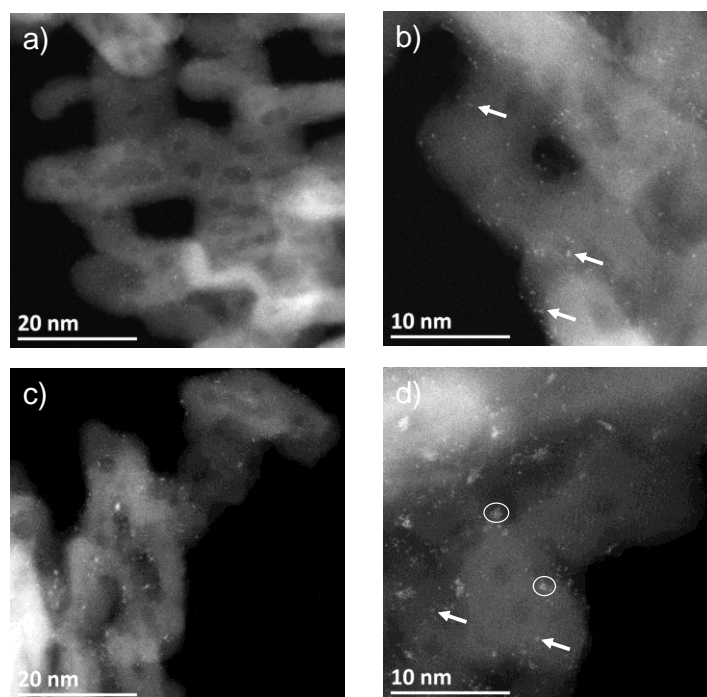


*Figure 2. HR-HAADF-STEM images of oxide catalysts a), b) 0.3%Pt/ $\gamma$ -Al<sub>2</sub>O<sub>3</sub>-Cl and c), d) 1%Pt/ $\gamma$ -Al<sub>2</sub>O<sub>3</sub>-Cl . White arrows highlight single atoms. Clusters composed of more than 5 atoms are circled in white in d).*

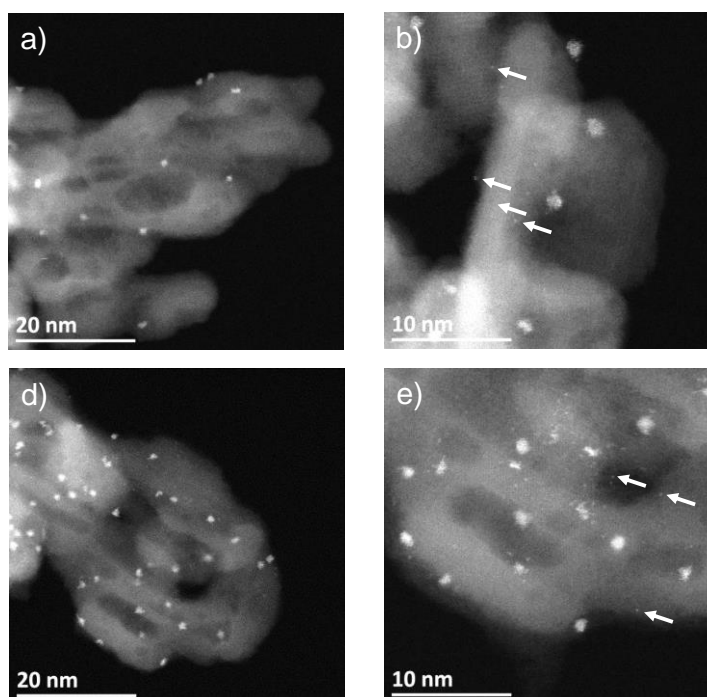


*Figure 3. HR-HAADF-STEM images of reduced catalysts a), b) 0.3%Pt/ $\gamma$ -Al<sub>2</sub>O<sub>3</sub>-Cl and c), d) 1%Pt/ $\gamma$ -Al<sub>2</sub>O<sub>3</sub>-Cl. White arrows highlight some single atoms.*

**HR-HAADF-STEM imaging of reduced catalysts.** The HR-HAADF-STEM images (Figure 3) for the same two catalysts, now after ex situ reduction at 500°C, are presented. Platinum is still

nicely dispersed, now in the form of well-defined nanoparticles (NPs) composed of 10 to 20 atoms. In both cases the average NP size is of about 0.9 nm and the size histograms (Figure 4) for both samples are similar, showing that 75% of measured NPs are in the 0.6-1.2 nm range. Thus, the catalyst preparation and reduction protocols consistently result in Pt NPs of homogeneous size, which is not sensitive to Pt loading. At the same time, at iso-NP-size, the increase of Pt loading simply results in the increased number of Pt NPs.

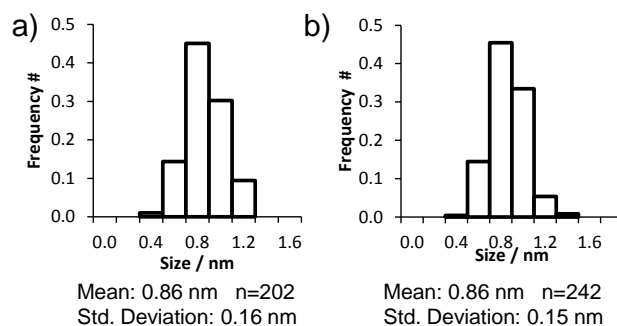


Figure 4. Nanoparticle size histograms obtained for reduced a) 0.3%Pt/γ-Al<sub>2</sub>O<sub>3</sub>-Cl and b) 1%Pt/γ-Al<sub>2</sub>O<sub>3</sub>-Cl.

The NPs were found to have a flat bi-planar morphology through HAADF intensity analysis (Figure 5), as the “atomic columns” aligned perpendicularly to the electron beam in the studied NPs are composed of at most 2 Pt atoms. The analysis was cautiously performed using relevant images obtained before the beam interaction caused the atoms in the NPs to move. This bi-planar morphology is fully compatible with the previously found by DFT studies of Pt<sub>13</sub> clusters on the (100) alumina surface.<sup>21</sup> Other microscopy analyses also referred to such nanoparticles as “raft-like”.<sup>12,13</sup>

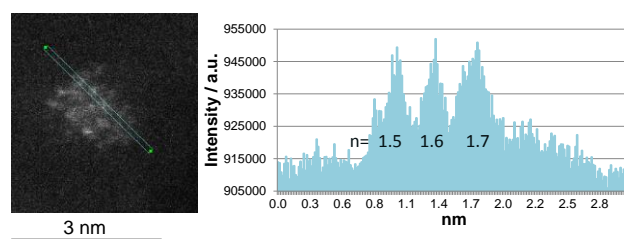


Figure 5. HAADF intensity profile and respective atom column quantification for a nanoparticle belonging to 1%Pt/γ-Al<sub>2</sub>O<sub>3</sub>-Cl.

Lastly, single atoms (SA) are highlighted and their population was quantified by the ratio “number of SA / number of NP” which is close to 2.8 whatever the Pt loading, which thus has little impact on their relative abundancy.

**HAADF-STEM in situ experiments.** The homogeneous NP size distribution found between the two reduced samples was not expected, considering the observations made for the oxide catalysts, where differing Pt species are present. To gather information on nanoparticle formation, the 1%Pt/ $\gamma$ -Al<sub>2</sub>O<sub>3</sub>-Cl catalyst was imaged during reduction using a dedicated in situ holder and set-up. Images obtained at different steps of the treatment are shown in Figure 6, for two analyzed regions. Before reduction, a few of the larger clusters of the oxide sample, such as those described previously, are visible (Figure 6-a), and the situation does not change at the end of the pre-calcination (Figure 6-b). Once under H<sub>2</sub> and at 500°C, Pt nanoparticles appear with a better contrast, indicator of the metallic state of NPs (Figure 6-c,d). Even after two hours at 500°C under H<sub>2</sub>, there is no sign of mobility nor of coalescence of the nanoparticles. Only when the temperature is raised to 700°C it can be observed that some NPs have coalesced. Similar final states were found in the zones that were not exposed to the beam during the experiment.

During the in situ experiment the signal to noise ratio of the HAADF image intensity is not as good as in the classical (under vacuum) TEM mode, because the additional electron diffusion effect provided by the SiC chip membranes and the gas in the samples holder. Moreover high magnification observations are not used to avoid beam damages. Thus, resolution is decreased and this means Pt single atoms, abundant in the oxide catalyst and also found in the reduced one, cannot be observed. As the NPs become visible during reduction, without any mobility of the original oxide clusters nor of the newly formed NPs, the single atoms are expected to play a role on the NP formation mechanism as recently suggested.<sup>18</sup>

**HAADF-STEM electron tomography.** Figure 7 shows one 3D segmented volume for each catalyst (two other volumes shown in Figure S2 of SI). Note that the Pt single atoms are below the resolution of this technique. With these volumes, it is possible to assess what is the preferred location of NPs on the support crystallites.

For the 0.3%Pt/ $\gamma$ -Al<sub>2</sub>O<sub>3</sub>-Cl reduced catalyst, the two reconstructed objects present a total of 43 NPs. The NP location on the support crystallite was unambiguously assessed visually for 22 NPs. Out of those, 18 are located on the crystallites edges (as represented in inset of Figure 7) or other defaults (steps or kinks) and 4 are located on crystallite planes. For the 1%Pt/ $\gamma$ -Al<sub>2</sub>O<sub>3</sub>-Cl reduced catalyst, there are 186 NPs between the two reconstructed objects.

Again, NP location was clearly assigned for 58 NPs. Out of those, 45 were found to be located on the crystallites edges (inset of Figure 7) or other defects and 13 were found to be located on planes. More details are available in Table S2 of SI.

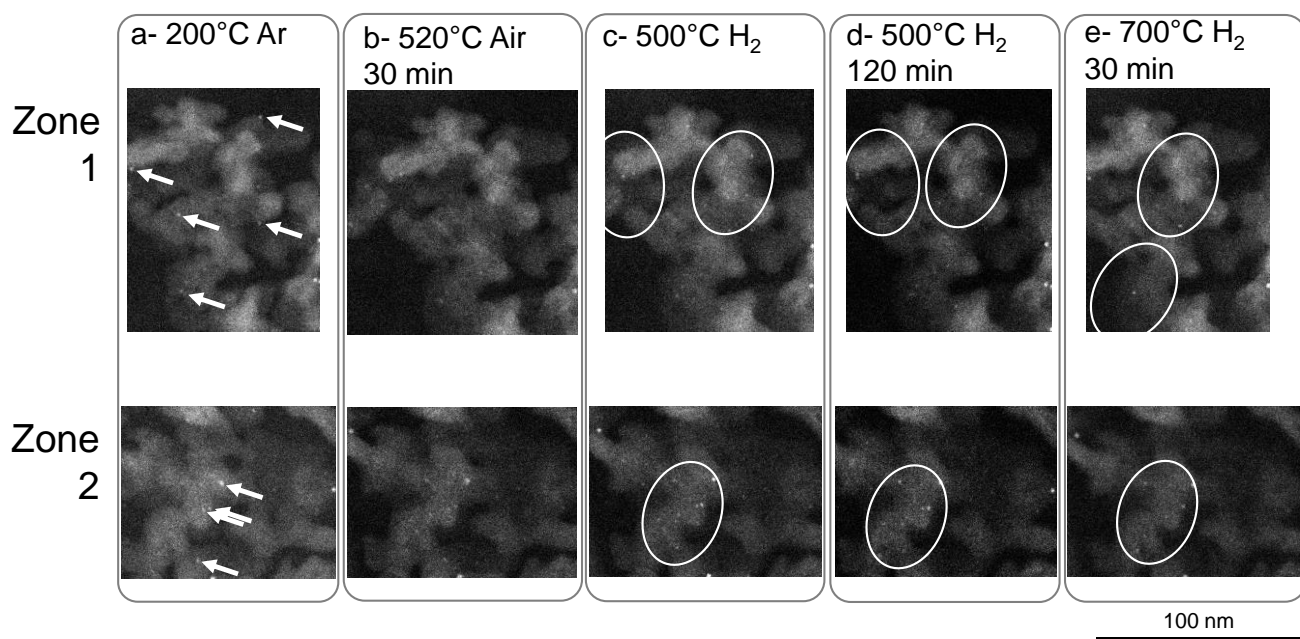


*Figure 6. HAADF-STEM images acquired during in-situ reduction of 1%Pt/ $\gamma$ -Al<sub>2</sub>O<sub>3</sub>-Cl in two zones, 1 and 2, at different moments of the treatment: a – initial state under Ar at 200°C, b – at the end of the pre-calcination of 30 minutes under air, c – at 500°C under H<sub>2</sub> immediately after heating to 500°C at 5°C/min under H<sub>2</sub>, d – at the end of the reduction plateau of 2h under H<sub>2</sub>, e – after further heating and 30 min plateau at 700°C. White arrows indicate clusters already present on the oxide catalysts and white circles highlight regions where changes can be observed.*

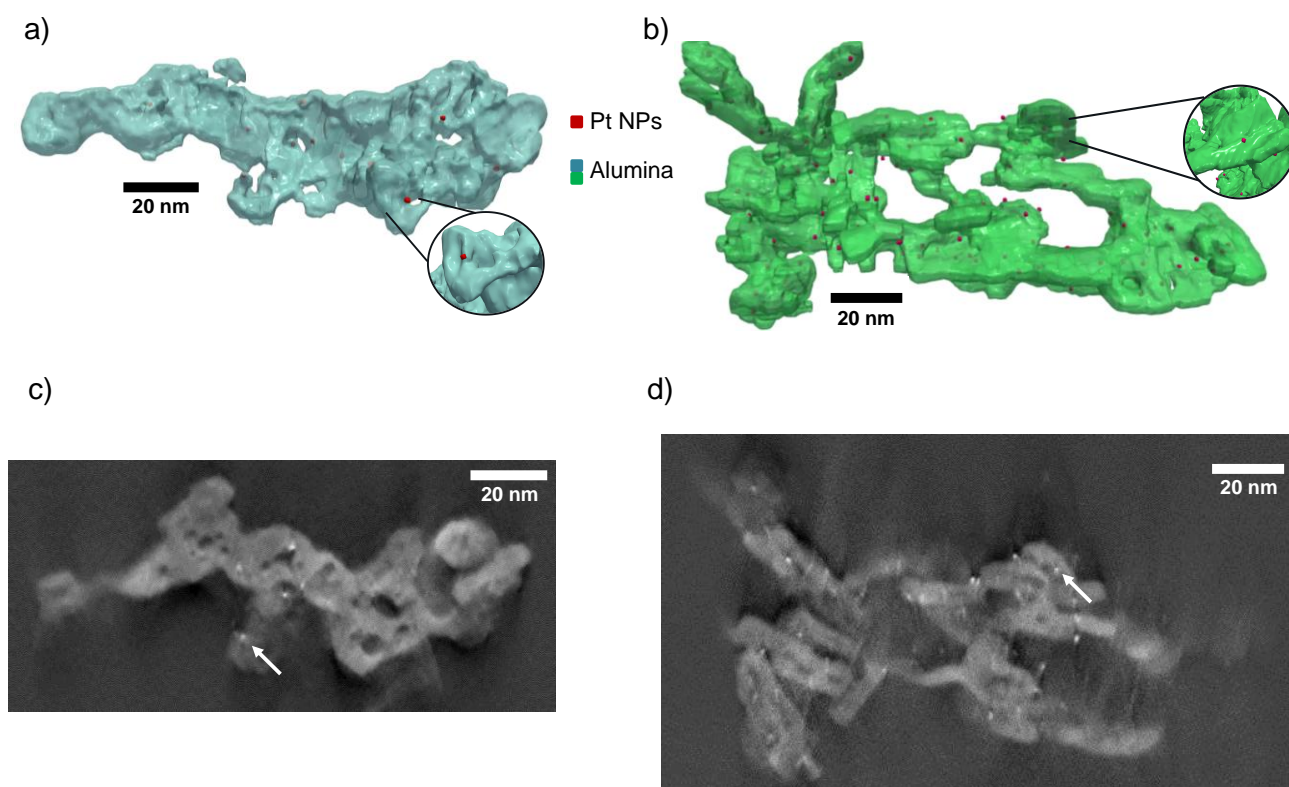


*Figure 7. Segmented volumes a) and b) and slice of reconstruction c) and d) obtained from tomographic series of 0.3%Pt/ $\gamma$ -Al<sub>2</sub>O<sub>3</sub>-Cl and of 1%Pt/ $\gamma$ -Al<sub>2</sub>O<sub>3</sub>-Cl reduced catalysts, respectively, where an example of nanoparticle located on the alumina crystallite edge is highlighted in the segmentation and indicated by a white arrow in the reconstruction slice.*

## DISCUSSION

The present electron tomography analysis shows that Pt nanoparticles on industry relevant catalysts are preferably located on crystallite edges or edge-like defaults (steps and kinks), as 78% of studied NPs are located on those structures. Crystallite edges are thought to harbor strong Lewis sites and highly resistant hydroxyls groups with respect to facets, having potentially a role in alumina surface reactivity.<sup>67</sup> Indeed, in a recent study<sup>63</sup> by some of the present authors, the first DFT model of alumina (110)-(100) edge was built and it was shown by NMR and DFT analysis that hydroxyls located at edges are preferentially exchanged with chlorine.

A first approach to evaluate the Pt NP stability on edges was thus conducted. Different configurations of Pt<sub>13</sub> supported on the (110)-(100) edge with varying degrees of hydration and of chlorination were considered (see SI). The most stable model was obtained for Pt<sub>13</sub> on the Al-side of the hydrated (110)-(100) edge with a binding energy of -409 kJ/mol (see SI), which makes it as thermodynamically stable as the reference Pt<sub>13</sub>/surface models. When the Al-side is saturated with chlorine (Figure 8) the binding energy is very similar at -404 kJ/mol.

Pt<sub>13</sub> on the O-side of the hydrated (110)-(100) edge has a similar binding energy of -403 kJ/mol (see SI). The binding energies for previously published models<sup>62</sup> of Pt<sub>13</sub>/(100) (dehydrated) and Pt<sub>13</sub>/(110) (with 11.8 OH/nm<sup>2</sup>) are -416 and -397 kJ/mol respectively. Thus, all the configurations simulated on edges can be considered as stable as the Pt<sub>13</sub>/surface models, indicating that within the DFT accuracy (~10-20 kJ/mol) the edge NP location competes with location on alumina terraces. According to our previous work<sup>63</sup>, the chlorine exchange step is thermodynamically more favored at edge than on the surfaces. Due to the high concentration of Cl atoms in close vicinity at edge (Figure 8), the formation of Pt NP at such location may be enhanced by a synergy effect with chlorine stabilization. Investigating this aspect remains beyond the scope of the present work and requires a dedicated study of the formation mechanisms of the Pt NP on chlorinated alumina.

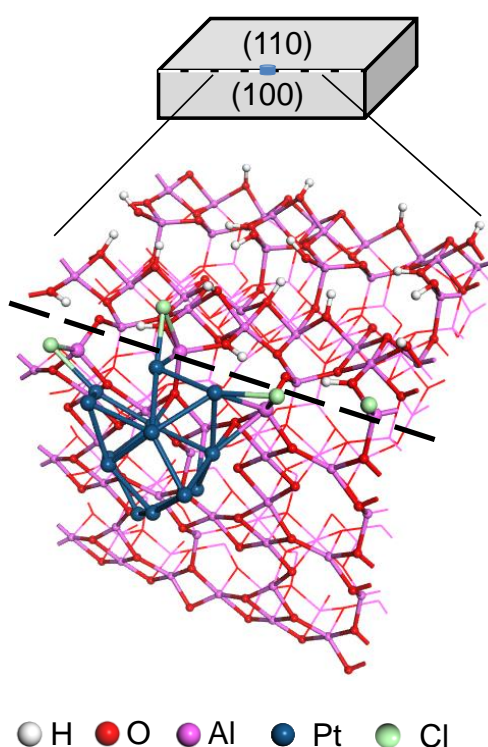


*Figure 8. Alumina platelet scheme and most stable Pt<sub>13</sub>/edge-Cl model with the NP on the chlorinated Al-side termination highlighted by the broken line.*

Note that in spite of the location of the particles at the edge, our models are compatible with the existence of an interaction of Pt with Al<sub>V</sub> atoms as shown by Kwak et al.<sup>5</sup> Indeed in the models, the platinum particle interacts with edge Al atoms (mostly distorted Al<sub>IV</sub>) but also with close-by Al<sub>V</sub> atoms from the (100) facet.

Qualitatively the images in Figure 3 suggest that for 1%Pt the NPs are closer to each other, as they are more numerous than for 0.3%Pt. Nevertheless, the distance between NPs cannot be assessed through the STEM images, as these provide no information on depth with respect to the alumina crystallites.

By means of the dedicated geometrical analysis, the geodesic distances between NPs following the support surface can moreover be quantified and the support tortuosity assessed as a method for solving the NP dispersion at the surface qualification, from electron tomography. In Figure 9 are shown the histograms of the distance of each NP to its closest neighbor grouped by catalyst sample.

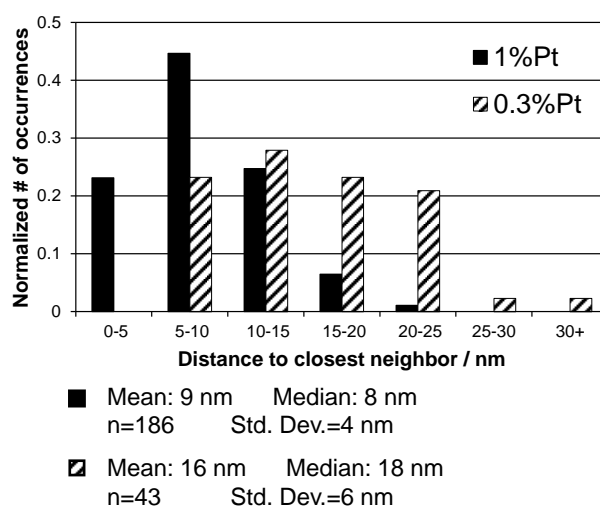


*Figure 9. Histogram for the geodesic distance following the support surface between a given nanoparticle and its closest nanoparticle neighbor obtained from both segmented objects of each catalyst, 1%Pt/ $\gamma$ -Al<sub>2</sub>O<sub>3</sub>-Cl in full black and 0.3%Pt/ $\gamma$ -Al<sub>2</sub>O<sub>3</sub>-Cl in stripes.*

The mean geometric tortuosity (see Experimental Section and Methods) calculated for the segmented images, shown in Figure 7, was also determined and analyzed. To identify if the Pt NPs are located on a specific pore region of the support, the tortuosity descriptors are calculated to evaluate the nanoparticles' distribution through the segmented object using either the NP positions or uniform density sampled points set. The histograms of mean geometric tortuosity (Figure 10) obtained using the NP positions are consistently concentrated over the most frequent values obtained using the point set. The statistic impact of number of points is clear, as for 0.3%Pt/ $\gamma$ -Al<sub>2</sub>O<sub>3</sub>-Cl there are fewer NPs in the object than for 1%Pt/ $\gamma$ -Al<sub>2</sub>O<sub>3</sub>-Cl, a much better match is obtained for 1%Pt/ $\gamma$ -Al<sub>2</sub>O<sub>3</sub>-Cl. Considering the resulting M-scalar descriptor (Table S3 of SI), it appears that the M-scalar values (~1.2) are

remarkably similar for both NP positions and the point set. For NP positions the impact of using fewer points in the case of 0.3%Pt  $\gamma$ -Al<sub>2</sub>O<sub>3</sub>-Cl is highlighted by higher  $\sigma_c$  values (0.07 vs 0.02). Overall, the mean geometric tortuosity evaluation of the alumina support is very similar for the point set and the Pt NP positions themselves, revealing that the nanoparticles are uniformly distributed in the alumina support's aggregates, which are made of individual alumina crystallites, as opposed to being concentrated in a given region.

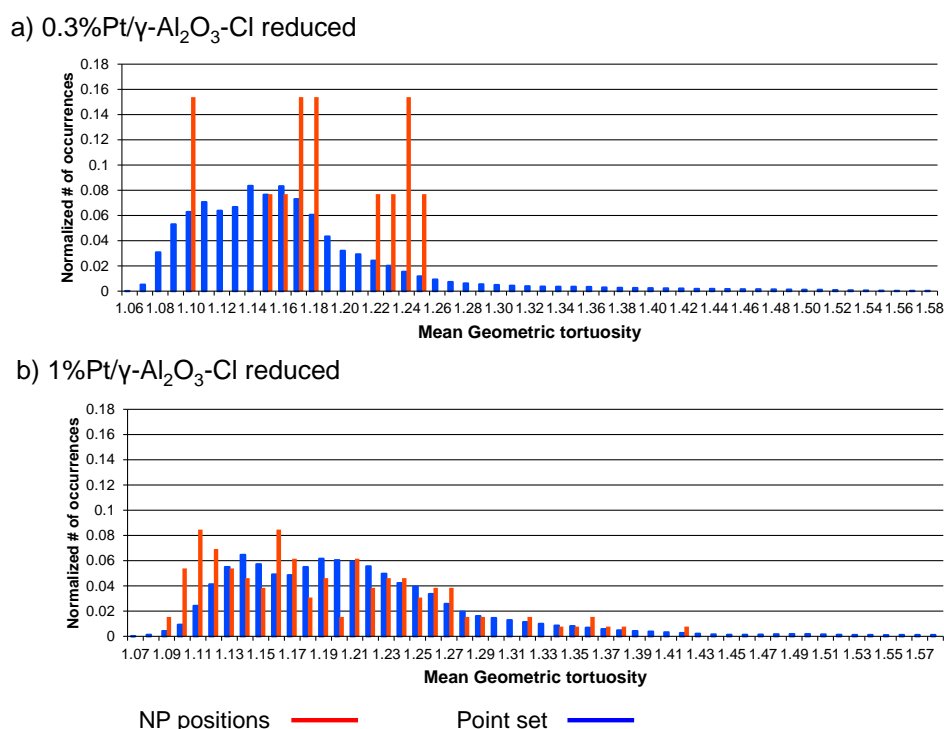


**Figure 10.** Comparison of normalized mean geometric tortuosity histograms obtained using the NP positions (red) or the point set (blue) for the segmented object presented in Figure 7 of each reduced catalyst, a) 0.3%Pt/ $\gamma$ -Al<sub>2</sub>O<sub>3</sub>-Cl and b) 1%Pt/ $\gamma$ -Al<sub>2</sub>O<sub>3</sub>-Cl.

In order to estimate a “theoretic distance” between NPs, a geometric model, illustrated in Figure 11, was built on the following assumptions: a) support crystallites are of a parallelepipedic morphology with the average size of about 4 x 14.5 x 9 nm as estimated from TEM images; b) all Pt is in the form of Pt<sub>13</sub> NPs (as analyzed in Figure 3 or invoked in several DFT studies<sup>7,18,21,62</sup> corresponding to a size of 0.9 nm, better representing our samples); c) Pt NPs are distributed in a square network. For a 1%<sub>w/w</sub>Pt loading, the distance between Pt NPs in a square network is found to be of 9.5 nm, while for 0.3%<sub>w/w</sub>Pt, the distance is of 17.3 nm. If the distribution of Pt on a alumina crystallite is now considered, for 1%Pt there would be about 5 NPs per crystallite whereas for 0.3%Pt there would be one single NP per crystallite. As the STEM images suggest, this geometric model indicates that



the two Pt loadings have an impact on the distance between NPs, which can be either intra- or inter- alumina crystallite. The mean inter-NP geodesic distance obtained from the tomographic volumes (Figure 9) is in remarkable agreement with those given by this simple geometric model (Figure 11). This implies that for these loadings, anchoring sites for NPs are abundant enough and lead to a uniform random distribution of inter-NP distances close to a distribution of a uniform density of samples points.

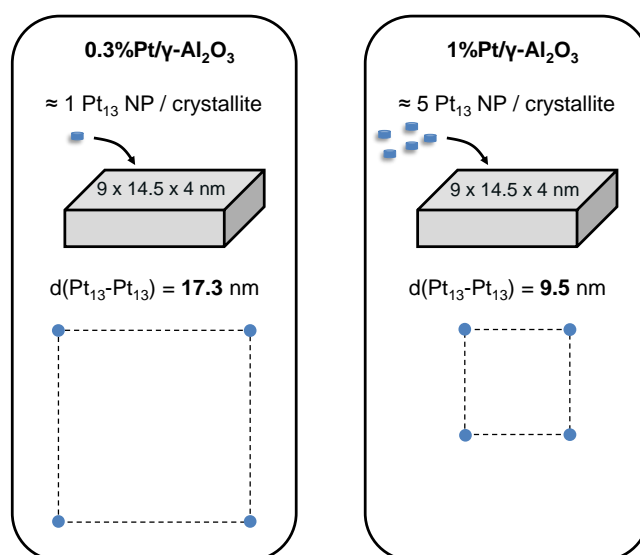


Figure 11. Illustration of the impact of platinum loading on inter-NP distance predicted by a simple geometric model.

## CONCLUSION

On industry relevant catalysts with low Pt loadings supported on high surface  $\gamma$ -alumina, once reduced, Pt is dispersed as flat NPs of 0.9 nm and scattered single atoms. The tomographic study showed for the first time that these NPs are located mostly on the edges of the crystallites and are uniformly distributed through the support aggregate. DFT calculations indicate that such location is equally as thermodynamically favorable as the surfaces. The role of chlorine to stabilize Pt NP at edges may be suspected, however it should be the matter of future DFT investigations devoted to the mechanisms of Pt NP formation on chlorinated alumina.

The average distance between NPs was quantified from the 3D tomography volumes and is fully compatible with a geometric model, showing that this distance between NPs is tuned through Pt loading and may be shifted from intra- to inter- alumina crystallite for 1% Pt to 0.3% Pt. We expect that this trend may impact the behavior of bifunctional catalysts. The NPs are very stable and show no mobility during the reduction treatment under  $H_2$  at 500°C.

Their formation mechanism is expected to depend on the coalescence of single atoms which are abundant in the oxide catalysts and are still present in the reduced catalysts. Gaining further insights on the genesis of NP particles will depend on the future improvements of the experimental analysis conditions in the in situ TEM mode in an environmental gas cell.

## REFERENCES

- (1) Sattler, J. H. B.; Ruiz-Martinez, J.; Santillan-Jimenez, E.; Weckhuysen, B. M. Catalytic Dehydrogenation of Light Alkanes on Metals and Metal Oxides. *Chem. Rev.* **2014**, *114*, 10613–10653.
- (2) Ravenelle, R. M.; Diallo, F. Z.; Crittenden, J. C.; Sievers, C. Effects of Metal Precursors on the Stability and Observed Reactivity of Pt/ $\gamma$ -Al<sub>2</sub>O<sub>3</sub> Catalysts in Aqueous Phase Reactions. *ChemCatChem* **2012**, *4*, 492–494.
- (3) Cui, X.; Junge, K.; Dai, X.; Kreyenschulte, C.; Pohl, M.-M.; Wohlrab, S.; Shi, F.; Brückner, A.; Beller, M. Synthesis of Single Atom Based Heterogeneous Platinum Catalysts: High Selectivity and Activity for Hydrosilylation Reactions. *ACS Cent. Sci.* **2017**, *3*, 580–585.
- (4) Oudenhuijzen, M. K.; van Bokhoven, J. A.; Miller, J. T.; Ramaker, D. E.; Koningsberger, D. C. Three-site model for hydrogen adsorption on supported platinum particles: influence of support ionicity and particle size on the hydrogen coverage. *J. Am. Chem. Soc.* **2005**, *127*, 1530–1540.
- (5) Kwak, J. H.; Hu, J.; Mei, D.; Yi, C.-W.; Kim, D. H.; Peden, C. H. F.; Allard, L. F.; Szanyi, J. Coordinatively unsaturated Al<sup>3+</sup> centers as binding sites for active catalyst phases of platinum on gamma-Al<sub>2</sub>O<sub>3</sub>. *Science* **2009**, *325*, 1670–1673.
- (6) Karim, W.; Spreafico, C.; Kleibert, A.; Gobrecht, J.; VandeVondele, J.; Ekinci, Y.; van Bokhoven, J. A. Catalyst support effects on hydrogen spillover. *Nature* **2017**, *541*, 68–74.
- (7) Gorczyca, A.; Moizan, V.; Chizallet, C.; Proux, O.; Del Net, W.; Lahera, E.; Hazemann, J.-L.; Raybaud, P.; Joly, Y. Monitoring morphology and hydrogen coverage of nanometric Pt/ $\gamma$ -Al<sub>2</sub>O<sub>3</sub> particles by in situ HERFD-XANES and quantum simulations. *Angew. Chem. Int. Ed.* **2014**, *53*, 12426–12429.
- (8) Nellist, P. D.; Pennycook, S. J. Direct Imaging of the Atomic Configuration of Ultradispersed Catalysts. *Science* **1996**, *274*, 413–415.
- (9) Szlachetko, J.; Ferri, D.; Marchionni, V.; Kambolis, A.; Safonova, O. V.; Milne, C. J.; Kröcher, O.; Nachttegaal, M.; Sá, J. Subsecond and in Situ Chemical Speciation of Pt/Al<sub>2</sub>O<sub>3</sub> during Oxidation–Reduction Cycles Monitored by High-Energy Resolution Off-Resonant X-ray Spectroscopy. *J. Am. Chem. Soc.* **2013**, *135*, 19071–19074.
- (10) Kovarik, L.; Genc, A.; Wang, C.; Qiu, A.; Peden, C. H. F.; Szanyi, J.; Kwak, J. H. Tomography and High-Resolution Electron Microscopy Study of Surfaces and Porosity in a Plate-like  $\gamma$ -Al<sub>2</sub>O<sub>3</sub>. *J. Phys. Chem. C* **2013**, *117*, 179–186.
- (11) M. Boudart. Catalysis by Supported Metals. *Adv. Catal.* **1969**, *20*, 153–166.
- (12) Bradley, S. A.; Sinkler, W.; Blom, D. A.; Bigelow, W.; Voyles, P. M.; Allard, L. F. Behavior of Pt Atoms on Oxide Supports During Reduction Treatments at Elevated Temperatures, Characterized by Aberration Corrected Stem Imaging. *Catal Lett* **2012**, *142*, 176–182.

- (13) Sinkler, W.; Sanchez, S. I.; Bradley, S. A.; Wen, J.; Mishra, B.; Kelly, S. D.; Bare, S. R. Aberration-Corrected Transmission Electron Microscopy and In Situ XAFS Structural Characterization of Pt/ $\gamma$ -Al<sub>2</sub>O<sub>3</sub> Nanoparticles. *ChemCatChem* **2015**, *7*, 3779–3787.
- (14) Jahel, A.; Avenier, P.; Lacombe, S.; Olivier-Fourcade, J.; Jumas, J.-C. Effect of indium in trimetallic Pt/Al<sub>2</sub>O<sub>3</sub>SnIn–Cl naphtha-reforming catalysts. *J. Catal.* **2010**, *272*, 275–286.
- (15) Jahel, A. N.; Moizan-Baslé, V.; Chizallet, C.; Raybaud, P.; Olivier-Fourcade, J.; Jumas, J.-C.; Avenier, P.; Lacombe, S. Effect of Indium Doping of  $\gamma$ -Alumina on the Stabilization of PtSn Alloyed Clusters Prepared by Surface Organostannic Chemistry. *J. Phys. Chem. C* **2012**, *116*, 10073–10083.
- (16) Lee, J.; Jang, E. J.; Kwak, J. H. Effect of number and properties of specific sites on alumina surfaces for Pt-Al<sub>2</sub>O<sub>3</sub> catalysts. *Appl. Catal., A* **2019**, *569*, 8–19.
- (17) Singh, J.; Nelson, R. C.; Vicente, B. C.; Scott, S. L.; van Bokhoven, J. A. Electronic structure of alumina-supported monometallic Pt and bimetallic PtSn catalysts under hydrogen and carbon monoxide environment. *Phys. Chem. Chem. Phys.* **2010**, *12*, 5668–5677.
- (18) Dessal, C.; Sangnier, A.; Chizallet, C.; Dujardin, C.; Morfin, F.; Rousset, J.-L.; Aouine, M.; Bugnet, M.; Afanasiev, P.; Piccolo, L. Atmosphere-dependent stability and mobility of catalytic Pt single atoms and clusters on  $\gamma$ -Al<sub>2</sub>O<sub>3</sub>. *Nanoscale* **2019**, *11*, 6897–6904.
- (19) Vaarkamp, M.; Miller, J. T.; Modica, F. S.; Koningsberger, D. C. On the Relation between Particle Morphology, Structure of the Metal-Support Interface, and Catalytic Properties of Pt/ $\gamma$ -Al<sub>2</sub>O<sub>3</sub>. *J. Catal.* **1996**, *163*, 294–305.
- (20) Ahmadi, M.; Mistry, H.; Roldan Cuenya, B. Tailoring the Catalytic Properties of Metal Nanoparticles via Support Interactions. *J. Phys. Chem. Lett.* **2016**, *7*, 3519–3533.
- (21) Hu, C. H.; Chizallet, C.; Mager-Maury, C.; Corral-Valero, M.; Sautet, P.; Toulhoat, H.; Raybaud, P. Modulation of catalyst particle structure upon support hydroxylation: Ab initio insights into Pd<sub>13</sub> and Pt<sub>13</sub>/ $\gamma$ -Al<sub>2</sub>O<sub>3</sub>. *J. Catal.* **2010**, *274*, 99–110.
- (22) Gorczyca, A.; Raybaud, P.; Moizan, V.; Joly, Y.; Chizallet, C. Atomistic Models for Highly-dispersed PtSn/ $\gamma$ -Al<sub>2</sub>O<sub>3</sub> Catalysts: Ductility and Dilution Affect the Affinity for Hydrogen. *ChemCatChem* **2019**, *500*, 271.
- (23) Mager-Maury, C.; Bonnard, G.; Chizallet, C.; Sautet, P.; Raybaud, P. H<sub>2</sub>-Induced Reconstruction of Supported Pt Clusters: Metal-Support Interaction versus Surface Hydride. *ChemCatChem* **2011**, *3*, 200–207.
- (24) Zhai, H.; Alexandrova, A. N. Local Fluxionality of Surface-Deposited Cluster Catalysts: The Case of Pt<sub>7</sub> on Al<sub>2</sub>O<sub>3</sub>. *J. Phys. Chem. Lett.* **2018**, *9*, 1696–1702.
- (25) Sun, G.; Sautet, P. Metastable Structures in Cluster Catalysis from First-Principles: Structural Ensemble in Reaction Conditions and Metastability Triggered Reactivity. *J. Am. Chem. Soc.* **2018**, *140*, 2812–2820.
- (26) Vila, F. D.; Rehr, J. J.; Nuzzo, R. G.; Frenkel, A. I. Anomalous Structural Disorder in Supported Pt Nanoparticles. *J. Phys. Chem. Lett.* **2017**, *8*, 3284–3288.
- (27) Zhai, H.; Alexandrova, A. N. Fluxionality of Catalytic Clusters: When It Matters and How to Address It. *ACS Catal* **2017**, *7*, 1905–1911.

- (28) Sangnier, A.; Matrat, M.; Nicolle, A.; Dujardin, C.; Chizallet, C. Multiscale Approach to the Dissociative Adsorption of Oxygen on a Highly Dispersed Platinum Supported on  $\gamma$ -Al<sub>2</sub>O<sub>3</sub>. *J. Phys. Chem. C* **2018**, *122*, 26974–26986.
- (29) Sinfelt, J. H. Bifunctional Catalysis. *Adv. Chem. Eng.* **1964**, *5*, 37–74.
- (30) *Acido-basic catalysis: Application to refining and petrochemistry*; Marcilly, C., Ed.; Editions Technip: Paris, 2006.
- (31) Zečević, J.; Vanbutsele, G.; Jong, K. P. de; Martens, J. A. Nanoscale intimacy in bifunctional catalysts for selective conversion of hydrocarbons. *Nature* **2015**, *528*, 245–248.
- (32) P. B. Weisz. Polyfunctional Heterogeneous Catalysis. *Adv. Catal.* **1962**, *13*, 137–190.
- (33) L. Kovarik; A. Genç; C. Wang; J. Szanyi; C. Peden; J. Kwak. Tomography and high resolution study of gamma-Al<sub>2</sub>O<sub>3</sub> porosity, surfaces and Pt surface interaction. *Microsc. Microanal.* **2012**, *18*, 1302–1303.
- (34) Dessal, C.; Len, T.; Morfin, F.; Rousset, J.-L.; Aouine, M.; Afanasiev, P.; Piccolo, L. Dynamics of Single Pt Atoms on Alumina during CO Oxidation Monitored by Operando X-ray and Infrared Spectroscopies. *ACS Catal* **2019**, *9*, 5752–5759.
- (35) Yang, E.; Jang, E. J.; Lee, J. G.; Yoon, S.; Lee, J.; Musselwhite, N.; Somorjai, G. A.; Kwak, J. H.; An, K. Acidic effect of porous alumina as supports for Pt nanoparticle catalysts in n-hexane reforming. *Catal. Sci. Technol.* **2018**, *8*, 3295–3303.
- (36) Mei, D.; Kwak, J. H.; Hu, J.; Cho, S. J.; Szanyi, J.; Allard, L. F.; Peden, C. H. F. Unique Role of Anchoring Penta-Coordinated Al<sup>3+</sup> Sites in the Sintering of  $\gamma$ -Al<sub>2</sub>O<sub>3</sub>-Supported Pt Catalysts. *J. Phys. Chem. Lett.* **2010**, *1*, 2688–2691.
- (37) Zhang, Z.; Chen, Y.; Zhou, L.; Chen, C.; Han, Z.; Zhang, B.; Wu, Q.; Yang, L.; Du, L.; Bu, Y.; Wang, P.; Wang, X.; Yang, H.; Hu, Z. The simplest construction of single-site catalysts by the synergism of micropore trapping and nitrogen anchoring. *Nat. Commun.*, *10*, 1657.
- (38) Bruix, A.; Lykhach, Y.; Matolínová, I.; Neitzel, A.; Skála, T.; Tsud, N.; Vorokhta, M.; Stetsovych, V.; Ševčíková, K.; Mysliveček, J.; Fiala, R.; Václavů, M.; Prince, K. C.; Bruyère, S.; Potin, V.; Illas, F.; Matolín, V.; Libuda, J.; Neyman, K. M. Maximum noble-metal efficiency in catalytic materials: atomically dispersed surface platinum. *Angew. Chem. Int. Ed.* **2014**, *53*, 10525–10530.
- (39) Jones, J.; Xiong, H.; DeLaRiva, A. T.; Peterson, E. J.; Pham, H.; Challa, S. R.; Qi, G.; Oh, S.; Wiebenga, M. H.; Hernández, X. I. P.; Wang, Y.; Datye, A. K. Thermally stable single-atom platinum-on-ceria catalysts via atom trapping. *Science* **2016**, *353*, 150–154.
- (40) Kunwar, D.; Zhou, S.; DeLaRiva, A.; Peterson, E. J.; Xiong, H.; Pereira-Hernández, X. I.; Purdy, S. C.; ter Veen, R.; Brongersma, H. H.; Miller, J. T.; Hashiguchi, H.; Kovarik, L.; Lin, S.; Guo, H.; Wang, Y.; Datye, A. K. Stabilizing High Metal Loadings of Thermally Stable Platinum Single Atoms on an Industrial Catalyst Support. *ACS Catal* **2019**, *9*, 3978–3990.
- (41) Pereira-Hernández, X. I.; DeLaRiva, A.; Muravev, V.; Kunwar, D.; Xiong, H.; Sudduth, B.; Engelhard, M.; Kovarik, L.; Hensen, E. J. M.; Wang, Y.; Datye, A. K. Tuning Pt-CeO<sub>2</sub> interactions by high-temperature vapor-phase synthesis for improved reducibility of lattice oxygen. *Nat. Commun.* **2019**, *10*, 1358.

- (42) González, J. C.; Hernández, J. C.; López-Haro, M.; del Río, E.; Delgado, J. J.; Hungría, A. B.; Trasobares, S.; Bernal, S.; Midgley, P. A.; Calvino, J. J. 3 D characterization of gold nanoparticles supported on heavy metal oxide catalysts by HAADF-STEM electron tomography. *Angew. Chem. Int. Ed.* **2009**, *48*, 5313–5315.
- (43) Midgley, P. A.; Weyland, M.; Thomas, J. M.; Johnson, B. F. G. Z-Contrast tomography: a technique in three-dimensional nanostructural analysis based on Rutherford scattering. *Chem. Commun.* **2001**, 907–908.
- (44) Hernández-Garrido, J.; Yoshida, K.; Gai, P.; Boyes, E.; Christensen, C. H.; Midgley, P. A. The location of gold nanoparticles on titania: A study by high resolution aberration-corrected electron microscopy and 3D electron tomography. *Catal. Today* **2011**, *160*, 165–169.
- (45) Friedrich, H.; Jongh, P. E. de; Verkleij, A. J.; Jong, K. P. de. Electron Tomography for Heterogeneous Catalysts and Related Nanostructured Materials. *Chem. Rev.* **2009**, *109*, 1613–1629.
- (46) Li, Y.; Zakharov, D.; Zhao, S.; Tappero, R.; Jung, U.; Elsen, A.; Baumann, P.; Nuzzo, R. G.; Stach, E. A.; Frenkel, A. I. Complex structural dynamics of nanocatalysts revealed in Operando conditions by correlated imaging and spectroscopy probes. *Nat. Commun.* **2015**, *6*, 7583–7589.
- (47) Vendelbo, S. B.; Elkjær, C. F.; Falsig, H.; Puspitasari, I.; Dona, P.; Mele, L.; Morana, B.; Nelissen, B. J.; van Rijn, R.; Creemer, J. F.; Kooyman, P. J.; Helveg, S. Visualization of oscillatory behaviour of Pt nanoparticles catalysing CO oxidation. *Nat. Mater.* **2014**, *13*, 884–890.
- (48) Dembele, K.; Moldovan, S.; Hirlimann, C.; Harmel, J.; Soulantica, K.; Serp, P.; Chaudret, B.; Gay, A.-S.; Maury, S.; Berliet, A.; Fecant, A.; Ersen, O. Reactivity and structural evolution of urchin-like Co nanostructures under controlled environments. *J. Microsc.* **2018**, *269*, 168–176.
- (49) Allard, L. F.; Overbury, S. H.; Bigelow, W. C.; Katz, M. B.; Nackashi, D. P.; Damiano, J. Novel MEMS-based gas-cell/heating specimen holder provides advanced imaging capabilities for in situ reaction studies. *Microsc. Microanal.* **2012**, *18*, 656–666.
- (50) David N. Mastronarde. Dual-Axis Tomography: An Approach with Alignment Methods That Preserve Resolution. *J. Struct. Biol.* **1997**, *120*, 343–352.
- (51) Gordon, R.; Bender, R.; Herman, G. T. Algebraic Reconstruction Techniques (ART) for three-dimensional electron microscopy and X-ray photography. *J. Theor. Biol.* **1970**, *29*, 471–481.
- (52) Messaoudii, C.; Boudier, T.; Sanchez Sorzano, C. O.; Marco, S. TomoJ: Tomography software for three-dimensional reconstruction in transmission electron microscopy. *BMC Bioinf.* **2007**, *8*, 288–292.
- (53) Fedorov, A.; Beichel, R.; Kalpathy-Cramer, J.; Finet, J.; Fillion-Robin, J.-C.; Pujol, S.; Bauer, C.; Jennings, D.; Fennessy, F.; Sonka, M.; Buatti, J.; Aylward, S.; Miller, J. V.; Pieper, S.; Kikinis, R. 3D Slicer as an image computing platform for the Quantitative Imaging Network. *Magn. Reson. Imaging* **2012**, *30*, 1323–1341.
- (54) 3DSlicer. <https://www.slicer.org/>.
- (55) Chaniot, J.; Moreaud, M.; Sorbier, L.; Fournel, T.; Becker, J.-M. Tortuosimetric operator for complex porous media characterization. *Image Anal Stereol* **2019**, *38*, 25–41.
- (56) plugim!: M-tortuosity. <https://www.plugim.fr/plugin/57>.
- (57) Perdew, J. P.; Burke, K.; Ernzerhof, M. Generalized Gradient Approximation Made Simple. *Phys. Rev. Lett.* **1996**, *77*, 3865–3868.

- (58) Steinmann, S. N.; Corminboeuf, C. Comprehensive Benchmarking of a Density-Dependent Dispersion Correction. *J. Chem. Theory Comput.* **2011**, *7*, 3567–3577.
- (59) Kresse, G.; Joubert, D. From ultrasoft pseudopotentials to the projector augmented-wave method. *Phys. Rev. B* **1999**, *59*, 1758–1775.
- (60) Kresse, G.; Hafner, J. *Ab initio* molecular-dynamics simulation of the liquid-metal–amorphous-semiconductor transition in germanium. *Phys. Rev. B* **1994**, *49*, 14251–14269.
- (61) Kresse, G.; Furthmüller, J. Efficiency of ab-initio total energy calculations for metals and semiconductors using a plane-wave basis set. *Comp. Mater. Sci.* **1996**, *6*, 15–50.
- (62) Mager-Maury, C.; Chizallet, C.; Sautet, P.; Raybaud, P. Platinum Nanoclusters Stabilized on  $\gamma$ -Alumina by Chlorine Used As a Capping Surface Ligand: A Density Functional Theory Study. *ACS Catal.* **2012**, *2*, 1346–1357.
- (63) Batista, A. T. F.; Wisser, D.; Pigeon, T.; Gajan, D.; Diehl, F.; Rivallan, M.; Catita, L.; Gay, A.-S.; Lesage, A.; Chizallet, C.; Raybaud, P. Beyond gamma-Al<sub>2</sub>O<sub>3</sub> crystallite surfaces: the hidden features of Edges revealed by Solid-State <sup>1</sup>H NMR and DFT calculations. *J. Catal.* **2019**, *378*, 140–143.
- (64) Krokidis, X.; Raybaud, P.; Gobichon, A.-E.; Rebours, B.; Euzen, P.; Toulhoat, H. Theoretical Study of the Dehydration Process of Boehmite to  $\gamma$ -Alumina. *J. Phys. Chem. B* **2001**, *105*, 5121–5130.
- (65) Lynch, J. Development of Structural Characterisation Tools for Catalysts. *Oil Gas Sci. Technol.* **2002**, *57*, 281–305.
- (66) Lietz, G.; Lieske, H.; Spindler, H.; Hanke, W.; Völter, J. Reactions of platinum in oxygen- and hydrogen-treated Pt $\gamma$ -Al<sub>2</sub>O<sub>3</sub> catalysts: II. Ultraviolet-visible studies, sintering of platinum, and soluble platinum. *J. Catal.* **1983**, *81*, 17–25.
- (67) Busca, G. The surface of transitional aluminas: A critical review. *Catal. Today* **2014**, *226*, 2–13.

### 4.2.3 Reduced catalysts

The catalysts at 1.4%Cl loading reduced ex situ were analysed by HR-HAADF-STEM and by HERFD-XANES and EXAFS after in situ re-reduction.

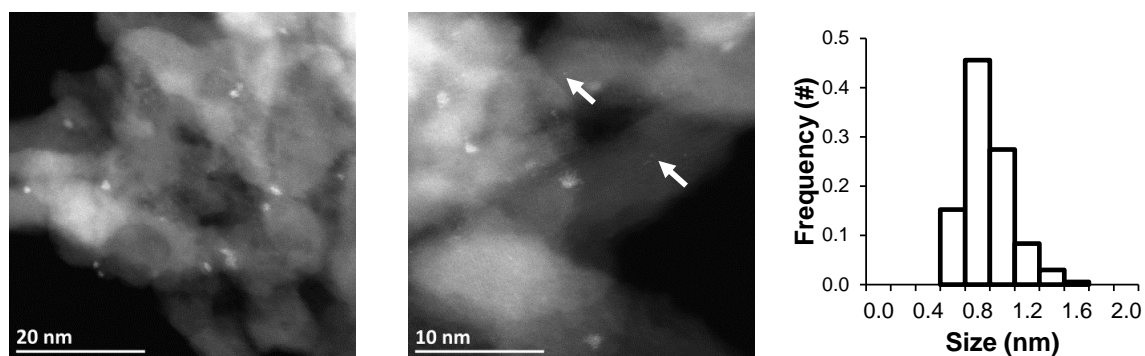
#### 4.2.3.1 Electron microscopy: HR-HAADF-STEM

STEM images of the PuralSB3 catalysts are presented in Figure 4-16. Images of the TH100 catalysts are available above in section 4.2.2. After reduction, well dispersed nanoparticles are formed which are clearly distinct from the species observed in the oxide samples. Again, NPs are more numerous in the samples with higher Pt loading. Histograms of NP size are shown in Figure 4-16 for PuralSB3 and in section 4.2.2 for TH100 and the average size is detailed in Table 4-8 for all samples. Nanoparticle size is on average 0.9 nm regardless of support type, metal loading or of chlorine loading.

*Table 4-8 – Detailed results of nanoparticle size study, complementary to histograms of Figure 4-16 and of section 4.2.3.*

Sample	# measured NPS	Average NP size (nm)	Standard deviation (nm)	%[0.6; 1.2] nm
0.3%Pt/PuralSB3-1.4%Cl	204	0.87	0.19	72
1%Pt/PuralSB3-1.4%Cl	214	0.91	0.18	69
0.3%Pt/TH100-1.4%Cl	202	0.86	0.16	74
1%Pt/TH100-1.4%Cl	242	0.86	0.15	75

a) 0.3%Pt/PuralSB3-1.4%Cl reduced



b) 1%Pt/PuralSB3-1.4%Cl reduced

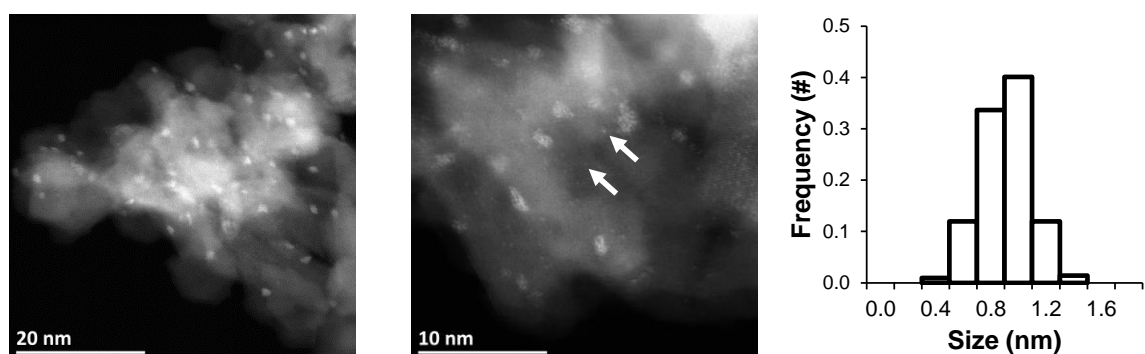


*Figure 4-16 – HR-HAADF-STEM images and nanoparticle size histograms of PuralSB3 reduced catalysts a) 0.3%Pt/PuralSB3-1.4%Cl and b) 1%Pt/PuralSB3-1.4%Cl. White arrows highlight single atoms.*

HAADF intensity analysis was performed for this set of samples indicating again a bi-planar morphology, as illustrated in section 4.2.2. Several single atoms are also identified in the samples, highlighted by the white arrows in Figure 4-16, and the number of single atoms vs number of nanoparticles ratio was determined. The results are shown in Figure 4-17. Among samples at 1.4%Cl, Figure 4-17 a, overall 19% of platinum atoms are in the form of SA and only the support type has an impact on the ratio as the SA proportion is greater for PuralSB3 supported catalysts, in agreement with the observations for 0.1%Cl samples. However, the impact of metal loading identified previously is levelled at highest chlorine content. Indeed, at 1.4%Cl there is enough chlorine coverage to stabilize all single atoms. In Figure 4-17 b the samples at both chlorine loadings are compared, showing that the proportion of single atoms is consistently lower for the samples at 0.1%Cl (decrease from 15% up to 48%). This is evidence of the stabilizing effect of chlorine on the smallest platinum species, particularly the single atoms, as predicted by DFT computational studies [132].



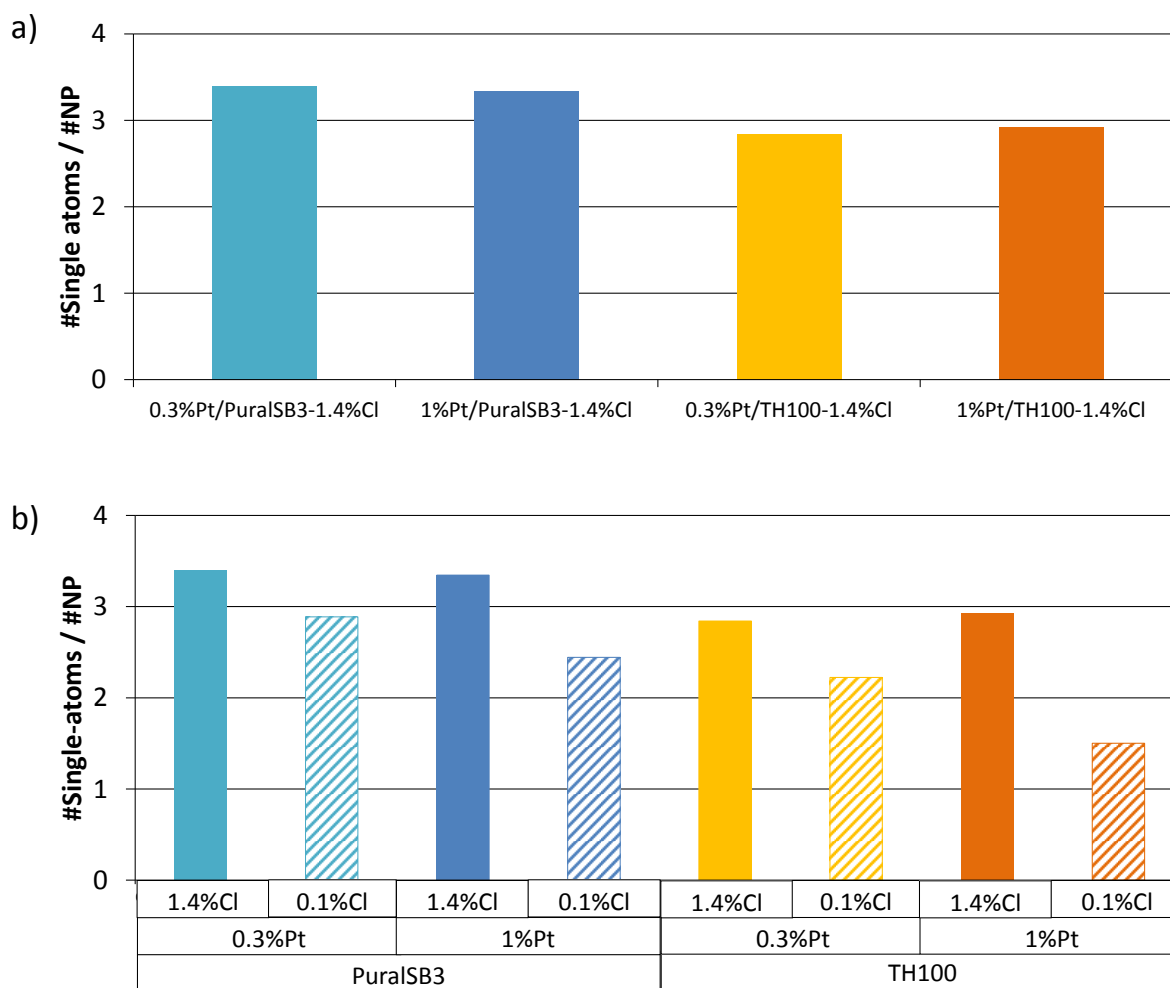
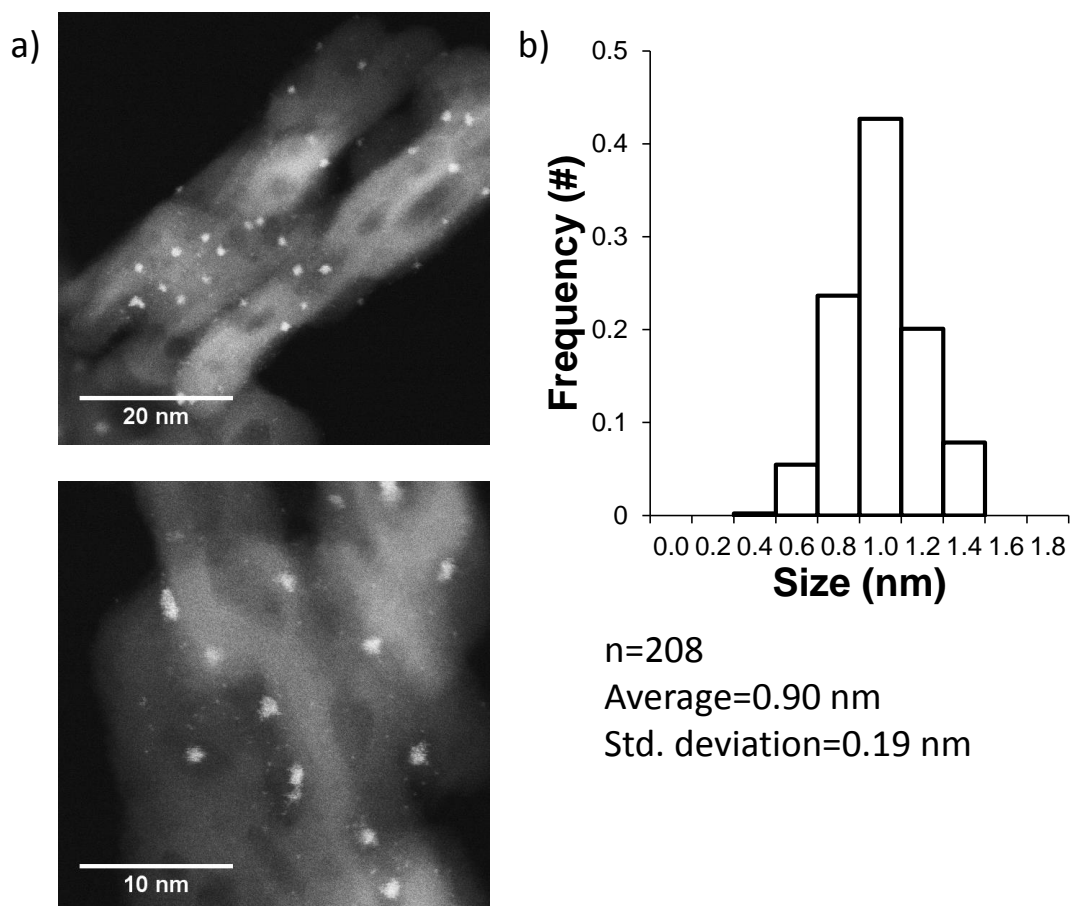


Figure 4-17 – Quantification of single atom population through #Single atom/#NP ration calculated for a) reduced catalysts at 1.4%Cl loading and b) for all reduced catalysts, 1.4%Cl loading in full colour and 0.1%Cl loading in stripes.

#### 4.2.3.1.1 Analysis of used catalyst after catalytic testing

Throughout this work, fresh catalyst samples have been studied. It is reasonable to wonder to what degree the fine points discussed here are altered when the catalyst is put into contact with an hydrocarbon (HC) charge and under reaction conditions. Thus, STEM imaging was performed on one catalyst sample, 1%Pt/TH100-1.4%Cl (Figure 4-18), after n-heptane reforming catalytic testing, part of the doctoral works of Olivier Said-Aizpuru (IFPEN, IRCELYON) [210]. The test lasts about 9 days and a n-heptane charge is used,  $H_2/HC$  (mol/mol) goes up to 5 and temperature up to 420°C (Appendix I).



*Figure 4-18 – HR-HAADF-STEM images a), and nanoparticle size histogram b) of 1%Pt/TH100-1.4%Cl catalyst after catalytic test.*

The images are similar to those obtained for the fresh catalyst: high platinum dispersion, well defined nanoparticles and even single atoms. Indeed, the nanoparticle size histogram shows that no sintering occurred and the average NP size is still 0.9 nm.

As the in situ experiments suggested, the  $\gamma$ -alumina supported Pt NPs are very stable and do not show signs of sintering nor of single atom agglomeration even when exposed to reaction conditions. This result justifies a posteriori the reliability of the characterizations obtained throughout this work mainly on fresh catalysts.

### 4.2.3.2 X-ray adsorption spectroscopy (XAS)

#### 4.2.3.2.1 HERFD-XANES

The HERFD-XANES spectra acquired at room temperature under He after in situ re-reduction are presented in Figure 4-19. As previously, small differences in the descending portion of the edge are related to the evolution of this region during acquisition (taking from 3 to 8h)

due to hydrogen desorption and will not be discussed. The spectra were normalized using Athena from the Demeter 0.9.26 software package [184].

As Figure 4-19 e and f show, the XANES spectra of all reduced catalysts, 0.1%Cl included, are remarkably identical with the exception of small shifts in edge energy inferior to 1 eV. Indeed STEM observations revealed the same average NP size and shape for all samples. No clear impact of metal loading or of support type on the metallic state of platinum is found at the loading of 1.4%Cl (Figure 4-19 a to d).

The spectra of 1%Pt/PuralSB3-1.4%Cl can be found to stand out from the others, as its white line is a bit more intense than that of other samples and the descending portion of the edge does not exhibit the evolving feature at 11569 eV associated with the undesired H<sub>2</sub> desorption occurring during acquisition under He flow (section 2.2.2.3.3). These fine differences are acknowledged but could not be interpreted.

The experimental spectra of reduced 1%Pt/TH100-1.4%Cl and 0.3%Pt/TH100-1.4%Cl are compared to XANES spectra simulated using the FDMNES code [194] in Figure 4-20. These two catalysts show a small energy shift of 0.3 eV between them so it is interesting to put that into perspective with the simulated spectra of DFT models of Pt<sub>13</sub>, Pt<sub>13</sub>H<sub>18</sub> and Pt<sub>1</sub> supported on the dehydrated (100) surface. As found previously, the edge shared between all the reduced samples corresponds best to Pt<sub>13</sub> models. As there is also a good agreement between the experimental spectra and Pt<sub>13</sub>H<sub>18</sub> simulated spectrum, it is also confirmed that it is likely there is still hydrogen adsorbed on the platinum even under He.

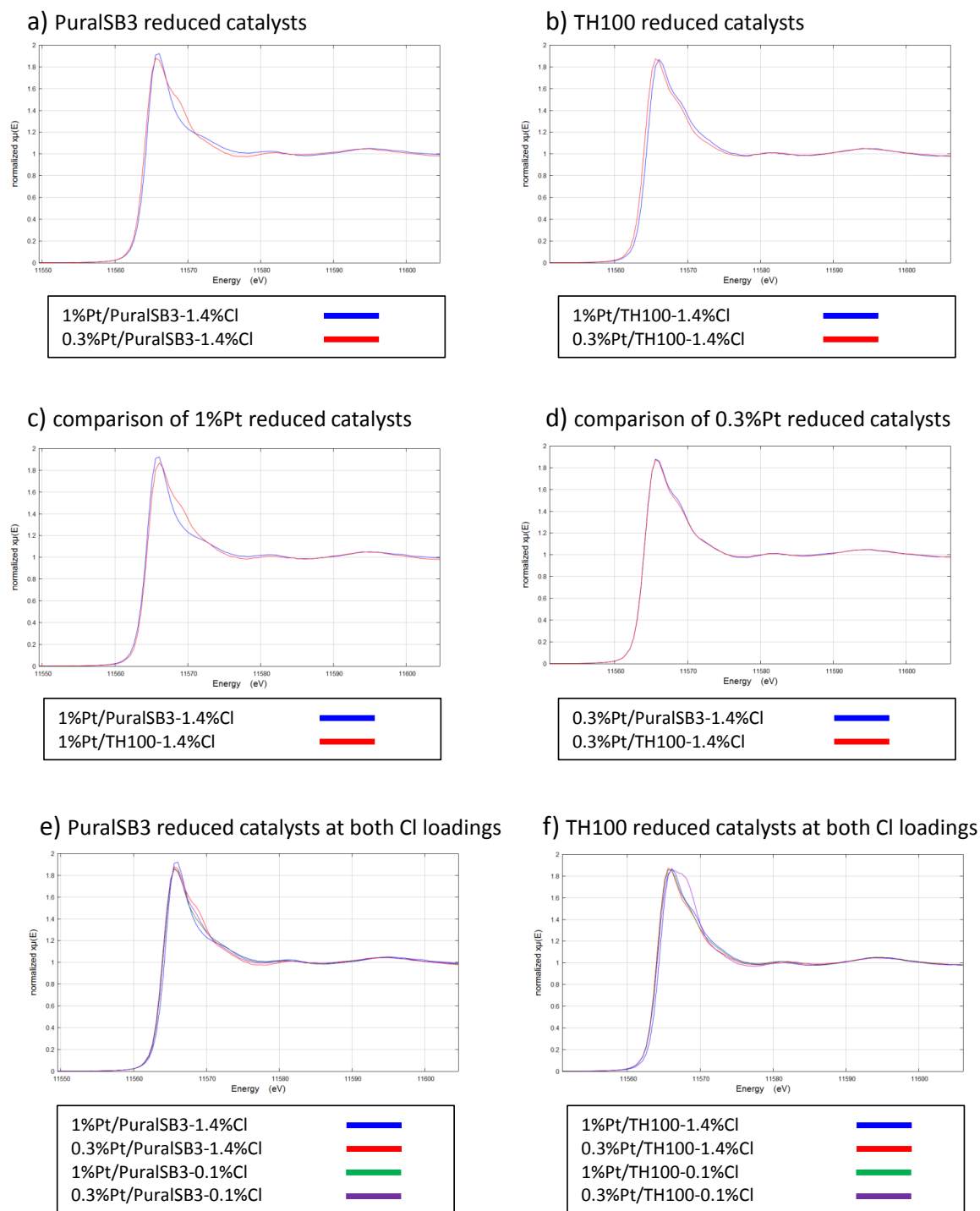


**Figure 4-19 – Pt  $L_3$  edge HERD-XANES spectra of reduced catalysts at 1.4%Cl loading: a) supported on PuralSB3, b) supported on TH100, comparison of c) samples at 1%Pt loading, d) samples at 0.3%Pt loading, and comparison of e) all PuralSB3 samples and f) all TH100 samples.**

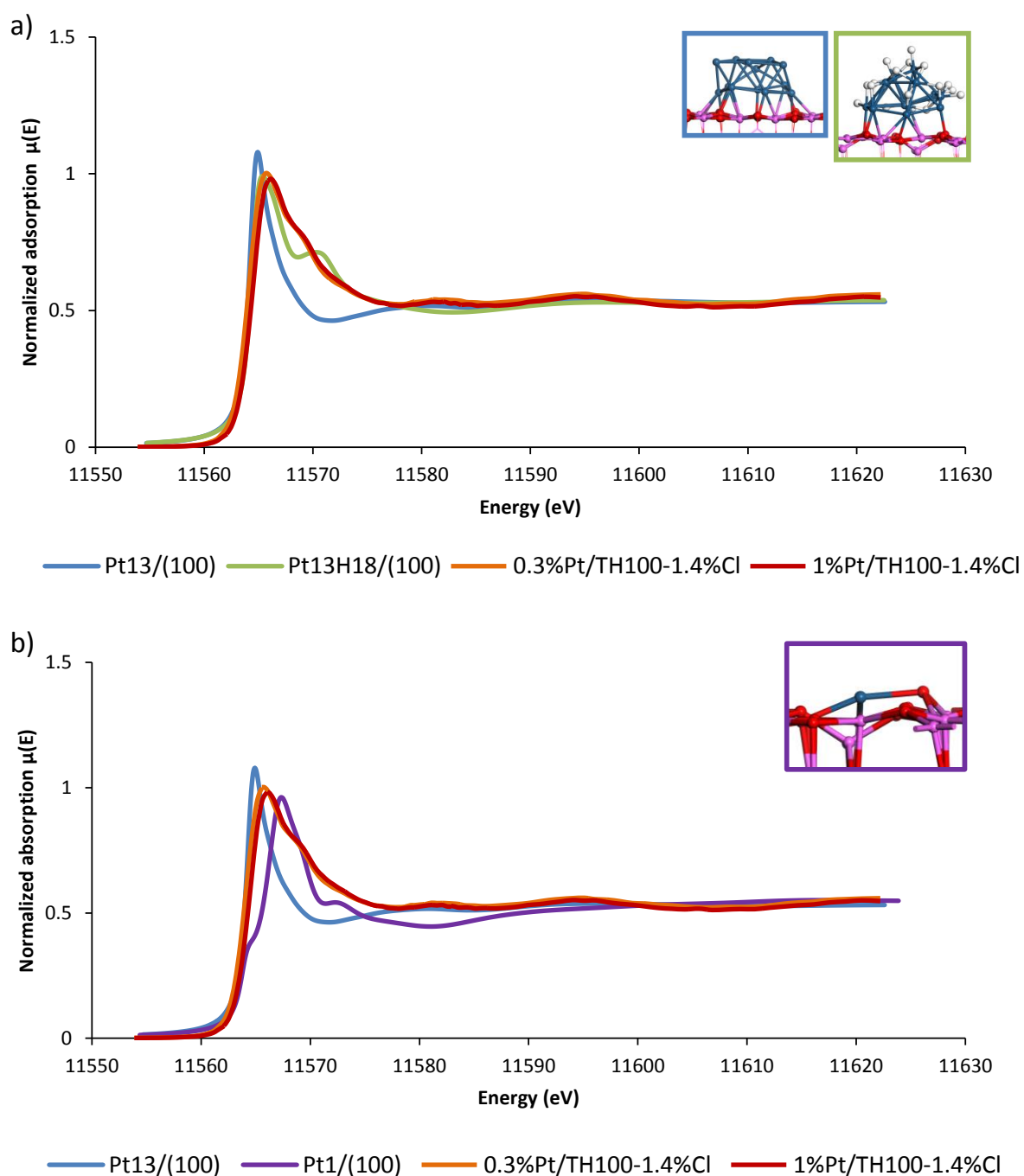
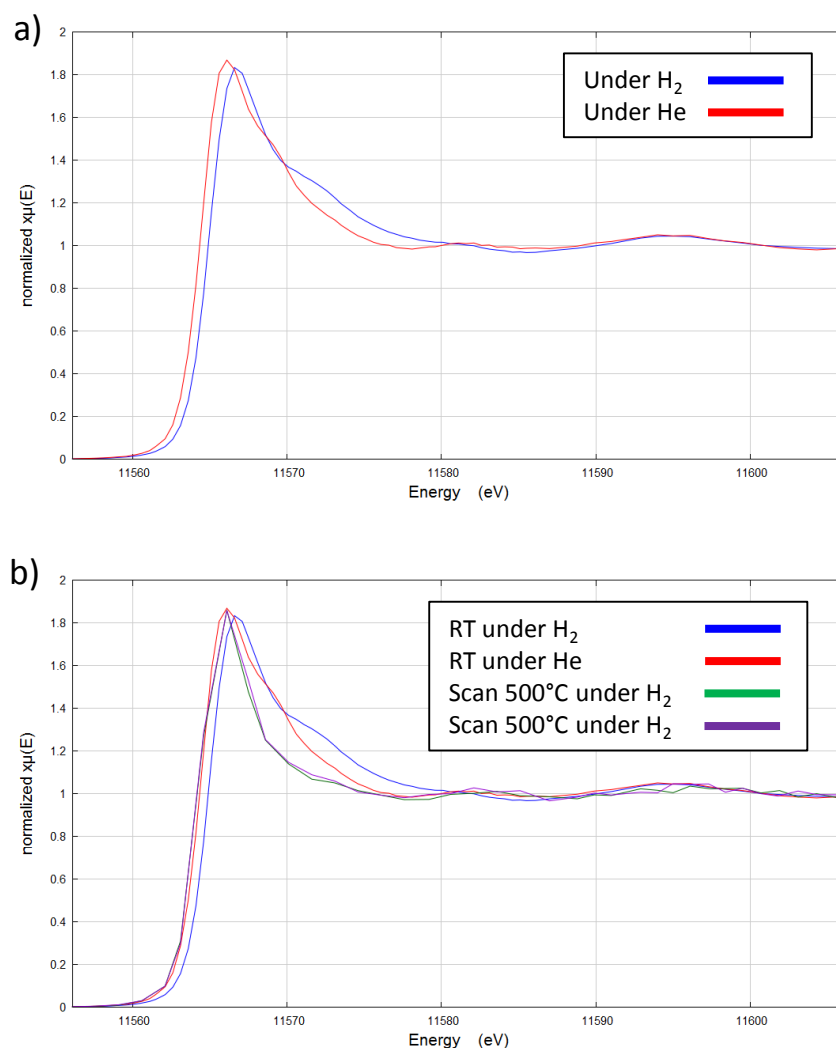


Figure 4-20 –Comparison between Pt  $L_3$  edge HERFD-XANES spectra of reduced 0.3%Pt/TH100-1.4%Cl (orange dotted line) and 1%Pt/TH100-1.4%Cl (red dotted line) and the simulated XANES spectra of DFT models a) Pt<sub>13</sub> and Pt<sub>13</sub>H<sub>18</sub>/(100)<sub>dehyd</sub> and b) Pt<sub>13</sub> and Pt<sub>1</sub>/(100)<sub>dehyd</sub>. Insets illustrate the DFT model used in the respective simulation.

For the 1%Pt/TH100-1.4%Cl reduced catalyst, its spectrum was also acquired under H<sub>2</sub> at room temperature, right after cooling down from 500°C. Figure 4-21 presents the XANES spectra acquired at room temperature under H<sub>2</sub> and under He and also compares them to

two XANES scans recorded at 500°C under H<sub>2</sub> during the re-reduction treatment (note that a spectrum is the result of the merger of several scans).



**Figure 4-21** –Pt L<sub>3</sub> edge HERD-XANES spectra of reduced 1%Pt/TH100-1.4%Cl acquired a) at room temperature under H<sub>2</sub> and under He after purging and b) XANES scans recoded during re-reduction at 500°C under H<sub>2</sub>.

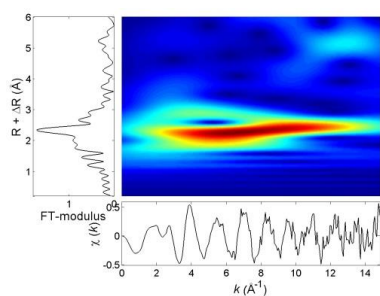
Under H<sub>2</sub> three effects on the spectrum can be observed in comparison to acquisition under He: the edge energy shifts to higher value by 0.6 eV, the white line is less intense and an adsorption feature at 11572 eV is present. These observations are in agreement with previous reports [115,118,129] and indicate clearly the adsorption of hydrogen on platinum at room temperature. These effects are also the same exhibited in the simulated XANES spectra of Pt<sub>13</sub> and Pt<sub>13</sub>H<sub>18</sub> DFT models (Figure 4-20 a, blue and green lines). At 500°C the hydrogen coverage is lower than at room temperature as the XANES scans resemble mostly the spectrum acquired under He.

#### **4.2.3.2.2 EXAFS**

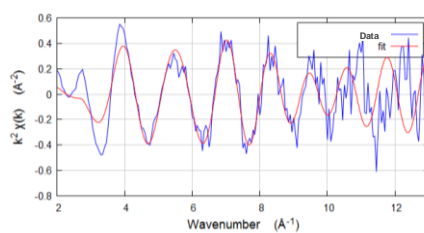
The EXAFS spectra are presented in Figure 4-22,  $\chi(k)$  and magnitude of the Fourier transform, as well as the respective wavelet analysis. The data was fitted using Artemis from the Demeter software package and the best fit is shown in red in Figure 4-22.

The  $\chi(k)$  spectra are similar between samples and the magnitude of the Fourier transform reveals two main signals which the wavelet analysis suggests should be of a light and of a heavy scatterer. As for the reduced samples at 0.1%Cl loading, those were fitted as Pt-Al or Pt-O<sub>long</sub> and as Pt-Pt, respectively. The Pt-Al or Pt-O<sub>long</sub> paths were obtained with the QFS tool setting a distance of 2.5 Å (see respective discussion in section 4.1.2.2). It was not possible to definitely establish whether the light scatterer signal corresponds to Al, O or both. It was also not possible to successfully fit a Pt-O path at 2 Å nor a Pt-Cl path at 2.3 Å. The “best fit” represented in Figure 4-22 was obtained using Pt-Al and the respective parameters are summarized in Table 4-9. Table 4-10 presents the fit results using the Pt-O<sub>long</sub> path.

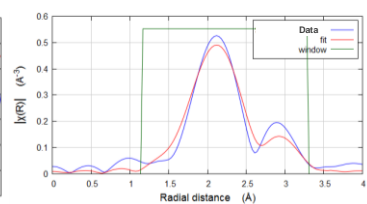
a1) 0.3%Pt/PuralSB3-1.4%Cl reduced



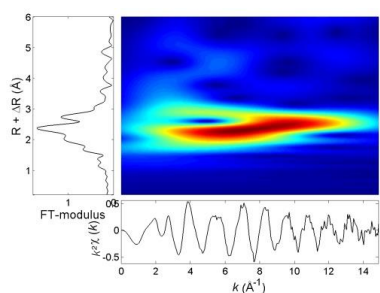
a2)



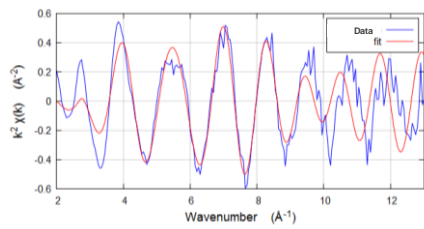
a3)



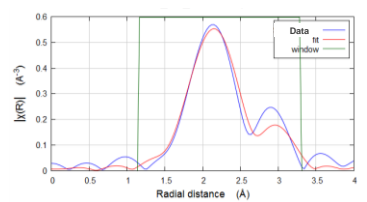
b1) 1%Pt/PuralSB3-1.4%Cl reduced



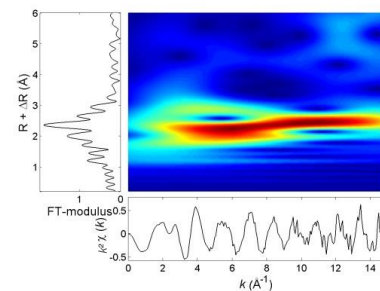
b2)



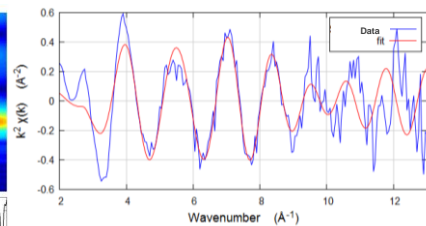
b3)



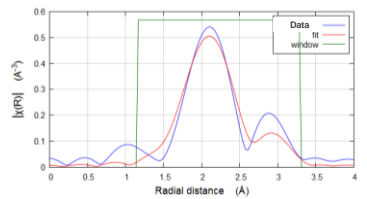
c1) 0.3%Pt/TH100-1.4%Cl reduced



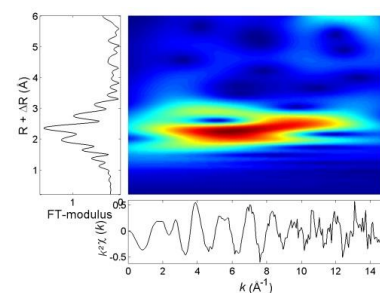
c2)



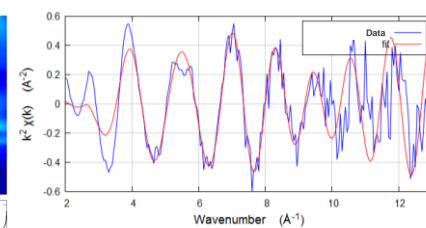
c3)



d1) 1%Pt/TH100-1.4%Cl reduced



d2)



d3)

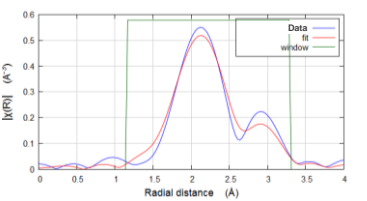


**Figure 4-22 - Wavelet transform analysis 1), EXAFS  $\chi(k)$  2) and magnitude of the Fourier transform  $|\chi(R)|$  (no phase correction) 3), all weighted by  $k^2$ , of reduced catalysts at 1.4%Cl loading. In 1) and 2) the red line represents the best fit. In 3), the fitting range is represented by the green line.**



**Table 4-9 – EXAFS fitting results for reduced catalysts considering Pt-Al coordination for the light scatterer.  $E_0=11566.1$  eV;  $1.15 < R < 3.2$  Å;  $N_{ind}=8$ ;  $N_{var}=7$  (\* $N_{var}=6$ ).**

Reduced catalyst	k-range (Å <sup>-1</sup> )	Path	Coordination number	R (Å)	$\sigma^2$ (Å <sup>2</sup> )	$\Delta E_0$	R-factor
0.3%Pt/PuralSB3-1.4%Cl	3.9 – 8.3	Pt-Al	1.5±0.5	2.42±0.05	0.006±0.004	6±1	0.04
		Pt-Pt	3±1	2.73±0.03	0.005±0.003		
1%Pt/PuralSB3-1.4%Cl	4 – 8.3	Pt-Al	1.0±0.3	2.44±0.03	0.001±0.003	6.9±0.8	0.03
		Pt-Pt	4±1	2.75±0.02	0.006±0.002		
0.3%Pt/TH100-1.4%Cl	3.9 – 8.3	Pt-Al	1.4±0.5	2.43±0.05	0.004±0.004	6±1	0.06
		Pt-Pt	3±1	2.73±0.05	0.006±0.004		
1%Pt/TH100-1.4%Cl*	4 – 8.3	Pt-Al	1.2±0.4	2.41±0.05	0.003±0.001	5.0±0.9	0.03
		Pt-Pt	3.2±0.7	2.73±0.03			

**Table 4-10 – EXAFS fitting results for reduced catalysts considering Pt-O<sub>long</sub> coordination for the light scatterer.  $E_0=11566.1$  eV;  $1.15 < R < 3.2$  Å;  $N_{ind}=8$ ;  $N_{var}=7$  (\* $N_{var}=6$ ).**

Reduced catalyst	k-range (Å <sup>-1</sup> )	Path	Coordination number	R (Å)	$\sigma^2$ (Å <sup>2</sup> )	$\Delta E_0$	R-factor
0.3%Pt/PuralSB3-1.4%Cl	3.9 – 8.3	Pt-O <sub>long</sub>	2.5±0.5	2.61±0.04	0.004±0.003	3.6±0.8	0.03
		Pt-Pt	2.7±0.6	2.68±0.02	0.003±0.002		
1%Pt/PuralSB3-1.4%Cl	4 – 8.3	Pt-O <sub>long</sub>	2.4±0.6	2.61±0.02	0.005±0.004	3.4±0.7	0.02
		Pt-Pt	3.3±0.6	2.70±0.01	0.003±0.002		
0.3%Pt/TH100-1.4%Cl	3.9 – 8.3	Pt-O <sub>long</sub>	2.7±0.7	2.58±0.05	0.005±0.004	2.4±0.9	0.04
		Pt-Pt	2.5±0.8	2.68±0.02	0.004±0.003		
1%Pt/TH100-1.4%Cl*	4 – 8.3	Pt-O <sub>long</sub>	2.3±0.8	2.60±0.04	0.003±0.001	4.0±0.9	0.04
		Pt-Pt	2.9±0.8	2.71±0.02			

Focusing on the fits using the Pt-Al path, the coordination number for the Pt-Pt path is between 3 and 4, comparable to the values obtained for reduced catalysts at 0.1%Cl and by other authors [95,108]. The distance found for this path is about 2.73 Å, still lower than the bulk distance of 2.773 Å as expected for nanoparticles, in agreement with the results obtained for the samples at 0.1%Cl. This value also suggests hydrogen is still adsorbed onto platinum to a degree [111], as the XANES data also indicated.

Overall the EXAFS analysis reveals the same results as for the catalysts at 0.1%Cl, no clear impact of chlorine loading being detected. As previously, the obtained structural parameters are also insensitive to the type of alumina support and platinum loading.

### 4.2.3.3 Conclusion

Reduced catalysts reveal well defined nanoparticles of 0.9 nm on average and flat morphology as well as single atoms. The single atom population is sensitive to chlorine loading, with higher Cl loading favouring the SA, and to type of alumina support while Pt loading has no impact on the SA population at 1.4%Cl.

XANES spectra confirm the reduced state of platinum and all samples share identical spectral features, where the white line notably corresponds to that of a  $\text{Pt}_{13}/(100)_{\text{dehyd}}$  DFT model obtained using the FDMNES code. Spectra acquired under  $\text{H}_2$  reveal the signature effects of hydrogen adsorption on the Pt  $\text{L}_3$  edge.

The EXAFS data fitting leads to the same conclusions as for the reduced samples at 0.1%Cl: a strong interaction with the support is revealed by an intense contribution centred at 2.5 Å for which assignment to Pt-Al, to Pt-O<sub>long</sub>, or to both could not be clearly stated. No impact of chlorine loading, metal loading or of support type was found.

### 4.3 Conclusion

The metallic phase supported on chlorinated alumina was characterized by STEM and XAS for a series of samples in oxide and reduced state, prepared using two different  $\gamma$ -Al<sub>2</sub>O<sub>3</sub> supports prepared from two different commercial boehmites, PuralSB3 and TH100, with two platinum loadings (0.3 and 1%<sub>w/w</sub> Pt) and two chlorine loadings (0.1 and 1.4%<sub>w/w</sub> Cl).

For the samples in oxide state, platinum is highly dispersed as a monoatomic oxide complex of the type PtCl<sub>x</sub>O<sub>y</sub>. STEM images reveal mostly single atoms, some platinum dimers or trimers and, exclusively for the 1%Pt loading, clusters of at least about 5 Pt atoms that are weakly cohesive. The XANES edge features of PuralSB3 are highly sensitive to aggregation level depending on metal loading as suggested by the simulated XANES spectra. TH100 samples' XANES features are virtually insensitive to metal loading but do seem more sensible to chlorine loading than PuralSB3's. This is particularly intriguing considering the TPR results for Impregnated and calcined samples (section 2.3.2.4) that showed an impact of platinum loading on the temperature of maximum H<sub>2</sub> consumption for both supports, parameter usually interpreted as indicative of the metal-support interaction. EXAFS analysis reveals no Pt-Pt contribution, but the existence of Pt-O and Pt-Cl distances, confirming the mononuclear nature of the oxide complex being PtCl<sub>x</sub>O<sub>y</sub>, with x/y ratio being dependent on chlorine loading (about 0.2 and 0.7 for 0.1%Cl and 1.4%Cl respectively), and the high dispersion.

After reduction, platinum is, for all samples, mostly in the form of nanoparticles of 0.9 nm of a flat bi-planar morphology constituted of about 10 to 20 Pt atoms. XANES spectral features are compatible with Pt<sub>13</sub> signatures of simulated spectra, probably with some degree of hydrogen adsorbed onto the platinum. Single atoms of platinum are also visible in STEM images and their population was quantified to find that overall 18% of deposited platinum atoms are in that form and that it is impacted: negatively by increasing platinum loading only for 0.1%Cl loading; positively by increasing chlorine loading independently of metal loading showing the stabilization of the smallest Pt species by Cl; and by type of alumina support. A XANES feature at 11567.8 eV found for one catalyst, 0.3%Pt/TH100-0.1%Cl, was associated with simulated signature features of a reduced single atom Pt<sub>1</sub> DFT model.

Further evaluation of TH100 catalysts at 1.4%Cl loading, the resulting conclusions being generally extended to the rest of the samples, found that more than 70% of the platinum nanoparticles are located on crystallite edges or other defects (steps or kinks). Such location was found to be thermodynamically competitive with that on the extended surfaces by a first DFT investigation. The average shortest inter-nanoparticle distance following the support surface were quantified to find that such distance is controlled by platinum loading through the absolute quantity of nanoparticles, it corresponds to a statistic distribution indication that anchoring sites are abundant in these circumstances and it can be either inter- or intra nanoparticle also depending on platinum loading. A statistic evaluation of alumina aggregate (composed of crystallites) tortuosity was used to evaluate the distribution of the nanoparticles on the support aggregates studied which was found to be homogeneous.

In situ electron microscopy experiments were conducted to enlighten the reduction mechanism that transforms the oxide samples into the reduced samples, with the particularity that the reduced state is remarkably similar independently of the three varying parameters (%Pt, %Cl and support type).

This result raises the question about how is the same final result obtained from distinct initial conditions? It was confirmed that reduced nanoparticles are visible at 500°C under H<sub>2</sub> and that they are immobile and stable up to 700°C, at which temperature some will coalesce. It is likely that nanoparticle genesis is dependent on single atoms, but the technique's resolution does not allow for their observation during in situ reduction. Two scenarios are proposed here to enrich the discussion.

On the one hand, one may consider all surface Pt anchoring sites to be equally favourable. In the oxide state at 0.3%Pt there are enough sites to stabilize one monoatomic oxide complex per site whereas at 1%Pt the sites are saturated and weakly cohesive cluster aggregates form. During reduction, platinum migrates coalescing into nanoparticles, the driving force being the loss of O and Cl coordination, independently of being initially in a lax oxide cluster or not. On the other hand, different categories of surface anchoring sites can be imagined, which may be more or less able to stabilize single atoms (oxide or reduced). The most single atom stabilizing sites may already be saturated at 0.3%Pt loading, but monoatomic oxide complexes may also not be exclusive to such sites. Overall site saturation at 1%Pt leads to

the formation of the oxide cluster aggregates. Upon reduction only the Pt atoms in the most stabilizing sites will remain as such despite likely Cl and O coordination loss, ensuring a given single atom population. The remaining Pt atoms would coalesce on the sites more favourable for nanoparticle stabilization. Either way, understanding the role of chlorine in stabilizing the  $\text{PtCl}_x\text{O}_y$  oxide complex and in the reduction mechanism is still a challenge and should continue to be investigated.

# **Chapter 5**

## **Site proximity assessment**

This chapter starts with a summary of the most important results presented in the previous chapters related the location of active sites that are then used towards the building of a geometrical model capable of estimating the distance between metallic and acidic sites.

## ***5.1 Location of metallic and acidic sites in Pt/ $\gamma$ -Al<sub>2</sub>O<sub>3</sub>-Cl catalysts***

The extensive multi-technique characterization of a series of Pt/ $\gamma$ -Al<sub>2</sub>O<sub>3</sub>-Cl catalysts (presented in the two previous chapters) aimed at determining the location of metallic and acidic active sites on the support crystallites and at evaluating what is the impact of their proximity on each other. This section summarizes the main findings and presents the results of the <sup>1</sup>H NMR study of Pt/ $\gamma$ -Al<sub>2</sub>O<sub>3</sub>-Cl catalysts which constitute an indirect assessment of proximity between Pt and OH groups.

### **5.1.1 Location of acidic sites (summary)**

Chlorine is known to increase the acidity of  $\gamma$ -Al<sub>2</sub>O<sub>3</sub> [82,86,211] and indeed low temperature CO adsorption showed the Brønsted sites to be more acidic in the samples with 1.4%Cl loading than in the original non-chlorinated alumina samples. It is considered that the acidic active sites are hydroxyl groups that are Brønsted sites (not all OH are) which are under the influence of chlorine. Indeed saying “under the influence of chlorine” is quite vague, but there is an inherent difficulty in probing the acid sites on the surface of alumina and in discerning acidic OH that can act as active sites from the remaining OH population. Thus, for the remaining of the chapter the location of chlorine atoms is taken as indicative of the location of acidic sites.

DFT chemical shift calculations and the development of the first alumina crystallite edge model for the (110)-(100) edge have allowed the proposal of a new  $\gamma$ -Al<sub>2</sub>O<sub>3</sub> <sup>1</sup>H NMR peak assignment [4]. Spectra interpretation in light of this assignment and DFT calculated exchange energies suggest that chlorine will most preferably be exchanged with  $\mu_1$ -OH located on the crystallite edge (namely on the Al-side). Exchange energies indicate the second best groups for exchange with Cl will be  $\mu_1$ -OH on the (110) surface. For PuralSB3, with a rather *roundish* morphology allowing for high edge/surface ratios, at 1.4%Cl target loading all chlorine atoms seem to be exchanged predominantly with hydroxyls on the edge. Thus Brønsted acid sites would be in close vicinity to the edge. TH100 exhibits a platelet like shape with lower proportion of edge  $\mu_1$ -OH and these seem to be exhausted at 0.5%Cl. The remaining Cl atoms needed to reach the 1.4%Cl loading target is exchanged with surface  $\mu_1$  hydroxyls, most likely on the (110) type surface.



### 5.1.2 Location of metallic sites (summary)

Upon reduction mostly monoatomic  $\text{PtCl}_x\text{O}_y$  oxide complexes ( $x/y$  depends on Cl loading) transform into Pt nanoparticles with an homogeneous average size of 0.9 nm and a flat bi-planar morphology. These nanoparticles were found to be mostly located on the edges of the crystallites or on other edge-like defaults (steps, kinks). For the Pt loadings considered, they are uniformly dispersed over the support aggregates. The average shortest inter-NP distance was quantified and found to be tuned by platinum loading, it being of 16 nm for 0.3%Pt and of 9 nm for 1%Pt.

A population of single atoms is still present after reduction. Its quantification through a  $\#SA/\#NP$  ration suggests it represents around 20% of the deposited platinum atoms. This proportion was found to be higher for the catalysts at 1.4%Cl, demonstrating the stabilizing effect of chlorine. The location of the single atoms could not be evaluated as they are below the resolution attainable in electron tomography of such samples.

### 5.1.3 $^1\text{H}$ NMR study of Pt/ $\gamma\text{-Al}_2\text{O}_3$ -Cl catalysts

Catalyst samples at 1%Pt and 0.5% and 1.4%Cl loading were analysed by  $^1\text{H}$  NMR in the same way as the alumina samples, detailed in chapter 3, aiming to detect an impact of platinum on the hydroxyl groups which would be an indication of proximity. To evaluate the proximity of the different OH groups on the alumina surface, two dimensional  $^1\text{H}$ - $^1\text{H}$  SQ-DQ BABA (see section 2.2.2.2.2) spectra were also acquired, for samples with and without platinum, and are presented and discussed in this section using the peak assignment proposed in chapter 3.

As previously, all samples were submitted to the same thermal treatment before analysis, which is equal to the reduction described in section 2.1.3.3, being sealed in vacuum in an ampoule that was opened in a glove box for rotor filling.

The  $^1\text{H}$  DEPTH spectra of PuralSB3 and TH100 samples are presented in Figure 5-1 and Figure 5-2.

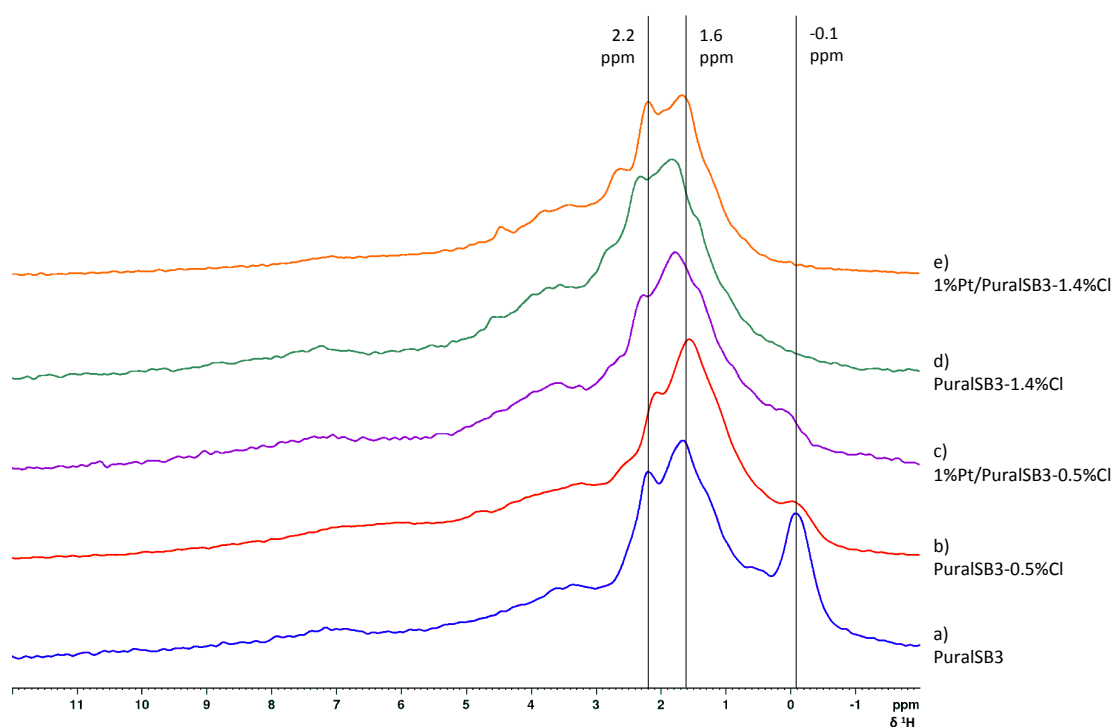


Figure 5-1 –  $^1\text{H}$  NMR DEPTH spectra of a) PuralSB3, b) PuralSB3-0.5%Cl, c) 1%Pt/PuralSB3-0.5%Cl, d) PuralSB3-1.4%Cl and e) 1%Pt/PuralSB3-1.4%Cl.

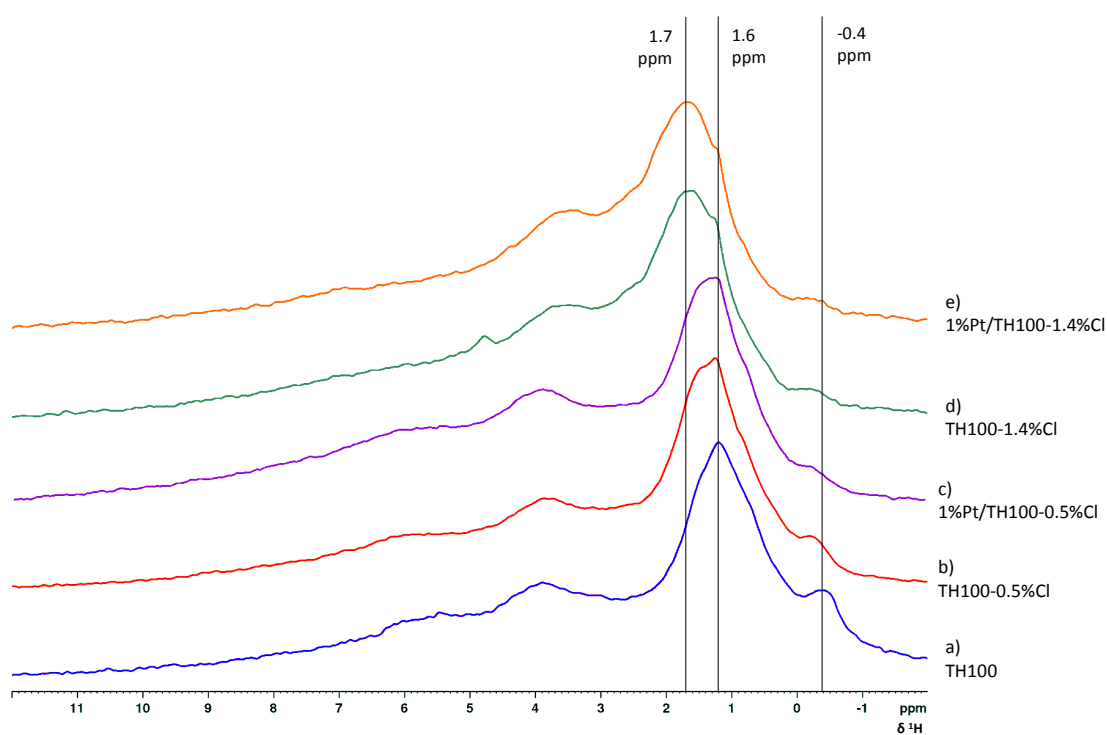


Figure 5-2 –  $^1\text{H}$  NMR DEPTH spectra of a) TH100, b) TH100-0.5%Cl, c) 1%Pt/TH100-0.5%Cl, d) TH100-1.4%Cl and e) 1%Pt/TH100-1.4%Cl.

The spectra of the alumina and chlorinated alumina samples of both supports are the same as already presented in chapter 3. Spectra of catalysts with 1%Pt (c and e) are no different from the spectra of the alumina samples with the same chlorine loading without Pt (b and d, respectively). Spectral decomposition also resulted in equivalent results. This observation is consistent with IR investigations which also revealed no impact of 1% platinum loading on the OH region spectra (Appendix J). This can be explained by the large excess of surface OH groups in comparison with the number of supported platinum atoms.

In Figure 5-3 and Figure 5-4 are represented the two dimensional  $^1\text{H}$ - $^1\text{H}$  SQ-DQ BABA spectra of PuralSB3 and TH100 samples respectively. The spectra obtained is in the form of a two-dimensional map. Since this technique allows one to visualize protons that are dipolar coupled, the presence of a signal indicates that two protons are in close proximity of each other (few Ångström). Auto-correlation peaks are observed along the diagonal ( $\delta_A$ ,  $2\delta_A$ ) corresponding to equivalent protons (same chemical shift) dipolar coupled. The off-diagonal peaks correspond to ( $\delta_A$ ,  $\delta_A+\delta_B$ ) and ( $\delta_B$ ,  $\delta_A+\delta_B$ ) to dipolar coupling between two different protons (different chemical shift).

The detected correlations are summarized in Table 5-1. Two factors impact correlation signal intensity: the proximity in space between the correlating protons and their quantity. Thus, an intense correlation reflects a close proximity between protons (typically distances shorter than 5 Å).

*Table 5-1  $^{-1}\text{H}$  frequencies that correlate in  $^1\text{H}$ - $^1\text{H}$  SQ-DQ BABA spectrum of each PuralSB3 and TH100 sample, in ppm.  
When only one value is displayed per line it is an auto-correlation.*

PuralSB3		PuralSB3-0.5%Cl		1%Pt/PuralSB3-0.5%Cl		PuralSB3-1.4%Cl		1%Pt/PuralSB3-1.4%Cl	
$\delta_1$	$\delta_2$	$\delta_1$	$\delta_2$	$\delta_1$	$\delta_2$	$\delta_1$	$\delta_2$	$\delta_1$	$\delta_2$
-0.1	-								
-0.1	2.2								
1.7	-	1.5	-	1.7	-	1.7	-	1.7	-
2.1	3.1	1.9	3.1	2.1	2.9	2	3	2	3
		1.8	3.8			3.6	-		
TH100		TH100-0.5%Cl		1%Pt/TH100-0.5%Cl		TH100-1.4%Cl		1%Pt/TH100-1.4%Cl	
$\delta_1$	$\delta_2$	$\delta_1$	$\delta_2$	$\delta_1$	$\delta_2$	$\delta_1$	$\delta_2$	$\delta_1$	$\delta_2$
-0.4	1.3								
1.2	-	1.2	-	1.3	-	1.7	-	1.7	-
1.4	3.5	1.4	3.5	1.5	3.5	1.9	2.6	2	3
						3.8	-		

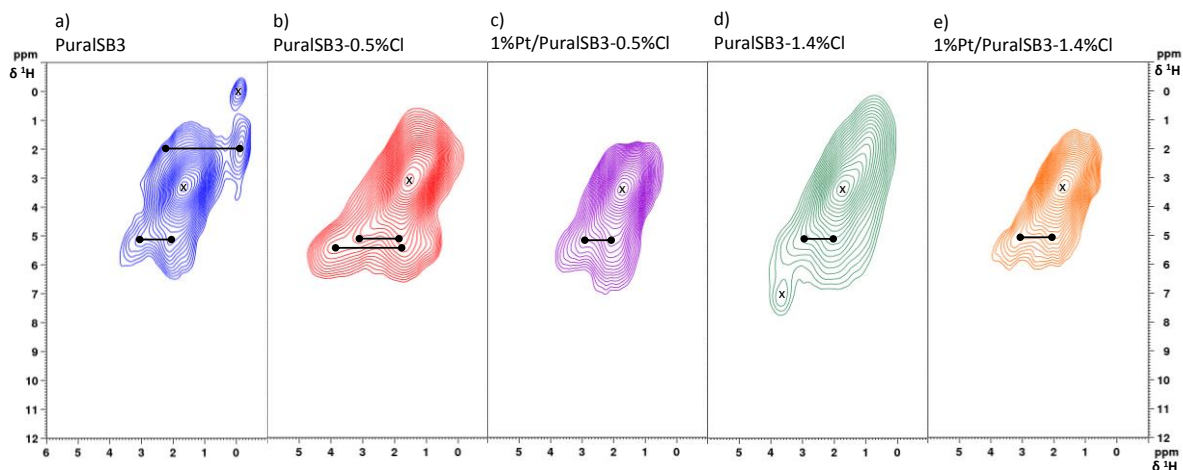


Figure 5-3 –  $^1\text{H}$ - $^1\text{H}$  SQ-DQ NMR spectra of a) PuralSB3, b) PuralSB3-0.5%Cl, c) 1%Pt/PuralSB3-0.5%Cl, d) PuralSB3-1.4%Cl and e) 1%Pt/PuralSB3-1.4%Cl. Horizontal lines depict cross-correlations and crosses depict auto-correlations.

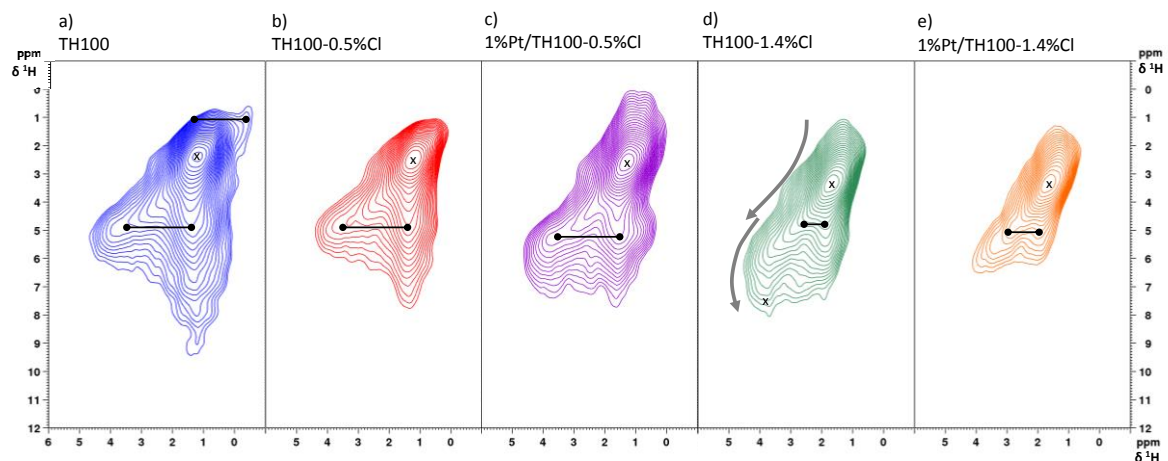


Figure 5-4 -  $^1\text{H}$ - $^1\text{H}$  SQ-DQ NMR spectra of a) TH100, b) TH100-0.5%Cl, c) 1%Pt/TH100-0.5%Cl, d) TH100-1.4%Cl and e) 1%Pt/TH100-1.4%Cl. Grey arrows indicate the change in format of the signal. Horizontal lines depict cross-correlations and crosses depict auto-correlations.

Focusing first on the PuralSB3 series, there is one intense autocorrelation that is common to all spectra between protons at 1.7 ppm, the most intense signal in the  $^1\text{H}$  DEPTH spectra. This signal is in the range assigned to free  $\mu_2$ -OH on the O-side of the (110)-(100) edge and to  $\mu_1$  or  $\mu_2$ -OH on the surface planes that are not hydrogen bond donors.

Another correlation is present in all spectra, between proton at around 2 and 3 ppm. Note that the second most intense signal of the  $^1\text{H}$  DEPTH spectra is at 2.2 ppm and may correspond to OH on the edges or on the surface. At 3 ppm is the beginning of the large signal in the  $^1\text{H}$  DEPTH spectra. Thus, species that are hydrogen bond donors are expected to

contribute to this signal, even if they could not be determinately assigned through the DFT study.

For the non-chlorinated PuralSB3 alumina two other signals are present, an autocorrelation corresponding to the 0 ppm edge  $\mu_1$ -OH protons, which are very abundant in this alumina, and a correlation between those 0 ppm edge  $\mu_1$ -OH and the signal at 2.2 ppm (the 2<sup>nd</sup> most intense in DEPTH spectra). This suggests proximity between the edge hydroxyls and the surface hydroxyls. The spectrum is quite similar to that obtained by Taoufik et al. [75].

When chlorine is added, starting at 0.5%, correlations involving the 0 ppm edge  $\mu_1$ -OH are no longer present as these hydroxyls are preferentially exchanged with chlorine. Auto-correlation between protons at 1.7 ppm and cross-correlation between protons at around 2 and 3 ppm are still observed. Additionally, an additional correlation is detected between signals at around 2 and 4 ppm, suggesting a disturbance of the hydrogen bond network in the surface planes surrounding PuralSB3 crystallite edges or even a proton transfer that could induce a new correlation. When 1%Pt is impregnated this additional correlation can no longer be detected which seems to indicate that Pt NPs are located in close vicinity of Cl atoms since they directly counter the effect of Cl. If so, this would be consistent with the fact that Pt NPs are observed by electron tomography to be located near the edge where Cl atoms are also located.

Further chlorine addition up to 1.4%Cl reveals the appearance of an autocorrelation between protons at 3.5 ppm which may correspond to previously H-bond donor species that see their chemical shift displaced to a lower value as that H-bond is broken by the presence of chlorine. The spectrum of the equivalent sample with 1%Pt no longer displays this autocorrelation, which again seems to indicate proximity of Pt NPs to Cl atoms.

In the case of the TH100 sample without chlorine nor platinum, the autocorrelation at 0 ppm is no longer detected, in agreement with the  $^1\text{H}$  DEPTH spectra showing a low intensity for that signal, meaning fewer edge  $\mu_1$ -OH for TH100, but the correlation with signals around 1.3 ppm is still detected.

Two correlations are always present, as in the PuralSB3 series, an intense autocorrelation from 1.2 to 1.7 ppm and a correlation between signals at 3 to 3.5 ppm and 1.4 to 1.9 ppm,

both slightly shifting position with the appearance of the 1.7 ppm shoulder on the DEPTH spectra as chlorine loading increases.

When chlorine is present the correlation of the 0 ppm peak disappears. That is the only difference in the 0.5%Cl sample spectrum and no impact of Pt is detected at that particular loading. For 1.4%Cl an autocorrelation around 3.5 ppm may be present, as a change in the shape of the signal similar to that of PuralSB3-1.4%Cl spectrum is observed as shown by the arrows in Figure 5-4. Yet it is difficult to be sure as there is some noise in that region. In the presence of 1%Pt the hint of that autocorrelation is no longer present, as the shape change is not observed, reproducing the results obtained for PuralSB3.

Overall, while the  $^1\text{H}$  DEPTH spectra is composed of a complex mixture of signals only a fraction of them show proximity through the BABA spectra. With this type of mapping, effects of alumina chlorination on the proton species can be detected that are also alumina type dependent. Despite no impact being observed in the  $^1\text{H}$  DEPTH spectra, the presence of 1%Pt changes the correlations observed in the 2D spectra, especially at 1.4%Cl loading. This influence of Pt on surface hydroxyls of  $\gamma$ -alumina is thus revealed and is another result that stands in contrast with the proposal by Kwak et al. that Pt is preferably anchored on the (100) surface [92]. The TH100 samples seem to be less affected by the addition of Cl and of Pt when compared to PuralSB3 samples, perhaps explained by better developed hydrogen bond networks, less susceptible to be impacted, on the extended surface planes of the crystallites that will be larger than PuralSB3's or by a differing location of Cl atoms at that loading (on edges and on surfaces). The  $^1\text{H}$  signal assignment proposed here for the 1D spectra does not allow the BABA spectra to be fully explained because of the coexistence of many signals in some regions of the DEPTH spectra that could not be distinctly assigned, of which only two or three correlate in the 2D maps. A more complete view of the alumina crystallite would be necessary, considering other types of edges for example, and larger sets of  $^1\text{H}$  NMR data for several aluminas each treated at different temperatures, to improve upon the assignment.

## ***5.2 Geometric models to evaluate site proximity in Pt/ $\gamma$ -Al<sub>2</sub>O<sub>3</sub>-Cl catalysts***

The information gathered through characterization of the catalysts sets, described in the previous chapters and summarized above, is here used to construct a geometric model of the catalyst in its reduced state that can be used to estimate the distance between the acidic and metallic acid sites.

A simple approach at solving the issue assuming a parallelepipedic platelet morphology and a square network distribution of surface species, already partially presented in section 4.2.2, is described in the next section. This first model was improved upon and complexified as presented later in the text by adapting the platelet morphology to each support.

### **5.2.1 First simple 2D geometric model**

Considering a single alumina platelet of a chosen morphology and size as first model, and for given Pt and Cl loadings, the following parameters are obtained: number of Pt<sub>13</sub> NPs and Cl atoms per platelet, inter-NP and inter-Cl distance (supposing they are distributed in a square network) and chlorine loading at which the platelet edge sites are saturated with Cl atoms.

These are then used to estimate the distance between acid and metallic sites. The following simplification is applied: the distance is evaluated between Cl atoms and Pt NPs. It is understood that the acid sites involved in reaction mechanisms are alumina hydroxyls with sufficient Brønsted acidity *enhanced* by chlorine. It is thus considered that such acidic sites are under the influence of Cl and thus in its close proximity, so Cl location can be considered as a proxy for acid site location. Indeed, in weak acidic supports such as halogenated aluminas the characterization of Brønsted acidity is difficult, as is pinpointing which of the many OH on the support have the capacity to act as acid sites.

For this first approach the following assumptions were considered:

- The shape of both PuralSB3 or TH100 alumina crystallites was set as a parallelepipedic platelet of dimensions a, b and c. When simulating PuralSB3 or TH100, the respective size average from measurements obtained by TEM is used for those dimensions.

- The alumina surface types are assigned in this morphology as illustrated in Figure 5-5. Note that a parallelepiped does not exposed the (111) surface. The surface planes are considered to be flat, without steps or kinks.
- Stacking of multiple platelets was not considered.
- A surface area of the crystallite in g/m<sup>2</sup> is calculated using an alumina density of 4 g/cm<sup>3</sup>. [212]
- All deposited Pt atoms are considered to be in the form of Pt<sub>13</sub> NPs.

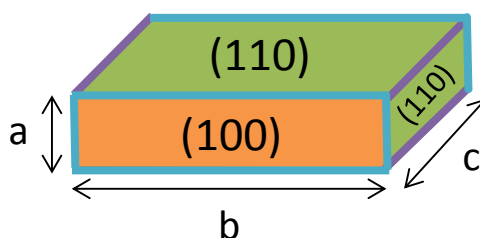


Figure 5-5 – Scheme of platelet morphology in which the geometric model is based showing how surface types were allocated, (110) – green, (100) – orange, and distinguishing the two types of edge present, (110)-(100) – blue and (110)-(110) – purple.

The geometric parameters thus obtained when modelling a PuralSB3 alumina or a TH100 alumina catalyst are presented in Table 5-2 and Table 5-3, respectively.

Table 5-2 – Geometric parameters and Pt and Cl coverages obtained for PuralSB3 model.

Geometric parameters		Pt and Cl coverage				
Input		Input	Output			
a	5	% <sub>w/w</sub> Pt	Pt/nm <sup>2</sup>	Pt <sub>13</sub> /nm <sup>2</sup>	Square dist. distance (nm)	#Pt <sub>13</sub> /platelet
b	12.5	0.3	0.041	0.003	17.7	1
c	6	0.6	0.084	0.006	12.5	2
Output		1	0.140	0.011	9.7	4
Total S. area (platelet) (nm <sup>2</sup> )	335	% <sub>w/w</sub> Cl	Cl/nm <sup>2</sup>		Square dist. distance (nm)	#Cl/platelet
S. area (m <sup>2</sup> /g)	223	0.1	0.077		3.6	26
Total Edge length (nm)	94	1	0.778		1.1	261
(110)-(100) Edge length (nm)	70	1.4	1.094		0.9	366



*Table 5-3 – Geometric parameters and Pt and Cl coverages obtained for TH100 model.*

Geometric parameters		Pt and Cl coverage				
Input		Input	Output			
a	4	% <sub>w/w</sub> Pt	Pt/nm <sup>2</sup>	Pt <sub>13</sub> /nm <sup>2</sup>	Square dist. distance (nm)	#Pt <sub>13</sub> /platelet
b	14.5	0.3	0.043	0.003	17.3	1
c	9	0.6	0.086	0.007	12.3	3
Output		1	0.145	0.011	9.5	5
Total S. area (platelet) (nm <sup>2</sup> )	449	% <sub>w/w</sub> Cl	Cl/nm <sup>2</sup>		Square dist. distance (nm)	#Cl/platelet
S. area (m <sup>2</sup> /g)	215	0.1	0.080		3.5	36
Total Edge length (nm)	110	1	0.808		1.1	362
(110)-(100) Edge length (nm)	74	1.4	1.136		0.9	510

The platelet morphology and dimensions used result in a surface area of around 200 m<sup>2</sup>/g. The values are in good agreement with  $S_{\text{BET}}$  obtained for the samples (183 m<sup>2</sup>/g and 149 m<sup>2</sup>/g, for PuralSB3 and TH100 respectively). Nevertheless, they are superior to the experimental results because only one platelet is considered, and thus crystallite size/shape heterogeneities and stacking are not taken into account. The trend of  $S_{\text{PuralSB3}} > S_{\text{TH100}}$  is however maintained. Thus, Pt and Cl coverages X/nm<sup>2</sup> (X=Pt, Cl) can be calculated from the model. The results are in the same range than those obtained for the prepared catalysts (section 2.3.2.1). In the case of TH100 modelling the calculated coverages are a bit different from the experimental ones because the difference in calculated surface area and  $S_{\text{BET}}$  is more significant than in the case of PuralSB3.

The first useful insight concerns the impact of loading on the number of Pt<sub>13</sub> NPs per crystallite. As already discussed in section 4.2.2, while at 0.3%Pt the inter-NP distance is inter-crystallite it becomes intra-crystallite for higher loadings. This trend observed when modelling both supports.

The distance between Pt<sub>13</sub> NPs or between Cl atoms if disposed in a square network was calculated as an indicator of the average distance between them. In this first approach, the “first neighbour” Pt<sub>13</sub>-Cl distance was estimated based on these square networks as the distance between a Pt<sub>13</sub> NP in the centre of a Cl network square, which is half the diagonal length of that square. This is summarized in Figure 5-6 for extreme cases with the values obtained when modelling PuralSB3.

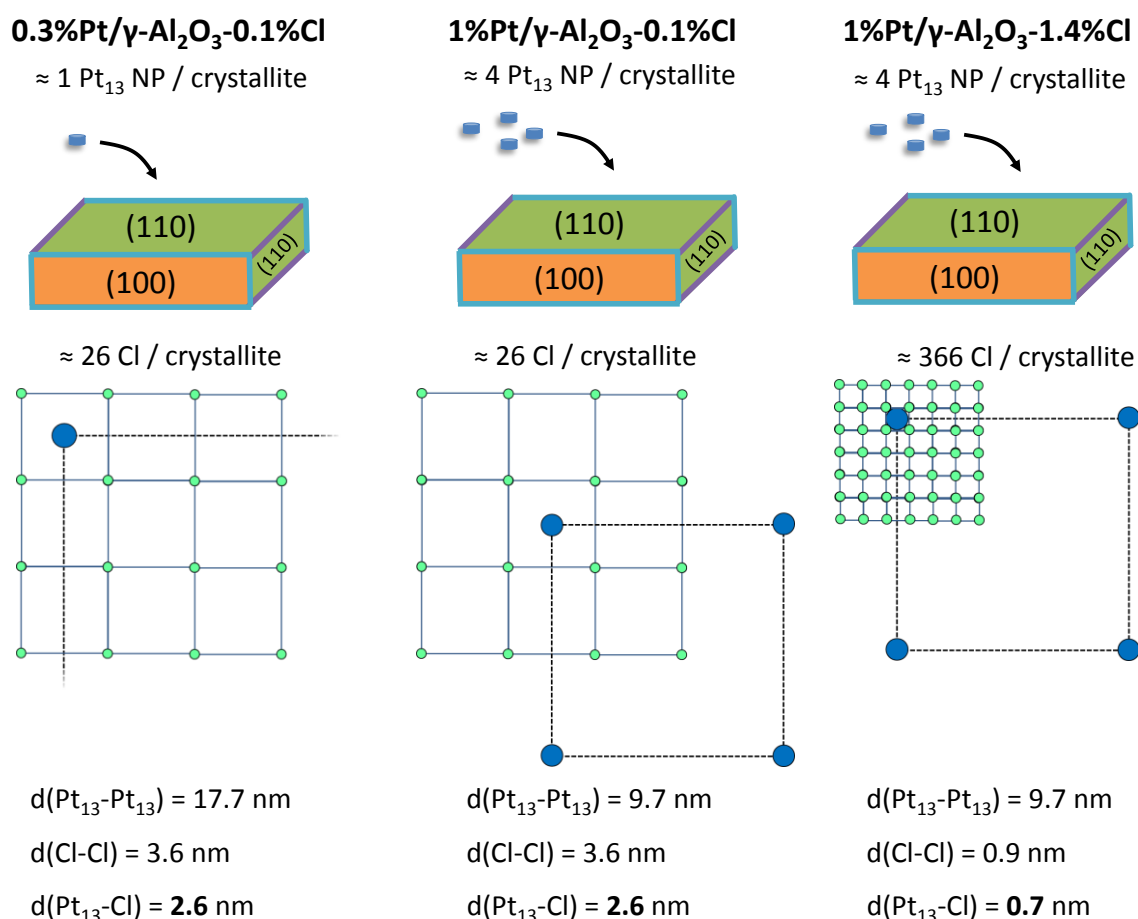


Figure 5-6 – Geometrical model of Pt<sub>13</sub> NP and Cl repartition on a square network and estimation of Pt<sub>13</sub>-Cl distances, as calculated with the PuralSB3 model.

This suggests the Pt<sub>13</sub>-Cl distance varies with chlorine loading but not with platinum loading within the range of Pt and Cl loadings studied here. The values are similar for TH100 modelling, as shown in Table 5-4. The typical chlorine loading used in commercial naphtha reforming catalysts which is of around 1% may then represent not only an optimum in terms of acidity but also in metal-acid site distance.

Table 5-4 – Pt<sub>13</sub>-Cl distance estimated for each alumina model and chlorine loading.

%w/wCl	d(Pt <sub>13</sub> -Cl) (nm)	
	PuralSB3 model	TH100 model
0.1	2.6	2.5
1	0.8	0.8
1.4	0.7	0.6

However, in placing the NP in the centre of a Cl square network the knowledge of the preferential Cl and Pt NP locations determined by the previous NMR, STEM and DFT study is not being used.

The maximum chlorine loading at which edge anchoring sites are saturated was also estimated, the results are shown in Table 5-5. In chapter 3 it is shown that the Al side hydroxyls of the (110)-(100) edge model are the most favourable to be exchanged with chlorine, the distance between consecutive Cl atoms on the edge being about 0.44 nm, and that chlorine is located exclusively in the edges for up to 1.4%Cl in the case of PuralSB3 and for up to 0.5%Cl for TH100.

*Table 5-5 - Maximum chlorine loading at which edge anchoring sites are saturated.*

	Half (110)-(100) Edge length	Half total Edge length
PuralSB3 model	0.3%	0.4%
TH100 model	0.2%	0.4%

First, half (“Al side of the edge only”) of the (110)-(100) type edge length was used. As Table 5-5 shows, this results in maximum loadings inferior to 0.5%Cl, much lower than the experimental data suggests. While the features of a (110)-(110) edge type structure can only be the object of speculation for now, it seems reasonable to admit it may harbour similar edge hydroxyls favourable for Cl exchange. Half the total edge length was then conservatively used. This estimation gives the much better result of 0.4%Cl for TH100, which is very close what was found by the NMR experiments. But the value for PuralSB3 is still less than a third of the expected loading.

Indeed, the factor that explained the different “edge chlorine uptakes” of the two aluminas was the edge to facet ratio which was higher for PuralSB3 due to its crystallite morphology. By setting a parallelepipedic platelet morphology in both cases the model is not accounting for this. While the TH100 crystallites observed in TEM (chapter 3) are not perfect parallelepipeds, this morphology is accurate enough to correctly predict the point of edge saturation by Cl.

Two shortcomings are thus identified, the square network approach to Pt<sub>13</sub>-Cl distance estimation and using a parallelepipedic morphology to model PuralSB3 samples. The following section describes how these can be corrected.

### 5.2.2 Morphology dependent geometrical model accounting for the location of Cl and Pt

To account for the high edge to facet ratio expected for PuralSB3 crystallites, the platelet morphology was set as a rhombicuboctahedron of edge length  $a$ . This polyhedron morphology is actually built from a perfect spinel type  $\text{MgAl}_2\text{O}_4$  bulk structure, of which crystallites expose the (110), (100) and (111) terminations in the following proportions, 55.9%, 28.0% and 16.1% respectively. Note that this ideal morphology is not the “true one”, observed by TEM (chapter 3) to be more oval following also the non-spinel nature of  $\gamma$ -alumina according to the topotactic transformation from its boehmite precursor. However, this assumed morphology helps to approximately represent the larger edge to surface ratio of PuralSB3.

In Figure 5-7 a) the solid is presented with the respective surface terminations. The solid can be constructed by assembling two square cupolas with an octagonal prism in the centre as shown in Figure 5-7 b). The diameter ( $d$ ) of the circumscribed circle of the octagon, which is the base of the octagonal prism, was set as the harmonic average of the crystallite dimensions obtained by TEM for PuralSB3 (5 x 12.5 x 6 nm). This allows the edge length  $a$  to be obtained. With this, new model geometric parameters could be calculated, as shown in Table 5-6.

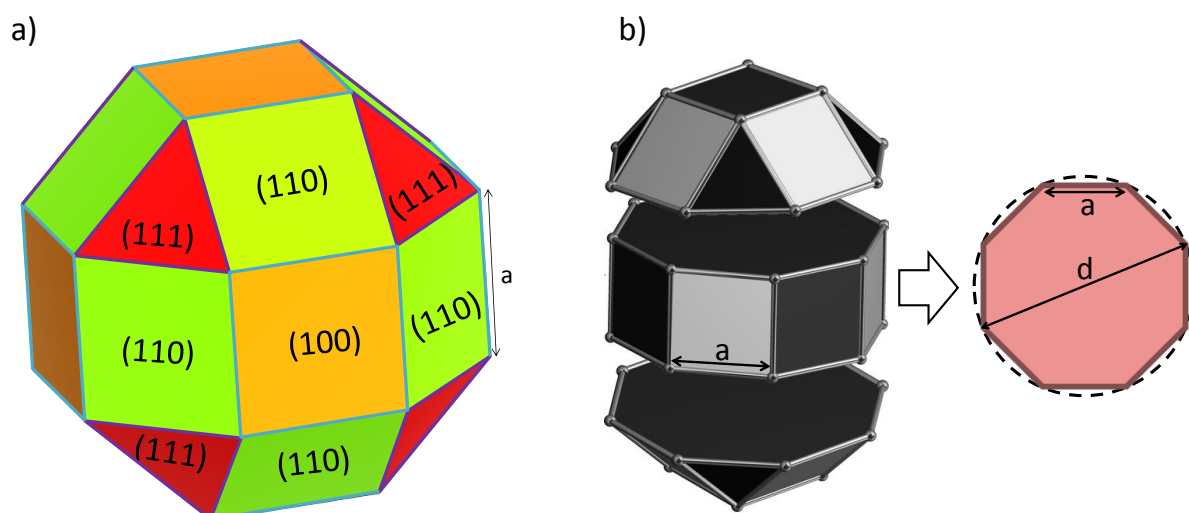


**Figure 5-7 – Scheme of rhombicuboctahedron platelet morphology on which the upgraded PuralSB3 geometric model is based** a) showing how surface types were allocated, (110) – green, (100) – orange, (111) – red, and distinguishing the two types of edge present, (110)-(100) – blue and (110)-(111) – purple, and b) scheme of how  $a$  was calculated by setting the value of the diameter  $d$  of the circumscribed circle (dashed black line) of the octagon (red) that is the base of the middle octagonal prism, one of the solids into which the rhombicuboctahedron can be decomposed.

**Table 5-6 - Geometric and Pt and Cl coverage parameters obtained for the upgraded PuralSB3 model.**

Geometric parameters		Pt and Cl distribution				
Input		Input	Output			
d (nm)	6.7	% <sub>w/w</sub> Pt	Pt/nm <sup>2</sup>	Pt <sub>13</sub> /nm <sup>2</sup>	Square dist. length (nm)	#Pt <sub>13</sub> /platelet
Output		0.3	0.042	0.003	17.6	0.5
a (nm)	2.8	0.6	0.0842	0.006	12.4	1
Total S. area (platelet) (nm <sup>2</sup> )	166	1	0.140	0.011	9.6	2
S. area (m <sup>2</sup> /g)	221	% <sub>w/w</sub> Cl	Cl/nm <sup>2</sup>		Square dist. length (nm)	#Cl/platelet
Total Edge length (nm)	133	0.1	0.078		3.58	13
(110)-(100) edge length (nm)	33	1	0.785		1.13	130
		1.4	1.104		1.0	183

In this way, for a surface area of 221 m<sup>2</sup>/g close to the one obtained in the previous section the total edge length is 40% larger than that of the parallelepipedic platelet. The platinum and chlorine coverages per nm<sup>2</sup> are also in the same range as the ones obtained for the prepared catalysts. The number of Pt<sub>13</sub> and Cl atoms per platelet is inferior to that obtained for the parallelepipedic platelet because the total area of the platelet (nm<sup>2</sup>) is smaller. But the inter to intra-crystallite trend of the Pt<sub>13</sub>-Pt<sub>13</sub> distance with increasing Pt loading still stands.

The maximum chlorine loading at which edge anchoring sites are saturated was again calculated knowing that the Al side hydroxyls of the (110)-(100) edge model are the most favourable to be exchanged with chlorine and the distance between consecutive Cl atoms on the edge is about 0.44 nm. A 0.6% maximum chlorine loading was now obtained when considering half the (110)-(100) type edge length. When half the total edge length is used this loading is 1.2%, remarkably similar to the loading of 1.4% found by NMR. With this more complex polyhedron containing many edges the PuralSB3 morphology can be correctly modelled. These values are summarized in Table 5-7 along with those obtained for TH100 (see above, section 5.2.1).

*Table 5-7 - Maximum chlorine loading at which edge anchoring sites are saturated.*

	Half (110)-(100) Edge length	Half total Edge length
PuralSB3 model	0.6%	1.2%
TH100 model	0.2%	0.4%

To estimate de  $\text{Pt}_{13}$ -Cl distance for both the PuralSB3 and TH100 cases the location of Cl and Pt NPs has to be taken into account. For example, 78% of the studied NPs were found to be located on the edges by electron tomography and the rest on facets. Several questions remain. Which edge type or surface termination would those be? Where along an edge would the NP be? Is it on chlorinated edges or not? For PuralSB3 catalysts Cl is located on the edges up to 1.2%Cl (from the model). For TH100 it's only up to 0.4%Cl, for higher loadings how should the rest of Cl atoms be distributed on the facets?

As this is clearly a system without a single solution, a distance estimation was made for two particular cases: the point at which the edge sites (half the total edge length) are saturated with chlorine (1) and for 1%Cl loading that is relevant for industrial catalytic reforming applications (2). These two cases essentially coincide for the PuralSB3 model but not for the TH100 model.

For each chlorine scenario, the shortest  $\text{Pt}_{13}$ -Cl distance is estimated for different fixed NP positions. One particular case is when the NP is located in a chlorinated edge, as the DFT models of  $\text{Pt}_{13}$ /edge-Cl presented in chapter 4 suggest the shortest NP-Cl distance can be in the angstrom scale, and if Cl migrates onto the NP it can correspond to a covalent bond with 2.3 to 2.5 Å. In this case however, it is not clear whether the chlorine attached to Pt (also

attached to the support, see inset in the figures) is at the origin of an enhanced acidity of the neighbouring OH groups or not. Otherwise, as shown in chapter 4, so far DFT calculations suggest NPs are also equally stable on non-chlorinated edges and on alumina facets. For these cases, some NP positions were chosen so as to represent the longest distances possible. This way both extreme cases can be considered. These NP positions are illustrated in Figure 5-8, Figure 5-9 and Figure 5-10 and the corresponding results are summarized in Table 5-8.

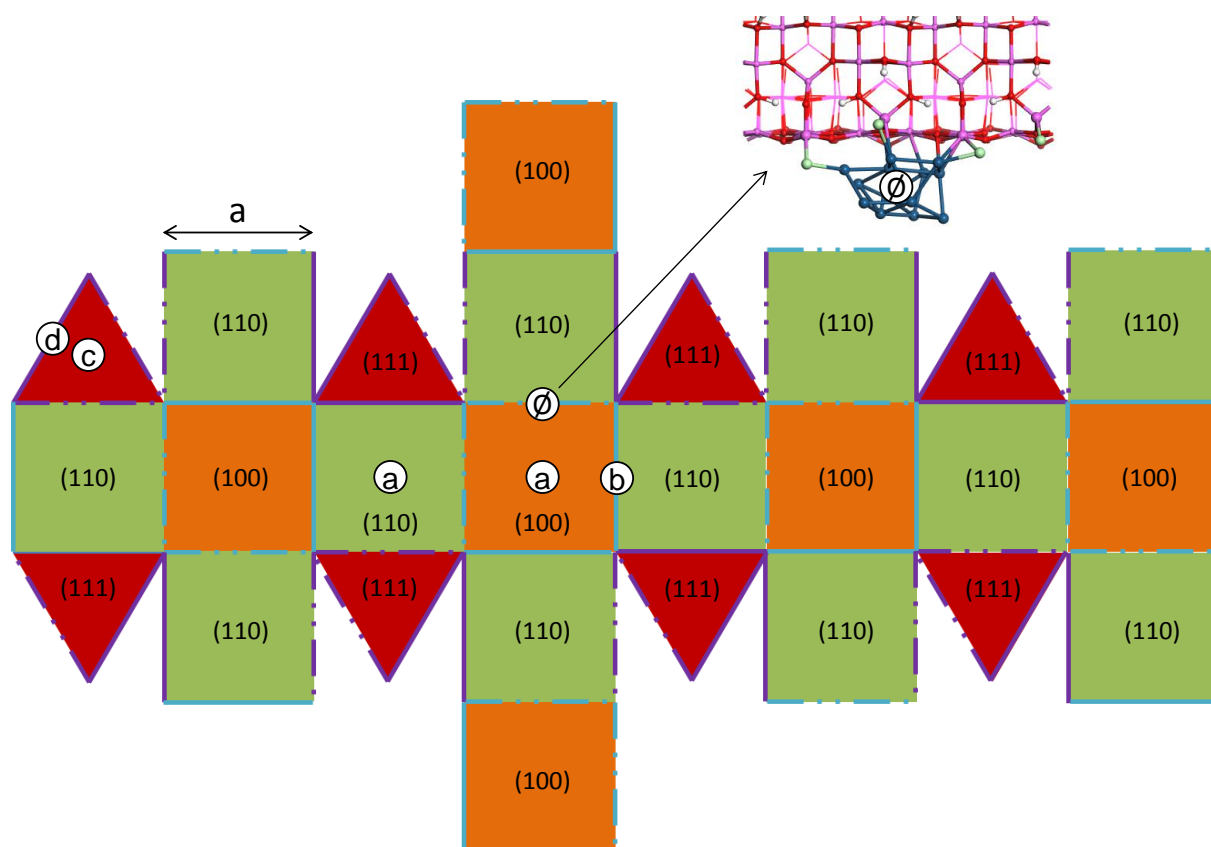


*Figure 5-8 – Polyhedral net of the rhombicuboctahedron platelet modelling PuralSB3 with NP positions considered for inter-site distance estimation a) to d). Colour coded as: green – (110); orange – (100); red – (111); full line blue edge – non-chlorinated (110)-(100) edge; broken line blue edge – chlorinated (110)-(100) edge; full line blue edge – non-chlorinated (110)-(111) edge; broken line blue edge – chlorinated (110)-(111) edge.*

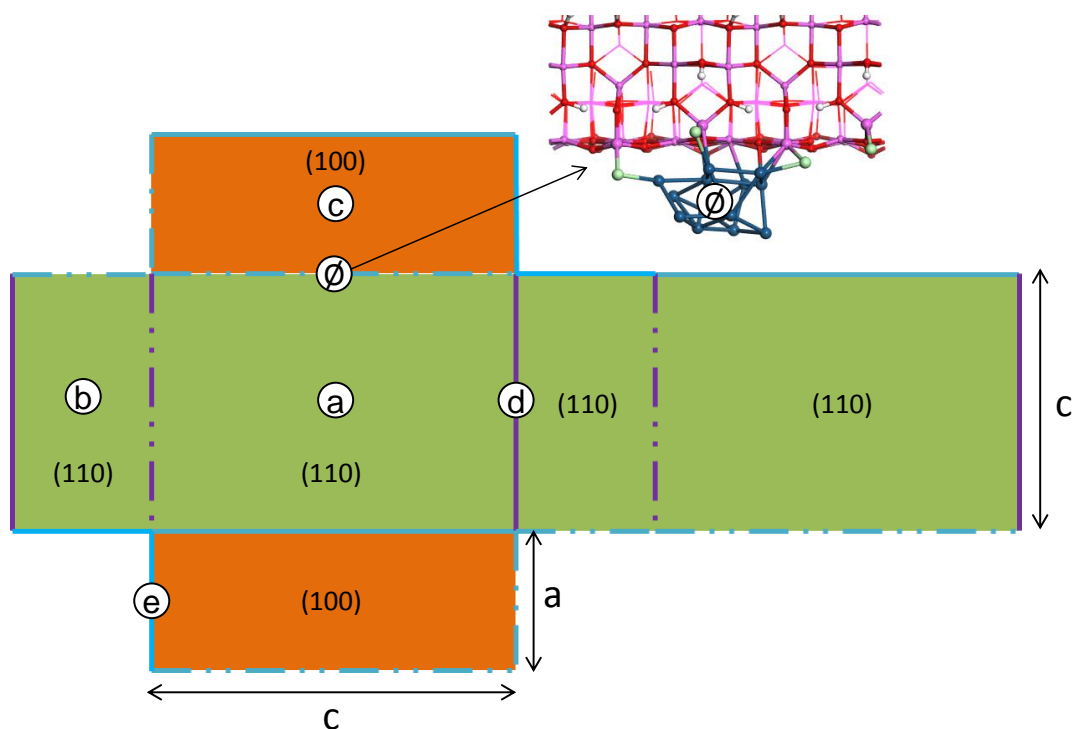
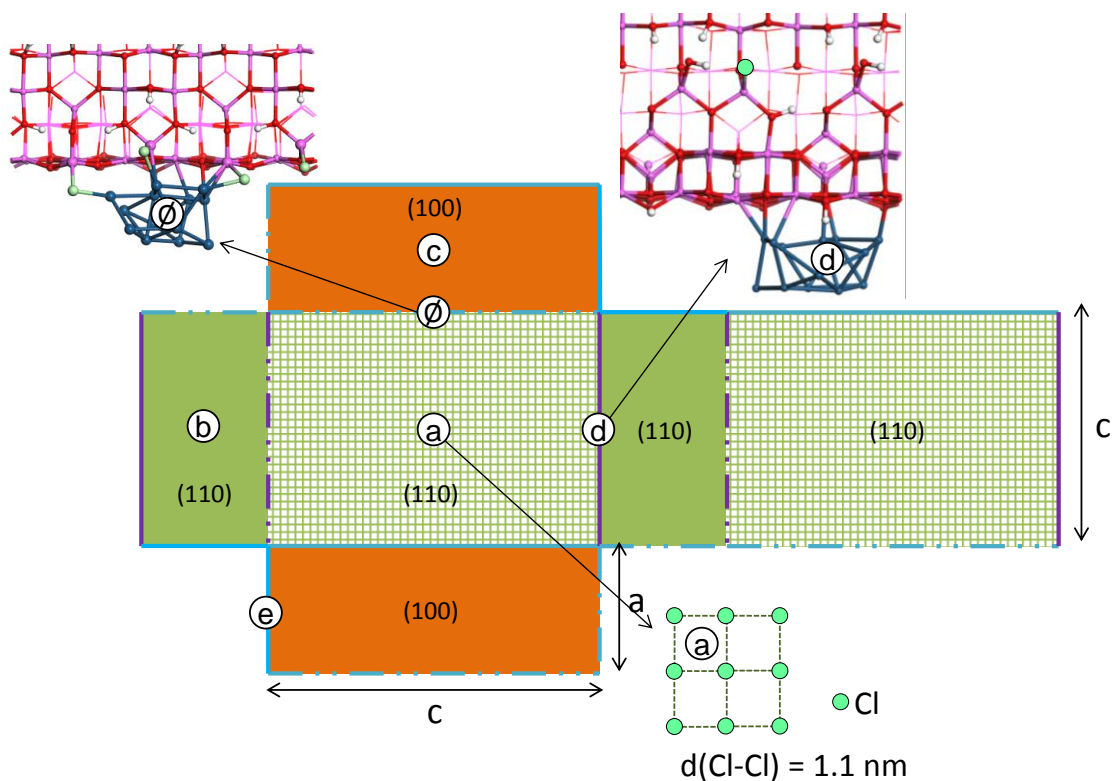


Figure 5-9 – Polyhedral net of the parallelepiped platelet modelling TH100 with NP positions considered for inter-site distance estimation a) to e) for case 1 (0.4%Cl). Colour coded as: green – (110); orange – (100); red – (111); full line blue edge – non-chlorinated (110)-(100) edge; broken line blue edge – chlorinated (110)-(100) edge; full line blue edge – non-chlorinated (110)-(110) edge; broken line blue edge – chlorinated (110)-(110) edge.





**Figure 5-10** – Polyhedral net of the parallelepiped platelet modelling TH100 with NP positions considered for inter-site distance estimation a) to e) for case 2 (1%Cl). Colour coded as: green – (110); orange – (100); red – (111); full line blue edge – non-chlorinated (110)-(100) edge; broken line blue edge – chlorinated (110)-(100) edge; full line blue edge – non-chlorinated (110)-(110) edge; broken line blue edge – chlorinated (110)-(110) edge.

**Table 5-8** – Estimation of  $\text{Pt}_{13}$ -Cl distances for cases of chlorine loading/location and several possible NP positions, excluding  $\text{Pt}_{13}$ /edge-Cl.

Case 1: Max. Cl loading on edge sites						Case 2: 1%Cl			
PuralSB3 model – 1.2%Cl				TH100 model – 0.4%Cl				TH100 model	
NP position		$d(\text{Pt}_{13}\text{-Cl})^*$	$d(\text{Pt}_{13}\text{-Cl})$ (nm)	NP position		$d(\text{Pt}_{13}\text{-Cl})^*$	$d(\text{Pt}_{13}\text{-Cl})$ (nm)	$d(\text{Pt}_{13}\text{-Cl})^*$	$d(\text{Pt}_{13}\text{-Cl})$ (nm)
∅	(110)-(100) edge - Cl	Pt-Cl bond	0.23	∅	(110)-(100) edge - Cl	Pt-Cl bond	0.23	Pt-Cl bond	0.23
a)	Centre of (110) or (100)	$\frac{a}{2}$	1.4	a)	Centre of basal (110)	$\frac{c}{2}$	4.5	-	0.7
b)	Middle of (110)-(100) edge	$\frac{a}{2}$	1.4	b)	Centre of lateral (110)	$\frac{a}{2}$	2	$\frac{a}{2}$	2
c)	Centre of (111)	$\frac{\sqrt{3/4a^2}}{2}$	1.2	c)	Centre of (100)	$\frac{a}{2}$	2	$\frac{a}{2}$	2
d)	Middle of (111)-(110) edge	$\frac{a}{2}$	1.4	d)	Middle of (110)-(110) edge	$\frac{c}{2}$	4.5	-	≈0.9
				e)	Middle of (110)-(100) edge	$\frac{a}{2}$	2	$\frac{a}{2}$	2

\*in function of the platelet dimensions, edge length  $a$  for PuralSB3's rhombicuboctahedron and  $a$ ,  $b$  and  $c$  for TH100's parallelepiped.

The first NP position,  $\emptyset$ , corresponds to the particular case of Pt/edge-Cl in which the shortest Pt-Cl distance corresponds to the Pt-Cl bond length. The remaining positions a) to e) represent specific possibilities for the other cases of NP on a facet or on a non-chlorinated edge.

In the case of PuralSB3's model, all but eight facets are squares, so the explored locations result mostly in a  $Pt_{13}$  to Cl distance of  $a/2$ . Since the PuralSB3 platelet is smaller than TH100's, this results in overall shorter distances.

For TH100 the two considered cases represent different chlorine loadings. In case 1, at 0.4%Cl, there are 125 Cl atoms on the TH100 crystallite. For case 2, in TH100's model, Cl atoms "overflow" to facet sites to reach a loading of 1%Cl, 238 more Cl atoms are needed. After the edge sites, now saturated, the most favourable anchoring site for Cl was a  $\mu_1$ -OH on the (110) facet when considering a 12.0 OH/nm<sup>2</sup> hydration. This  $\mu_1^{exch}$ -OH is present in the (110) facet with a density of 1.48  $\mu_1^{exch}$ -OH/nm<sup>2</sup>, which is enough to harbour all the "extra" 238 Cl atoms needed. It is then considered that those Cl atoms are located on the basal (110) planes, uniformly distributed in a square network resulting in a Cl-Cl distance on the facet of 1.1 nm.  $Pt_{13}$ -Cl distance for location a) was then calculated by positioning the NP in the centre of a Cl network square, as illustrated in Figure 5-10. For location d), while that edge is not chlorinated the adjacent surface now is. The  $Pt_{13}$ -Cl distance was then estimated by measuring the distance between a surface Cl atom and the closest Pt atom of the NP using the DFT  $Pt_{13}/O$  side-edge model (see Appendix H), as the O side edge is not chlorinated, as illustrated in Figure 5-10 showing the Cl atom in the position of the  $\mu_1^{exch}$ -OH.

Overall there are three major parameters impacting the  $Pt_{13}$ -Cl distance :

- 1) platinum NP location has the largest impact on the average NP-Cl distance. When NPs are located on the chlorinated edges that distance can even be that of a Pt-Cl bond. If on a facet without Cl, the situation that can lead to the longest NP-Cl distances, it's the NP position on that facet that will determine the NP-Cl distance.
- 2) alumina platelet morphology. As the individual facets are smaller for PuralSB3's model, the  $Pt_{13}$ -Cl distance ends up being shorter.
- 3) chlorine loading, here particularly in the case of TH100. For TH100, when the chlorine loading increases and Cl atoms "overflow" to the facets, sub-nanometric  $Pt_{13}$ -Cl distances become more frequent.

It is also possible to estimate an average NP-Cl distance for each alumina support. Facet locations are considered equiprobable amongst themselves and are weighted by the proportion of exposure of the respective surface type. Edge locations are also considered equiprobable amongst themselves. Edge and facet locations are then weighted by the proportion found by electron tomography, in which 78% of NPs were found on the edges. The results are summarized in Table 5-9. These average values reflect the trends identified from Table 5-8, NP-Cl distance is shorter for PuralSB3 than for TH100 and it becomes shorter with increased chlorine loading.

*Table 5-9 –Average NP-Cl distance calculated for each alumina model and each case.*

	PuralSB3	Case 1/2: 1%Cl		TH100	Case 1: 0.4%Cl		Case 2: 1%Cl	
	Facet Exposure (%)	Average facet NP-Cl distance (nm)	Average NP-Cl distance (nm)	Facet Exposure (%)	Average facet NP-Cl distance (nm)	Average NP-Cl distance (nm)	Average facet NP-Cl distance (nm)	Average NP-Cl distance (nm)
(110)	55.9	1.4	1.1	74	2.9	2.4	1.5	1.2
(100)	28	Average edge NP-Cl distance (nm)		26	Average edge NP-Cl distance (nm)		Average edge NP-Cl distance (nm)	
(111)	16.1	1.4		0	2.2		1.0	

One could then wonder, for the classical industrial 0.3%Pt and 1%Cl loadings, which type of alumina support would be the best for naphtha reforming. Let us consider that “the best” here means the most selective for  $>C_5$  hydrocarbons. Firstly, it is not known whether a shorter or longer distance between the two types of active sites is to be desired. Traditionally it was considered “the closer the better”, but recent works on other bifunctional catalyst systems suggest that is not the always case [3]. Secondly, since these distances seem to vary only by a couple of nm, it is unclear whether the catalyst performance is sensitive to such fine differences, particularly if they happen to already respect Weisz’s intimacy criterion [2]. To answer these questions, catalytic testing of the catalyst sets studied here is needed.

The discrete approach of fixing a number of NP positions used here to estimate the NP-Cl distance was considered representative enough to draw trends while also being relatively instinctive and of clear visual representation. Another method would be to tabulate all the NP-Cl distances for all possible NP positions over a given facet (considered equiprobable),

using a certain step, for all facets of the platelet and treating the edge positions as boundary conditions. This would result in an average value per facet which could then be weighted by its exposure on the platelet. Such an approach was considered too sensitive to small changes in the models' many assumptions.

### 5.3 Conclusion

Throughout this work it was possible to find the preferred location of Cl atoms and Pt NPs on high surface gamma-alumina crystallites. Two dimensional  $^1\text{H}$ - $^1\text{H}$  SQ-DQ BABA NMR experiments show that the introduction of 1%Pt disturbs some  $^1\text{H}$ - $^1\text{H}$  heteronuclear correlations, particularly for high Cl coverages, indicating Pt-Cl proximity. But the location of the perturbed hydroxyls cannot be determined without an even more detailed  $^1\text{H}$  NMR signal peak assignment, which is beyond the objectives of the present work.

A geometric catalyst model was developed to estimate the distance between metallic and acid sites, considering Cl atoms as a proxy for acid site location. Using the same parallelepipedic platelet morphology to model both types of alumina and setting  $\text{Pt}_{13}$  NPs and Cl atoms in square networks for  $\text{Pt}_{13}$ -Cl distance estimation proved to be over-simplistic. It is necessary to consider an adequate platelet morphology to model PuralSB3, here a rhombicuboctahedron, and to position Cl and  $\text{Pt}_{13}$  NPs in their most favourable positions, as found by the characterization study. For two well defined Cl loading cases and several possible  $\text{Pt}_{13}$  locations, it was found that the overall  $\text{Pt}_{13}$ -Cl distance depends mostly on:

- Location of Pt NPs (edge-Cl, edge or facet)
- Type of support (the NP-Cl distance being larger for TH100)
- Cl loading in the case of TH100 (the NP-Cl distance decreasing with increasing %Cl loading)

The average distance ranges from 1.1 nm for PuralSB3 (1%Cl) and up to 2.4 nm for TH100 (0.4%Cl). It was also found that inter-NP distance is either intra or inter-crystallite depending on metal loading.

# Conclusion

Catalytic naphtha reforming relies on a bifunctional catalyst to transform low-octane heavy naphtha into high-octane compounds for the production of gasoline. The proximity and relative location of the two types of active functions of the catalyst can impact its activity and selectivity. In this work the Pt/ $\gamma$ -Al<sub>2</sub>O<sub>3</sub>-Cl catalytic system was studied at the atomic scale with the aim of identifying the location of Pt and of Cl on the alumina support so as to quantify the distance between metallic and acid active sites in these materials.

Two series of catalysts with varying platinum and chlorine loadings were prepared using two  $\gamma$ -alumina samples obtained from two commercial boehmites (PuralSB3 and TH100) with different crystallite size and morphology. Changing Pt and Cl loadings, in a range comparable with industrial catalysts, was performed so as to vary the distance between active sites, to highlight the effect of chlorine on deposited platinum and on the support's surface and to study the impact of Pt loading on the supported metal phase. The two different supports were chosen to search for an impact of crystallite morphology that translates into variations in exposed facets and edges. Chlorinated aluminas (without Pt) were also synthesised to study chlorination in isolation.

In order to study the materials at an atomic level, four advanced techniques were used: HR-HAADF-STEM, HERFD-XANES and EXAFS, high field MAS NMR and DFT calculations. This multi technique approach resulted in a thorough characterization of the Pt/ $\gamma$ -Al<sub>2</sub>O<sub>3</sub>-Cl system.

First, the two distinct  $\gamma$ -alumina supports were studied. They present crystallites of distinct shape and size, with TH100 crystallites being larger and having a better defined and more parallelepipedic platelet-like morphology than PuralSB3 ones, which exhibit slightly smaller sizes and a round shape. This implies that PuralSB3 has a higher edge to surface ratio than TH100.

The <sup>1</sup>H NMR spectra of both non-chlorinated supports presented the main features expected of  $\gamma$ -alumina, but fine differences between them could not be interpreted through the classical peak attribution. Simulation of proton chemical shift by DFT showed that the hydroxyls present on all three alumina exposed surfaces at different hydration degrees could not fully explain the experimental spectra due to the predominant presence of hydrogen

bond networks between hydroxyls. The construction of the first DFT model of  $\gamma$ -Al<sub>2</sub>O<sub>3</sub> crystallite (110)-(100) edge allowed for this impasse to be broken and a refined <sup>1</sup>H NMR attribution to be suggested [4]. Calculated energies show this edge harbours the most stable  $\mu_1$ -OH groups that are isolated and free from H-bonds. It was found that the sharp peak at 0 ppm corresponds mostly to  $\mu_1$ -OH located on the edges of the crystallites. Challenging the simple empirical attribution, the 1-3 ppm region corresponds to signals from not only  $\mu_2$ -OH but also from  $\mu_1$ -OH located either on the surfaces or on the edge, and that are either H-bond acceptors or free hydroxyls. Hydroxyls that are hydrogen bond donors are abundant on the surfaces and contribute to the high chemical shift broad signals. With this signal attribution the experimental spectra could be rationalized in light of the alumina crystallite morphologies.

The impact of chlorination on the spectra of chlorinated supports was also successfully interpreted, showing that chlorine is located on the edges, as it preferentially exchanges with edge  $\mu_1$ -OH, where it finds its place up to 1.4%Cl for PuralSB3 but only up to 0.5%Cl for TH100, after which chlorine is exchanged with surface (most likely (110)) hydroxyls. Hence the potential role of edge sites in catalysis should be considered in future investigations. Following progressive chlorination by <sup>1</sup>H NMR could be used as method for edge to surface ratio quantification of alumina samples.

Second, the metallic phase supported on chlorinated alumina was characterized by STEM and XAS for samples with two extreme platinum and chlorine loadings of 0.3 and 1%<sub>w/w</sub> Pt and 0.1 and 1.4%<sub>w/w</sub> Cl. For catalysts in oxide state, platinum is highly dispersed as a monoatomic oxide complex of the type PtCl<sub>x</sub>O<sub>y</sub> with x/y ratio being dependent on chlorine loading. The XANES edge features of PuralSB3 are highly sensitive to oxide complex aggregation level depending on metal loading. After reduction, platinum nanoparticles are, regardless of %Pt and %Cl, of 0.9 nm in size (XANES spectral features are compatible with Pt<sub>13</sub> signatures of simulated spectra) and present a flat bi-planar morphology, being constituted of about 10 to 20 Pt atoms. Single atoms (SA) of platinum are also visible in STEM images of the reduced samples and overall their population corresponds to 20% of all deposited platinum atoms. This SA population is positively impacted by increasing chlorine loading independently of metal loading showing the stabilization of the smallest Pt species by Cl. STEM observations of a used catalyst after catalytic testing also showed the presence

of both 0.9 nm Pt NPs and single atoms, attesting to the stability of the metallic phase (as verified in the in situ STEM experiment) and thus validating the characterization performed on fresh catalysts.

The electron tomography study found that around 80% of the platinum nanoparticles are located on crystallite edges or other defects (steps or kinks). Such location was found to be thermodynamically competitive with that on the extended surfaces by a preliminary DFT investigation. Kinetic or geometric constraints during reduction may favour the edge location. A geometrical analysis of the segmented volumes reveals that the average shortest inter-nanoparticle distances correspond to a statistic distribution, indication that anchoring sites are abundant in these circumstances. Such distance is controlled by platinum loading through the absolute quantity of nanoparticles and it can be either inter- or intra nanoparticle also depending on platinum loading.

Finally, a geometric model of Pt/ $\gamma$ -Al<sub>2</sub>O<sub>3</sub>-Cl catalysts was built. In order to accurately represent the studied materials, it is mandatory to explicitly consider not only the size of the alumina platelets but also their morphology. In particular, a large edge to surface ratio must be respected in a PuralSB3 model. In this way, the models accurately predict the chlorine loading at which the edge anchoring sites are saturated, as evidenced by the NMR experiments, and the intra or inter crystallite nature of the distance between NPs highlighted by in the tomography results. The distance between active sites defined as the distance between Pt NPs and Cl atoms was estimated for specific scenarios. The average inter-site distance ranges from 1.1 nm for PuralSB3 (1%Cl) and up to 2.4 nm for TH100 (0.4%Cl). Since these are mean, the existence of a direct chemical bond between Cl atoms and Pt NPs cannot be excluded considering some extreme but energetically possible configurations, when both Cl atoms and Pt NPs are located on the same edge. Overall it was found to depend mostly on: location of Pt NPs (chlorinated edge, edge or facet), type of support (the NP-Cl distance is larger for TH100) and Cl loading (the NP-Cl distance decreases with increasing %Cl loading).

To conclude, Pt/ $\gamma$ -Al<sub>2</sub>O<sub>3</sub>-Cl type catalysts were studied at the atomic scale by HR-STEM, MAS NMR, XAS and DFT calculations in order to precisely locate Pt and Cl on the support and to estimate the distance between them. It was found that the edges of alumina crystallites play a major role in Cl and Pt anchoring and should not be ignored from consideration when



studying alumina supported catalysts. The novel DFT edge model developed is thus essential for a better understanding of  $\gamma$ -alumina surface chemistry. Indeed, both Cl atoms and Pt NPs are preferably located on the edges of crystallites. Platinum nanoparticles are incredibly homogeneous in size, shape and electronic structure and environment, regardless of platinum and chlorine loading. An important single atom population is also present, which is stabilized by the presence of chlorine. The same NP and SA were observed for a used catalyst, validating the STEM study performed on fresh catalysts. A geometric model of Pt/ $\gamma$ -Al<sub>2</sub>O<sub>3</sub>-Cl catalysts estimates average Pt NP – Cl distances of about 1.1 nm for both supports in the case of the industrially relevant 1%Cl loading.

The improved understanding of the location of active sites and their proximity in catalytic naphtha reforming catalysts gained through this work paves the way to catalyst improvement based on tuning of active site location.

# Perspectives

The overall understanding of the Pt/ $\gamma$ -Al<sub>2</sub>O<sub>3</sub>-Cl system and of  $\gamma$ -Al<sub>2</sub>O<sub>3</sub> supported catalysts in general can still be improved.

It will be essential to search for an impact of the active site relative location and proximity found in this work on the selectivity of the prepared catalysts in reforming, for instance. This is currently being investigated in the PhD work of O. Said-Aizpuru (IFPEN, IRCELYON). His work aims at characterizing the activity of the catalysts prepared for the present work and their bimetallic counterparts in model catalytic tests such as n-heptane reforming. The final goal is to study the effect of catalyst formulation on kinetic constants obtained through a n-heptane reforming model that is to be constructed and to find if a structure-selectivity relationship can be found. It will also be of interest to verify if the metallic site location found for monometallic catalysts is still valid for multimetallic catalysts.

Concerning the alumina support, it will be of great interest to keep working towards a more detailed <sup>1</sup>H NMR assignment. While the assignment proposed here represents a clear improvement, it could be refined for some regions of overlapping signals such as the 1-3 ppm part of the spectrum. The NMR assignment could be validated more extensively by using other alumina samples with yet distinct crystallite size and shape (nano-rods, for example), as well as varying the pre-treatment temperature of the samples to explore different hydration degrees.

This should be accompanied by the development of complementary DFT models, for other edges and stepped surfaces which are observed in TEM for alumina. Some ongoing DFT works investigate for instance the case of the (110)-(110) edge which may be present on the alumina platelet. The novel DFT edge model constructed here can also be used to complement the IR OH region spectrum assignment through vibrational calculations of OH bond stretching.

Another underlying aspect within the context of this work that was not explicitly investigated is the determination of which alumina hydroxyl groups are Brønsted acid active sites. The existing surface and edge DFT models, chlorinated or not, could be used in a

systematic approach of simulating probe molecules (such as CO or pyridine) adsorption and their vibrational vibration frequency for each OH in order to identify the most acidic.

It has been shown that Cl has an impact on platinum on all stages of the catalyst preparation and lifecycle. It will be thus essential to construct DFT models of supported chlorinated platinum oxide complexes in order to enlighten the reduction mechanism. Likewise, a more complete study should be performed on single atoms and nanoparticles supported on the edge structures. These advances could also allow for a better interpretation of XAS characterization results.

Concerning characterization techniques, some technical and methodological improvements would be welcome. Indeed, for XAS experiments, identifying an impact of Cl on the electronic structure of Pt by XANES was hampered by hydrogen adsorption/desorption effects inherent to the set up. Another protocol could be tested in which the sample is put under vacuum for acquisition after the re-reduction. Another example is the in situ reduction experiment followed by STEM, for which better resolution could allow the single atoms species to be observed.

# References

- [1] G. Ertl, H. Knözinger, F. Schüth, Weitkamp J., Handbook of heterogeneous catalysis, 2nd ed., Wiley-VCH, Weinhei, 2008.
- [2] P. B. Weisz, *Adv. Catal.* 13 (1962) 137–190.
- [3] J. Zečević, G. Vanbutsele, K.P. de Jong, J.A. Martens, *Nature* 528 (2015) 245–248.
- [4] A.T.F. Batista, D. Wisser, T. Pigeon, D. Gajan, F. Diehl, M. Rivallan, L. Catita, A.-S. Gay, A. Lesage, C. Chizallet, P. Raybaud, *J. Catal.* 378 (2019) 140–143.
- [5] C. Fehér, E. Kriván, Z. Eller, J. Hancsók, R. Skoda Földes, in: C. Lesieur (Ed.), Oligomerization of Chemical and Biological Compounds, InTech, 2014.
- [6] J.F. Le Page, Applied heterogeneous catalysis: Design, manufacture, use of solid catalysts, Éditions Technip, Paris, 1987.
- [7] G. J. Antos, A. M. Aitani, Catalytic Naphtha Reforming, 2nd Ed., Marcel Dekker, New York, 2004.
- [8] G. J. Antos, A. M. Aitani, J. M. Parera, Catalytic Naphtha Reforming, 1st ed., Marcel Dekker, New York, 1995.
- [9] Michell Instruments, Fixed-bed Semi-regenerative Platforming process: Critical moisture measurement in hydrogen rich re-cycle gas, 2015. Available from: [http://www.michell.com/downloads/appnotes/Fixed-bed\\_Semi-regenerative\\_Platforming\\_process.pdf](http://www.michell.com/downloads/appnotes/Fixed-bed_Semi-regenerative_Platforming_process.pdf).
- [10] Honeywell UOP, UOP CCR Platforming™ Process. Available from: <https://www.uop.com/reforming-ccr-platforming/>.
- [11] B. Domergue, P-Y. le Goff, J. Ross, Octanizing reformer options, 2006. Available from: <https://www.axens.net/document/703/octanizing-reformer-options/english.html>.
- [12] J. Zhang, Y.-T. Tsai, K. L. Sangkaewwattana, J. Goodwin, *J. Catal.* 280 (2011) 89–95.
- [13] B. H. Davis, *Catal. Today* 53 (1999) 443–516.
- [14] J.H. Sinfelt, *Adv. Chem. Eng.* 5 (1964) 37–74.
- [15] G. Busca, *Catal. Today* 41 (1998) 191–206.

- [16] G.A. Mills, H. Heinemann, T.H. Milliken, A.G. Oblad, *Ind. Eng. Chem.* 45 (1953) 134–137.
- [17] P. Mendes, A. Gregório, A. Daudin, C. Bouchy, J. Silva, M. Ribeiro, *Catal. Commun.* 89 (2017) 152–155.
- [18] E. Gutierrez-Acebo, C. Leroux, C. Chizallet, Y. Schuurman, C. Bouchy, *ACS Catal.* 8 (2018) 6035–6046.
- [19] C. Marcilly (Ed.), *Acido-basic catalysis: Application to refining and petrochemistry*, Editions Technip, Paris, 2006.
- [20] S. M. Augustine, G. N. Alemeddin, W. M. H. Schatler, *J. Catal.* 115 (1989) 217–232.
- [21] J. M. Grau, J. M. Parera, *Ind. Eng. Chem. Res.* 28 (1989) 1596–1600.
- [22] A. V. Mazzieri, J. M. Grau, C. R. Vera, J. C. Yori, J. M. Parera, C. L. Pieck, *Catal. Today* 107-108 (2005) 643–650.
- [23] F. Passos, M. Schmal, M. Vannice, *J. Catal.* 160 (1996) 106–117.
- [24] L. Carvalho, C. Pieck, M. Rangel, N. Fígoli, J. Grau, P. Reyes, J. Parera, *Appl. Catal., A* 269 (2004) 91–103.
- [25] A. Gorczyca, P. Raybaud, V. Moizan, Y. Joly, C. Chizallet, *ChemCatChem* 500 (2019) 271.
- [26] A. Jahel, Etude de l'ajout d'indium au système Pt-Sn/Al<sub>2</sub>O<sub>3</sub>-Cl utilisé en reformage catalytique: Doctoral dissertation, IFPEN, Université Montpellier II, 2010.
- [27] A. Jahel, V. Moizan-Baslé, C. Chizallet, P. Raybaud, J. Olivier-Fourcade, J.-C. Jumas, P. Avenier, S. Lacombe, *J. Phys. Chem. C* 116 (2012) 10073–10083.
- [28] J.-C. Jumas, M.T. Sougrati, J. Olivier-Fourcade, A. Jahel, P. Avenier, S. Lacombe, *Hyperfine Interact.* 217 (2013) 137–144.
- [29] P. Bogdan (2000) US6013173A.
- [30] B. Shelimov, J.-F. Lambert, M. Che, B. Didillon, *J. Catal.* 185 (1999) 462–478.
- [31] A. Castro, O. Scelza, E. Benvenuto, G. Baronetti, S. De Miguel, J.M. Parera, *Stud. Surf. Sci. Catal.* 16 (1983) 47–56.

- [32] R. Maatman, *Ind. Eng. Chem.* 51 (1959) 913–914.
- [33] W.A. Spieker, J.R. Regalbuto, *Chem. Eng. Sci.* 56 (2001) 3491–3504.
- [34] G. Baronetti, S. de Miguel, O. Scelza, M. Fritzler, A. Castro, *Appl. Catal.* 19 (1985) 77–85.
- [35] S.R.D. Miguel, G.T. Baronetti, A.A. Castro, O.A. Scelza, *Appl. Catal.* 45 (1988) 61–69.
- [36] R. Burch, *J. Catal.* 71 (1981) 348–359.
- [37] F.M. Dautzenberg, J.N. Helle, P. Biloen, W.M.H. Sachtler, *J. Catal.* 63 (1980) 119–128.
- [38] T.-H. Chao, W. Targos, M. Moser (1990) US4964975A.
- [39] S.I. Sanchez, M.D. Moser, S.A. Bradley, *ACS Catal.* 4 (2014) 220–228.
- [40] J. Barbier, G. Gorro, Y. Zhang, *Appl. Catal.* 13 (1985) 245–255.
- [41] T. Cholley, Etude de la redispersion de phases bimétalliques à base de platine supportées sur alumine chlorée ou neutralisée: Doctoral Dissertation, IFPEN, Université Paris 6, 1997.
- [42] G. Busca, *Catal. Today* 226 (2014) 2–13.
- [43] P. Euzen, P. Raybaud, X. Krokidis, H. Toulhoat, J.-L. Le Loarer, J.-P. Jolivet, C. Froidefond, in: F. Schuth, K.S.W. Sing, J. Weitkamp (Eds.), *Handbook of Porous Solids*, Wiley-VCH Verlag GmbH, Weinheim, Germany, 2002, pp. 1591–1677.
- [44] Allied Market Research, High Purity Alumina Market: Global Opportunity Analysis and Industry Forecast, 2018 - 2025. Available from: <https://www.alliedmarketresearch.com/high-purity-alumina-market>.
- [45] B. C. Lippens, Structure and Texture of Aluminas: Doctoral dissertation, Delft University, 1961.
- [46] K. Sohlberg, S.J. Pennycook, S.T. Pantelides, *Chem. Eng. Commun.* 181 (2000) 107–135.
- [47] J.H. Kwak, J. Hu, A. Lukaski, D.H. Kim, J. Szanyi, C.H.F. Peden, *J. Phys. Chem. C* 112 (2008) 9486–9492.

- [48] X. Krokidis, P. Raybaud, A.-E. Gobichon, B. Rebours, P. Euzen, H. Toulhoat, *J. Phys. Chem. B* 105 (2001) 5121–5130.
- [49] M. Digne, P. Sautet, P. Raybaud, H. Toulhoat, E. Artacho, *J. Phys. Chem. B* 106 (2002) 5155–5162.
- [50] M. Digne, P. Sautet, P. Raybaud, P. Euzen, H. Toulhoat, *J. Catal.* 211 (2002) 1–5.
- [51] M. Digne, P. Sautet, P. Raybaud, P. Euzen, H. Toulhoat, *J. Catal.* 226 (2004) 54–68.
- [52] G. Paglia, A.L. Rohl, C.E. Buckley, J.D. Gale, *Phys. Rev. B* 71 (2005) 30.
- [53] C. Wolverton, K.C. Hass, *Phys. Rev. B* 63 (2000) 1995.
- [54] J. Dong, J. Wang, L. Shi, J. Yang, J. Wang, B. Shan, M. Shen, *Phys. Chem. Chem. Phys.* 19 (2017) 27389–27396.
- [55] P. Nortier, P. Fourre, A.M. Saad, O. Saur, J.C. Lavalley, *Appl. Catal.* 61 (1990) 141–160.
- [56] L. Kovarik, A. Genc, C. Wang, A. Qiu, C.H.F. Peden, J. Szanyi, J.H. Kwak, *J. Phys. Chem. C* 117 (2013) 179–186.
- [57] J.-P. Beaufils, Y. Barbaux, *J. Chim. Phys.* 78 (1981) 347–352.
- [58] H.P. Pinto, R.M. Nieminen, S.D. Elliott, *Phys. Rev. B* 70 (2004) 1995.
- [59] G. Busca, *Prog. Mater. Sci.* 104 (2019) 215–249.
- [60] J.H. Kwak, D. Mei, C.H.F. Peden, R. Rousseau, J. Szanyi, *Catal. Lett.* 141 (2011) 649–655.
- [61] J. Szanyi, J.H. Kwak, *Phys. Chem. Chem. Phys.* 16 (2014) 15117–15125.
- [62] G. Ramis, G. Busca, *J. Mol. Struct.* 193 (1989) 93–100.
- [63] G. Busca, V. Lorenzelli, G. Ramis, R.J. Willey, *Langmuir* 9 (1993) 1492–1499.
- [64] C. Morterra, G. Magnacca, *Catal. Today* 27 (1996) 497–532.
- [65] J. B. Peri, *J. Phys. Chem.* 69 (1965) 220–230.
- [66] A.A. Tsyganenko, V.N. Filimonov, *J. Mol. Struct.* 19 (1973) 579–589.
- [67] H. Knözinger, P. Ratnasamy, *Catal. Rev.: Sci. Eng.* 17 (1978) 31–70.
- [68] G. Busca, *J. Catal.* 131 (1991) 167–177.

- [69] M. Lagauche, K. Larmier, E. Jolimaitre, K. Barthelet, C. Chizallet, L. Favergeon, M. Pijolat, *J. Phys. Chem. C* 121 (2017) 16770–16782.
- [70] R. Koerin, Influence du mode de synthèse de la boehmite sur l'état de surface de l'alumine-gamma mise en forme: application au reformage catalytique: Doctoral dissertation, IFPEN, Université de Caen Basse-Normandie, 2015.
- [71] P. Scherrer, *Nachr. Ges. Wiss. Goettingen, Math.-Phys. K2.* 2 (1918) 98–100.
- [72] E. C. DeCanio, J. C. Edwards, J. W. Bruno, *J. Catal.* 148 (1994) 76–83.
- [73] J. Hietala, A. Root, P. Knuuttila, *J. Catal.* 150 (1994) 46–55.
- [74] M. Delgado, F. Delbecq, C.C. Santini, F. Lefebvre, S. Norsic, P. Putaj, P. Sautet, J.-M. Basset, *J. Phys. Chem. C* 116 (2012) 834–843.
- [75] M. Taoufik, K.C. Szeto, N. Merle, I. Del Rosal, L. Maron, J. Trebosc, G. Tricot, R.M. Gauvin, L. Delevoye, *Chem. Eur. J.* 20 (2014) 4038–4046.
- [76] R. Wischert, P. Florian, C. Copéret, D. Massiot, P. Sautet, *J. Phys. Chem. C* 118 (2014) 15292–15299.
- [77] F.A. Perras, Z. Wang, P. Naik, I.I. Slowing, M. Pruski, *Angew. Chem. Int. Ed.* 56 (2017) 9165–9169.
- [78] J.B. Peri, *J. Phys. Chem.* 70 (1966) 1482–1491.
- [79] M. Tanaka, S. Ogasawara, *J. Catal.* 16 (1970) 157–163.
- [80] M. Marczewski, M. Derewinski, S. Malinowski, *Can. J. Chem. Eng.* 61 (1983) 93–97.
- [81] A. Kytokivi, M. Lindblad, *J. Chem. Soc. Faraday Trans.* 91 (1995) 941–948.
- [82] M. Digne, P. Raybaud, P. Sautet, D. Guillaume, H. Toulhoat, *J. Am. Chem. Soc.* 130 (2008) 11030–11039.
- [83] A. Ayame, K. Ohta, A. Kato, K. Honda, *Nippon Kagaku Kaishi* (1998) 388–389.
- [84] P. Sarrazin, S. Kasztelan, N. Zanier-Szydłowski, J.P. Bonnelle, J. Grimblot, *J. Phys. Chem.* 97 (1993) 5947–5953.
- [85] P. Berteau, M.-A. Kellens, B. Delmon, *J. Chem. Soc. Faraday Trans.* 87 (1991) 1425–1431.



- [86] D. Guillaume, S. Gautier, F. Alario, J. M. Deves, *Oil Gas Sci. Technol.* 54 (1999) 537–545.
- [87] P. Samoila, F. Epron, P. Marécot, C. Especel, *Appl. Catal., A* 462–463 (2013) 207–219.
- [88] C. Morterra, G. Cerrato, G. Meligrana, *Langmuir* 17 (2001) 7053–7060.
- [89] S.A. Bradley, W. Sinkler, D.A. Blom, W. Bigelow, P.M. Voyles, L.F. Allard, *Catal. Lett.* 142 (2012) 176–182.
- [90] C. Dessal, A. Sangnier, C. Chizallet, C. Dujardin, F. Morfin, J.-L. Rousset, M. Aouine, M. Bugnet, P. Afanasiev, L. Piccolo, *Nanoscale* 11 (2019) 6897–6904.
- [91] H. Yao, M. Sieg, H. Plummer, *J. Catal.* 59 (1979) 365–374.
- [92] J.H. Kwak, J. Hu, D. Mei, C.-W. Yi, D.H. Kim, C.H.F. Peden, L.F. Allard, J. Szanyi, *Science* 325 (2009) 1670–1673.
- [93] P.D. Nellist, S.J. Pennycook, *Science* 274 (1996) 413–415.
- [94] C. Dessal, T. Len, F. Morfin, J.-L. Rousset, M. Aouine, P. Afanasiev, L. Piccolo, *ACS Catal* 9 (2019) 5752–5759.
- [95] J. Berdala, E. Freund, J.P. Lynch, *J. Phys.* 47 (1986).
- [96] F.J. Gracia, J.T. Miller, A.J. Kropf, E.E. Wolf, *J. Catal.* 209 (2002) 341–354.
- [97] J. Lynch, *Oil Gas Sci. Technol.* 57 (2002) 281–305.
- [98] G. Lietz, H. Lieske, H. Spindler, W. Hanke, J. Völter, *J. Catal.* 81 (1983) 17–25.
- [99] J. Liu, *ACS Catal.* 7 (2017) 34–59.
- [100] X. Cui, K. Junge, X. Dai, C. Kreyenschulte, M.-M. Pohl, S. Wohlrab, F. Shi, A. Brückner, M. Beller, *ACS Cent. Sci.* 3 (2017) 580–585.
- [101] E. Yang, E.J. Jang, J.G. Lee, S. Yoon, J. Lee, N. Musselwhite, G.A. Somorjai, J.H. Kwak, K. An, *Catal. Sci. Technol.* 8 (2018) 3295–3303.
- [102] D. Mei, J.H. Kwak, J. Hu, S.J. Cho, J. Szanyi, L.F. Allard, C.H.F. Peden, *J. Phys. Chem. Lett.* 1 (2010) 2688–2691.
- [103] Z. Zhang, Y. Chen, L. Zhou, C. Chen, Z. Han, B. Zhang, Q. Wu, L. Yang, L. Du, Y. Bu, P. Wang, X. Wang, H. Yang, Z. Hu, *Nat. Commun.* 10 1657.

- [104] A. Bruix, Y. Lykhach, I. Matolínová, A. Neitzel, T. Skála, N. Tsud, M. Vorokhta, V. Stetsovych, K. Ševčíková, J. Mysliveček, R. Fiala, M. Václavů, K.C. Prince, S. Bruyère, V. Potin, F. Illas, V. Matolín, J. Libuda, K.M. Neyman, *Angew. Chem. Int. Ed.* 53 (2014) 10525–10530.
- [105] J. Jones, H. Xiong, A.T. DeLaRiva, E.J. Peterson, H. Pham, S.R. Challa, G. Qi, S. Oh, M.H. Wiebenga, X.I.P. Hernández, Y. Wang, A.K. Datye, *Science* 353 (2016) 150–154.
- [106] D. Kunwar, S. Zhou, A. DeLaRiva, E.J. Peterson, H. Xiong, X.I. Pereira-Hernández, S.C. Purdy, R. ter Veen, H.H. Brongersma, J.T. Miller, H. Hashiguchi, L. Kovarik, S. Lin, H. Guo, Y. Wang, A.K. Datye, *ACS Catal* 9 (2019) 3978–3990.
- [107] X.I. Pereira-Hernández, A. DeLaRiva, V. Muravev, D. Kunwar, H. Xiong, B. Sudduth, M. Engelhard, L. Kovarik, E.J.M. Hensen, Y. Wang, A.K. Datye, *Nat. Commun.* 10 (2019) 1358.
- [108] W. Sinkler, S.I. Sanchez, S.A. Bradley, J. Wen, B. Mishra, S.D. Kelly, S.R. Bare, *ChemCatChem* 7 (2015) 3779–3787.
- [109] A. M. Gänzler, M. Casapu, A. Boubnov, O. Müller, S. Conrad, H. Lichtenberg, R. Frahm, J.-D. Grunwaldt, *J. Catal.* 328 (2015) 216–224.
- [110] Y. Zhu, Z. An, J. He, *J. Catal.* 341 (2016) 44–54.
- [111] E. Bus, J.A. van Bokhoven, *Phys. Chem. Chem. Phys.* 9 (2007) 2894–2902.
- [112] J.M. Ramallo-López, F.G. Requejo, A.F. Craievich, J. Wei, M. Avalos-Borja, E. Iglesia, *J. Mol. Catal. A: Chem.* 228 (2005) 299–307.
- [113] Y. Li, D. Zakharov, S. Zhao, R. Tapper, U. Jung, A. Elsen, P. Baumann, R.G. Nuzzo, E.A. Stach, A.I. Frenkel, *Nat. Commun.* 6 (2015) 7583–7589.
- [114] Z. El Assal, S. Ojala, S. Pitkääho, L. Pirault-Roy, B. Darif, J.-D. Comparot, M. Bensitel, R.L. Keiski, R. Brahmi, *Chem. Eng. J.* 313 (2017) 1010–1022.
- [115] A. Gorczyca, V. Moizan, C. Chizallet, O. Proux, W. Del Net, E. Lahera, J.-L. Hazemann, P. Raybaud, Y. Joly, *Angew. Chem. Int. Ed.* 53 (2014) 12426–12429.
- [116] M.W. Small, S.I. Sanchez, L.D. Menard, J.H. Kang, A.I. Frenkel, R.G. Nuzzo, *J. Amer. Chem. Soc.* 133 (2011) 3582–3591.

- [117] S. Lee, S. Lee, M.D. Kumbhalkar, K.M. Wiaderek, J. Dumesic, R.E. Winans, *ChemCatChem* 9 (2017) 99–102.
- [118] A.I. Frenkel, M.W. Small, J.G. Smith, R.G. Nuzzo, K.O. Kvashnina, M. Tromp, *J. Phys. Chem. C* 117 (2013) 23286–23294.
- [119] A. Caballero, H. Dexpert, B. Didillon, F. LePeltier, O. Clause, J. Lynch, *J. Phys. Chem.* 97 (1993) 11283–11285.
- [120] J.-R. Chang, S.-L. Chang, T.B. Lin, *J. Catal.* 169 (1997) 338–346.
- [121] M.K. Oudenhuijzen, J.H. Bitter, D.C. Koningsberger, *J. Phys. Chem. B* 105 (2001) 4616–4622.
- [122] M. Vaarkamp, J.T. Miller, F.S. Modica, D.C. Koningsberger, *J. Catal.* 163 (1996) 294–305.
- [123] A.Y. Stakheev, Y. Zhang, A.V. Ivanov, G.N. Baeva, D.E. Ramaker, D.C. Koningsberger, *J. Phys. Chem. C* 111 (2007) 3938–3948.
- [124] C.H. Hu, C. Chizallet, C. Mager-Maury, M. Corral-Valero, P. Sautet, H. Toulhoat, P. Raybaud, *J. Catal.* 274 (2010) 99–110.
- [125] Y. Dai, T.J. Gorey, S.L. Anderson, S. Lee, S. Lee, S. Seifert, R.E. Winans, *J. Phys. Chem. C* 121 (2017) 361–374.
- [126] F. Behafarid, L.K. Ono, S. Mostafa, J.R. Croy, G. Shafai, S. Hong, T.S. Rahman, S.R. Bare, B.R. Cuenya, *Phys. Chem. Chem. Phys.* 14 (2012) 11766–11779.
- [127] S. N. Reifsnyder, M. M. Otten, D. E. Sayers, H. H. Lamb, *J. Phys. Chem. B* 101 (1997) 4972–4977.
- [128] S.I. Sanchez, L.D. Menard, A. Bram, J.H. Kang, M.W. Small, R.G. Nuzzo, A.I. Frenkel, *J. Amer. Chem. Soc.* 131 (2009) 7040–7054.
- [129] J. Singh, R.C. Nelson, B.C. Vicente, S.L. Scott, J.A. van Bokhoven, *Phys. Chem. Chem. Phys.* 12 (2010) 5668–5677.
- [130] C. Mager-Maury, G. Bonnard, C. Chizallet, P. Sautet, P. Raybaud, *ChemCatChem* 3 (2011) 200–207.

- [131] P. Raybaud, C. Chizallet, C. Mager-Maury, M. Digne, H. Toulhoat, P. Sautet, *J. Catal.* 308 (2013) 328–340.
- [132] C. Mager-Maury, C. Chizallet, P. Sautet, P. Raybaud, *ACS Catal.* 2 (2012) 1346–1357.
- [133] D. Mei, J.H. Kwak, J. Hu, S.J. Cho, J. Szanyi, L.F. Allard, C.H.F. Peden, *J. Phys. Chem. Lett.* 1 (2010) 2688–2691.
- [134] J. Lee, E.J. Jang, J.H. Kwak, *J. Catal.* 345 (2017) 135–148.
- [135] J.Z. Hu, S. Xu, J.H. Kwak, M.Y. Hu, C. Wan, Z. Zhao, J. Szanyi, X. Bao, X. Han, Y. Wang, C.H. Peden, *J. Catal.* 336 (2016) 85–93.
- [136] J. Lee, E.J. Jang, J.H. Kwak, *Appl. Catal., A* 569 (2019) 8–19.
- [137] F. Schuth, K. S. W. Sing, J. Weitkamp (Eds.), *Handbook of Porous Solids*, Wiley-VCH Verlag GmbH, Weinheim, Germany, 2002.
- [138] D. Fauchadour, F. Kolenda, L. Rouleau, L. Barré, L. Normand, in: E. Gaigneaux, D.E. De Vos, P. Grange, P.A. Jacobs, J.A. Martens, P. Ruiz, G. Poncelet (Eds.), *Scientific Bases for the Preparation of Heterogeneous Catalysts*, Elsevier, 2000, pp. 453–461.
- [139] D. Trimm, A. Stanislaus, *Appl. Catal.* 21 (1986) 215–238.
- [140] J. Lynch, *Physico-chemical Analysis of Industrial Catalysts: A practical guide to characterisation*, Editions Technip, 2003.
- [141] S. Brunauer, P.H. Emmett, E. Teller, *J. Amer. Chem. Soc.* 60 (1938) 309–319.
- [142] W.H. Bragg, W.L. Bragg, *Proc. R. Soc. A* 88 (1913) 428–438.
- [143] J. P. Eberhart, *Structural and chemical analysis of materials*, John Wiley & Sons, Ltd, 1995.
- [144] B.I. Lundqvist, in: R. Caudano, J.-M. Gilles, A.A. Lucas (Eds.), *Vibrations at Surfaces*, Springer US, Boston, 1982, pp. 541–572.
- [145] J. Benson, M. Boudart, *J. Catal.* 4 (1965) 704–710.
- [146] D.J. O’Rear, D.G. Löffler, M. Boudart, *J. Catal.* 121 (1990) 131–140.
- [147] A. Sangnier, M. Matrat, A. Nicolle, C. Dujardin, C. Chizallet, *J. Phys. Chem. C* 122 (2018) 26974–26986.

- [148] D.B. Williams, C.B. Carter, *Transmission Electron Microscopy*, Springer US, Boston, 2009.
- [149] L. De Broglie, *Recherches sur la théorie des Quanta*: Doctoral dissertation, Faculté des Sciences de Paris, 1924.
- [150] E. Ruska, *Kolloid-Z.* 100 (1942) 212–219.
- [151] H. Friedrich, P.E. de Jongh, A.J. Verkleij, K.P. de Jong, *Chem. Rev.* 109 (2009) 1613–1629.
- [152] P. Ercius, O. Alaidi, M.J. Rames, G. Ren, *Adv. Mater.* 27 (2015) 5638–5663.
- [153] J. Liu, *J. Electron Microsc.* 54 (2005) 251–278.
- [154] H.H. Rose, *J. Electron Microsc.* 58 (2009) 77–85.
- [155] P.E. Batson, N. Dellby, O.L. Krivanek, *Nature* 418 (2002) 617–620.
- [156] G. Fritz, U.G. Oppel, *Mathematical Aspects of Computerized Tomography*, Springer Berlin Heidelberg, Berlin, Heidelberg, 1981, pp. 57–80.
- [157] R.A. Crowther, D.J. DeRosier, A. Klug, *Proc. R. Soc. A* 317 (1970) 319–340.
- [158] M. Radermacher, W. Hoppe, *W. Proc. 7th Eur. Congr. Electr. Micr.* (180) 132.
- [159] David N. Mastronarde, *J. Struct. Biol.* 120 (1997) 343–352.
- [160] R. Gordon, R. Bender, G.T. Herman, *J. Theor. Biol.* 29 (1970) 471–481.
- [161] C. Messaoudii, T. Boudier, C.O. Sanchez Sorzano, S. Marco, *BMC Bioinf.* 8 (2007) 288–292.
- [162] A. Fedorov, R. Beichel, J. Kalpathy-Cramer, J. Finet, J.-C. Fillion-Robin, S. Pujol, C. Bauer, D. Jennings, F. Fennessy, M. Sonka, J. Buatti, S. Aylward, J.V. Miller, S. Pieper, R. Kikinis, *Magn. Reson. Imaging* 30 (2012) 1323–1341.
- [163] 3DSlicer. Available from: <https://www.slicer.org/>.
- [164] F. Wu, N. Yao, *Nano Energy* 13 (2015) 735–756.
- [165] S. Giorgio, S. Sao Joao, S. Nitsche, D. Chaudanson, G. Sitja, C.R. Henry, *Ultramicroscopy* 106 (2006) 503–507.

- [166] L.F. Allard, S.H. Overbury, W.C. Bigelow, M.B. Katz, D.P. Nackashi, J. Damiano, *Microsc. Microanal.* 18 (2012) 656–666.
- [167] D. Gardinier, F. Walden, J. Damiano (2015) US9466459B2.
- [168] J. Damiano, D. Nackashi, S. Mick (2011) US8829469B2.
- [169] E.O. Stejskal, J.D. Memory, *High resolution NMR in the solid state: Fundamentals of CPMAS*, Oxford University Press, New York, 1994.
- [170] M.J. Duer, *Solid-state NMR: Principles and applications*, Blackwell Science, Malden, 2002.
- [171] J. Feng, J.A. Reimer, *J. Magn. Reson.* 209 (2011) 300–305.
- [172] S.P. Brown, H.W. Spiess, *Chem. Rev.* 101 (2001) 4125–4156.
- [173] D. Massiot, F. Fayon, M. Capron, I. King, S. Le Calvé, B. Alonso, J.-O. Durand, B. Bujoli, Z. Gan, G. Hoatson, *Magn. Reson. Chem.* 40 (2002) 70–76.
- [174] J. van Bokhoven, C. Lamberti (Eds.), *X-ray absorption and X-ray emission spectroscopy: Theory and applications*, John Wiley & Sons Inc, Chichester, West Sussex, 2016.
- [175] M. Munoz, *Spectroscopie d'adsorption des rayons X: Lecture, Formation en Absorption X pour la Maitrise de l'Expérience et le Pilotage d'une Ligne Utilisant un Synchrotron*, CNRS, 2017.
- [176] S. Calvin, *XAFS for everyone*, CRC Press, Boca Raton, 2013.
- [177] J.-D. Grunwaldt, A. Baiker, *Phys. Chem. Chem. Phys.* 7 (2005) 3526–3539.
- [178] Y. Joly, S. Grenier, in: J. van Bokhoven, C. Lamberti (Eds.), *X-ray absorption and X-ray emission spectroscopy: Theory and applications*, John Wiley & Sons Inc, Chichester, West Sussex, 2016, pp. 73–97.
- [179] International Union of Crystallography, *Online Dictionary of Crystallography: Extended X-ray absorption fine structure (EXAFS)*. Available from: [http://reference.iucr.org/dictionary/Extended\\_X-ray\\_absorption\\_fine\\_structure\\_\(EXAFS\)](http://reference.iucr.org/dictionary/Extended_X-ray_absorption_fine_structure_(EXAFS)).

- [180] G. Brown and G. Waychunas, X-ray Absorption Spectroscopy: Introduction to Experimental Procedures. Available from: [http://www-ssrl.slac.stanford.edu/mes/xaafs/xas\\_intro.html](http://www-ssrl.slac.stanford.edu/mes/xaafs/xas_intro.html).
- [181] ESRF, BM16 - FAME-UHD. Available from: <http://www.esrf.eu/home/UsersAndScience/Experiments/CRG/bm16.html>.
- [182] O. Proux, E. Lahera, W. Del Net, I. Kieffer, M. Rovezzi, D. Testemale, M. Irar, S. Thomas, A. Aguilar-Tapia, E.F. Bazarkina, A. Prat, M. Tella, M. Auffan, J. Rose, J.-L. Hazemann, *J. Environ. Qual.* 46 (2017) 1146–1157.
- [183] A. Aguilar-Tapia, S. Ould-Chikh, E. Lahera, A. Prat, W. Delnet, O. Proux, I. Kieffer, J.-M. Basset, K. Takanabe, J.-L. Hazemann, *Rev. Sci. Instrum.* 89 (2018) 35109.
- [184] B. Ravel, M. Newville, *J. Synchrotron Radiat.* 12 (2005) 537–541.
- [185] M. Munoz, P. Argoul, F. Farges, *Am. Mineral.* 88 (2003) 694–700.
- [186] M. Munoz, P. Argoul, F. Farges, Wavelet Transform of XAFS Spectra. Available from: <http://perso.u-pem.fr/farges/wav/>.
- [187] M. Ochi, I. Yamada, K. Ohgushi, Y. Kusano, M. Mizumaki, R. Takahashi, S. Yagi, N. Nishiyama, T. Inoue, T. Irifune, *Inorg. Chem.* 52 (2013) 3985–3989.
- [188] K.-J. Range, F. Rau, U. Klement, A.M. Heyns, *Mater. Res. Bull.* 22 (1987) 1541–1547.
- [189] H. Hoekstra, S. Siegel, F. Gallagher, in: *Platinum Group Metals and Compounds*, American Chemical Society, 1971, pp. 39–53.
- [190] S. Calvin, Iffeffit mailing list: k range, 2004. Available from: <http://millenia.cars.aps.anl.gov/pipermail/iffeffit/2004-April/000902.html>.
- [191] B. Ravel, Iffeffit mailing list: Amplitude and the EXAFS equation, 2002. Available from: <http://millenia.cars.aps.anl.gov/pipermail/iffeffit/2002-October/000158.html>.
- [192] F. Rau, U. Klement, K.-J. Range, *Z. Kristallogr.* 210 (1995).
- [193] B. Ravel, S.D. Kelly, AIP Conference Proceedings, AIP, 2007, pp. 150–152.
- [194] O. Bunau, Y. Joly, *J. Phys.: Condens. Matter* 21 (2009) 345501–345512.
- [195] P. Hohenberg, W. Kohn, *Phys. Rev.* 136 (1964) B864–B871.

- [196] W. Kohn, L.J. Sham, *Phys. Rev.* 140 (1965) A1133-A1138.
- [197] J.P. Perdew, K. Burke, M. Ernzerhof, *Phys. Rev. Lett.* 77 (1996) 3865–3868.
- [198] S.N. Steinmann, C. Corminboeuf, *J. Chem. Theory Comput.* 7 (2011) 3567–3577.
- [199] G. Kresse, J. Hafner, *Phys. Rev. B* 49 (1994) 14251–14269.
- [200] G. Kresse, J. Furthmüller, *Comp. Mater. Sci.* 6 (1996) 15–50.
- [201] G. Kresse, D. Joubert, *Phys. Rev. B* 59 (1999) 1758–1775.
- [202] J.R. Yates, C.J. Pickard, F. Mauri, *Phys. Rev. B* 76 (2007) 24401.
- [203] C.J. Pickard, F. Mauri, *Phys. Rev. B* 63 (2001) 245101.
- [204] R. Wischert, P. Laurent, C. Copéret, F. Delbecq, P. Sautet, *J. Amer. Chem. Soc.* 134 (2012) 14430–14449.
- [205] A. Jahel, P. Avenier, S. Lacombe, J. Olivier-Fourcade, J.-C. Jumas, *J. Catal.* 272 (2010) 275–286.
- [206] H. Lieske, *J. Catal.* 81 (1983) 8–16.
- [207] S. Miguel, O.A. Scelza, A.A. Castro, *Appl. Catal.* 44 (1988) 23–32.
- [208] A. Munoz-Paez, D.C. Koningsberger, *J. Phys. Chem.* 99 (1995) 4193–4204.
- [209] M. Moses-DeBusk, M. Yoon, L.F. Allard, D.R. Mullins, Z. Wu, X. Yang, G. Veith, G.M. Stocks, C.K. Narula, *J. Am. Chem. Soc.* 135 (2013) 12634–12645.
- [210] O. Said-Aizpuru, Intégration de descripteurs catalytiques dans des modèles cinétiques. Application en aromatisation du n-heptane.: Doctoral project, IFPEN, IRCELYON, 2017-2020.
- [211] G. Clet, J.-M. Goupil, D. Cornet, *Bull. Soc. Chim. Fr* 134 (1997) 223–233.
- [212] ILO, International Chemical Safety Cards: Aluminium oxide. Available from:  
[http://www.ilo.org/dyn/icsc/showcard.display?p\\_lang=en&p\\_card\\_id=0351&p\\_version=2](http://www.ilo.org/dyn/icsc/showcard.display?p_lang=en&p_card_id=0351&p_version=2).





# Appendixes



## A. XANES spectra and EXAFS fitting of reference compounds

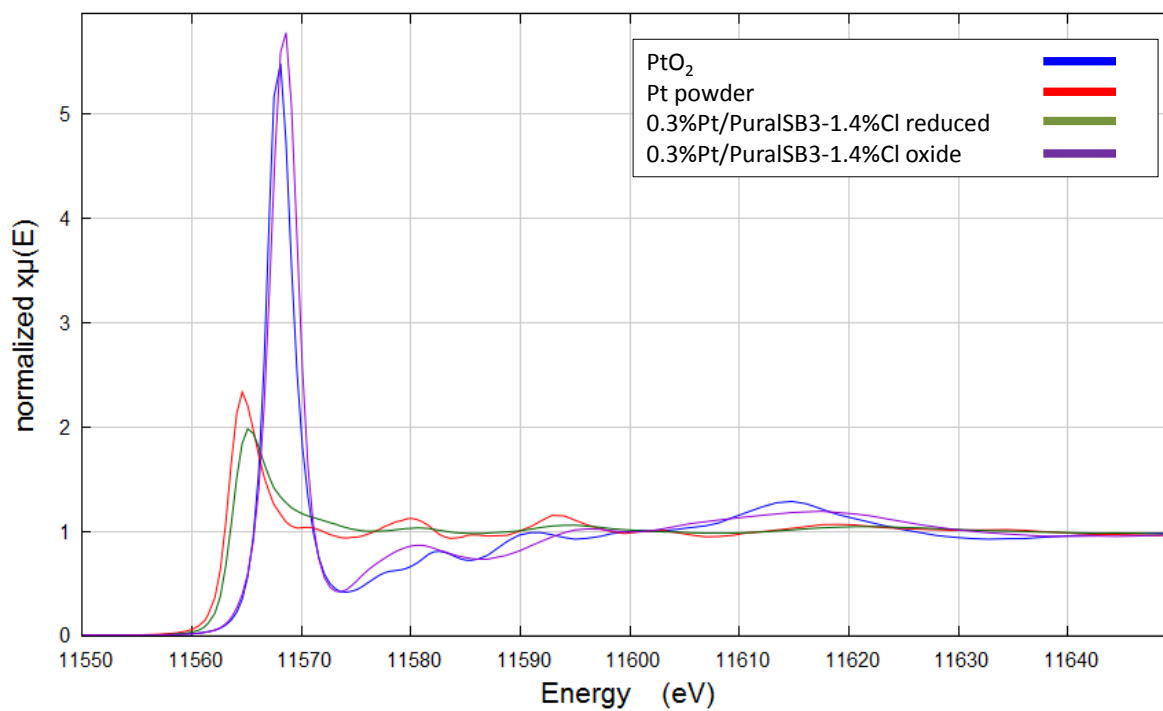
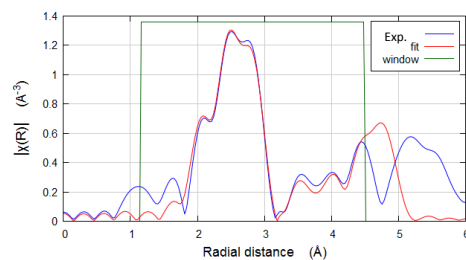
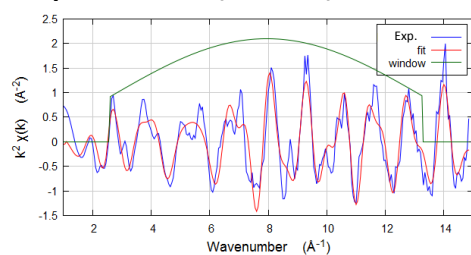
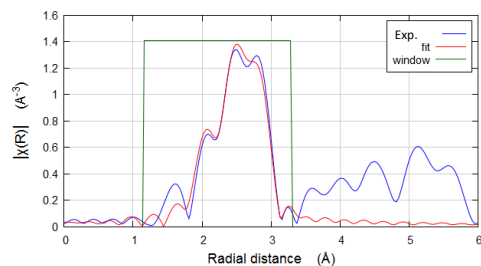
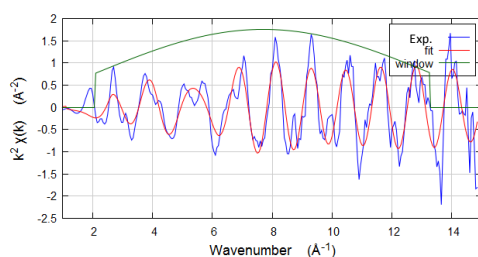


Figure Appendix- 1 – Pt L<sub>3</sub> edge HERFD-XANES spectra of references PtO<sub>2</sub> and metallic Pt powder obtained at BM16 in 2017 and of reduced and oxide 0.3%Pt/PuralSB3-1.4%Cl for comparison.

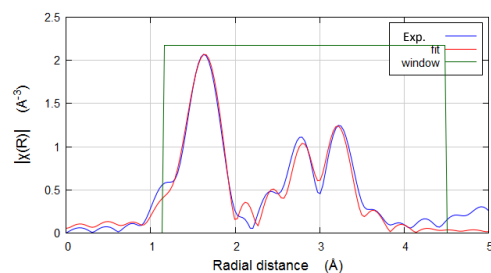
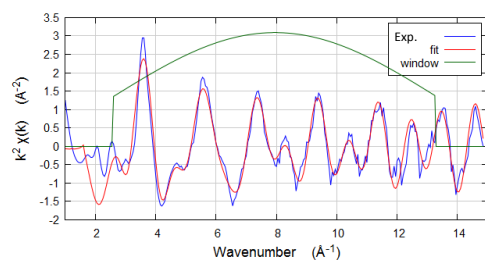
### a) Pt powder (2017)



### b) Pt powder (2018)



### c) PtO<sub>2</sub> (2017)



### d) PtO<sub>2</sub> (2018)

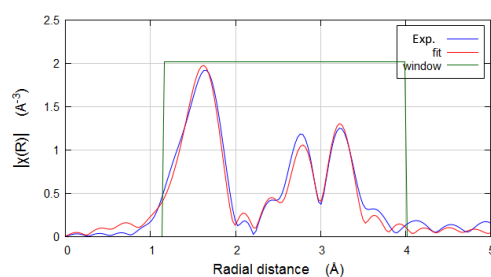
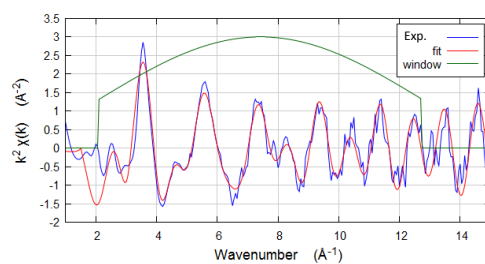


**Figure Appendix- 2 – EXAFS and magnitude of the Fourier Transform weighted by  $k^2$  of the references Pt powder and PtO<sub>2</sub> (acquired in 2017 and 2018 at BM16).**

*Table Appendix- 1 – EXAFS fitting of reference corresponding to the red line on the figure above. \*Crystallographic structure ID in parenthesis; \*\*Coordination number is fixed*

	Path origin*	Path	Coordination number**	R (Å)	$\sigma^2$ (Å <sup>2</sup> )	$S_0^2$	$\Delta E_0$	R-factor	N <sub>ind</sub>	N <sub>par</sub>
Pt powder (2017)	Pt bulk (4334349)	Pt-Pt (1)	12	2.764±0.005	0.006±0.001	0.81±0.03	4.29±0.73	0.02	20	10
		Pt-Pt (2)	6	3.89±0.02	0.007±0.002					
		Pt-Pt (3)	24	4.79±0.01	0.06±0.002					
		Pt-Pt (4)	48	4.2±0.1	0.03±0.04					
Pt powder (2018)	Pt bulk (4334349)	Pt-Pt	12	2.773	0.005±0.001	0.77±0.09	4.69±0.92	0.02	15	4
PtO <sub>2</sub> (2017)	PtO <sub>2</sub> (1530633)	P-O (1)	6	2.013±0.006	0.002±0.002	0.89±0.04	9.93±0.76	0.02	18	10
	PtO <sub>2</sub> (1537410)	Pt-Pt	6	3.102±0.006	0.002±0.001					
		Pt-O (2)	6	3.66±0.03	0.004±0.006					
		Pt-O (3)	6	4.04±0.04	0.01±0.01					
PtO <sub>2</sub> (2018)	PtO <sub>2</sub> (1530633)	P-O (1)	6	2.009±0.008	0.003±0.002	0.86±0.05	8.65±0.94	0.02	18	12
	PtO <sub>2</sub> (1537410)	Pt-Pt	6	3.100±0.010	0.002±0.001					
		Pt-O (2)	6	3.67±0.05	0.003±0.007					
		Pt-O (3)	6	3.6±0.1	0.01±0.02					
		Pt-O (4)	6	4.05±0.08	0.02±0.02					

## B. XRD diffractograms of PuralSB3 and TH100 $\gamma$ -aluminas

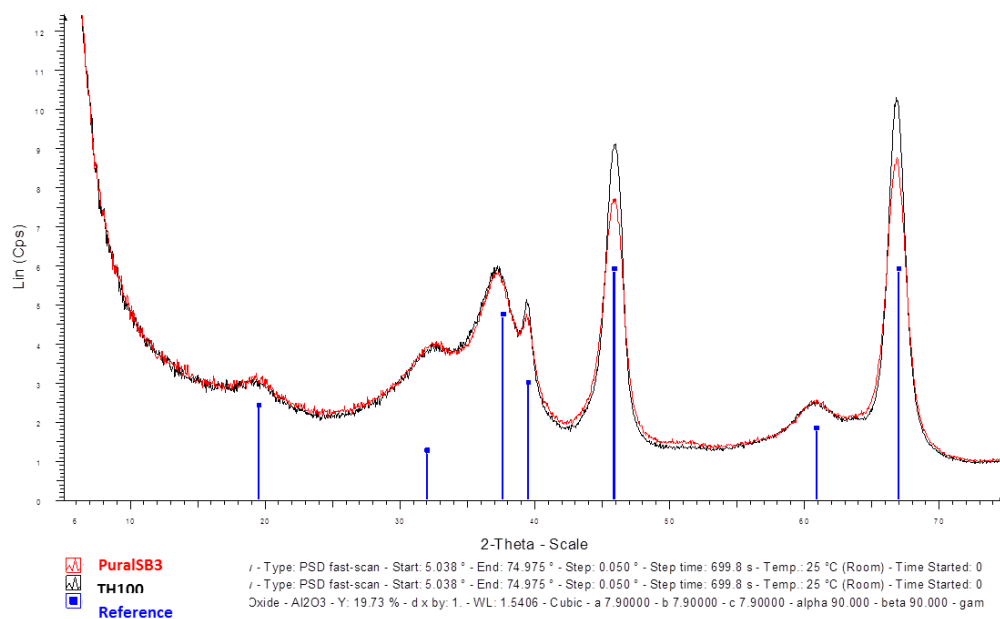


Figure Appendix- 3 – XRD diffractograms of PuralSB3 and TH100  $\gamma$ -alumina supports.

### ***C. Consumed H<sub>2</sub> volume and temperature of maximum H<sub>2</sub> consumption issued from TPR analysis of PuralSB3 impregnated+calcined materials and oxide catalysts***

*Table Appendix- 2 – Temperature interval (T<sub>i</sub> and T<sub>f</sub>) for peak integration used to calculate consumed H<sub>2</sub> volume and temperature of maximum H<sub>2</sub> consumption issued from TPR analysis of PuralSB3 impregnated+calcined materials and oxide catalysts.*

Sample		T <sub>i</sub> for integration (°C)	T <sub>f</sub> for integration (°C)	Consumed H <sub>2</sub> volume (mL/g <sub>cata.</sub> )	T of max consumption (°C)
0.3%Pt/PuralSB3	Impreg+Calc	174	474	0.8 ± 0.1	327 ± 15
	1.4%Cl oxide	140	410	0.7 ± 0.1	289 ± 15
	1%Cl oxide	160	400	0.6 ± 0.1	305 ± 15
	0.5%Cl oxide	140	410	0.7 ± 0.1	304 ± 15
	0.1%Cl oxide	180	440	0.6 ± 0.1	308 ± 15
0.6%Pt/PuralSB3	Impreg+Calc	140	460	1.5 ± 0.2	306 ± 15
	1.4%Cl oxide	160	450	1.4 ± 0.2	312 ± 15
	1%Cl oxide	130	415	1.5 ± 0.2	299 ± 15
	0.5%Cl oxide	140	430	1.3 ± 0.2	315 ± 15
	0.1%Cl oxide	180	470	1.2 ± 0.2	329 ± 15
1%Pt/PuralSB3	Impreg+Calc	100	410	2.4 ± 0.4	283 ± 15
	1.4%Cl oxide	100	435	2.2 ± 0.3	306 ± 15
	1%Cl oxide	100	425	2.4 ± 0.4	299 ± 15
	0.5%Cl oxide	140	440	2.3 ± 0.3	329 ± 15
	0.1%Cl oxide	140	465	2.3 ± 0.3	324 ± 15



## D. $E_0$ edge energy value found for each sample analysed by XAS

Table Appendix- 3 -  $E_0$  value found by Athena for each samples analysed by XAS according to two definitions: as the energy of the peak of the white line or as the first peak of the first derivative of  $\mu(E)$ .

	$E_0$ (eV)	
	Peak of WL	First peak of $d\mu(E)/dE$
Oxide catalysts		
0.3%Pt/PuralSB3-0.1%Cl	11568.7	11567.6
0.3%Pt/PuralSB3-1.4%Cl	11568.5	11567.6
1%Pt/PuralSB3-0.1%Cl	11568.6	11567.1
1%Pt/PuralSB3-1.4%Cl	11568.4	11567.1
0.3%Pt/TH100-0.1%Cl	11567.7	11567.1
0.3%Pt/TH100-1.4%Cl	11568.3	11567.5
1%Pt/TH100-0.1%Cl	11567.9	11567.1
1%Pt/TH100-1.4%Cl	11568.2	11567.5
Reduced catalysts		
0.3%Pt/PuralSB3-0.1%Cl	11565.7	11564.1
0.3%Pt/PuralSB3-1.4%Cl	11565.2	11564.1
1%Pt/PuralSB3-0.1%Cl	11565.7	11564.1
1%Pt/PuralSB3-1.4%Cl	11565.8	11564.1
0.3%Pt/TH100-0.1%Cl	11566.1	11564.6
0.3%Pt/TH100-1.4%Cl	11566.1	11564.6
1%Pt/TH100-0.1%Cl	11565.8	11564.6
1%Pt/TH100-1.4%Cl	11565.7	11564.1
References		
PtO <sub>2</sub>	11567.9	11567.1
Pt powder	11564.6	11563.6

The parameter  $E_0$  has many definitions in the context of XAS being usually called “edge energy”, although it is formally the energy used to calculate  $k$ . It can be chosen as the first peak of the first derivative of the spectrum (how it is automatically determined in Athena), halfway up the edge, at the top of the white line, etc. As indicated in the text, when comparing XANES spectra, this work uses the term “edge energy” to refer to the peak of the white line. This definition was found the most useful to discuss visual comparison between spectra. As described, for data treatment proposes the “ $E_0$ ” parameter in Athena was set to the same value for all samples. The  $E_0$  energy found by Athena using two methods, peak of the white line and first peak of the first derivative, is presented here for each sample to

serve as reference and to illustrate how the definition chosen can have an impact of a couple of eV.

### ***E. XANES spectra of reduced 0.3%Pt/TH100-0.1%Cl***

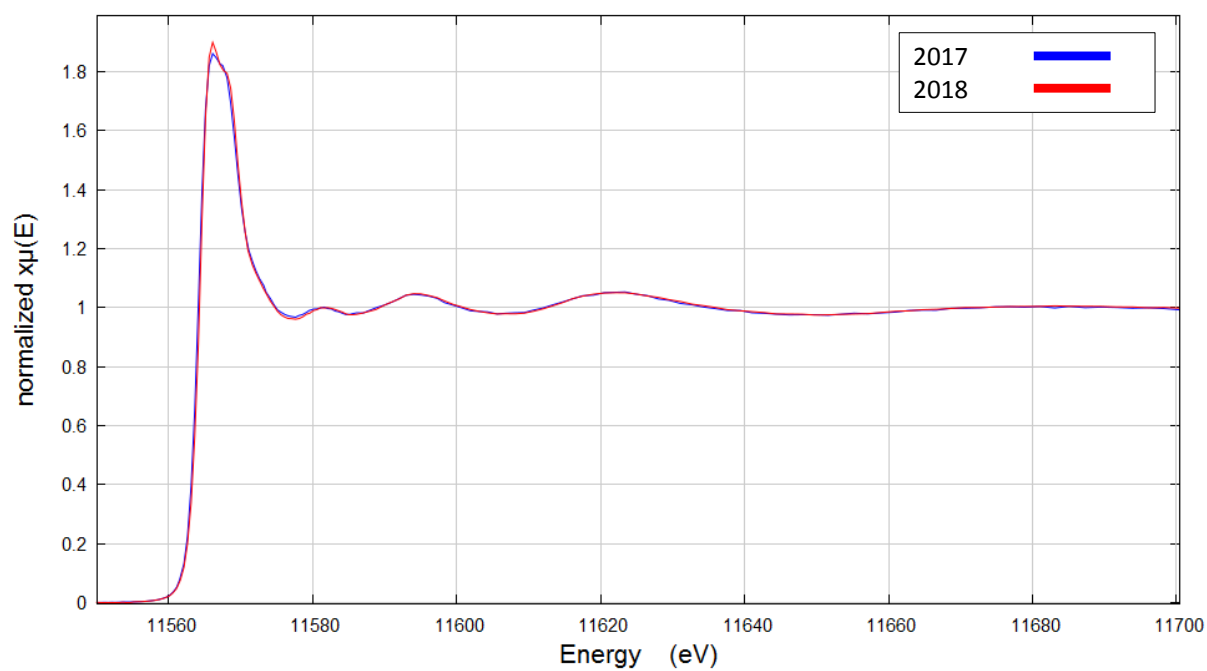


*Figure Appendix- 4 – Pt L<sub>3</sub> edge HERFD-XANES spectra of reduced 0.3%Pt/TH100-0.1%Cl acquire in two successive synchrotron runs in 2017 and 2018.*

## ***F. EXAFS Pt-Pt path amplitude at high wavenumber***

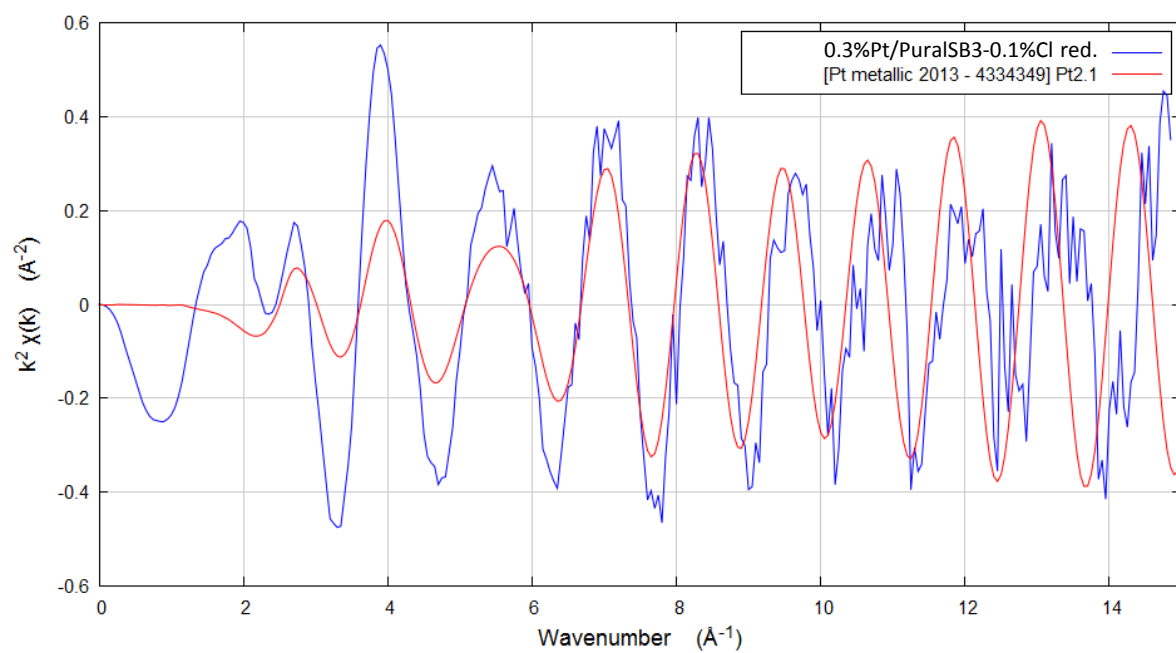


*Figure Appendix- 5 – EXAFS weighted by  $k^2$  of reduced 0.3%Pt/PuralSB3-0.1%Cl and of Pt-Pt path illustrating the amplitude of the Pt-Pt path at high wavenumbers.*

## G. EXAFS fitting of reduced catalysts with both Pt-O<sub>long</sub> and Pt-Al paths

Table Appendix- 4 - EXAFS fitting results for reduced catalysts considering both Pt-Al and Pt-O coordination for the light scatterer.  $E_0=11566.1$  eV;  $1.15 < R < 3.3$  Å.

Reduced catalyst	Path	Coordination number	R (Å)	$\sigma^2$ (Å <sup>2</sup> )	$\Delta E_0$ (eV)	R-factor
0.3%Pt/PuralSB3-0.1%Cl	Pt-O <sub>long</sub>	1.7±0.7	2.48±0.09	0.005±0.004	3.2±0.9	0.03
	Pt-Al	1.4±0.5	2.42±0.07			
	Pt-Pt	2.0±0.9	2.69±0.04	0.002±0.003		
1%Pt/PuralSB3-0.1%Cl	Pt-O <sub>long</sub>	1.3±0.6	2.49±0.09	0.005±0.005	3.1±0.9	0.03
	Pt-Al	1.0±0.5	2.47±0.07			
	Pt-Pt	2.9±0.9	2.70±0.03	0.002±0.002		
0.3%Pt/TH100-0.1%Cl	Pt-O <sub>long</sub>	1.1±0.6	2.44±0.5	0.005±0.004	2±1	0.05
	Pt-Al	1±0.6	2.45±0.08			
	Pt-Pt	3±1	2.69±0.08	0.003±0.002		
1%Pt/TH100-0.1%Cl	Pt-O <sub>long</sub>	1.5±0.6	2.47±0.07	0.006±0.004	2±1	0.04
	Pt-Al	1.5±0.6	2.45±0.07			
	Pt-Pt	3±1	2.72±0.04	0.003±0.002		

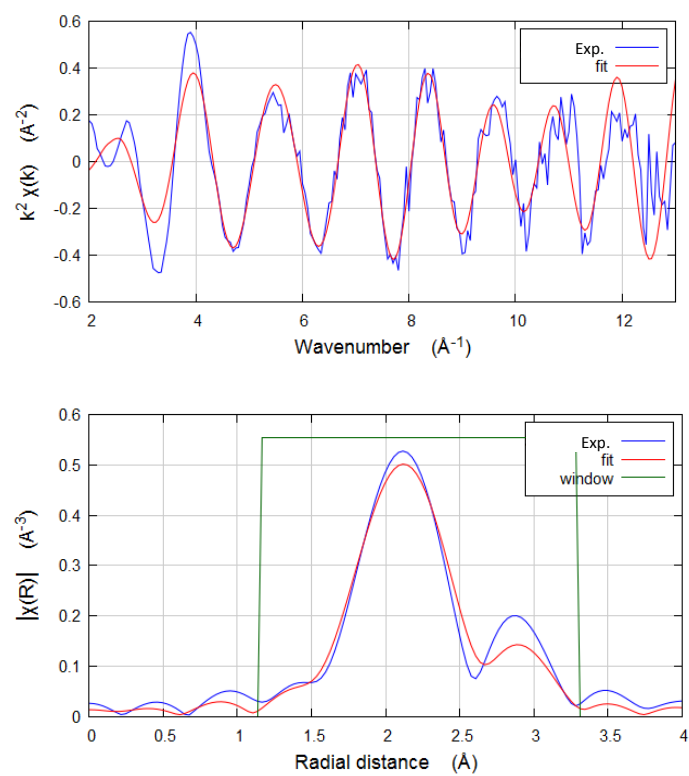


*Figure Appendix- 6 - EXAFS and magnitude of the Fourier Transform weighted by  $k^2$  of 1%Pt/PuralSB3-0.1%Cl in blue and fit of Table Appendix- 5 in red.*

## H. Supporting Information for publication draft of section 4.2.2

### DFT Pt<sub>13</sub>/edge models and binding energy

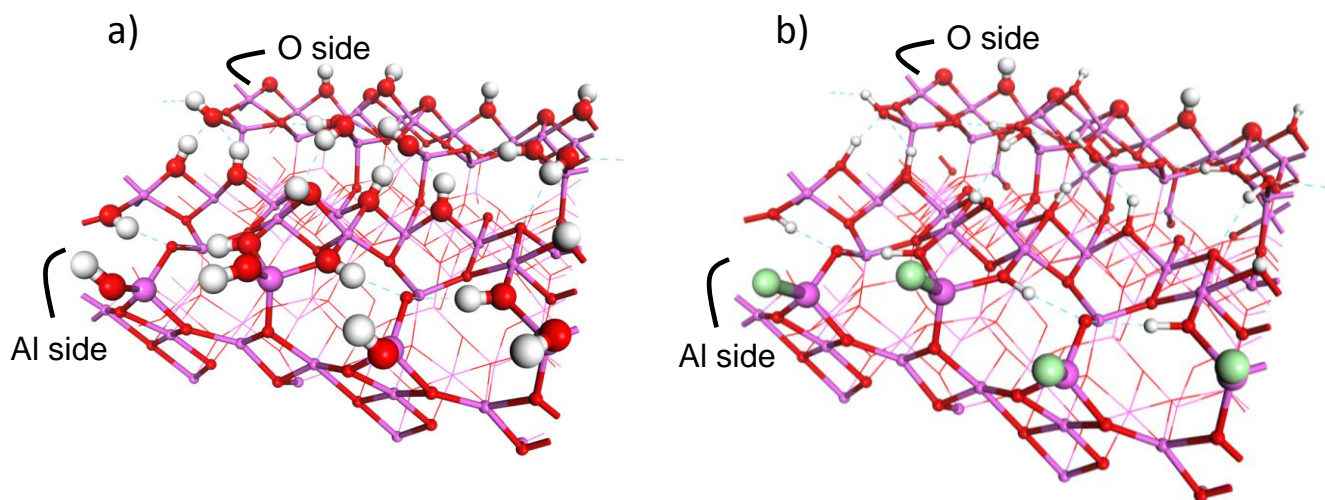
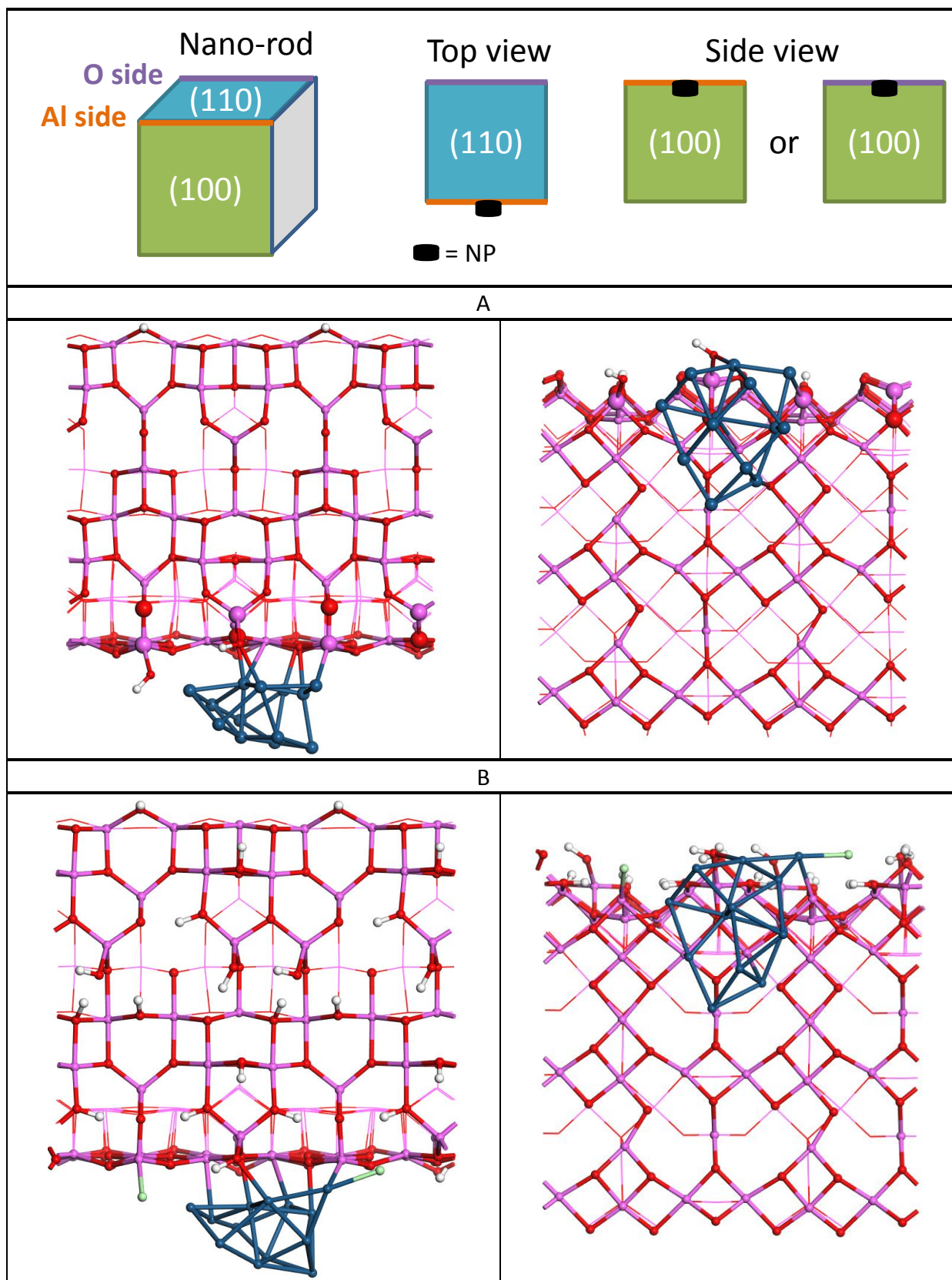


Figure S1.  $\gamma$ -Alumina (110)-(100) edge models a) hydrated with 6H<sub>2</sub>O and b) chlorinated with 2 Cl reported in reference[4].

Table S1. Binding energies of Pt<sub>13</sub>/edge models. Each model is identified by a letter (ID) and further details of the model are given, namely the hydration degree of the edge, the chlorination of the Al side, in which edge termination the NP was grafted and if an edge OH was migrated onto the NP. The models are ranked by order of stability.

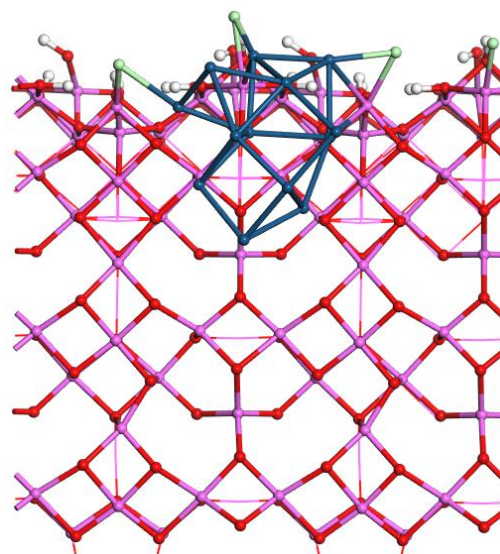
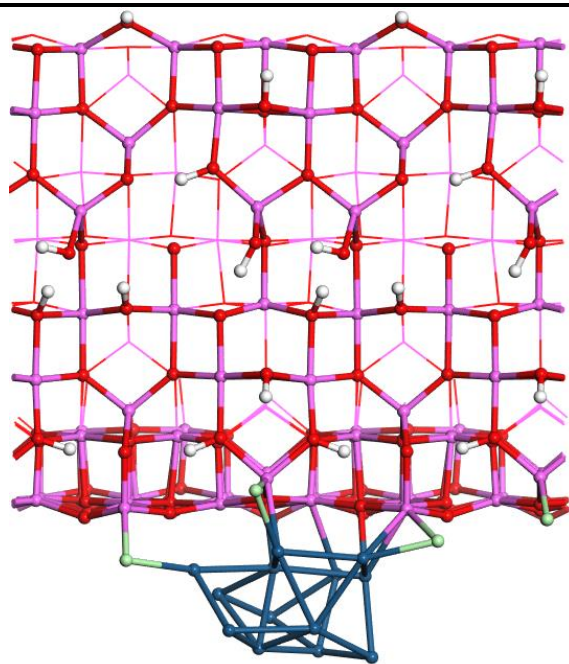
ID	Edge hydration	Edge chlorination	Edge termination	OH migration	E <sub>b</sub> (kJ.mol <sup>-1</sup> .Pt atom <sup>-1</sup> )
A	1H <sub>2</sub> O	-	Al side	-	-409
B	6H <sub>2</sub> O	1 Cl	Al side	-	-404
C	6H <sub>2</sub> O	2 Cl	Al side	-	-404
D	6H <sub>2</sub> O	-	O side	-	-403
E	6H <sub>2</sub> O	-	Al side	-	-400
F	6H <sub>2</sub> O	-	Al side	yes	-397
G	6H <sub>2</sub> O	-	Al side	yes	-395
H	6H <sub>2</sub> O	-	Al side	yes	-394
I	6H <sub>2</sub> O	-	Al side	yes	-393

Table S2. Optimized  $\text{Pt}_{13}$ /edge models as identified in Table 1 (ID). The first scheme illustrates the views of the nano-rod that are presented which are as follows: left - top view of the (110) side with Al-side edge facing down and O-side edge facing up; right - side view of the (100) side with edge facing up on the right side. Models color coded white – H; red – O; pink – Al; green – Cl; blue – Pt.

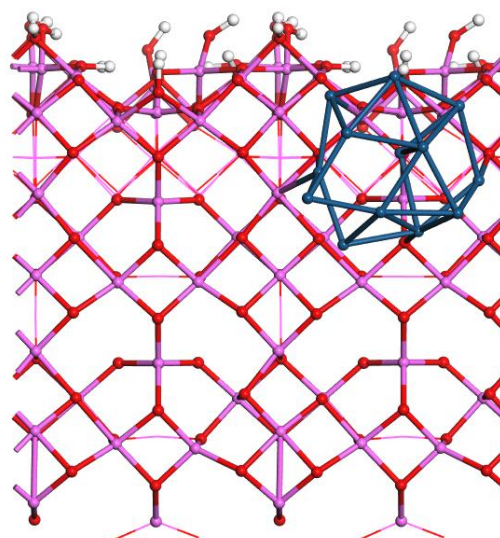
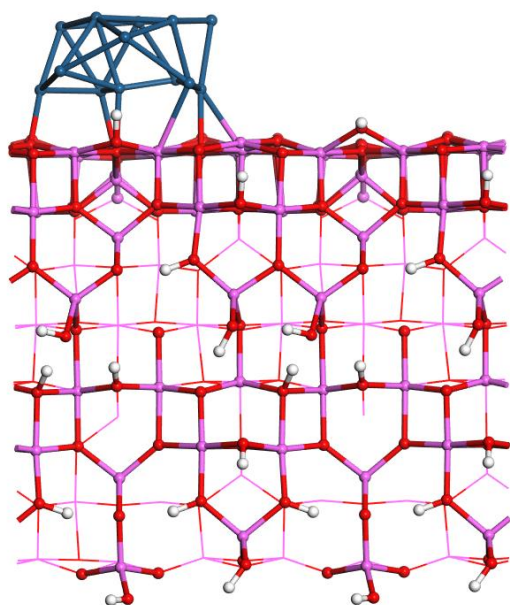




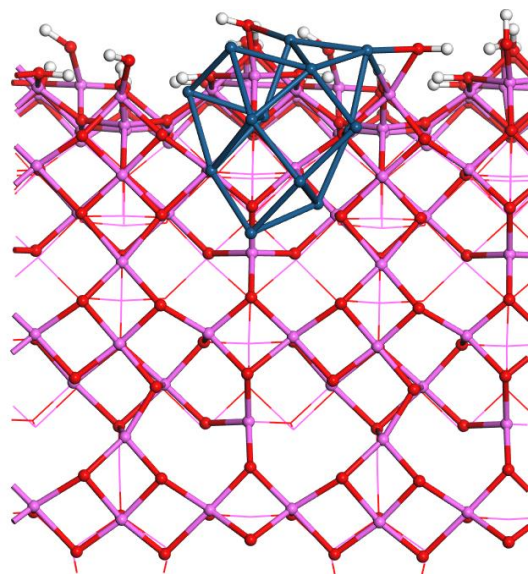
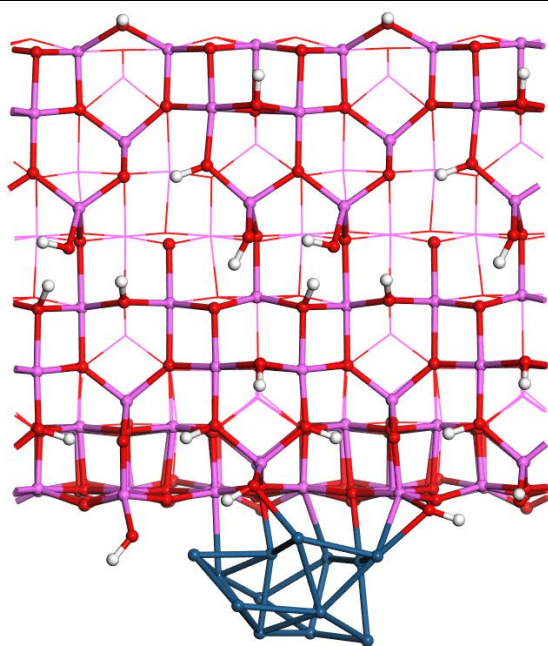
C



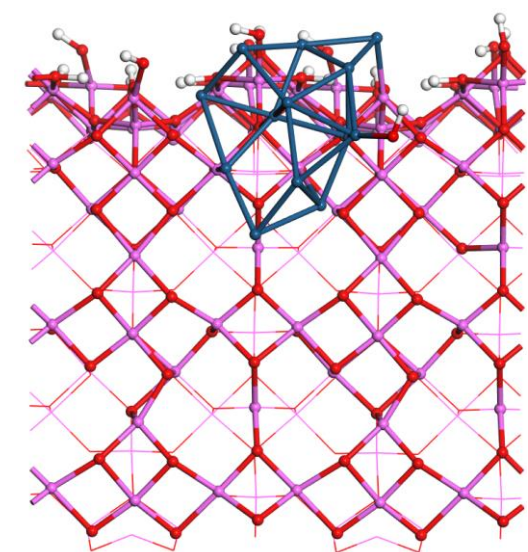
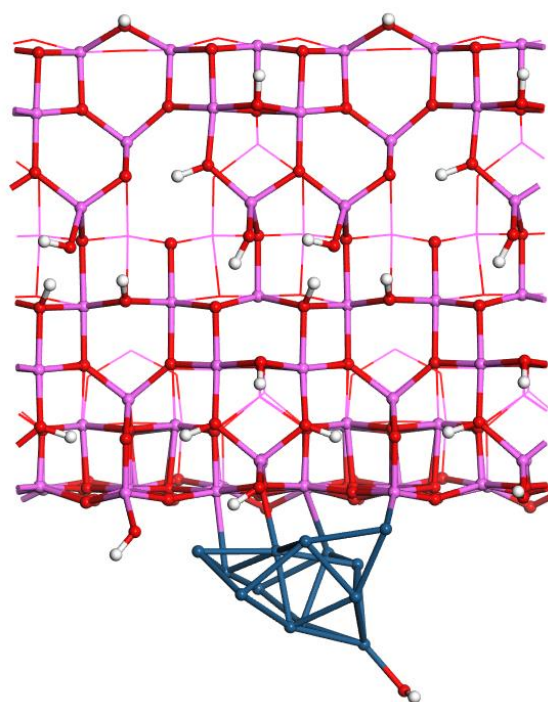
D



E

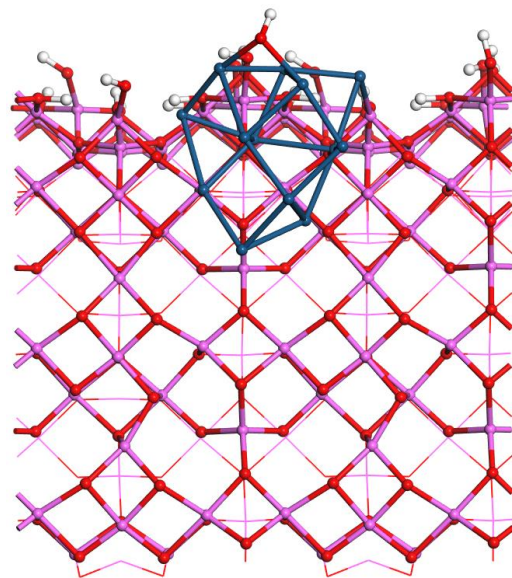
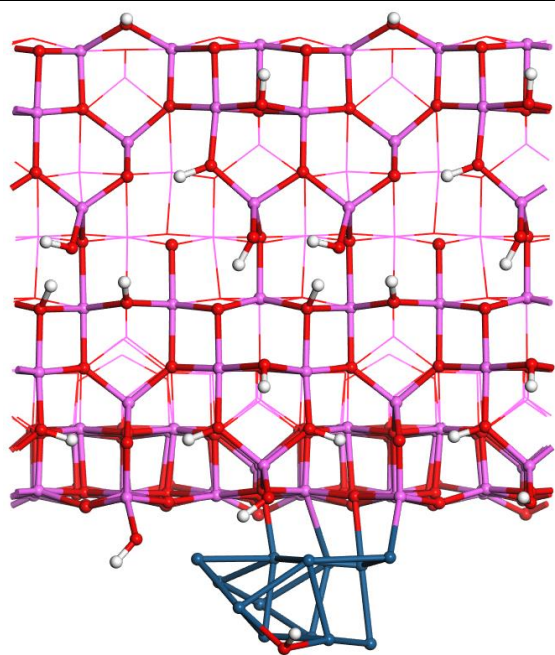


F

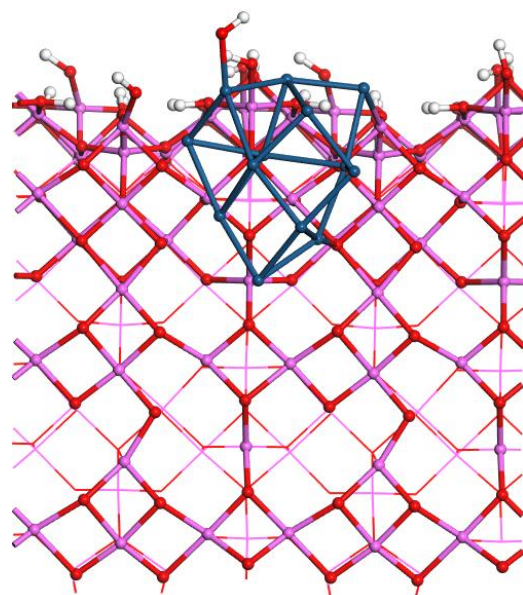
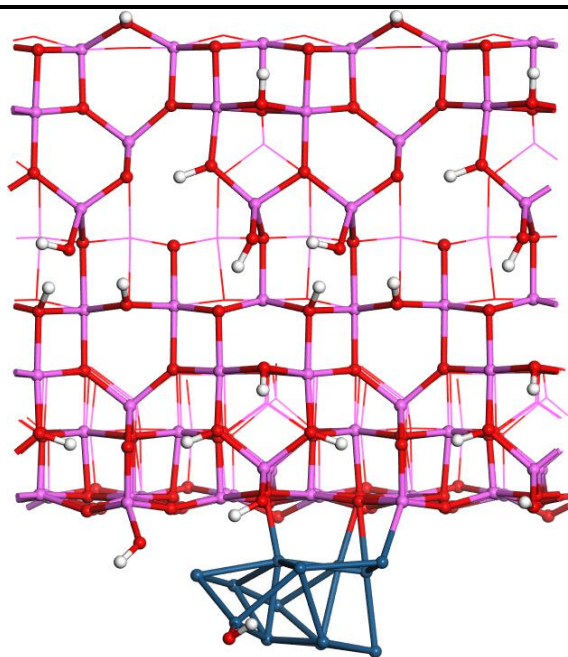


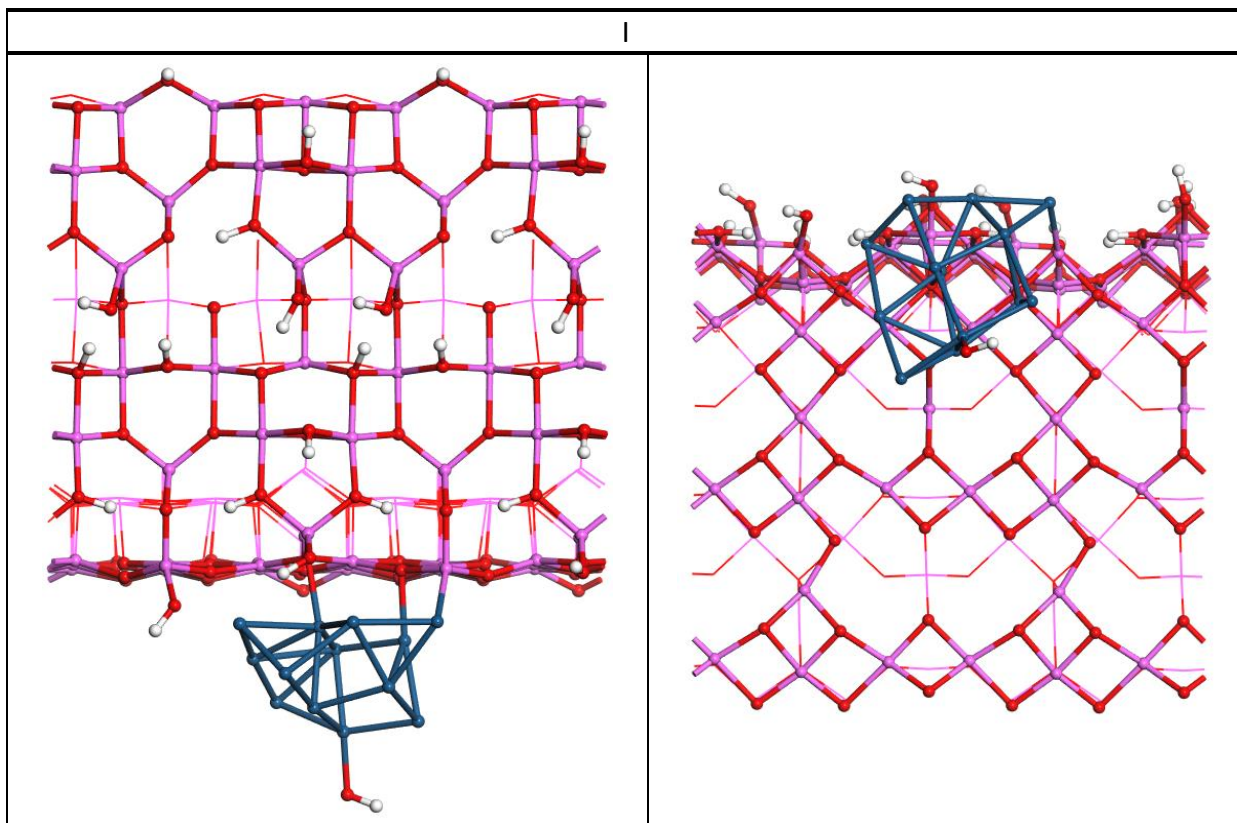


G



H





## Tomographic volumes

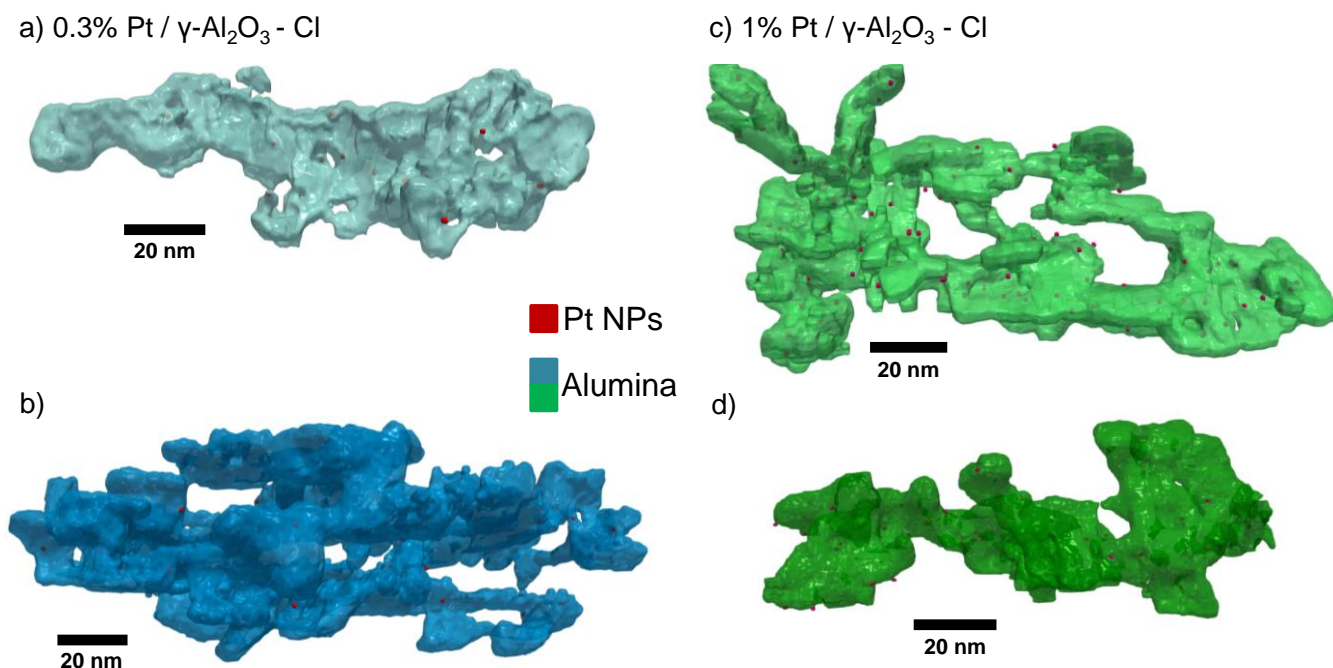


Figure S2. Segmented volumes obtained for both reduced catalysts: a) and b) 0.3%Pt/ $\gamma$ -Al<sub>2</sub>O<sub>3</sub>-Cl; c) and d) 1%Pt/ $\gamma$ -Al<sub>2</sub>O<sub>3</sub>-Cl.

Table S3. Detail, for each volume, of the number of NPs for which their location was evaluated and of which how many were located on edges of edge like structures (steps, kinks), on surface planes and for how many the location could not be unambiguously determined (Undetermined, due to deviations during segmentation the NP could be floating in the emptiness or inside the alumina).

# of NPs:	0.3%Pt/ $\gamma$ -Al <sub>2</sub> O <sub>3</sub> -Cl		1%Pt/ $\gamma$ -Al <sub>2</sub> O <sub>3</sub> -Cl	
	a)	b)	c)	d)
Evaluated for location	13	12	61	18
On edges/kinks/steps	11	7	38	7
On surface planes	2	2	9	4
Undetermined	0	3	14	7

## M-scalar and $\sigma_C$

*Table S4. M-scalar values and  $\sigma_C$  obtained for the segmented object of each catalyst shown in Figure 7 of the main article using either the Pt nanoparticle positions or the homogeneously distributed points set.*

	M-scalar			
	NP positions	$\sigma_C$	Point set	$\sigma_C$
0.3%Pt/ $\gamma$ -Al <sub>2</sub> O <sub>3</sub> -Cl	1.27 <sup>a</sup>	0.07	1.25 <sup>c</sup>	0.01
1%Pt/ $\gamma$ -Al <sub>2</sub> O <sub>3</sub> -Cl	1.20 <sup>b</sup>	0.02	1.22 <sup>d</sup>	0.01

Number of NPs: a – 13, b – 131; Number of points in set: c – 182, d – 147

## ***I. Catalytic test protocol***

Testing of the catalysts for n-heptane reforming was performed as part of the doctoral works of Olivier Said-Aizpuru (IFPEN, IRCELYON), who also developed the test protocol.

An high throughput unit with several isothermal down flow fixed bed quartz reactors was used. The catalytic bed is filled with crushed catalyst only ( $>200\mu\text{m}$ ) and is placed above a layer of inert powder (Microblast<sup>TM</sup> B-120, Saint Gobain). In a first step the catalyst is reduced by heating at  $5^{\circ}\text{C}/\text{min}$  up to  $500^{\circ}\text{C}$  followed by a 10 minute plateau under  $\text{N}_2$  to dry the catalyst and then shifting to  $\text{H}_2$  flow (mixed with  $10\%_{\text{mol}}$  He), staying at  $500^{\circ}\text{C}$  for 2h more, after which the temperature is brought down to testing temperature at a rate of  $5^{\circ}\text{C}/\text{min}$ . During the reduction procedure, set up to mimic the ex situ reduction protocol (Reduction treatment 2.1.3.3), the reactor pressure is about atmospheric pressure. The test starts with a stabilization/deactivation stage under hydrocarbon (HC) flow (n-heptane, Reagent grade purity  $>99\%$ , AlfaAesar),  $\text{H}_2/\text{HC}=5$  (mol/mol), for 48h at  $410^{\circ}\text{C}$ . To explore n-heptane conversions ranging from 10% up to 80% in a single run, a test lasts for up to 9 days with varying conditions: the temperature varies from  $390$  to  $420^{\circ}\text{C}$ , pressure was set to 5 or 10 barg, and  $\text{H}_2/\text{HC}$  (mol/mol) to 3 or 5.

## J. IR analysis

To complement the NMR experiments, the alumina supports, acidified aluminas and some catalysts were also studied by infrared spectroscopy (IR) using a Bruker Vertex 70 spectrometer in transmission mode using about 20 mg of sample to prepare a self-supporting pellet. All samples were subjected to the reduction treatment described in section 2.1.3.3 and sealed in glass ampoules. The ampoules were opened and the pellet was then prepared in ambient air. The pellets were then treated in situ for 10h at 450°C under secondary vacuum before analysis. Surface properties information were obtained directly from the analysis of the hydroxyl region and indirectly using CO molecule to probe (at 77K) the acidic properties.

Figure Appendix- 7 presents the comparison between the IR spectra in the OH region of the two alumina supports (PuralSB3 and TH100) and corresponding acidified alumina samples with 1.4%Cl. The spectra exhibit the seven main features previously described in the literature for  $\gamma$ -alumina (see section 1.3.3.1). The impact of chlorine is clear with the disappearance of the signals at 3800  $\text{cm}^{-1}$  and 3775  $\text{cm}^{-1}$ . Note that the signal at 3725  $\text{cm}^{-1}$  seems to be more impacted by chlorine in the case of TH100 than of PuralSB3.

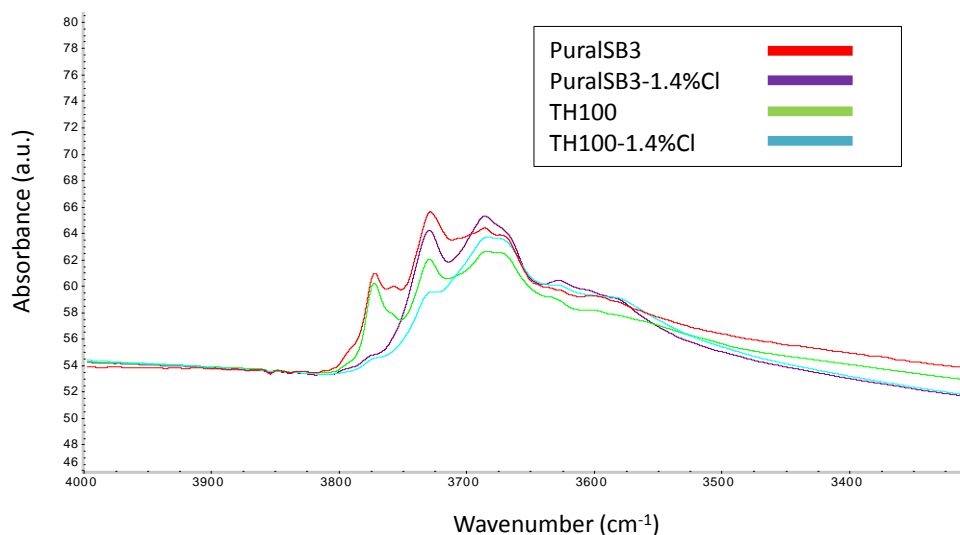


*Figure Appendix- 7 – IR spectra of alumina samples (normalized a.u./g) and acidified aluminas with 1.4%Cl loading in the 4000-3300  $\text{cm}^{-1}$  OH region.*

In addition, catalysts with 1%Pt loading and either 1.4%Cl or 0.1%Cl loading were analysed, and the presence of platinum had no impact on the OH spectra, as shown in Figure Appendix- 8. Indeed, the platinum surface coverage is very small compared to that of



hydroxyl groups. Note that the catalysts with 0.1%Cl loading are distinct from the corresponding non-chlorinated alumina samples in that the latter were never in contact with chlorine during their preparation and subsequent thermal treatments.

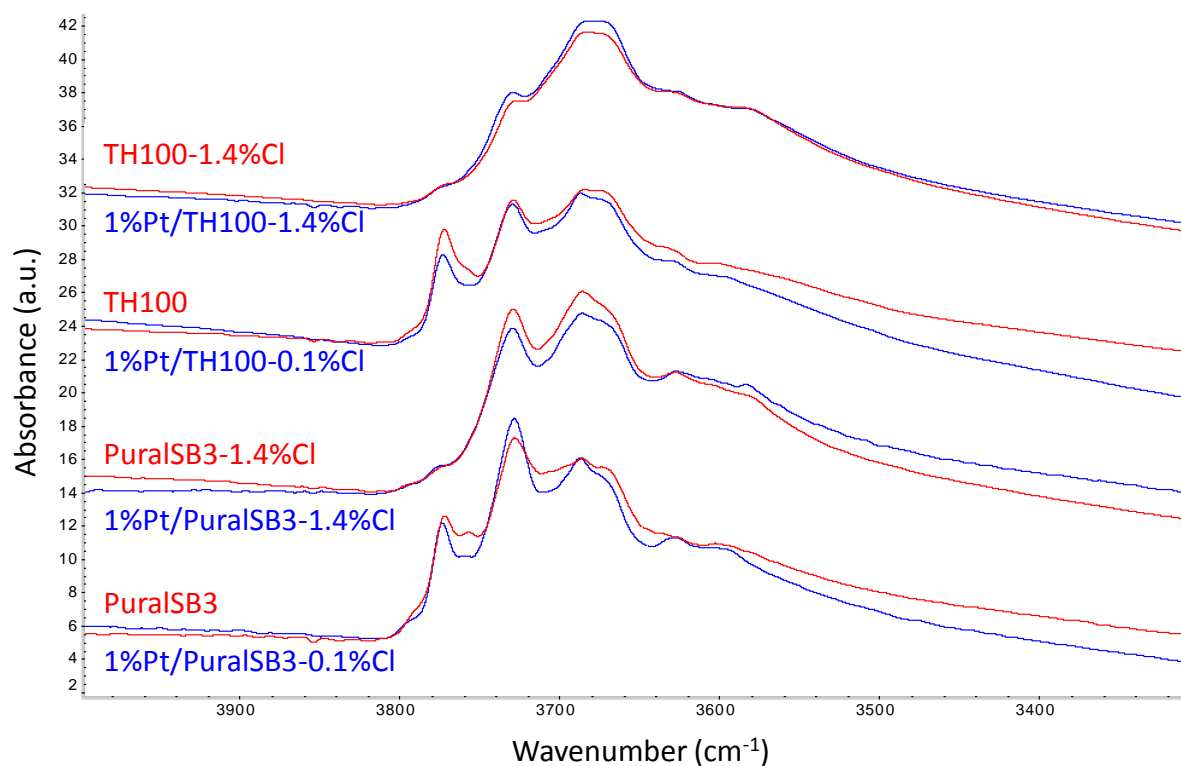


*Figure Appendix- 8 - IR spectra of alumina samples, acidified aluminas and selected catalysts with 1%Pt loading in the 4000-3300  $\text{cm}^{-1}$  OH region.*

The Lewis and Brønsted acid sites were characterized by CO adsorption, resulting in an acid site quantification per surface unit (in  $\text{a.u./m}^2$ ) as summarized in Figure Appendix- 9. Within measurement uncertainty, the quantity of Lewis and Brønsted acid sites per surface unit does not vary significantly regardless of support type, chlorine loading and presence or absence of platinum.

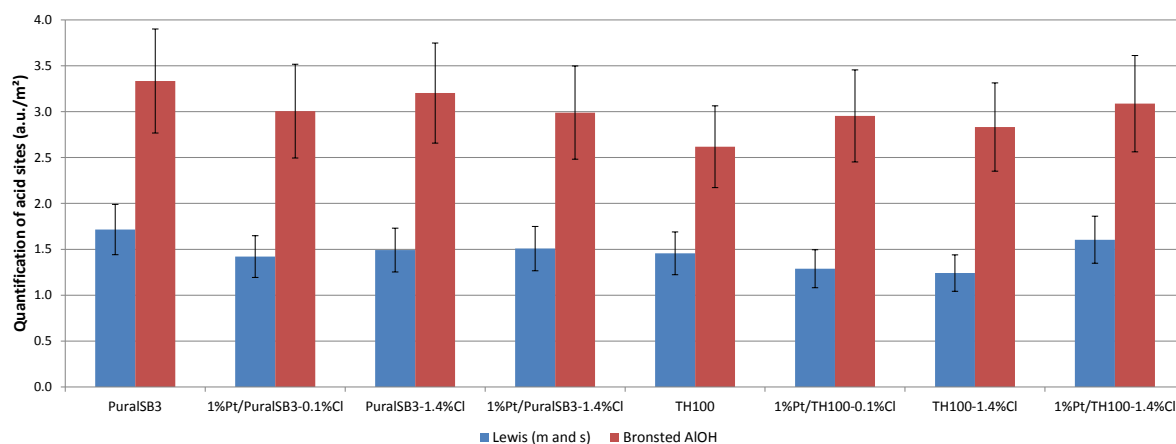


Figure Appendix- 9 – Relative quantification of acid sites, medium and strong Lewis sites in blue and Brønsted sites in red.

It is however noted that in presence of Cl, a blue shift of the  $\nu_{\text{CO}}$  band is observed in the IR spectra measured at CO saturation (Figure Appendix- 10), which indicates that the acidic strength of hydroxyl sites increases with the presence of 1.4%Cl.

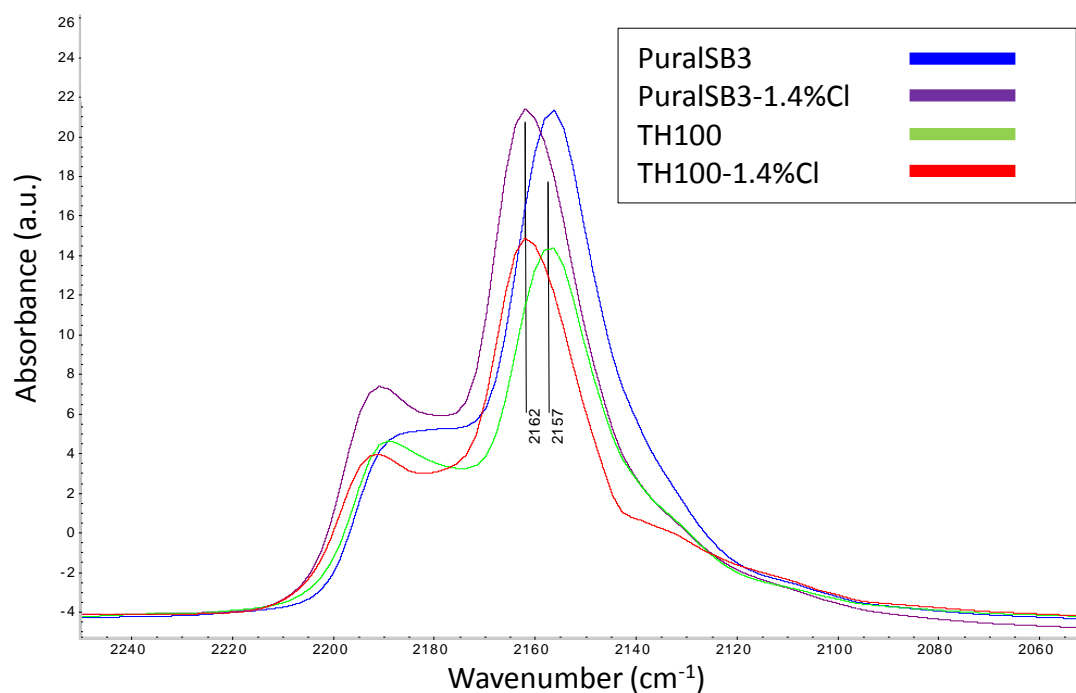


Figure Appendix- 10 –IR spectra in the CO region at saturation.





**Abstract:** Bifunctional heterogeneous catalysts consisting of metallic sites and acidic sites are used in various processes and the impact of active site proximity in catalytic efficiency can be expressed as an “intimacy criterion” according to the literature. Platinum supported on chlorinated  $\gamma$ -Al<sub>2</sub>O<sub>3</sub> is the traditional catalyst for catalytic naphtha reforming and is at the core of the present work. Herein, a multi-technique approach, including HR-HAADF-STEM, electron tomography, high field MAS NMR, HERFD-XANES, EXAFS, and DFT calculations, was applied to determine the location of the metallic and acidic sites on the Al<sub>2</sub>O<sub>3</sub> support crystallites for Pt/ $\gamma$ -Al<sub>2</sub>O<sub>3</sub>-Cl catalysts and to estimate the distance between such sites. The samples, representative of the industrial catalysts, were synthesized so as to vary the distance between the two types of sites as a function of three key parameters: %Pt, %Cl and Al<sub>2</sub>O<sub>3</sub> crystallite size and shape.

By building the first DFT model of crystallite edge between the (110) and (100) surfaces, an improved <sup>1</sup>H NMR peak assignment was proposed and it was found that  $\mu_1$ -OH on the edge are preferably exchanged with Cl. STEM analysis showed that reduced Pt nanoparticles are of 0.9 nm and that around 20% of Pt is in the form of single atoms, which are stabilized by Cl. By electron tomography it was revealed that Pt nanoparticles are mostly located on the edges of alumina crystallites and that the quantified inter-Pt particles distance is directly tuned through %Pt. A first geometrical model of the location of Pt and Cl on the catalyst is proposed. The improved understanding of the location of active sites and their proximity in catalytic reforming catalysts gained through this work paves the way to catalyst improvement based on tuning of active site location.

**Key-words:** platinum, alumina, chlorine, STEM, DFT, NMR, XANES, EXAFS, tomography, nanoparticle, edge, reforming

---

**Titre:** Exploration à l'échelle atomique de catalyseurs constitués de platine supporté sur alumine gamma chlorée

---

**Résumé:** Plusieurs procédés industriels utilisent des catalyseurs hétérogènes bifonctionnels avec des sites actifs métalliques et acides. L'influence de la distance entre les deux types de site actif sur l'activité et la sélectivité du catalyseur a souvent été décrite par un « critère d'intimité » dans la littérature. Les travaux reportés dans la présente thèse revisitent ce critère en étudiant des catalyseurs constitués de nanoparticules de platine supportées sur alumine gamma chlorée, utilisés en reformage catalytique des coupes pétrolières de type naphtha. Plusieurs techniques, dont la microscopie HR-HAADF-STEM, la tomographie électronique, les spectroscopies RMN MAS à hauts champs, HERFD-XANES, EXAFS et la simulation quantique (DFT), ont été utilisées pour déterminer la localisation des sites métalliques et acides sur les cristallites du support de façon à estimer la distance inter-sites. Les échantillons ont été préparés en faisant varier trois paramètres : teneur en Pt, teneur en Cl et taille et forme des cristallites.

Grâce au premier modèle DFT d'arête entre les surfaces (110) et (100) de l'alumine, une attribution plus détaillée des signaux <sup>1</sup>H NMR a été proposée montrant que les hydroxyles  $\mu_1$ -OH des arêtes sont plus favorablement échangés avec le Cl. L'étude STEM a révélé des nanoparticules de Pt de 0.9 nm et des atomes isolés qui représentent environ 20% du Pt et qui sont stabilisés par le Cl. Par tomographie électronique, il a été montré que les nanoparticules de Pt sont localisées sur les arêtes des cristallites et que la distance entre elles varie en fonction du %Pt. Enfin, un modèle géométrique du système catalytique Pt/ $\gamma$ -Al<sub>2</sub>O<sub>3</sub>-Cl est proposé. Grâce à cette compréhension avancée de la localisation des sites actifs, ce travail ouvre la voie à des améliorations futures des performances de cette famille de catalyseurs grâce au contrôle à l'échelle atomique de l'emplacement des sites actifs.

**Mots clés :** platine, alumine, chlore, STEM, DFT, RMN, XANES, EXAFS, tomographie, nanoparticule, arête, reformage

---